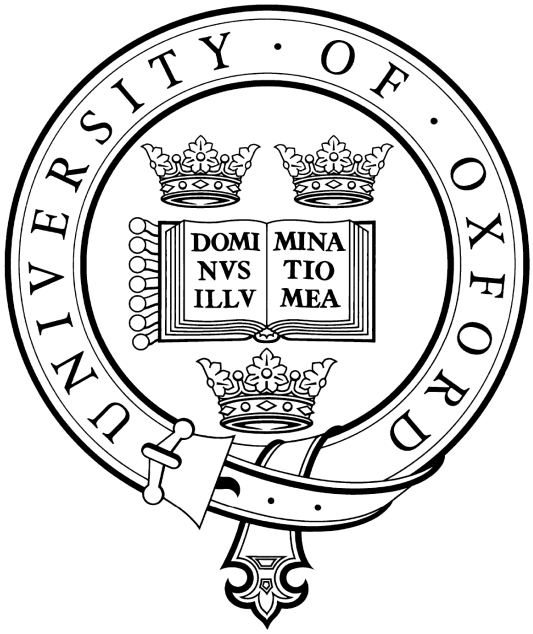
STARK DECELERATION AND REACTIVITY OF POLYATOMIC MOLECULES AND IONS AT LOW TEMPERATURES

Lee D. Harper

Merton College

University of Oxford



A thesis submitted for the degree of Doctor of Philosophy

Trinity Term 2013

STARK DECELERATION AND REACTIVITY OF POLYATOMIC MOLECULES AND IONS AT LOW TEMPERATURES

Lee D. Harper, Merton College

A thesis submitted in partial fulfilment of the requirements
for the degree of Doctor of Philosophy of the University of Oxford

Trinity Term, 2013

Abstract

This thesis describes the development of a new experimental technique for studying tunable-collision-energy, quantum state-selected, low-temperature ion-molecule reactions. This has been achieved through the combination of a Stark decelerator for neutral dipolar molecules, and a linear Paul ion trap.

The Stark deceleration process for ND_3 was examined in detail, through the analysis of experimental data in combination with newly written molecular dynamics simulation programs. In order to prepare a sample of molecules appropriate for collision studies, additional beamline components were introduced after the decelerator. These components were: two hexapoles, to provide transverse focussing, maximising the molecular density; a molecular buncher, providing increased longitudinal velocity resolution; and a fast-opening shutter, to separate decelerated molecules from undecelerated molecules. The sympathetic-cooling of Xe^+ ions and ND_3^+ ions by laser-cooled, Coulomb crystallised $^{40}Ca^+$ ions with the ion trap was also studied. In particular, the stable trapping of Xe^+ was demonstrated for the first time, and the experimental developments that led to this are discussed.

The work in this thesis represents significant progress towards studying the reaction of tunable-energy ND_3 in the $|j, mk\rangle = |1, -1\rangle$ quantum state with cold Xe^+ ions. Ion-molecule reactions utilising ND_3 molecules electrostatically guided through the Stark decelerator were performed. It was observed that the main source of error in these experiments was in the calculation of the initial number of Xe^+ ions that had been sympathetically cooled into the Coulomb crystal. The sensitivity of the crystal morphology to the number of Xe^+ ions was evaluated using molecular dynamics simulations. Strategies have been developed to reduce this uncertainty in future studies.

In addition to experimental work, the theory of low temperature ion-molecule reactions has been developed further. The temperature at which classical and quantum mechanical calculations diverge due to purely statistical effects has been investigated using different model intermolecular potentials, for closed-shell and open-shell species, and in the ground and rotationally excited states. From the results of these calculations, several promising candidate reactions have been suggested that might exhibit statistical quantum behaviour at experimentally achievable temperatures.

Acknowledgements

I'd like to start by giving thanks to all of the people that have believed in me over the years, and given me the motivation to succeed: Mrs. Newton at Wyke Primary School, Mrs. Fordyce and Mrs. Murray at St. Joseph's, Mrs. Swallow at Salesian College. To the amazing teachers at Alton College: Fiona Revell, Hilary Briggs, Roja Clark, Irene Middlemore and Andy Hibbert. To the academics of the Department for Applied Mathematics and Theoretical Physics and the Department of Chemistry at Cambridge University, particularly: Dr. Francis Pope and Dr. Tony Cox for their attentive and supportive research supervision; Dr. Mark Miller, Prof. Ian Smith, Dr. David Jefferson, Dr. Alston Misquita and Dr. Ken Riley for instilling in me the love of physical and theoretical chemistry, and applied mathematics.

I would like to thank Prof. Tim Softley for supervising me these last five years. I also offer particular thanks to Dr. Brianna Heazlewood and Prof. Heather Lewandowski for their help and support in this last year: this thesis would not exist without you. I would also like to thank Laura Pollum, Nabanita Deb, Katrin Dulitz and Dr. Chris Rennick for their support, both personally and with the project; and Dr. Claire Vallance and Dr. Stuart Mackenzie for listening. My thanks to the excellent staff in the electronics and mechanical workshops, particular Kevin, Phil and Charlie. And for previous work done on this project, to Dr. Martin Bell, Dr. Alex Gingell and James Oldham.

To Suzanne, for being my guardian angel in these last nine months, and to my family for always supporting unquestionably, if not always understanding the complex ins and outs of DPhil life. To my friends that have been supportive at various points over the years: Duncan, Ads, Frosty, Sian, Lorna, Kristine, Abi, James (both of you), Simon (yes both of you too!), Jason, Theresa, HMS, Fifi, Matt, Gi, Ant, Oz and all of the members of OUTriC, COSC and OUCCC that I have had the pleasure of training and competing with.

Contents

Abstract i

Acknowledgements ii

1 Introduction **1**

1.1 Introduction to Low Temperature Chemical Reactions 4

1.1.1 Barrierless Reactions and the Capture Model 4

1.1.2 The Quantum Nature of Low Temperature Reactions 7

1.2 Production and Trapping of Cold Species 10

1.2.1 Indirect Methods: Ultracold Molecules From Ultracold Atoms . 10

1.2.2 Direct Cooling of Molecular Beams 13

1.2.3 Trapping Cold Ions and Molecules 23

1.2.4 Applications of Cold Atoms and Molecules 26

1.3 Studying Low Temperature Chemistry 27

1.3.1 Studying Cold Chemistry With Molecular Beams 27

1.3.2 Cold Chemistry Using Trapped Ions and Molecules 29

1.4 Outline of This Thesis 30

2 Low Temperature Behaviour of Ion-Molecule Capture **33**

2.1 Theoretical Methods 34

2.1.1 Potential Energy Surfaces 34

2.1.2 The Effective Potential for Ion-Molecule Collisions 35

2.1.3 Rotationally Adiabatic Potentials 37
2.1.4 Low Temperature Classical Calculations 42
2.1.5 Statistical Adiabatic Channel Model 43
2.1.6 Statistical Quantum Capture Theory 44
2.2 The Onset of Quantum Behaviour 50
2.2.1 The Quantum-Classical Divergence Temperature 50
2.2.2 Ground State Linear Molecules 52
2.2.3 Excited Rotational States of Linear Molecules 57
2.2.4 Other Types of Molecule 61
2.3 Intermediate Temperature Behaviour For Selected Systems 67
2.3.1 The Ion-Dipole-Quadrupole Potential 67
2.3.2 Two-Temperature Rate Constant 69
2.4 Concluding Remarks 71
2.4.1 Suggested Experimental Directions 71
2.4.2 Limitations of the Model 73

3 The Stark Effect and Stark Decelerator Beamline for Ammonia 75
3.1 The Stark Effect for Ammonia Isotopologues 76
3.1.1 Zero Field Hamiltonian 77
3.1.2 The Stark Hamiltonian 80
3.1.3 Stark Splitting of Ammonia Isotopologues 81
3.2 Stark Deceleration of Ammonia 84
3.2.1 The Synchronous Trajectory 86
3.2.2 Molecular Dynamics Simulations 89
3.2.3 Non-Synchronous Longitudinal Trajectories 90
3.2.4 Transverse Stability 93
3.3 Experimental Setup 97

3.4 The Stark Decelerator Beamline 100
3.4.1 Transverse Hexapole Focussing 101
3.4.2 Longitudinal Bunching 104
3.5 Experimental Characterisation 108
3.5.1 High Voltage Conditioning 108
3.5.2 Phase Space Matching 109
3.5.3 Performance of the Stark Decelerator Beamline 110
3.6 Conclusions and Outlook 115

4 Ion Trapping of Xenon Ions with Laser-Cooled Calcium Ions 117

4.1 Spatial Confinement of Ions 117
4.1.1 The Principles of Ion Trapping 117
4.1.2 The Linear Paul Ion Trap 119
4.2 Production of Translationally Cold $^{40}Ca^{+}$ Ions 124
4.2.1 The Principle of Doppler Cooling 124
4.2.2 Laser Cooling Scheme for $^{40}Ca^{+}$ 126
4.3 Behaviour of Cold Trapped Ions 128
4.3.1 Coulomb Crystals 128
4.3.2 Sympathetic Cooling of Dark Ions 130
4.4 The Ion Trapping Experiment 132
4.4.1 Experimental Apparatus 132
4.4.2 Experimental Details 138
4.5 Characterisation of Coulomb Crystals 141
4.5.1 Simulation of Coulomb Crystals 141
4.5.2 Dark Core Volume Analysis 144
4.5.3 Experimental Considerations 146
4.6 Conclusions and Outlook 149

5 Towards Tunable-Energy, State-Selected Ion-Molecule Reactions 150

5.1 Chemical Background 150

5.1.1 The Reaction of Xenon Ions with Ammonia 150

5.1.2 Chemistry Involving Sympathetically-Cooled Ions 153

5.1.3 Determination of Rate Constants 156

5.1.4 Experimental Set-up 157

5.2 Results 157

5.2.1 The Stark Decelerator as an Electrostatic Guide 158

5.2.2 State-Selectivity in the Stark Decelerator 162

5.2.3 Sensitivity to Sympathetically Cooled Xenon Ions 162

5.2.4 Reaction of Guided ND_3 with Sympathetically-Cooled Xe^+ . . . 170

5.2.5 Comparison With the Dark Core Volume Analysis 175

5.3 Conclusions and Outlook 176

6 Conclusions and Further Work 179

6.1 Summary 179

6.2 Improvements and Future Work 181

A Supplementary Reaction Data 184

References 189

Chapter 1

Introduction

For centuries, one of the key goals of chemistry has been to understand precisely the kinetics of chemical reactions: how does a chemical reaction happen, and how can the progress of a chemical reaction be monitored and manipulated? For many chemical reactions, the kinetics are described by a simple underlying potential energy surface, that assumes that there is a set of reactants and products, with a thermal activation barrier separating the two along the reaction coordinate. A chemical reaction can occur if two molecules collide with sufficient kinetic energy to surmount this barrier. As a result, the rate of reaction depends upon the temperature and the concentrations of reactants. As the temperature is increased, more reactant molecules have sufficient energy to surmount the activation barrier E_a when a molecular collision occurs. This relationship between the rate of reaction and the temperature, T, is simply described by the well-known Arrhenius equation [1]:

$$k_2 = A \exp\left(-\frac{E_a}{RT}\right) \tag{1.1}$$

where k_2 is the bimolecular rate constant, A is the (reaction dependent) Arrhenius factor and R is the molar gas constant. As the concentrations of reactants increases,

so does the rate: higher number densities mean that more molecular collisions can occur per unit time. This is embodied in the rate law for the reaction. As a result of Arrhenius kinetics, many chemical reactions in the fields of organic and inorganic synthesis are performed using high number densities of reactants (often in the aqueous state), and, if the stability of the reactants allows, at elevated temperatures [2].

There exist environments where it is not possible to have high number densities or temperatures, but where chemical reactions are still observed at appreciable rates. The chemistry of the atmosphere is perhaps the most studied example. In the lower atmosphere (troposphere), the hydroxyl radical initiates chemical processes that remove many pollutants from the troposphere [3]. This is despite an extremely low number density on the order of 10^6 molecules cm^{-3} (when compared to an atmospheric gas number density of the order of 10^{19} molecules cm^{-3}). In the stratosphere (between approximately 10 and 30 km above sea level), temperatures of around 220 K are typical, and yet chemical processes, particularly involving ozone, still occur at appreciable rates. The first mechanism introduced in an attempt to explain the steady state ozone distribution in the stratosphere was proposed by Chapman [4]. This model involved reactions of open shell oxygen species (radicals), formed following photolysis of oxygen molecules (O_2). Almost all atmospheric reactions of trace species involve open shell species such as these. Certain chemical reactions involving open-shell radical species proceed on a fundamentally different potential energy surface to the Arrhenius-type reactions: activation barriers are typically very small or absent, permitting rapid reaction rates at low temperatures and at low number densities (as almost every collision can result in a chemical reaction).

The atmosphere is a relatively "hot" environment. The coldest natural environments (with the lowest number densities of molecules) are to be found in the interstellar medium (ISM) where temperatures of 2.728 K have been observed, limited by the cosmic microwave background. Lower temperatures (around 1 K) have been ob-

served in the Boomerang nebula [5]. Number densities of molecules in the interstellar medium are extremely low, ranging from 10^{-4} molecules cm^{-3} to 10^{5} molecules cm^{-3} [6]. Despite these conditions, under which Arrhenius-type reactions would have negligible rates, a rich chemistry involving the reaction of ions and radicals with neutral molecules (such as the enigmatic polyaromatic hydrocarbons [7]) has been established [6]. Much of the chemistry is thought to be initiated by the H_3^+ ion, which is abundant in both its ground state and excited rotational states [8]. This ion has an extremely low proton affinity (4.4 eV), and so acts as a universal proton donor to almost any neutral species, particularly CO. The reaction of H_3^+ with carbon atoms has been implicated as the first stage in the production of long chain hydrocarbons [9]. Despite the vanishingly small collision rate, the barrierless nature of the ion-neutral reaction ensures a near unity reaction probability at the low temperatures in the ISM.

The demonstration of techniques such as atomic laser cooling [10], first demonstrated by Wineland *et al.* in the late 1970s, paved the way for studies in the sub-K regime. Although this is a somewhat artificial environment, it does enable observation of exotic chemical behaviour, and thus can facilitate a deeper understanding of chemical reaction kinetics at a very fundamental level. This is mostly on account of the large de Broglie wavelength exhibited by atoms and molecules at extremely low velocities. When the de Broglie wavelength becomes sufficiently large, the quantum nature of matter emerges. Barrierless chemical reactions in the sub-K regime can exhibit novel behaviour, such as quantum tunnelling and reflection [11]; and multiple scattering resonances [12]. Crucially, the studies of molecules at these "cold" and "ultracold" temperatures also provide benchmarking of theoretically modelled barrierless processes. This is particularly important for reactions relevant to the chemistry of the ISM, where accurate rate constants for elementary chemical reactions frequently cannot be measured *in-situ* or under laboratory conditions. In addition, molecules at extremely low temperatures enable ultra-high resolution molecular spectroscopy to

be performed, and have been predicted to provide an effective framework for quantum information processing [13] and models (quantum simulators) of exotic condensed matter systems [14].

1.1 Introduction to Low Temperature Chemical Reactions

1.1.1 Barrierless Reactions and the Capture Model

As previously mentioned there exist a subset of reactions that are termed "fast" or "barrierless", because they have zero activation energy as a result of proceeding almost solely via the dominating attractive long-range region of the underlying potential energy surface (PES)[15]. The corresponding rate of reaction therefore remains finite even at the lowest temperatures. The mechanism for such a reaction is:

$$\mathrm{A} + \mathrm{B} \overset{k_c}{\rightleftharpoons} [\mathrm{AB}]^* \xrightarrow{\text{fast}} \text{Products}$$

Species A and B come together to form an activated collision complex [AB]* at long range, corresponding to a deep well on the underlying PES. Its formation is the rate determining step of the reaction, making this a fundamentally different mechanism to the transition state model often used for "direct" reactions [1]. This rate, combined with the possibility of reversibility, is included in the capture rate constant, k_c. The subsequent formation of products is assumed to occur quickly, such that the overall rate equation is simply second order:

$$\frac{d[A]}{dt} = -k_c[A][B] \tag{1.2}$$

A schematic PES for a capture reaction is shown in Fig. 1.1. It is briefly worth noting that, despite the lack of an activation energy barrier, there are still centrifugal barriers

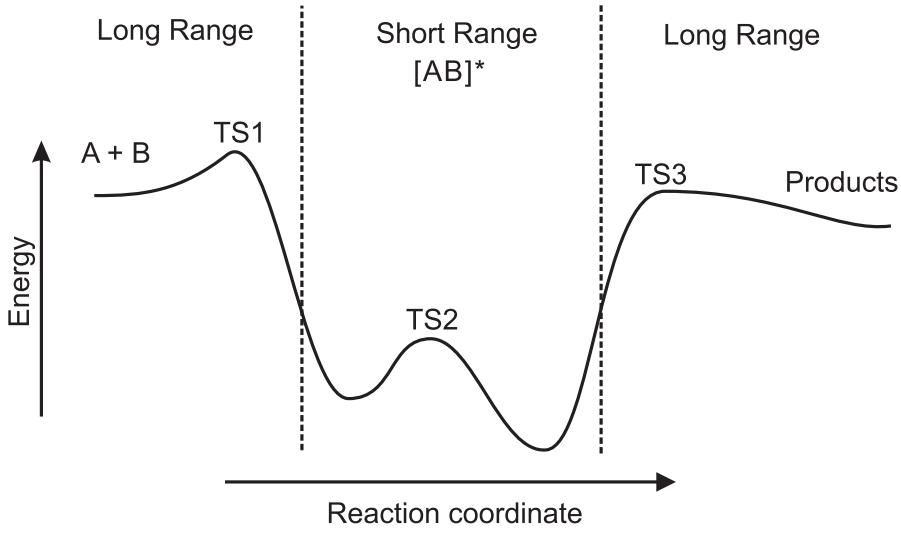


Figure 1.1: An illustration of the reaction profile of a barrierless chemical reaction with three transition states (labelled TS). The only significant barriers present in the entrance channel arise from the interaction between the long-range potential and the centrifugal barriers for a given relative orbital angular momentum state. The bound states and second transition state exist in deep wells on the potential energy surface, so occur on a much faster timescale than the initial capture event.

arising from the relative motion of the collision partners that need to be surmounted [16], so only the ground orbital angular momentum state (also referred to as the ground partial wave or *s*-wave state) is genuinely barrierless.

Several different kinds of chemical reaction have been shown to exhibit barrierless dynamics. These include atom-molecule reactions involving open-shell species (eg $O(^3P)$+ $OH(X^2\Pi)$) [17, 18], molecule-radical reactions (eg $CH(X^2\Pi)$+D_2) [19], reactions of electronically excited (including Rydberg) species (eg Ne* + NH_3) [20, 21], unimolecular decomposition including photodissociation (eg SO_2 [22, 23] or formaldehyde [24] photodissociation, which proceed via excited complexes), and ion-molecule reactions (eg Ca^+ + CH_3F [25] and the focus of this thesis, Xe^+ + ND_3 charge exchange). Calculations that elucidate the low temperature behaviour of ion-molecule reactions are presented in Chapter 2.

Not all barrierless reactions obey simple capture dynamics. A notable exception is

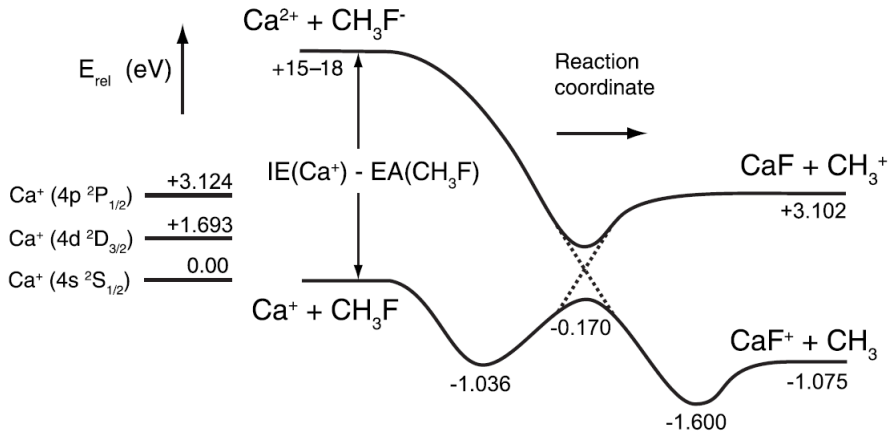


Figure 1.2: Schematic short-range PES for the $Ca^+ + CH_3F$ reaction, showing a significant submerged barrier leading to a key transition state, arising from the indicated avoided crossing. E_{rel} is the relative collision energy, $IE(Ca^+)$ is the ionization energy of a singly charged calcium ion and $EA(CH_3F)$ is the electron affinity of methyl fluoride. The image is taken from [26] and reproduced under licence from the American Institute of Physics.

the following reaction, studied by Gingell *et al.* [26]:

$$Ca^+ + CH_3F \longrightarrow CaF^+ + CH_3 \tag{1.3}$$

The potential energy surfaces for the ground state and a charge exchange excited state are shown in Fig. 1.2. There are two features in the double minimum, short-range potential that make the reaction unsuitable for a theoretical description involving capture theory. A large submerged barrier along the reaction coordinate creates a kinetic bottleneck, reducing the rate significantly compared to that which might be predicted. This is thought to occur as a result of a strongly avoided crossing between the ground state and an excited state, corresponding to charge exchange between the reaction partners [26].

1.1.2 The Quantum Nature of Low Temperature Reactions

The thermal de Broglie wavelength of a molecule is given by:

$$\Lambda = \frac{h}{\sqrt{2\pi m k_B T}} \tag{1.4}$$

where h is Planck's constant, k_B is Boltzmann's constant, and m is the mass of the molecule. At ambient temperatures, when T is large, Λ is much smaller than the scale of the intermolecular potential. This naturally leads to descriptions of reaction dynamics based upon classical physics, with the molecules treated as distinct particles. However, as T is reduced and Λ becomes sufficiently large, the quantum (wave) nature of matter emerges. This can be summarised by the phase space density, D:

$$D = n\Lambda^3 \tag{1.5}$$

where n is the molecular number density. Therefore, as D increases, the quantum nature of matter comes to dominate any chemical processes. Under such conditions, a chemical process can only be considered in terms of quantum "reactive scattering".

The behaviour of the elastic and inelastic/reactive scattering cross-sections, σ, in the cold and ultracold regimes are schematically illustrated in Fig. 1.3. Conventionally, the cold regime corresponds to temperatures below 1 K, and the ultracold regime to temperatures below 1 mK. At the lowest temperatures only a single reaction channel, corresponding to the ground internal quantum states of the reactants, is typically open. Thus, any behaviour is dominated by the relative orbital angular momentum (partial waves) l of the reaction, which introduces small centrifugal barriers to the potential energy surfaces. The behaviour in the ultracold regime was originally described by Wigner [28], and is summarised by the well-known Wigner threshold laws for elastic

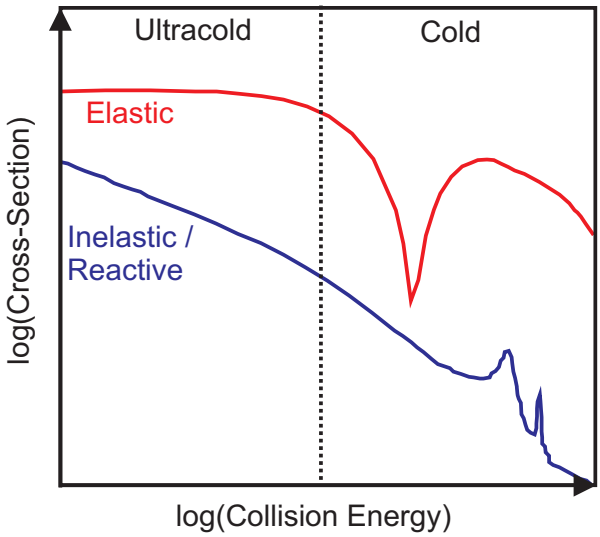


Figure 1.3: Illustration of the variation of the collision cross sections for elastic and inelastic/reactive scattering in the cold and ultracold regime, for neutral reaction partners. Threshold behaviour occurs in the ultracold (sub-mK) regime, and the presence of scattering resonances is visible in the cold (sub-K) regime [27]. The axes are logarithmically scaled.

scattering:

$$\sigma_l^{el}(k) \sim k^{4l} \tag{1.6}$$

and for the inelastic or reactive scattering cross-section:

$$\sigma_l^{re}(k) \sim k^{2l-1} \tag{1.7}$$

where the wavevector k is proportional to the square root of the collision energy. Thus, at the lowest temperatures, when only the s-wave ($l = 0$) contributes to the scattering cross section, the elastic cross-section is constant and the inelastic/reactive cross-section scales inversely with the relative velocity (since the collision energy is proportional to the square of the velocity). This increase in the reaction cross section can be understood in terms of an increased time spent in the strongly interacting part of the potential at lower velocities, v. Since the rate constant k_2 for a reaction is given

by [16]

$$k_2(v) = v\sigma(v) \tag{1.8}$$

the rate constant for reactive scattering is expected to reach a constant value, well known in nuclear physics as the Bethe limit [29], as $T \to 0$. This behaviour is explored in some detail for ion-molecule reactions in Chapter 2.

Although the ultracold region within which threshold behaviour can be observed is out of reach in the experiments detailed in this thesis, there are certain regions within the cold regime where the cross-section undergoes rapid changes, increasing or decreasing by orders of magnitude. These changes can be attributed to scattering resonances, whereby quasi-bound states can be formed between the reaction partners. The can happen if the collision energy becomes resonant with states associated with the internal degrees of freedom of the reaction system, resulting in the formation of an activated collision complex. This may increase (for instance in the case of the reactive scattering of two ^{15}NH molecules [27]) or decrease (for instance in the case of isotopic exchange in the reaction of ^{6}Li^{7}Li with ^{7}Li [30]) the reaction cross-section.

Reactive resonances are difficult to observe in standard molecular crossed-beam experiments, as the high temperatures involved result in many partial-waves and quantum states contributing to the cross-section. The consequent thermal averaging "washes out" the structure. The first observation of a verifiable reactive resonance was in the F + HD reaction [31], but despite a large theoretical effort to suggest good candidate molecules for collision studies, only recently has an experimentally determined rate constant demonstrated several clear reactive resonances as a function of collision energy (for sub-wavenumber collision energies [12]).

1.2 Production and Trapping of Cold Species

Modern experiments seek to produce samples of cold and ultracold molecules in the laboratory frame of reference. There are many advantages to such techniques, including a high degree of control over properties of the molecules, and increased experimental interrogation times, particularly if molecules are trapped. There exist no generally applicable methods to cool a molecule into the cold or ultracold regime. However, several methods have been developed to produce samples of cold molecules by exploiting certain properties. A method is selected depending upon the molecule of interest, the temperature regime of interest, and the intended experiments. All of the methods discussed in this section have advantages and disadvantages, and can each be applied to only a subset of molecular species.

Methods of cold molecule production generally fall into two categories [32]: direct methods cool molecules without changing their chemical composition; indirect methods produce cold molecules from the association of ultracold laser-cooled atoms, or from the dissociation of larger molecules. The most widely used methods for the production of cold, neutral molecules are discussed below.

1.2.1 Indirect Methods: Ultracold Molecules From Ultracold Atoms

The introduction of laser cooling (discussed in detail in Chapter 4) has revolutionised the field of ultracold physics, opening up the sub-mK regime for study. Briefly, a Doppler-shifted photon can be resonantly absorbed and spontaneously emitted by an atom or ion moving towards it. The recoil produced by such an event removes momentum from the species being cooled, and over many cycles temperatures as low as tens of μK (the photon recoil limit) can be obtained. For effective laser cooling, the species of interest must be an effective two-level system. That is, a system where

only transitions between the ground electronic state and a single electronically excited state are possible. In practice, this can be achieved using additional laser systems to repump any population from undesirable states that might be populated outside the main cooling cycle. Although any species can be laser-cooled in principle, the sheer number of repumping lasers required in the majority of systems makes this feasible only for a limited selection of species. The availability of continuous-wave laser sources at the specific wavelengths corresponding to atomic transitions also limits the number of species that can be laser-cooled. As a result, group I and group II metal atoms and ions are the most common species that are used in laser-cooling experiments.

Once laser cooled, an atomic species can be loaded into an optical trap, such as a far off-resonance optical dipole trap (FORT) [33] or a magneto-optical trap (MOT) [34], typically producing atoms at temperatures of tens of μK. "Hotter" atoms are removed from the trap by evaporative cooling [35], whereby the trap depth is lowered (for instance by reducing the magnetic trapping field), and the most energetic atoms are lost from the trap. Elastic collisions within the trap cause the sample to rethermalise, and lowering the trap depth again causes yet more energetic atoms to be lost. Repeated field ramping can reduce the sample to below its quantum degeneracy temperature, resulting in the formation of a Bose-Einstein condensate (BEC), ^{87}Rb being the first reported example [35].

Ultracold atoms can also be used to produce ultracold diatomic molecules through photoassociation and magnetoassociation, as illustrated in Fig. 1.4. During photoassociation, two colliding cold atoms, A and B, can absorb a photon of energy E_{PA}. This photon energy corresponds to a resonance between the free atoms (with kinetic energy E_{thresh} above the AB ground state dissociation threshold) and a vibronically excited, bound state [36]. During magnetoassociation, an external magnetic field is used to tune the energy of a colliding pair of atoms, bringing them into a scattering resonance with a bound state in a closed channel. This is achieved by tuning the energy between

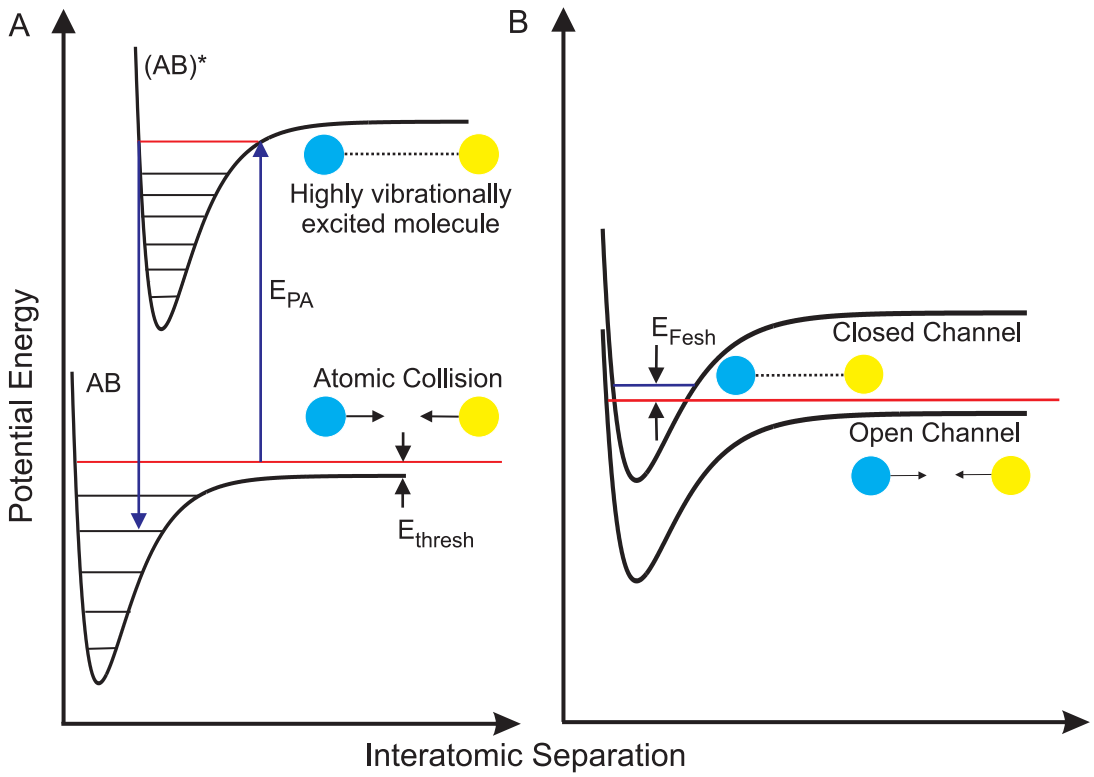


Figure 1.4: Schematic illustration of the creation of a highly vibronically excited bound state from two ultracold atoms by (A) Photoassociation and (B) Magnetic association by tuning through a Feshbach resonance between an energetically open and energetically closed collision channel.

the bound and unbound states, E_{Fesh}, to zero in the vicinity of a Feshbach resonance [37]. Both of these methods associate atoms that were initially at long separations, and so the bound molecules are formed in highly excited (typically $v > 20$) vibrational states. Techniques such as stimulated adiabatic Raman passage (see [38] for more details) can subsequently be employed to transfer such molecules into the ground rovibronic state. The use of a Feshbach resonance, in particular, enables production of ultracold molecules in the sub-μK regime.

Many ultracold diatomic molecules have been made from alkali metal atoms. Bosonic homonuclear diatomic molecules such as $^{40}K_2$ [39], $^{6}Li_2$ [40], $^{85}Rb_2$ [41] can be made from fermionic atomic species below the quantum degeneracy temperature, leading to the formation of molecular BECs. The formation of ultracold KRb by Stwalley and coworkers [42] has led to the production of several other heteronuclear diatomic molecules such as LiK [43] and LiCs [44]. These molecules are particularly exciting as the dipole moment, and hence the interaction potential, of an ultracold gas of dipolar molecules can be tuned using external electric fields [45]. It is predicted that samples of ultracold dipolar molecules will be effective model systems for exotic condensed matter physics [46].

1.2.2 Direct Cooling of Molecular Beams

The earliest attempts to create "cold" molecules arose in high-resolution molecular spectroscopy. Spectral linewidths are affected by several factors, including Doppler broadening. The random motion of molecules in a sample creates small, random Doppler shifts in the molecular energy levels. Forcing a sample of gas through a small orifice (where the orifice diameter is much smaller than the mean free path of the sample), creates a supersonic expansion. If the centre of the supersonic expansion is selected using a skimmer, the resolution of atomic and molecular spectroscopy is

increased through the creation of a high-velocity, but highly unidirectional, beam. Although the molecules are moving fast in the laboratory frame of reference, they have a very low internal velocity spread, typically corresponding to internal temperatures of a few Kelvin.

Mechanical Slowing using a Rotating Nozzle

A rotating nozzle was initially introduced by Gupta and Herschbach [47], and later improved upon and combined with a quadrupole guide by Strebel *et al.* [48]. Gas continually flows through the nozzle, and emerges perpendicular to the nozzle rotational axis (such that it has no angular momentum in the laboratory frame; see Fig. 1.5). A skimmer is positioned such that molecules are only released from the source chamber when the instantaneous linear velocity of the nozzle, v_{rot}, is perpendicular to the required direction of propagation. In this way, if the supersonic expansion of the molecular beam has linear velocity v_s in the rotating frame of reference, the laboratory velocity becomes $v_s - v_{rot}$. This can be tuned by changing the angular velocity of the nozzle.

In principle, this technique is quite general, although it is not yet mechanically possible to use this as a pulsed source, due to the high centrifugal forces that the nozzle experiences. As a result, extremely high pumping rates ($\approx$ 8000 ls^{-1}) are required to maintain the source chamber at around 10^{-4} mbar, limiting the practical applicability of this technique. Typical linear velocities corresponding to a few Kelvin have been demonstrated for molecules such as O_2, CH_3F, SF_6 [49], and the noble gases [48, 49].

Stark Deceleration

Several modern methods of direct molecular beam deceleration make use of time-varying, inhomogeneous electromagnetic fields to directly decelerate molecules pro-

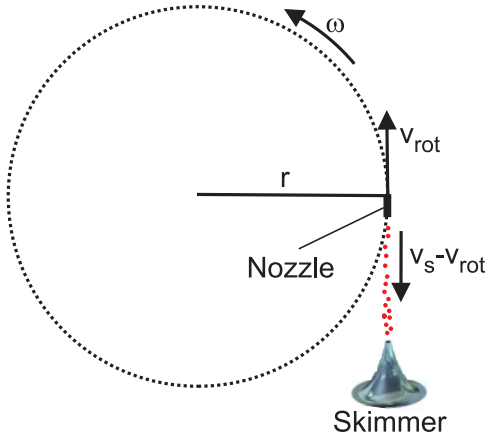


Figure 1.5: The principle of mechanical cooling using a rotating nozzle. A constant effusive beam of molecules is produced with velocity v_s when the nozzle is stationary. When rotating at angular velocity ω, the linear velocity of the nozzle is $v_{rot} = r\omega$. The actual emergent beam velocity is then $v_s - v_{rot}$. The skimmer only allows molecules that are following the correct path to leave the source chamber.

duced via a supersonic expansion to low velocities. The first example of this was the Stark decelerator, originally described by Bethlem *et al.* [50], which employed rapidly switched electric fields to decelerate dipolar molecules in a selected low-field seeking (LFS, see Chapter 3) state to rest. This was achieved by converting kinetic energy into Stark potential energy, a method that lends itself well to miniaturisation [51]. It is also possible to use the method of alternate gradient focussing to decelerate certain molecules that are in high-field seeking states [52]. Control of the switching pattern allows for control of the final velocity, and hence the final translational kinetic energy of the species. To date, several species have been Stark decelerated, including radicals such as OH [53] and NO [54]; and closed shell molecules such as CO (in the $^3\Pi$ electronically excited state) [55] and ND_3. The Stark deceleration of ND_3 is discussed in detail in Chapter 3.

Zeeman Deceleration

A Zeeman decelerator is based upon the same principles as a Stark decelerator, except that pulsed magnetic fields are used instead of pulsed electric fields to convert kinetic energy into Zeeman potential energy. As such, a Zeeman decelerator can be used to decelerate paramagnetic atoms and molecules that exhibit a LFS Zeeman effect. The technique was originally demonstrated by Vanhaecke *et al*. for atomic hydrogen [56], and by Narevicius *et al*. for metastable neon atoms [57]. The method has been demonstrated to decelerate metastable neon atoms to translational temperatures as low as 50 mK [58] using 91 deceleration stages. The technique has also been used to decelerate molecular oxygen [59], although the large number of deceleration stages required to decelerate paramagnetic molecules to low velocities limits the technique to relatively low-mass species.

Optical Stark Deceleration

In optical Stark deceleration, two high-powered pulsed lasers, are spatially overlapped and near counter-propagating. The resulting interference pattern creates an optical lattice, as illustrated in Fig. 1.6. If the optical fields are detuned far below any molecular resonances, a dipole moment can be induced in polarisable molecules. The resulting Stark shift is negative (HFS state), and proportional to the molecular polarisability, drawing molecules into the high-field region. The lattice moves along the propagation axis of the molecular beam, and depends upon the relative detuning of the two crossed lasers. If the lattice is moving at half the velocity of the initial supersonic expansion, and the optical potential is deep enough to actually trap the molecules, a significant number of molecules can be decelerated to near zero velocity, although these molecules have an energy spread that is comparable to that within the molecular beam. Thus far, only benzene has been decelerated to low velocity [60], although the deceleration

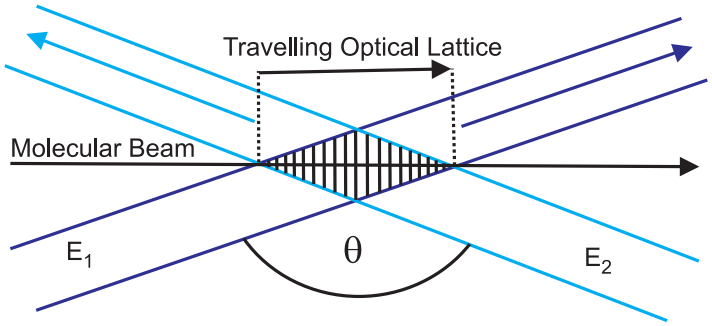


Figure 1.6: The principle of optical Stark deceleration. Two near-counterpropagating (with separation angle θ), far off-resonance laser beams with optical fields E_1 and E_2 are spatially overlapped to create a travelling optical lattice, which moves at half the initial molecular beam speed. The interaction of high-field seeking states with this optical lattice results in molecular deceleration.

of NO has also been demonstrated [61]. Higher energy resolution should be achievable with schemes based on frequency chirped laser systems (due to continuous deceleration of the optical lattice within the molecular beam); such systems have recently been developed [62].

This technique should be quite general, as all molecules are - in principle - polarisable. However, multiphoton ionisation and molecular photodissociation limit the laser power than can practically be used [63].

Rydberg-Stark Deceleration

Atoms or molecules in highly excited electronic (Rydberg) states make excellent candidates for Stark deceleration. The electron distribution in these species is highly polarisable, and large dipole moments can be induced with relatively small external electric fields (< 1 kV cm^{-1}). Deceleration to low velocities can be achieved for hydrogen atoms ($n \approx 30$) with only two stages of deceleration [64]. As a result, this technique has been miniaturised for use on a chip for hydrogen atoms in the range $n = 23 - 70$ [65]. The deceleration of molecular hydrogen in states where $n = 21 - 37$ and $|m_J| = 3$ [66], and of deuterium atoms [67] has also been demonstrated. This

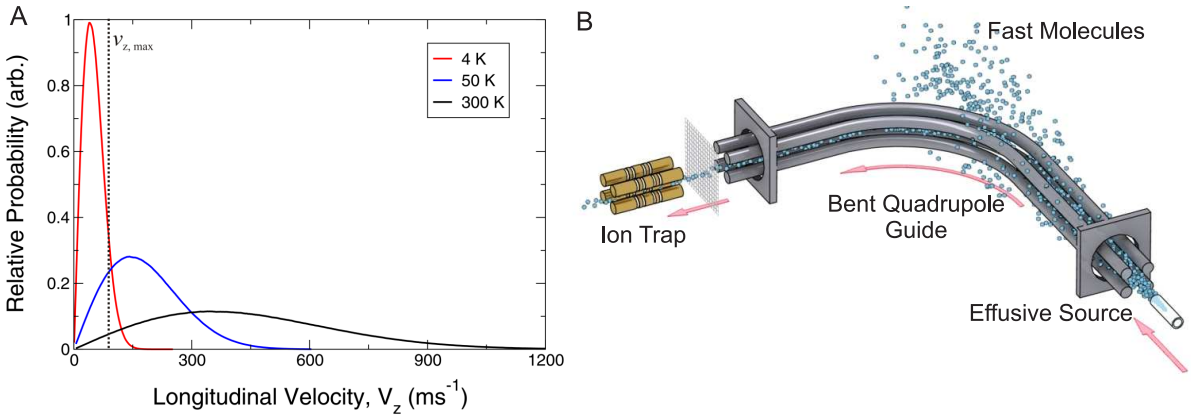


Figure 1.7: (A): Maxwell-Boltzmann distribution of velocities from an effusive source, where the source temperature is varied. The cutoff velocity $v_{z,max}$ for guiding around the bend of the quadrupole guide under typical operating conditions is also indicated. (B): The combination of an ion trap and bent quadrupole guide, originally described in [69], for studying ion-molecule reactions.

technique is currently limited to hydrogenic species, due to the extremely short lifetimes (of the order of μs) and complex nonadiabatic behaviour of the Rydberg-Stark states of larger species.

Velocity Selection Using a Bent Electrostatic Guide

The velocity spread in a thermal gas is described by the Maxwell-Boltzmann distribution. As illustrated in Fig. 1.7A, a small proportion of a 300 K distribution will have low velocities. Originally demonstrated by Rempe and coworkers [68], velocity selection is achieved when an effusive beam of dipolar molecules is directed into a high-voltage ($\pm$5 kV) quadrupole guide that contains a sharp 90° bend. Molecules that are in rotational states that increase in energy as a function of electric field (LFS states) due to the Stark effect can be guided around this bend only if their velocities are sufficiently low. This method therefore acts like a low-pass velocity filter, as shown in Fig. 1.7B.

Any molecule with low-lying LFS quantum states can be velocity-filtered in this way, such as H_2CO, ND_3 [68], CH_3F [69] and the three isotopologues of water [70].

Translational temperatures corresponding to a few Kelvin are typically achieved [71], with the final temperature of the filtered beam dependent on the bend radius and the applied voltage. The simplicity of this method lends itself well to combination with other apparatus. Thus far, velocity selectors have been combined with ion traps [69] to study ion-molecule reactions (see Chapter 5), and cryogenic effusive sources to lower the rotational temperature of the filtered beam [71]. Cryogenically cooling the source of the effusive beam has two advantages: a larger proportion of the Maxwell-Boltzmann distribution can be guided (see Fig. 1.7B); and the rotational and vibrational degrees of freedom can be cooled, as well as the translational motion.

Buffer Gas Cooling

All of the methods described thus far produce highly non-thermal samples of translationally cold molecules; most of these methods do not directly cool the internal degrees of freedom. Immersion of a sample of molecules in a thermal bath held at cryogenic temperatures can cool all degrees of freedom, yielding samples of cold molecules near their absolute ground states. Cryogenic temperatures (below 77 K) are achieved with a cryogenic, thermalised "buffer gas", typically neon or helium, which collisionally cools the molecules of interest. This technique was first demonstrated by Messer and de Lucia [72] and subsequently developed by Doyle and coworkers [73] to produce paramagnetic Europium thermalised with a helium buffer gas at 300 mK [74]. Thermalisation was achieved inside a magnetic trap, before the buffer gas was pumped away. Many diverse atomic and molecular paramagnetic species have been cooled this way, including NH [75], CaH [76], and the van der Waals molecule Ag - ^{3}He [77] This technique has been combined with evaporative cooling in a magnetic trap to form a Bose-Einstein condensate of metastable ^{4}He atoms [78].

This apparatus lends itself well to combination with other techniques, such as electrostatic velocity selection. Recently, Rempe and coworkers have demonstrated a

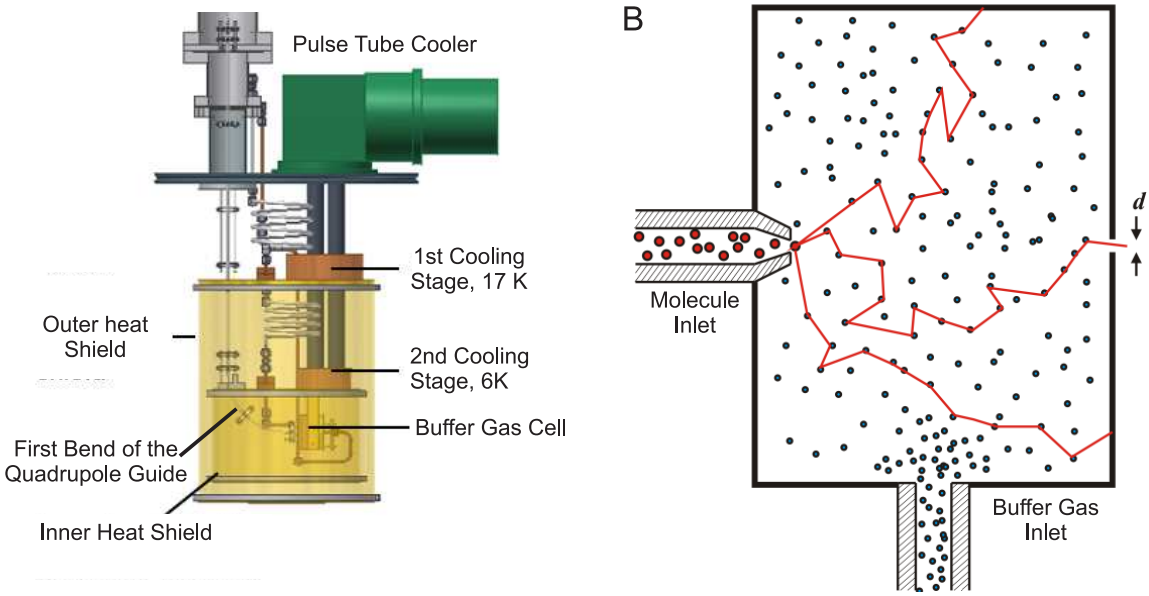


Figure 1.8: (A): The combination of a helium buffer gas cell and a quadrupole guide for producing beams of translationally and rotationally cold molecules in our laboratory. (B): Illustration of the inside the buffer gas cell. An effusive beam of 300 K molecules enters the cell, and elastic collisions with the buffer gas result in thermalisation to the temperature of the buffer gas. Only molecules that diffuse to the exit aperture are loaded into the quadrupole guide.

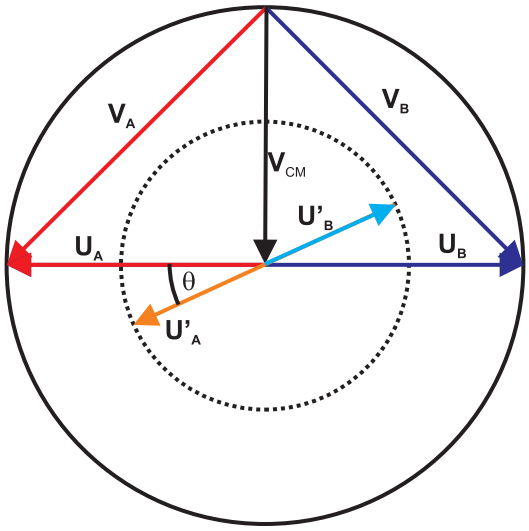


Figure 1.9: Newton diagram showing the kinematic cooling process for two species A and B, inelastically scattered, with an initial relative angle of 90°. Laboratory frame velocities are labelled v_i, and centre-of-mass frame velocities as u_i. For inelastic scattering, the lowest laboratory frame velocity is obtained for a given set of initial conditions at a scattering angle θ in the centre-of-mass frame.

helium buffer gas cell from which dipolar molecules can be extracted using an electric quadrupole guide [79]. The technique has been demonstrated for ND_3 and H_2CO [80], as well as CH_3F and CF_3H [79]. Such an apparatus has been constructed in our laboratory, and is illustrated in Fig. 1.8A. This apparatus can be used to cool molecules using helium (when both heat shields are in place) or neon (using a single heat shield) as the buffer gas, at temperatures of 6 K and 17 K respectively. Molecules are cooled by elastic collisions with the buffer gas (shown in Fig. 1.8B). Only those that diffuse to the exit aperture can be loaded in to the bent electrostatic quadrupole guide, which is located a few mm beyond the exit aperture.

Kinematic Cooling by Momentum Cancellation

It is possible to produce cold molecules by directly colliding them in a crossed-beam apparatus with a beam of noble gas atoms. The final recoil momenta of the molecule of interest (in the centre of mass frame of reference) can undergo vector cancellation,

where the final recoil velocity of that molecule precisely cancels the initial laboratory frame velocity (elastic scattering), or excess energy is converted to internal energy (inelastic scattering). This is illustrated in a Newton diagram in Fig. 1.9. The presence of cold molecules can be confirmed using velocity map imaging (VMI) to image the Newton sphere as a function of time. This process has been shown to produce cold samples of NO by inelastic collisions with argon [81], ND_3 in several different quantum states by inelastic collisions with neon [82] and elastically cooled krypton atoms [83], the latter achieving temperatures on the order of 100 mK.

A related, if indirect, method for producing cold species involves using near-threshold photodissociation of a molecule. If the correct laser polarisation, alignment and ionisation wavelength are used, it is possible for all of the laboratory-frame kinetic energy to be taken away by a single product fragment, leaving the other fragment at rest in the laboratory frame. The production of cold NO from the photodissociation of NO_2 [84] was the first clear demonstration of the technique, and it has since been used to create cold Br atoms from molecular Br_2 [85]; it is the only method thus far to have produced cold halogen atoms.

Since atoms and molecules typically exhibit a range of velocities, only a relatively small fraction of the total number of molecules in a sample can be slowed in this way. However, kinematic techniques lend themselves well to being performed inside a magnetic trap, whereby density could be accumulated over sequential pulsed valve and laser shots.

Laser Cooling of Molecules

Although laser cooling can be readily applied to a number of atoms and atomic ions, the large number of internal degrees of freedom present in molecules makes laser cooling generally unfeasible. However, in 2010 DeMille and coworkers succeeded in observing laser cooling of a single translational degree of freedom in the transverse direction in

SrF, using a three-laser cooling scheme [86] producing a transverse temperature of a few mK. Recently the longitudinal velocity has also been reduced, to less than 50 ms^{-1} [87]. While this represents a significant advancement of the technique, laser cooling remains impractical for all but a very select few molecular species.

1.2.3 Trapping Cold Ions and Molecules

The trapping of ions in ion traps for many hours (see Chapter 4), and atoms in optical traps (see section 1.2.1) for up to a few minutes [88], has been well established. It is, however, somewhat more difficult to trap neutral molecules. The interaction between an applied potential and a neutral molecule is much weaker than that between an electric field and an ion. Closed optical cooling cycles are not practical for the majority of molecules, due to a large number of possible rotational and vibrational transitions. This prohibits the optical trapping of molecular species.

For many applications, it is not merely sufficient to create a sample of cold molecules; spatial confinement is often required. This can enhance the sensitivity of spectroscopic measurements, as the interaction time between electromagnetic radiation and the molecules is increased [89]; confined molecules also make good candidates for scattering studies, again due to the increased interaction times compared with conventional slow molecular beams.

The loading of quadrupolar electrostatic traps with Stark decelerated neutral dipolar molecules in LFS states has been demonstrated by Meijer and coworkers for several species including ND_3 [90], OH [53] and NH [91]. Trap lifetimes of the order of 1 s are achievable, with the loss rate from the trap dominated by nonadiabatic transitions between hyperfine energy levels, induced when molecules enter field-free regions of the trap [92]. The trapping of CO in the $^3\Pi$ metastable state using a miniturised electrostatic trap on a chip has also been demonstrated [51]. For paramagnetic species,

confinement can be achieved using magnetic traps. As mentioned previously, such a trap can be loaded by cooling the species of interest below the trap depth using buffer gas cooling techniques, or *in situ* formation of paramagnetic species, for instance via photodissociation. Alternatively, a magnetic trap can be loaded with radicals such as OH, using the output from a Stark decelerator [93], or radicals such as H atoms using the output from a Zeeman decelerator [94].

Pioneering experiments in the laboratory of Jun Ye have applied some of the methods used to trap ultracold atoms to neutral dipolar molecules. Evaporative cooling, a key step towards the formation of an atomic BEC, is difficult for molecules, due to high inelastic scattering rates compared with elastic thermalisation. These difficulties have recently been overcome for OH. By trapping Stark decelerated OH in a magnetic trap, a microwave pulse facilitated the transfer of "hot" molecules into a different hyperfine state, whereby a DC electric field pulse was applied to remove these molecules from the trap [95]. Temperatures as low as 5.1 mK were achieved using this evaporative cooling technique. In another experiment, a two-dimensional MOT was used to transversely cool $^{89}Y^{16}O$ molecules, created using a buffer gas cell combined with an electrostatic guide, to as low as 2 mK [96]. This result, combined with the demonstrated three-dimensional laser cooling of SrF already discussed in section 1.2.2 [87], suggests that it might be possible to create a three-dimensional MOT that could be used to trap neutral molecules.

A novel microstructured trap designed by Rempe and coworkers has also been demonstrated to produce *in situ* optoelectrical cooling of CH_3F molecules [97]. Rather than using molecular laser cooling, the Stark effect is used to remove energy from dipolar molecules that move towards the edge of the trap. In order to permanently remove energy from the molecules, a radio-frequency field is applied. This transfers molecules into a less strongly trapped state, with a weaker Stark effect. Thus, molecules regain less kinetic energy than they started with when they return to the centre of the trap.

Microwave and infra-red fields are used to repump any population lost to other states as a result of spontaneous emission. In this way, the temperature of the molecules was reduced by a factor of 13.5, with trapping times of up to 27 s. It is expected that such trap-based cooling schemes will be applicable to a wider range of molecules than laser cooling or evaporative cooling schemes.

Sympathetic cooling has emerged as a powerful technique in the study of trapped molecular ions and neutral molecules. The intermolecular forces between laser-cooled atoms or ions and non-laser-cooled species can be used to significantly reduce the kinetic energy of the non-laser-cooled ions, in principle enabling the translational cooling of any general species. This technique is well established in ion trapping, and is discussed in this context in Chapter 4, where the sympathetic cooling of molecular ions is achieved through their Coulombic interaction with directly laser-cooled atomic ions (within a Coulomb crystal). It is also well established in the context of ultracold atoms, for instance in the overlapping and subsequent equilibration of two Bose-Einstein condensates in spatially overlapped magnetic traps [98].

The recent implementation of a combined ion-trap and MOT apparatus by Willitsch and coworkers demonstrates the versatility of ion traps [99]. Additionally, sympathetic cooling of $BaCl^+$ molecular ions in a linear Paul trap has been achieved using their interaction with ultracold Ca atoms in an overlaid MOT [100]. As the range of the intermolecular potential is shorter in the atom-ion case than the ion-ion case, it was possible to cool both the translational and internal degrees of freedom of $BaCl^+$ in this way.

The CryPTEx trap, recently built by Drewsen and coworkers [101], is a linear Paul trap that can operate at temperatures as low as 4 K for storage times of up to 30 hours. This enables the thermal equilibration of the internal degrees of freedom of molecular ions that are sympathetically cooled by laser-cooled ions to low temperatures, as well as inhibiting blackbody-mediated internal energy redistribution of state-selected

molecular ions.

1.2.4 Applications of Cold Atoms and Molecules

Long observation times and diminished Doppler broadening, collision rates and longitudinal motion allow for lifetime-limited ultra-high resolution spectroscopy to be performed. Perhaps the most widely known application of this is in atomic clocks, where a cloud of cold atoms is exposed to radiofrequency radiation. The precise resonant frequency of the narrow transition is used to define the second. Cold atoms (usually caesium or, more recently, rubidium [102]) produced via "fountain techniques", whereby gravity decelerates a vertically moving cloud, allow measurements to be carried out at the apex of the trajectory. The most accurate modern atomic clocks make use of ultracold atoms trapped in optical lattices. The National Institute of Standards and Technology (NIST) have just developed an atomic clock using optically trapped ultracold ^{171}Yb atoms that can perform measurements of the second to an accuracy of 1.6×10^{-18} [103].

The spectroscopy of cold and ultracold molecules has also been predicted to provide tests of fundamental physics. Recent experiments on the splitting of the hyperfine states of YbF, induced by the interaction of the unpaired electron with an electric field, have put a new upper bound on the electric dipole moment of the electron [104], helping to discount some of the theories beyond the Standard Model of particle physics. Experiments to perform such measurements on Stark decelerated and electrostatically trapped heavy, dipolar, paramagnetic molecules have been proposed [105], and these would be expected to provide orders of magnitude more accuracy than current techniques. It has also been suggested that spectroscopic measurements of cold molecules could be used to test the time-invariance of fundamental constants, such as by looking at deviations in the spectroscopy of near-degenerate rotational quantum states in the

$^3\Pi$ metastable state of CO [106].

1.3 Studying Low Temperature Chemistry

1.3.1 Studying Cold Chemistry With Molecular Beams

In order to experimentally study low temperature chemical reactions, all of the reactants must be (at least translationally) cold. Typically, this requires the combination of two or more low temperature sources or techniques. The earliest attempts to study low temperature reactions used a flow tube apparatus that was cryogenically cooled with liquid nitrogen to 77 K for the study of the three body recombination of hydrogen [107]. Later, liquid helium was used to cool an ion-drift apparatus to 15 K [108], and processes such as the three body reaction rate of He^+ with H_2 were studied. These techniques were performed in a moving frame of reference and were limited to light atomic and molecular species with high vapour pressures [109], as thermal equilibration must be able to occur with the walls of the flow tube without significant condensation of the reactants.

In the mid 1980s, the CRESU (Cinétique de Réaction en Ecoulement Supersonique Uniforme) technique was developed by Rowe to take advantage of the low internal temperatures possible within supersonic flows [110]. A high-density molecular beam, with a well-defined temperature, was created by expansion through a de Laval nozzle. With liquid nitrogen cooling of the nozzle, equilibrated moving-frame temperatures down to 13 K were reported [111]. Reactions can be initiated by ionisation or dissociation of species within the molecular beam, or by merging a pulsed ion beam with the supersonic flow. The success of the CRESU technique can be seen in the extensive number of chemical reactions have been studied using this method [112], including radical-radical reactions (such as CN + O_2) and ion-molecule reactions (such as H_3^+

+ CO). This technique is limited to reactions that are sufficiently fast, with rate constants $> 5 \times 10^{-13}$ molecule^{-1} cm^3 s^{-1}, due to limitations in the lifetime of the uniform supersonic flow. In addition, a particular de Laval nozzle can only produce a single well-defined internal temperature. As a result, there is a discrete number of achievable temperatures in practice.

The merged supersonic beam concept has recently been developed further in experiments by Naravicius and coworkers [12]. A magnetic quadrupole guide has been developed that can be used to merge a beam of metastable helium atoms with a molecular beam of H_2 or Ar atoms. This yielded Penning ionisation of the H_2 or Ar species, and the resulting ions were detected using a quadrupole mass spectrometer. This process allows for remarkable energy resolution, and collision energies as low as 1 μeV were achieved. Multiple reactive scattering resonances were observed in the experimentally determined rate constant as a function of collision energy for the Penning ionisation of both Ar and H_2, as was the onset of ultracold reactive behaviour predicted by the Wigner threshold laws.

Although crossed molecular beam experiments using thermal sources are unsuitable for low-temperature reaction studies (even with a low crossing angle), crossed molecular beam studies using decelerated molecular beams have been reported. In 2006, Meijer and coworkers reported the collision-energy-dependent inelastic scattering of Stark decelerated OH radicals with a crossed beam of Xe atoms [113]. Recently, this concept has been developed with the demonstration of state-resolved and collision-energy controlled bimolecular inelastic collisions between Stark decelerated OH and hexapole selected NO molecules at collision energies down to 70 cm^{-1} [114]. One could imagine a crossed-beam experiment consisting of two Stark decelerated molecular beams, which would enable complete quantum state selection of the molecules, in addition to velocity selection, for reactions in the lowest temperature regimes [115]. However, the extremely low number densities that are routinely achieved from the

output of a Stark decelerator would make such an experiment challenging to realise.

1.3.2 Cold Chemistry Using Trapped Ions and Molecules

Experiments studying chemical processes in the ultracold temperature regime have been reported using molecules that have been formed from the association of ultracold group I atoms. The first observation of such an ultracold reaction was reported by Knoop *et al.*. A mixture of Cs_2 molecules (consisting of Cs atoms in the same hyperfine state) and Cs atoms (in a different hyperfine state) was produced, and the subsequent atom exchange reaction was tuned to be either endoergic (closed) or exoergic (open) through the use of an external magnetic field [116].

More recently, $^{40}K^{87}Rb$ molecules have been used to demonstrate several interesting aspects of ultracold chemical behaviour. This is a fermionic molecule, and the symmetry of its wavefunction is therefore necessarily antisymmetric under the exchange of particle labels. As a consequence, samples of $^{40}K^{87}Rb$ can be prepared such that only the s-wave ($l = 0$) or p-wave ($l = 1$) orbital angular momentum states are populated. Ye and coworkers demonstrated that, at temperatures of a few 100 nK, there is a factor of 10-100 increase in the barrierless s-wave reactive scattering rate (mixture of hyperfine states) compared with the p-wave rate (spin-polarised) [117]. Later, trapped KRb molecules were prepared in different orientations, and "end-on" vs. "side-on" collisions were studied, demonstrating that stereochemistry can be observed and investigated in the ultracold regime [118].

Trapped, cold ions in ion traps facilitate the study of a range of low-temperature, barrierless, ion-molecule reactions. Cold ions are stable for long periods of time, and hence can be used to study chemical reactions over relatively long timescales, potentially compensating for the low number densities that often plague cold chemistry. At mK temperatures, ions have large associated de Broglie wavelengths. When such ions

fluoresce, they appear to be several tens of micrometers in size. This makes it possible to image individual fluorescent ions, hence to follow the progress of a chemical reaction over many hours with high precision and single ion resolution, as demonstrated in [25]. The use of ion traps and decelerated molecular beams to study ion-molecule reactions is a key aim of this thesis, and is explored in detail in Chapters 4 and 5.

1.4 Outline of This Thesis

In this thesis, new theoretical and experimental methods are introduced that have enhanced the understanding of the dynamics governing cold ion-molecule reactions.

Chapter 2 applies and further develops both classical and quantum capture theory models describing ion-molecule reactions. The theories are applied to model potentials, exploring the divergence between classical and quantum mechanical rate constants at low temperatures. Several classes of molecules are considered: dipolar and non-dipolar neutral molecules; ground and excited rotational state molecules; and molecules with $^1\Sigma$ and $^2\Pi$ ground electronic states. The effect of strong quadrupole moments relative to the dipole moment on the rate constant is explored at intermediate temperatures. A model for the adiabatic separation of the translational and rotational degrees of freedom is also applied to predict how different internal energy distributions might affect rate constants. From these results, several target systems are suggested for experimental observation of these theoretically examined phenomena.

Chapter 3 is concerned with the design and commissioning of a Stark decelerator beamline that can be used as a source of low-velocity, tunable-energy, quantum state-selected ND_3 molecules. Introducing several beamline components after the Stark decelerator has improved upon the original design, and facilitated combination with an ion trap apparatus. Hexapole focussing elements provide increased number densities, and the inclusion of a molecular buncher provides increased longitudinal velocity reso-

lution. Simulation programs written to model the deceleration process are described. These programs have facilitated a deeper understanding of the Stark decelerator beamline, and enabled the interpretation of the initial experimental results.

The concept of ion trapping is introduced in Chapter 4. The methods used to laser-cool and trap $^{40}Ca^+$ ions are described, along with the subsequent formation of Coulomb crystals. Such crystals provide an extremely sensitive framework within which to study ion-molecule reactions. Several experimental modifications, such as the inclusion of a liquid nitrogen cold finger and fibre-optic coupling scheme for laser cooling, are described. These have enabled the stable trapping and sympathetic cooling of Xe^+ ions. The sympathetic cooling of light ions, particularly ND_3^+ ions, is discussed, as is a new technique for estimating the number of ND_3^+ ions that are present in the ion trap. This can be used to rapidly analyse the kinetics of the ion-molecule reaction between Xe^+ and ND_3.

This reaction is further explored in Chapter 5. The combination of the Stark decelerator and ion trap apparatus - discussed separately in Chapters 3 and 4 - is reported, and significant progress is made towards studying the kinetics of a rotationally state-selected ion-molecule reaction as a function of collision energy. A simple model of the observed reaction kinetics is introduced. The operation of the Stark decelerator as an electrostatic guide is discussed as a method of estimating the relative density of the molecular beam, and the variation of integrated flux with guiding voltage is explored. In order to overcome difficulties in using the kinetic model, a simulation study is presented, enabling more accurate determination of the initial number of sympathetically cooled Xe^+ ions present in the ion trap before the molecular beam is admitted. The results of this study are used to interpret the reaction between ND_3 that is electrostatically guided through the Stark decelerator beamline, and sympathetically-cooled Xe^+. The kinetics of the reaction are analysed in terms of the kinetic model presented earlier in the chapter.

Finally, the conclusions of the thesis are presented in Chapter 6, alongside several possible avenues for future work, building on the work both presented in this thesis and elsewhere.

Chapter 2

Low Temperature Behaviour of Ion-Molecule Capture

What do we mean by the term "ultracold"? One might consider two possible definitions. Firstly, a chemical species might be considered ultracold if it is held below a certain temperature [119] often informally considered to be 1 mK [120]. Alternatively, the ultracold regime might be considered to occur when the temperature is low enough to detect the dominance of quantum phenomena.

The first of these criteria is, of course, system independent and straightforward to define, but it is an arbitrary cut-off point, making no distinction between the different kinds of behaviour that different systems might exhibit in different temperature ranges. The second is very dependent on the system under consideration and is made harder still to define due the range of possible quantum effects that could be observed.

In this chapter, the effect of changing molecular parameters on the temperature at which quantum effects might emerge is explored for barrierless chemical reactions. A set of simple analytical intermolecular potentials is employed within the capture approximation to achieve this. Ion-molecule reactions will be principally considered. The quantum-classical divergence temperature T_Q will be established by initially com-

paring the results of quantum scattering theory with classical calculations, and applying the results of this comparison to increasingly more complicated potentials. The simplicity of the model potentials prevents any robust predictions being made about specific molecules, for which an accurate potential energy surface (PES) would be required. However, it does allow for the establishment of general trends that provide some physical insight into the problem.

2.1 Theoretical Methods

2.1.1 Potential Energy Surfaces

There are several theoretical prescriptions with which it is possible to describe the dynamics of a chemical reaction. A unifying feature of them all is the consideration of the motion of the molecules on a multidimensional PES [121].

This surface may be considered to consist of two parts, as illustrated in Fig. 1.1. The first is the long-range part of the potential, and this consists primarily of interactions between the permanent multipoles (charge, dipole, quadruple etc.) of the collision partners. It is dominant at distances that are sufficiently large that it is often possible, in the case of small molecules, to neglect the internal structure of the collision partners. These terms can be described very well by the analytical multipole expansion [122].

There is also a short-range aspect to the potential. In this region, overlap of the molecular orbitals of the colliding species occurs, leading to quantum mechanical chemical bonding effects, such as electronic tunnelling, penetration, damping [123]. Collision energy resonances also become important. It is also the region in which chemical bonds are broken and formed. As a result, the internal structure of the reaction partners, including their vibrational quantum states, must be considered.

The complexity and high multi-dimensionality thus introduced requires the use of computers to create an *ab initio* or semi-empirical PES for the reaction, and in the case of large atoms or molecules achieving sufficient accuracy may be prohibitively expensive in terms of computing power and time.

In this chapter, only the reaction between an ion and a neutral molecule will be considered. The ionic field extends far beyond the electron distribution of the ion, and for this and other reasons to be detailed later, only the long-range part of the potential will be considered.

2.1.2 The Effective Potential for Ion-Molecule Collisions

The long-range part of the potential can successfully be described by an analytic multipole expansion [122], which includes the interactions between the ion of charge q and various moments of the multipole expansion of the neutral molecule. From here on, all equations will be in Hartree atomic units unless otherwise stated.

The long-range potential energy function for an ion-molecule collision is described by only two Jacobi coordinates, as shown in Fig. 2.1. The first is the distance between the centre of mass of the molecule and centre of charge of the ion, R. The second is the angle between the highest symmetry axis of the electrical multipole distribution, and the R vector, θ.

Regardless of the identity of the neutral species, the ion will induce a dipole, the magnitude of which depends on its isotropic polarisability, α. This is the well known Langevin potential [125] V_L:

$$V_L = -\frac{q^2\alpha}{2R^4} \tag{2.1}$$

Using classical capture theory, this potential yields a temperature independent rate

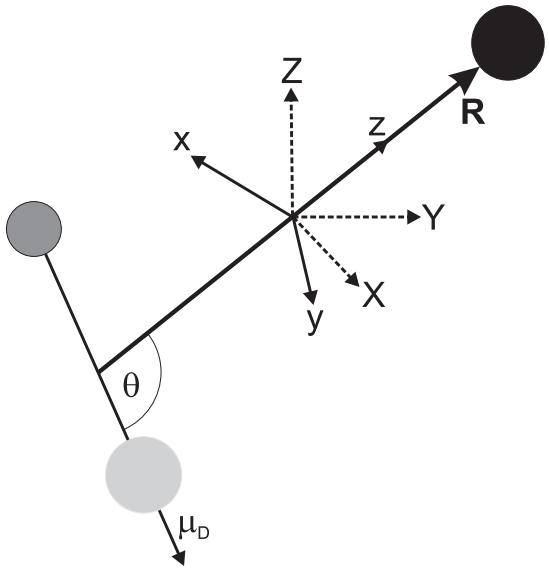


Figure 2.1: The coordinate system used in the calculations. The potential energy is described in terms of the Jacobi coordinates (R,θ). The relationship between the space fixed axes (X,Y,Z) and body fixed axes (x,y,z) at the centre of mass of the reaction system are also shown. A diatomic molecule is shown for clarity, but these coordinates apply equally well to larger molecules, providing θ is defined with respect to the dipole moment direction [124].

constant k_L [125] that is regularly used as a reference in capture calculations:

$$k_L = 2\pi\sqrt{\frac{q^2\alpha}{\mu}} \tag{2.2}$$

If a molecule is asymmetric, it will have a permanent dipole moment oriented along its axis of highest symmetry, μ_D. This case is of particular interest as these molecules can be most easily manipulated experimentally with electric fields. Both dipolar and non-dipolar molecules may possess a permanent quadruple moment, Q, characterised by the Θ_{zz} component of the quadrupole moment tensor. The ion-dipole potential V_{ID} and the ion-quadrupole potential V_{IQ} are both anisotropic, with $P_2(x)$ being the second Legendre polynomial:

$$V_{ID} = -\frac{q\mu_D}{R^2}cos\theta \tag{2.3}$$

$$V_{IQ} = \frac{qQ}{R^3} P_2(cos\theta) \tag{2.4}$$

The angular part of the ion-dipole potential is equivalent to the electric dipole potential that describes the Stark effect. It is also possible to induce a dipole through the interaction of the anisotropic polarisabiliy, $\Delta\alpha$ and the ion. The corresponding potential $V_{I\alpha}$ is:

$$V_{I\alpha} = -\frac{q^2\Delta\alpha}{3R^4} P_2(cos\theta) \tag{2.5}$$

In the Schrödinger equation, the interaction potential can be combined with the relative angular momentum operator. Including the quantisation of the angular momentum arising from relative motion [16] in a space fixed basis (see Fig. 2.1), a set of effective potentials V_{eff} that govern the capture process can be generated:

$$V_{eff} = V_{total} + \frac{L(L+1)}{2\mu R^2} \tag{2.6}$$

where V_{total} is the total potential energy and L is the relative angular momentum quantum number (also known as the centrifugal or orbital quantum number).

2.1.3 Rotationally Adiabatic Potentials

The nuclear motion of the molecules consists of translational, rotational and vibrational motion. Due to the small amplitude of the vibrational motion compared to the length scales of the long-range potential, vibration can be neglected [126]. The translational motion will be treated both classically and quantum mechanically within the different models that will be described later. This leaves only the rotational motion, which is described quantum mechanically according to the rigid rotor model.

The most complete, and expensive, solution of the rotational problem would involve computing a 2-dimensional wavefunction $\Phi(R,\theta)$. However, there is an alternative

method suggested by Clary [126], and later modified by Troe [127].

Consider the Schrödinger equation for a prolate symmetric top within the rigid rotor approximation, interacting with an ion, with unique rotational constants A and B :

$$\left(B\hat{j}^2 + (A-B)\hat{j_z}^2 + \frac{|\hat{J}-\hat{j}|^2}{2\mu R^2} + V(R,\theta) - V_n(R) \right) \Phi(R,\theta) = 0 \tag{2.7}$$

where V_i is the effective one-dimensional potential to be computed for a given reaction channel n, $\hat{J}$ is the total angular momentum operator for the collision system, $\hat{j}$ is the angular momentum of the rotating neutral molecule, with z-component $\hat{j_z}$. The energy levels of the prolate symmetric top, corresponding to an infinitely separated system, are:

$$F(j,k) = Bj(j+1) + (A-B)k^2 \tag{2.8}$$

where j is the rotational quantum number and k is the quantised projection of this onto the principal rotation axis of the molecule. The description of the rotational state of the molecule is completed with the quantum number m, the projection of j onto the intermolecular axis.

Historically, the potential was analytically expanded using a perturbation expansion based on the weak and strong field Stark effects [128]. Using modern computers, this equation can be solved exactly using a wavefunction expansion in the basis of the rigid rotor eigenfunctions [129]:

$$|jkm\rangle = \sqrt{\frac{2j+1}{8\pi^2}} D^{j*}_{mk}(\phi,\theta,\chi) \tag{2.9}$$

where D^{j*}_{mk} are the Wigner rotation matrices, which are a function of the Euler angles ϕ, θ and χ. A parity adapted basis set can greatly accelerate calculations, as the parity

quantum number ϵ is a conserved quantity:

$$|jkm\epsilon\rangle = \frac{1}{\sqrt{2}}\left(|jkm\rangle + \epsilon|j-k-m\rangle\right) \tag{2.10}$$

Within the body-fixed representation, the matrix elements of the potential energy operator, expressed in terms of Wigner $3j$ symbols and the Kronecker delta and diagonal in J, are derived using standard angular momentum theory [129]:

$$\begin{aligned}
&V^{BF}_{Jjkm\epsilon j'k'm'\epsilon'}(R) = \langle jkm\epsilon|V(R,\theta)|j'k'm'\epsilon'\rangle = \\
&-\frac{q^2\alpha}{2R^4}\delta_{jj'}\delta_{kk'}\delta_{mm'}\delta_{\epsilon\epsilon'} \\
&-\frac{q\mu_D}{R^2}\sqrt{(2j+1)(2j'+1)}(-1)^{m'-k'}\begin{pmatrix} j & 1 & j' \\ k & 0 & -k' \end{pmatrix}\begin{pmatrix} j & 1 & j' \\ m & 0 & -m' \end{pmatrix}\delta_{\epsilon\epsilon'} \\
&+\left(\frac{qQ}{R^3}-\frac{q^2\Delta\alpha}{3R^4}\right)\sqrt{(2j+1)(2j'+1)}(-1)^{m'-k'}\begin{pmatrix} j & 2 & j' \\ k & 0 & -k' \end{pmatrix}\begin{pmatrix} j & 2 & j' \\ m & 0 & -m' \end{pmatrix}\delta_{\epsilon\epsilon'}
\end{aligned} \tag{2.11}$$

Within the body fixed representation, the matrix elements of the centrifugal operator, including the Coriolis coupling contribution, are also diagonal in J:

$$\begin{aligned}
&\langle jkm\epsilon||\hat{J}-\hat{j}|^2|j'k'm'\epsilon'\rangle = \\
&[J(J+1)+j(j+1)-2m^2]\delta_{jj'}\delta_{kk'}\delta_{mm'}\delta_{\epsilon\epsilon'} \\
&-\sqrt{J(J+1)-m(m-1)}\sqrt{j(j+1)-m(m-1)}\delta_{jj'}\delta_{kk'}\delta_{mm'-1}\delta_{\epsilon\epsilon'} \\
&-\sqrt{J(J+1)-m(m+1)}\sqrt{j(j+1)-m(m+1)}\delta_{jj'}\delta_{kk'}\delta_{mm'+1}\delta_{\epsilon\epsilon'}
\end{aligned} \tag{2.12}$$

The body fixed representation is appropriate for classical calculations. However, the space fixed representation must be used for quantum capture calculations (see section 2.1.6). In the space fixed frame, at infinite separation, the orbital angular momentum quantum number L is well defined, but the body-fixed projection m is

not. Hence at finite separation the potential introduces couplings between the different L states. The potential energy matrix elements in this frame of reference are most conveniently computed via a basis set transformation from the body fixed frame. The transformation, given in terms of Clebsch-Gordan coefficients, is:

$$V^{SF}_{Jjk L\epsilon j'k'L'\epsilon'}(R) = \frac{\sqrt{(2L+1)(2L'+1)}}{2J+1} \sum_m \langle Jm|jm, L0\rangle \langle j'm, L'0|Jm\rangle V^{BF}_{Jjkm\epsilon j'k'm'\epsilon'}(R) \tag{2.13}$$

Within the space fixed representation, the matrix elements of the centrifugal operator have a particularly simple form:

$$\langle jkL\epsilon||\hat{J}-\hat{j}|^2|j'k'L'\epsilon'\rangle = L(L+1)\delta_{jj'}\delta_{kk'}\delta_{LL'}\delta_{\epsilon\epsilon'} \tag{2.14}$$

Either of these representations, together with the energy levels of the symmetric top, can be used to create the Hamiltonian. This is computed and diagonalised on a grid of intermolecular distances to generate a set of effective potential energy curves, examples of which are shown in Figs. 2.2 and 2.3 for the capture of the HCl diatomic molecule by the H_3^+ molecular ion, the latter being modelled as a point charge. This system has been the subject of several previous theoretical studies [130, 131, 132], making it an excellent choice for benchmarking calculations. The parameters for this system are summarised in Table 2.1. Each curve represents a different reaction channel, and each converges asymptotically to a specific quantum state of the neutral molecule. Classical methods assume that the reaction system adiabatically follows one of these curves throughout the capture process. Three different methods that make use of these adiabats have been used to investigate the low temperature behaviour of ion-molecule reactions.

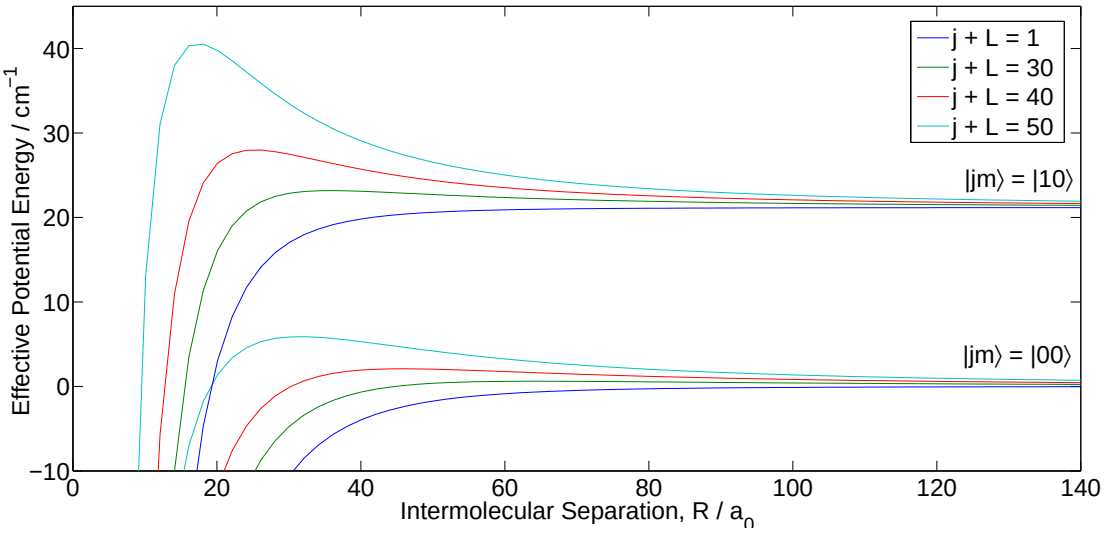


Figure 2.2: Illustration of a selected set of long-range adiabatic potential energy curves for the H_3^+ + HCl reaction. The quantum states shown correspond to the HCl molecule in the asymptotic limit.

Table 2.1: The parameters used for calculations on the H_3^+ + HCl system. Unless otherwise stated, the values given are in Hartree atomic units, and come from [130].

Parameter	Value
B	10.593 cm^{-1} [133]
μ_D	0.436
α	17.55
μ	2.79 amu
q	1
Q	2.8
$\Delta\alpha$	1.7 [134]

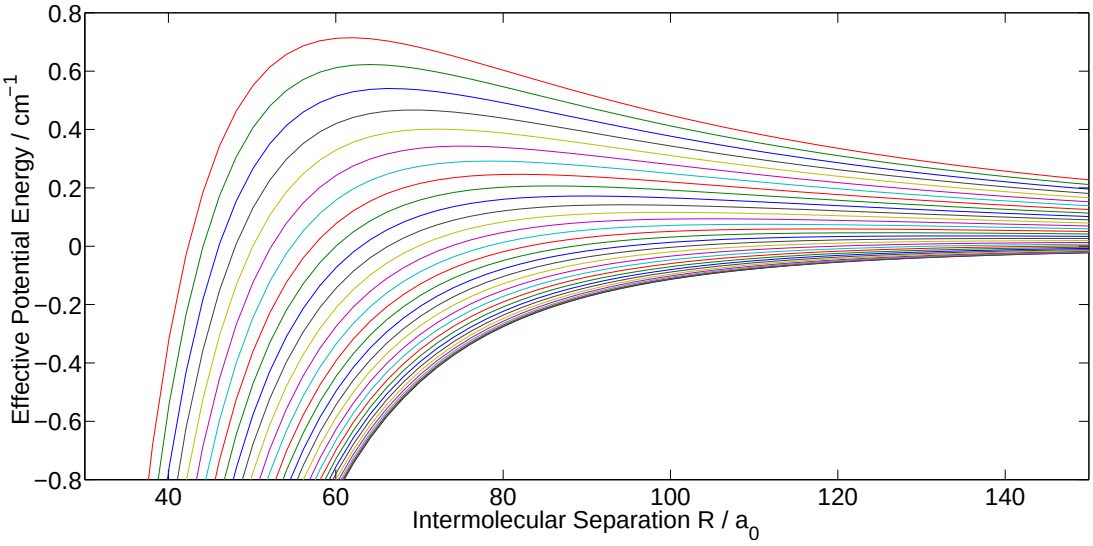


Figure 2.3: Enlarged set of long-range adiabatic potential energy curves for the first 31 values of the relative angular momentum quantum number L for the ground state of HCl in the asymptotic limit.

2.1.4 Low Temperature Classical Calculations

Over the years, there have been many classical descriptions of the rate constant between a multipolar ion and a molecule. In previous work [135, 136], the average dipole orientation theory of Su and Bowers [137] was used in a parameterised form [138]. This can be further extended with the average quadrupole orientation theory [139].

More recent methods, originally developed for isotropic potentials [140, 141] but later applied to the ion-dipole potential [130], allow the molecule to follow classical trajectories over the adiabats, which are parameterised according to the perturbed rotor approximation. This is known as adiabatic channel classical capture theory (ACCl), and avoids the divergence that the ADO/AQO theories experience as T→0 in the ultracold temperature regime.

One formulation of this method involves numerically evaluating integrals of the form [140]:

$$k_c(T) = -\sqrt{\frac{\pi}{2\mu k^3 T^3}} \sum_n \int_0^\infty R^3 U_n' (U_n'' R + 3U_n') \Theta(U_n') \exp\left[-\frac{RU_n' + 2U_n}{2kT}\right] dR \quad (2.15)$$

where n represents a given molecular quantum state $|jkm\rangle$, U_n are the parameterised adiabatic potential energy curves, in this case parameterised within the perturbed rotor approximation, and $\Theta(z)$ is the Heaviside step function. The integral is general, although the perturbed rotor potentials have only been computed for linear molecules, For which k=0 only. The perturbed rotor potentials are computed via series expansion to be [130]:

$$\begin{aligned} U_{00} &= -\frac{q^2\alpha}{2R^4} - \frac{q^2\mu_D^2}{6BR^4} \\ U_{jm} &= -\frac{q^2\alpha}{2R^4} + \left(\frac{qQ}{R^3} - \frac{q^2\Delta\alpha}{3R^4} + \frac{q^2\mu_D^2}{2j(j+1)BR^4}\right)\frac{j(j+1)-3m^2}{(2j-1)(2j+3)} \end{aligned} \tag{2.16}$$

2.1.5 Statistical Adiabatic Channel Model

The statistical adiabatic channel model (SACM) for barrierless processes was originally suggested by Troe and Quack as a way to describe unimolecular dissociation [142], and was quickly adapted to include bimolecular processes [131].

After computing the rotationally adiabatic potential energy curves (as in section 2.1.3), the maximal value of each, $E_{0,n}$, is located. The fundamental assumption made by this model is that, for a given energy E, the probability of capture occurring is:

$$P(E) = \begin{cases} 1 & \text{if } E > E_{0,n} \\ 0 & \text{otherwise} \end{cases} \tag{2.17}$$

that is, a step function. These quantised energies can be thermally averaged to give an "activated complex" partition function:

$$Z^*(T) = \sum_n (2L+1)\exp\left(-\frac{E_{0,n}}{kT}\right) \tag{2.18}$$

where n now corresponds to a single $|jkm\rangle|L\rangle$ state. An analogue of the statistical

mechanical Eyring equation is then used to compute the thermally averaged capture rate constant:

$$k_c(T) = \frac{kT}{h}\left(\frac{h^2}{2\pi\mu kT}\right)^{3/2}\frac{Z^*(T)}{Z(T)} \tag{2.19}$$

where $Z(T)$ is the rotational partition function for the isolated neutral molecule [1].

The shortcomings of this method are clear: the capture boundary condition fails to account for any sort of quantum mechanical behaviour, such as tunnelling, reflection or non-adiabatic behaviour, during the capture process itself. However, it is accurate to high temperatures, unlike the ACCl theory, and is computationally inexpensive compared to quantum mechanical methods. Notice also that as $T \to 0$, $Z^*(T) \to 1$ and $Z(T) \to 1$. As a result, $k_c(T)$ will diverge as $T^{-1/2}$.

2.1.6 Statistical Quantum Capture Theory

In the ultracold temperature regime, where only a few quantum states contribute to the reaction dynamics, a fully quantum mechanical description is required. This is provided here through the statistical quantum capture model of Rackham and Manolopoulos [143, 144, 145].

The Coupled Equations

As with all statistical quantum problems, the time-independent Schrödinger equation must be solved directly. The equation is cast in matrix form within the coupled channel capture theory [146]:

$$\mathbf{\Psi}''(R) = \mathbf{W}(R)\mathbf{\Psi}(R) \tag{2.20}$$

where the coupling matrix contains information about both the rotationally adiabatic potentials and the collision energy [145]:

$$\mathbf{W}(R) = 2\mu\mathbf{V}(R) + \frac{L(L+1)}{R^2} - \mathbf{K}^2 \tag{2.21}$$

$$\mathbf{K}^2 = 2\mu(E\mathbf{I} - \mathbf{F}) \tag{2.22}$$

where $\mathbf{V}(R)$ is the matrix representation of the potential energy in the space fixed coordinate representation, E is the total available collision energy, $\mathbf{I}$ is the identity matrix and $\mathbf{F}$ is the diagonal matrix of asymptotic molecular rotational energies.

This equation cannot be directly integrated, as there will be points where the determinant of the wavefunction is zero. Instead, the log-derivative matrix $\mathbf{Y}(R)$ is used, defined such that:

$$\mathbf{\Psi}'(R) = \mathbf{Y}(R)\mathbf{\Psi}(R) \tag{2.23}$$

This transforms the second-order differential equation into a first order equation, which can solved directly using numerical methods..

Log-Derivative Propagation

An absorbing boundary condition is placed at the capture radius R_0. This is the point at which the complex can be assumed to have formed, and is treated as a convergence parameter in these calculations. It is defined as the largest possible value of the intermolecular distance R at which the boundary condition can be applied such that the calculations remain convergent. To enable these calculations to be used for both closed shell and open shell molecules, an Airy function boundary condition is used. It generates a diagonal matrix $\mathbf{y}(R_0)$, with elements $y_n(R_0)$ that correlate with the

eigenvalues of the coupling matrix at the capture radius, $w_n(R_0)$

$$y_n(R_0) = \begin{cases} \alpha_0 \dfrac{Ai'(x_0)}{Ai(x_0)} & \text{if } w_n'(R_0) < 0 \\ \alpha_0 \dfrac{Bi'(x_0) + iAi'(x_0)}{Bi(x_0) + iAi(x_0)} & \text{if } w_n'(R_0) > 0 \end{cases} \tag{2.24}$$

where

$$\alpha_0 = [w_n'(R_0)]^{1/3} \qquad x_0 = \frac{w_n(R_0)}{\alpha_0^2} \tag{2.25}$$

$Ai(x)$ and $Bi(x)$ are the Airy functions of the first and second kinds [147]. The initial log-derivative matrix is obtained using the unitary transformation given by the matrix of eigenvectors of the original coupling matrix, $\mathbf{C}(R_0)$:

$$\mathbf{Y}(R_0) = \mathbf{C}(R_0)\mathbf{y}(R_0)\mathbf{C}(R_0)^\dagger \tag{2.26}$$

The log-derivative matrix is then propagated over sequential intervals $[a, b]$, to progressively integrate the wavefunction out to infinite intermolecular separation. In a single propagation step, the coupling matrix $\mathbf{W}(\mathrm{c})$ is computed, where c is the midpoint of the $[a, b]$ interval. It is diagonalised to give eigenvalues $w_n(c)$ and the unitary transformation matrix $\mathbf{C}(\mathrm{c})$. The log-derivative matrix $\mathbf{Y}(a)$ is transformed into this local basis:

$$\mathbf{y}(a) = \mathbf{C}(c)^\dagger \mathbf{Y}(a)\mathbf{C}(c) \tag{2.27}$$

Within this basis, the transformed log-derivative matrix is propagated to the point b using the log-derivative propagator matrices $\mathcal{Y}_i(a, b)$:

$$\mathbf{y}(b) = \mathcal{Y}_1(a, b) - \mathcal{Y}_2(a, b)[\mathbf{y}(a) + \mathcal{Y}_1(a, b)]^{-1}\mathcal{Y}_2(a, b) \tag{2.28}$$

where the log-derivative propagator matrices are diagonal and have elements correlat-

ing with the eigenvalues of the coupling matrix [148]:

$$\mathcal{Y}_{1n}(a,b) = \begin{cases} |\sqrt{w_n(c)})|\coth|\sqrt{w_n(c)}|h & \text{if } w_n(c) \geq 0 \\ |\sqrt{w_n(c)})|\cot|\sqrt{w_n(c)}|h & \text{if } w_n(c) < 0 \end{cases} \tag{2.29}$$

$$\mathcal{Y}_{2n}(a,b) = \begin{cases} |\sqrt{w_n(c)})|\mathrm{csch}|\sqrt{w_n(c)}|h & \text{if } w_n(c) \geq 0 \\ |\sqrt{w_n(c)})|\csc|\sqrt{w_n(c)}|h & \text{if } w_n(c) < 0 \end{cases} \tag{2.30}$$

where $h = a - b$ is the interval length. Finally, the new log-derivative matrix is transformed back to the original basis set:

$$\mathbf{Y}(b) = \mathbf{C}(c)\mathbf{y}(b)\mathbf{C}(c)^{\dagger} \tag{2.31}$$

Evaluating the Scattering Matrix

In the asymptotic region of the potential, characterised by the converged intermolecular distance R_∞, there is no interaction, and the solution of the coupled equations in analytically known in the space-fixed frame of reference. This means that the scattering matrix for the capture process can be extracted via asymptotic matching [145]: comparing the actual log-derivative matrix to the form it is expected to take in the absence of any scattering or capture. The asymptotic form of the wavefunction is [149]:

$$\mathbf{\Psi}(R \to \infty) = \mathbf{I}(R_\infty) - \mathbf{O}(R_\infty)\mathbf{S}(E) \tag{2.32}$$

where $\mathbf{I}(R_\infty)$ and $\mathbf{O}(R_\infty)$ are matrices representing incoming and outgoing waves, and $\mathbf{S}(E)$ is the scattering matrix. The incoming and outgoing waves take the form of Ricatti-Hankel functions $\hat{h}_L^-(x)$ and $\hat{h}_L^+(x)$ [147], weighted by the elements of the

wavevector matrix $\mathbf{K}^2$ (eqn. 2.22):

$$I_{jkL}(R_\infty) = K_{jk}^{-1/2}\hat{h}_L^-(K_{jk}R_\infty) \tag{2.33}$$

$$O_{jkL}(R_\infty) = K_{jk}^{-1/2}\hat{h}_L^+(K_{jk}R_\infty) \tag{2.34}$$

where j,k and L are quantum numbers with their usual meanings. The scattering matrix is calculated using these and the asymptotic log-derivative matrix:

$$\mathbf{S}(E) = \mathbf{A}(R_\infty) + 2i\mathbf{B}(R_\infty)[\mathbf{Y}(R_\infty) - \mathbf{C}(R_\infty)]^{-1}\mathbf{B}(R_\infty) \tag{2.35}$$

where $\mathbf{A}(R_\infty)$, $\mathbf{B}(R_\infty)$ and $\mathbf{C}(R_\infty)$ are diagonal matrices given by:

$$\begin{aligned}\mathbf{A}(R_\infty) &= \mathbf{O}(R_\infty)^{-1}\mathbf{I}(R_\infty)\\ \mathbf{B}(R_\infty) &= \mathbf{O}(R_\infty)^{-1}\\ \mathbf{C}(R_\infty) &= \mathbf{O}'(R_\infty)\mathbf{O}(R_\infty)^{-1}\end{aligned} \tag{2.36}$$

This generates the scattering matrix in the space-fixed frame. However, more experimentally relevant information about the dynamics can be obtained in the body-fixed representation, and so the scattering matrix is transformed back via a unitary transformation. The elements of the body-fixed scattering matrix are:

$$S^{BF}_{J\epsilon,jkm,j'k'm'}(E) = \sum_{LL'}(U_{J\epsilon jmL})^* S^{SF}_{J\epsilon,jkL,j'k'L'}(E)U_{J\epsilon j'm'L'} \tag{2.37}$$

where the elements of the unitary transformation matrix $\mathbf{U}$ are evaluated in terms of Clebsch-Gordan coefficients:

$$U_{J\epsilon jmL} = \frac{i^L}{\sqrt{2(1+\delta_{k0})}}[\langle jm, J-m|L0\rangle + \epsilon(-1)^J\langle j-m, Jm|L0\rangle] \tag{2.38}$$

Capture Probabilities and the Rate Constant

During a capture process, unlike a pure scattering process [149], flux is removed from the reaction system, and so the resulting scattering **S**-matrix is non-unitary. The magnitude of the deviation from unitarity can be interpreted as the probability of capture arising from a single quantum state as a function of collision energy:

$$p_{J\epsilon jkm}(E) = 1 - \sum_{j'k'm'} |S^{BF}_{J\epsilon,jkm,j'k'm'}(E)|^2 \tag{2.39}$$

The cumulative reaction probability function is:

$$N(E) = \sum_{J}(2J+1)\sum_{jkm\epsilon} p_{J\epsilon jkm}(E) \tag{2.40}$$

This cumulative capture probability can be converted directly into a capture rate constant via a modified Laplace transform [150]:

$$k_c(T) = \frac{1}{2\pi\hbar Z(T)}\int_{-\infty}^{\infty} e^{-E/kT} N(E) dE \tag{2.41}$$

where $Z(T)$ is the asymptotic translational-rotational partition function.

Although the quantum capture model effectively calculates the adiabatic potential energy curves described previously, it does not make any assumptions about rotational adiabaticity. The dynamics are therefore not assumed to follow a single potential energy curve, potentially allowing nonadiabatic effects such as Coriolis coupling and couplings due to the kinetic energy operator to manifest.

In principle, these calculations are exact up to the level of accuracy of the potential. However, due to the computational expense of the propagation method the calculations can not be done for many quantum states. The method is therefore effectively limited to sub-Kelvin temperatures without access to a computing cluster.

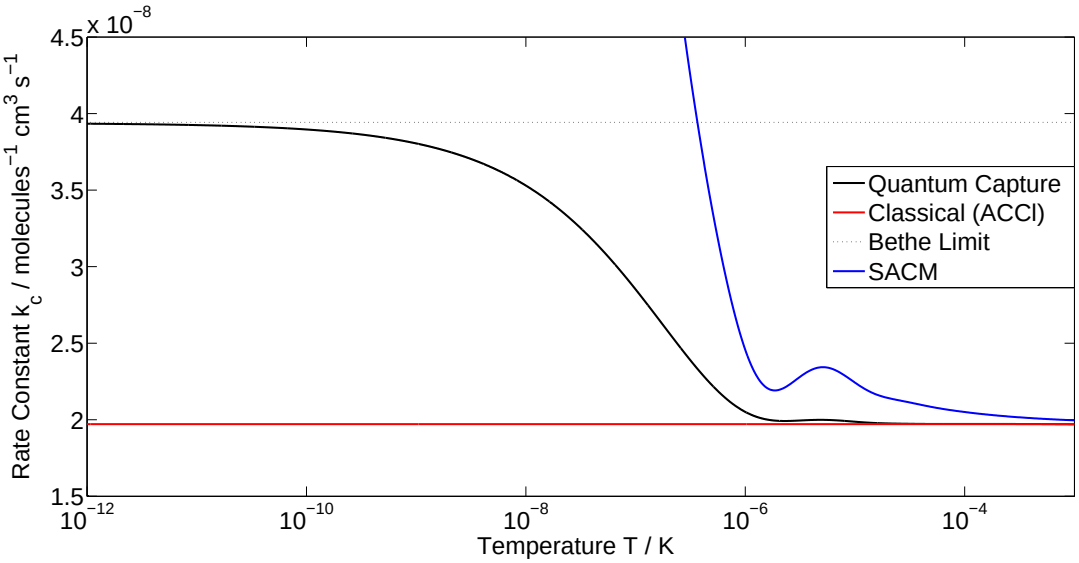


Figure 2.4: Comparison of the three different methods for the calculation of the capture rate constant for the H_3^+ + HCl reaction system, over the range 1 pK to 1 mK.

2.2 The Onset of Quantum Behaviour

2.2.1 The Quantum-Classical Divergence Temperature

A comparison of low temperature rate constants, computed from the previously described theories for H_3^+ + HCl capture can be found in Fig. 2.4. The potential used in these calculations uses all of the long-range terms defined in section 2.1.2.

It is immediately clear that the SACM diverges from both classical and quantum results over all of the range, giving an inadequate description of the low temperature dynamics, even at temperatures close to 1 mK, although above this range it is somewhat more successful [131, 132].

The classical rate constant has a constant limiting value as $T \to 0$. The quantum capture rate constant is roughly equal to this (within the level of the approximations) to around 20 μK, at which point it too diverges from the ACCl rate constant (most clearly visible in Fig. 2.5): at this temperature only the ground state and approximately five partial waves are contributing. This can be identified as the point at which

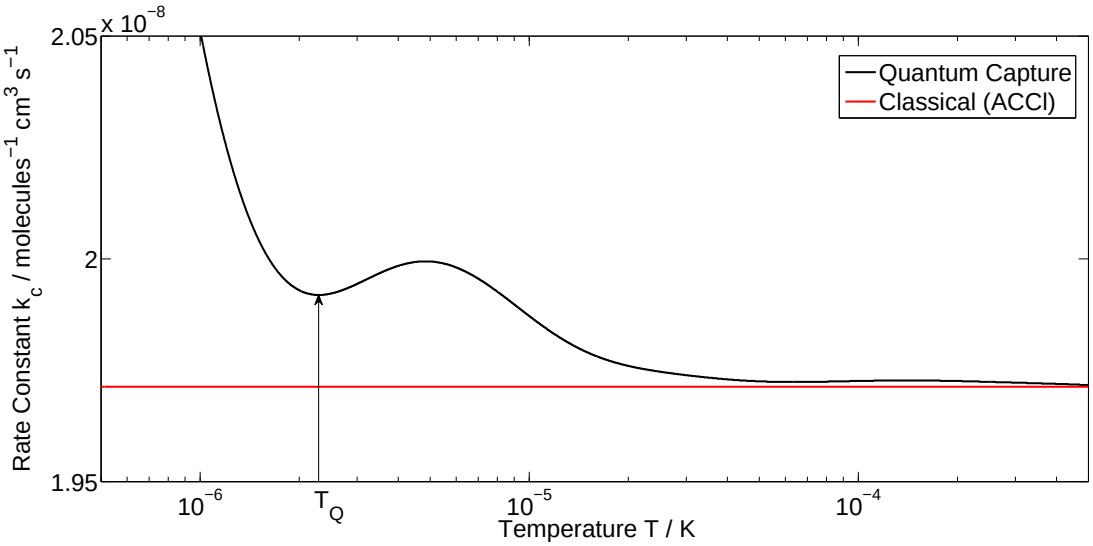


Figure 2.5: Enlarged comparison between the classical and quantum capture theories. The quantum-classical divergence temperature defined and used in this work is labelled.

quantum mechanics is beginning to manifest. This feature, a small peak, is ubiquitous in the quantum capture rate constant for ion-molecule capture, appearing in these calculations for any experimentally realistic value of the potential parameters.

The "bump" in the quantum capture rate constant that becomes visible increases as the temperature decreases, corresponding to the contribution of progressively fewer partial waves to the quantum capture rate constant. This corresponds to a reduction in the thermal statistical averaging. In the temperature range in which only the s (L=0) and p (L=1) partial waves contribute, the rate constant instead decreases, reaching a minimum at the temperature approximately corresponding to the transition to pure s-wave capture.

The maximum in this peak at 20 μK is only 2% larger than the total rate constant. Typical experimental rate constants have larger errors than this [135, 136]. As it is also only 2% above the classical rate constant, this would make it difficult to experimentally distinguish between the quantum and classical cases. However, the larger increase as temperature decreases, corresponding to pure s-wave capture, perhaps could be. The

ultimate limit as $T \to 0$ of the quantum capture rate constant is the Bethe limit [29], where formally:

$$\lim_{T\to 0} k_{c,Quantum} = 2 \lim_{T\to 0} k_{c,Classical} \tag{2.42}$$

In an attempt to characterise and place an upper bound on the onset of quantum behaviour in the rate constant, the quantum-classical divergence temperature, T_Q, was defined as shown in Fig. 2.5. This parameter was chosen as the temperature corresponding to the minimum that precedes the final quantum capture rate constant increase to the Bethe limit. This makes the value both experimentally relevant and theoretically reproducible.

The remainder of this section is devoted to exploring how T_Q changes as the molecular parameters in the intermolecular potential are changed. As these calculations are designed to guide future experimental studies which might try to identify where the transition to pure quantum behaviour occurs, the parameter space is limited to physically realistic values.

2.2.2 Ground State Linear Molecules

Calculations are performed in an attempt to gain a deeper understanding of T_Q, and how it is influenced by different potentials and molecules. As a first step, the case of linear molecules is considered. These have a simple rotational energy level structure, and serve as a good first step before increasing complexity.

The Langevin Potential Revisited

It is interesting to see whether the methods presented above can be used to add any understanding to the dynamics of the simple, isotropic, Langevin potential, given in equation 2.1. Classical methods predict a temperature independent rate constant, however the application of quantum capture theory does find a temperature depen-

dence emerging at sub-mK temperatures, with the same features presented in Fig. 2.5.

The Schrödinger equation for this situation contains four adjustable parameters, q, α, μ and B. These are systematically varied in an attempt to empirically derive an expression for T_Q. Since q^2 and α have the same weight within the potential, only α is varied. As a given parameter is varied, all other parameters remain at the values presented in Table 2.1 for H_3^+ + HCl capture, except for the permanent dipole and quadrupole moments which are set to zero.

The raw and linearised results of this analysis are presented in Fig. 2.6. Using linear regression analysis on these results [151], the following empirical equation was deduced for T_Q, with all molecular parameters in SI units:

$$T_Q \approx 0.3 \frac{\hbar^4}{(4\pi\epsilon_0)^2 q^2 \mu^2 \alpha k_B} \tag{2.43}$$

The form of this equation matches closely with the parameter θ_{VLT}, which was defined by Nikitin and Troe [130] based upon a consideration of the Massey adiabaticity parameter [152]. Equation 2.43 builds on that previous work by quantifying the pre-factor and giving the quantity a physical interpretation.

The equation can be rationalised thus: the intermolecular potential is isotropic, so the molecular rotation, and hence B, which only alters the orientation, would not be expected to affect the capture process for the Langevin case. Increasing the strength of the attractive interaction potential by increasing q or α, or decreasing the repulsive centrifugal term by increasing μ, causes the barriers in the rotationally adiabatic potential energy curves for partial wave states with $L > 0$ to decrease. A lower collision energy is therefore required to surmount or tunnel through them, and this corresponds to a lower T_Q. For this potential, values of T_Q seem to typically be of the order of 1 - 10 mK.

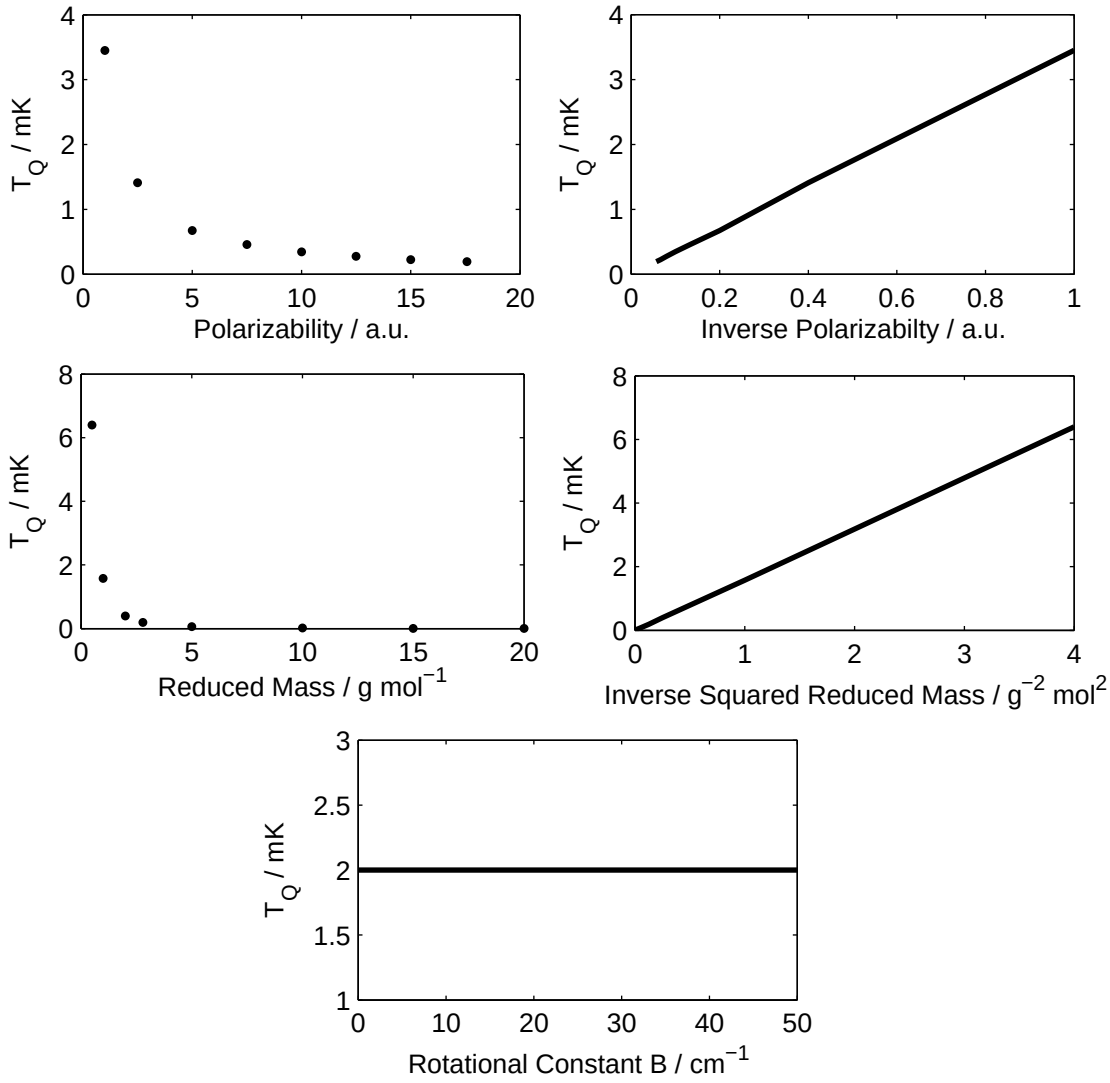


Figure 2.6: Graphs showing the relationship between T_Q and the molecular parameters relevant to the Langevin model. Raw data is shown in the left hand figures, and linearised data in the right hand figures. T_Q is independent of B.

Unfortunately, the Langevin potential is a poor approximation to the behaviour of many real molecules, especially those with permanent dipole moments. The capture radius for systems modeled with the Langevin potential is of the order of $10a_0$. In this regime, it is likely that the short-range potential will be important, including the vibrational component of the wavefunction. In addition, even homonuclear diatomic molecules, despite having zero dipole moments, often have significant quadrupole moments. The ion-quadrupole potential may then dominate any long-range behaviour.

The Ion-Dipole Potential

From an experimental point of view, this potential is perhaps the most relevant, as many of the methods that can produce samples of cold neutral molecules, such as Stark deceleration, rely on the electric dipole moment to work. To reflect the real physics as closely as possible, the potential function used for the following calculations consists of both the ion-dipole potential (equation 2.3) and the Langevin potential (equation 2.1).

The ion-dipole interaction varies as R^{-2}, as opposed to the Langevin interaction which varies as R^{-4}. As a result, for all intermolecular distances apart from the smallest, the ion-dipole term is expected to dominate the behaviour. Correspondingly, the capture radius for this system is typically around $100a_0$ for moderate dipole moments in the lowest rotational states, so this long-range model should provide a reasonable description of the capture dynamics.

There are now five parameters to vary: the four Langevin parameters and the additional dipole moment. A possible complication is the potential existence of three different dynamical regimes, depending on the relative values of μ_D and α, although in reality this is only a problem for non-zero dipole moments that are unrealistically small. The ion-dipole potential dominates the low temperature dynamics even for weak dipolar molecules such as carbon monoxide.

Using the same method as before, the following expression for T_Q is obtained, where the molecular parameters are in atomic units.

$$T_Q \approx 0.35 \frac{B}{q^2 \mu_D^2 \mu^2 k_B} \tag{2.44}$$

This equation is different to the Langevin case. The polarisability now contributes negligibly to the capture process. In the same way as before, increasing the ion-dipole potential parameters or μ will lower the barriers in the rotationally adiabatic potential curves, reducing T_Q. The dependence on B is new. This arises due to the coupling between the j=0 state, and the j=1 excited state. These states are coupled by the ion-dipole potential. This is independent of B, but B does control the energy spacing between states, indirectly affecting the magnitude of the coupling through the body-fixed to space-fixed basis set transformation. A larger B value means that these two states are further apart in energy, reducing the coupling. This reduces the j=1 character of the lowest adiabatic potential energy curve, making it less attractive and hence increasing T_Q, as capture occurs less readily.

A useful way of thinking about this is to consider that increased j=1 character in the ground quantum state enables some limited reorientation of the molecule. This can happen more readily as the amount of j=1 character of the ground state increases.

Unfortunately, for experimentally viable dipole moments (molecules to which current cooling methods can be applied), T_Q is predicted to lie in the range 1 - 10 μK, which puts it 2-3 orders of magnitude below the reach of direct cooling methods. Alkali metal diatomics such as KRb can be formed at sub μK temperatures, but they also have extremely large dipole moments (μ_D for KRb $\approx 0.30 e a_0$ [153]), resulting in an order of magnitude estimate of 10-100 nK for T_Q, which is still beyond the capability of current experiments using indirect methods to create ultracold molecules. It is also well below the lowest recorded ion trap temperatures, achieved using modern

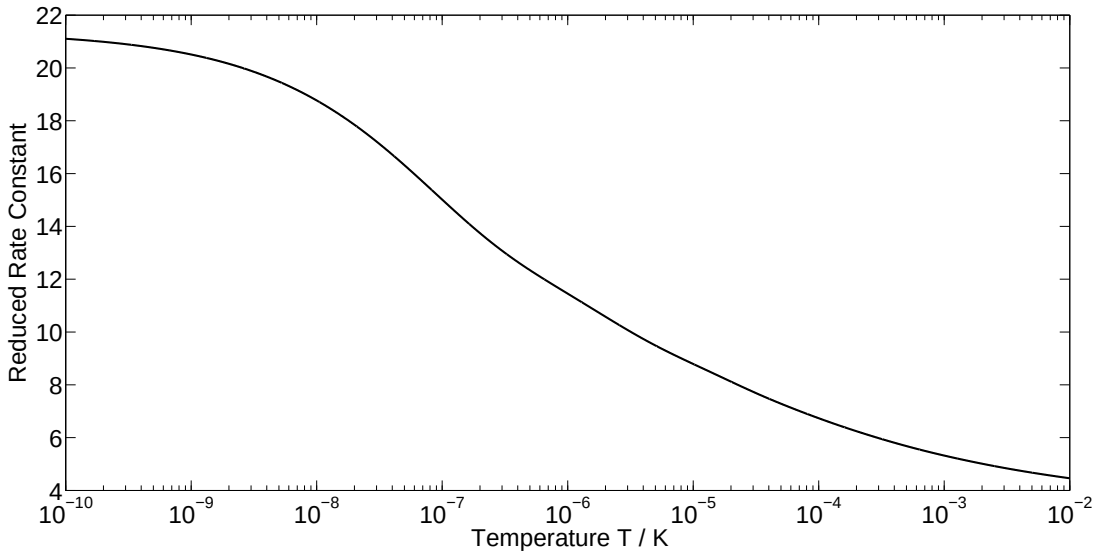


Figure 2.7: Total reduced rate constant for the j=1 rotational quantum state of HCl capture by H_3^+.

sideband cooling methods [154]. Many ion traps work by creating a harmonic pseudopotential at the centre of the trap. This means the ion trap has its own set of quantised translational energy levels, and moreover that the ground state has a finite zero-point energy. This potentially puts a fundamental lower limit on the ion-trap temperature that can be achieved, even if molecular cooling methods improve significantly in the future. Thus, the quantum-classical divergence temperature may never be reached for an ion-dipole system.

2.2.3 Excited Rotational States of Linear Molecules

Thermalised calculations of the capture rate constant amount to a consideration of the absolute rotational ground state only, as this is the only populated level. As the statistical onset temperature of quantum behaviour in this state is extremely low, the possibility of observing the onset of quantum behaviour for an excited rotational state is considered.

A calculation of the reduced rate constant ($\chi = k_c/k_L$, where k_L is given in equation

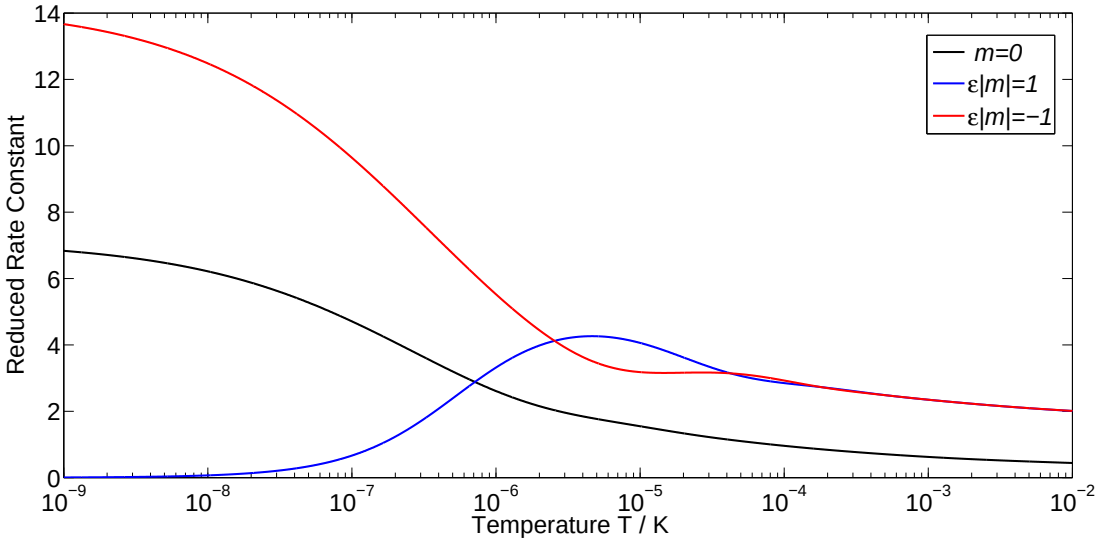


Figure 2.8: State specific reduced rate constants for the j=1 rotational manifold between 1 nK and 10 mK.

2.2) for the j=1 quantum state of HCl + H_3^+ capture is shown in Fig. 2.7. This function is featureless, giving little insight into quantum behaviour. However, there are three parity adapted m sub levels within the j=1 manifold, where m is defined with respect to the body fixed quantisation axis, over which the rate constant is calculated. But for the thermalised calculations, quantum behaviour was visible when a single quantum state (the ground state), contributed. A comparable situation considers the rate constants for each $|jm\epsilon\rangle$ state of the neutral molecule in isolation, as shown in Figs. 2.8 and 2.9 for both the $j = 1$ and $j = 2$ manifolds.

Several features should be noted. At high temperatures, where classical behaviour dominates, rate constants for states with the same $|m|$ are identical. This is consistent with the underlying adiabatic potential energy curves for these states. As the temperature decreases, the rate constants diverge from this expected behaviour, and at the lowest temperatures, the rate constants tend to precisely three separate constant values depending solely on either the parity of the state or if the state is the m=0 state. This is unexpected, and can be explored by considering the underlying capture probabilities as a function of collision energy for the s-wave capture process, as shown

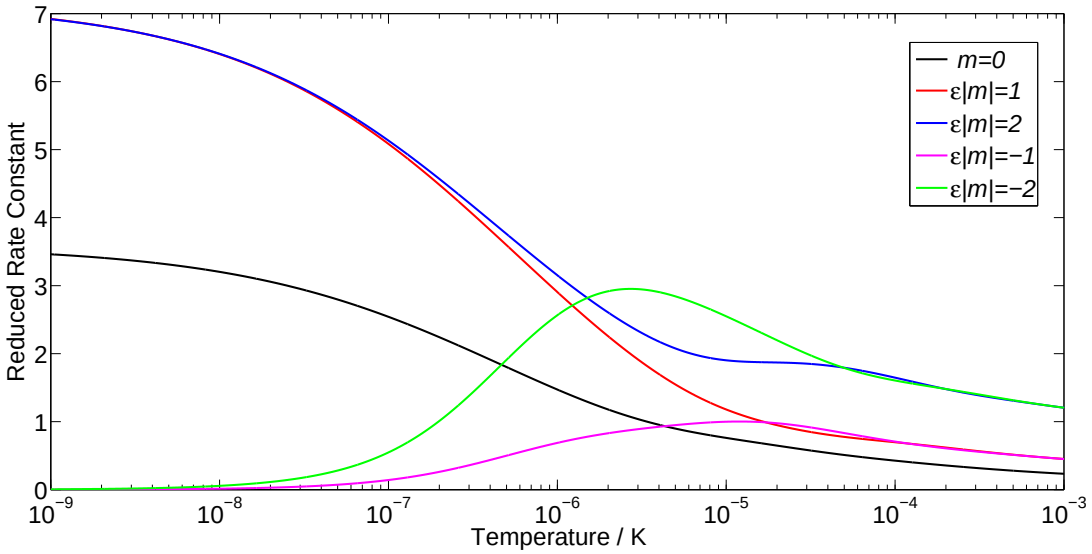


Figure 2.9: State specific reduced rate constants for the j=2 rotational manifold between 1 nK and 10 mK.

in Fig. 2.10 for the j=2 manifold.

At high collision energies, the capture probabilities for the states that have barriers in their adiabats (m=0 and $|m|$=1) increase with collision energy as expected. The probability of capture is zero below the corresponding barrier height $E_{0,n}$ of the adiabatic potential energy curves. The probabilities increase at collision energies near $E_{0,n}$, with a probability of 0.5 occurring at $E_{0,n}$. The probabilities finally asymptote at values of one. However, as the collision energy is lowered past about 10^{-6} au, the capture probabilities for m=0 and $|m|$=1 begin to increase, before decaying again at the lowest collision energies. The probabilities corresponding to positive parity states coalesce in this region. In addition, at roughly the same collision energy, the barrierless $\epsilon|m|$=-2 state's capture probability is seen to undergo a sudden change in gradient, rapidly diminishing to zero as E decreases. Curiously, the capture radius corresponding to the lowest temperatures is converged to be $120a_0$, which is about 3 times larger than the intermolecular distance corresponding to the barrier locations. These findings are consistent with earlier calculations performed by Nikitin and Troe on the j=1 state

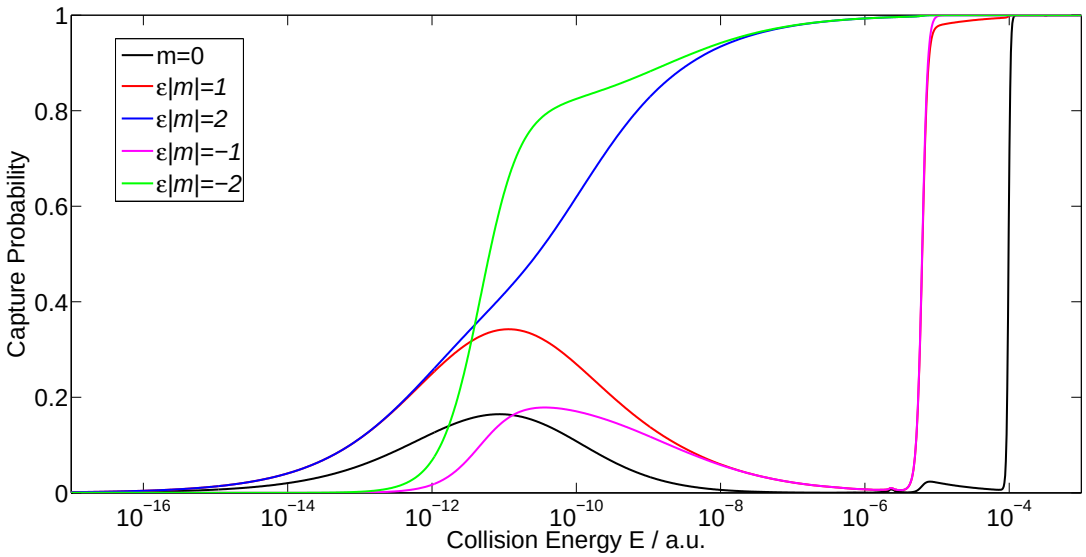


Figure 2.10: Capture probabilities as a function of collision energy for the s-wave substates within the j=2 rotational manifold. The collision energy is measured in Hartrees.

for the $H_2 + H_3^+$ capture process [130].

As in the $H_2 + H_3^+$ case, it is likely that nonadiabatic effects are responsible for this behaviour. The Coriolis interaction is known to mix m-states during a collision process, being particularly important at low temperatures. The mixed states thus produced in the rotationally adiabatic picture might then be acted upon by the kinetic energy operator, mixing them further and leading to non-adiabatic transitions between rotationally adiabatic states. This is consistent with the large capture radius, which implies capture occurs on or by coupling to a barrierless potential energy curve. This is further supported by the observation that, at the very lowest temperatures, capture can only arise from states with the same parity as the m=0 state (negative for odd j, positive for even j).

It is clear that this effect is quantum mechanical in origin. For the benchmarking system used, the temperature at which quantum and classical results begin to diverge is approximately 50 μK, more than an order of magnitude higher than the calculated value of T_Q in the ground state for this system.

2.2.4 Other Types of Molecule

Dipolar Molecular Ions

Molecular ions are rarely as structureless as the calculations thus far assume. They have rotational and vibrational structure, and potentially have permanent multipole moments of their own that can interact with the neutral molecules. The leading order term in this interaction potential is the dipole-dipole interaction, given by [123]:

$$V(R, \theta_1, \theta_2, \phi) = -\frac{\mu_1 \mu_2}{R^3}(2\cos\theta_1 \cos\theta_2 - \sin\theta_1 \sin\theta_2 \cos\phi) \tag{2.45}$$

where θ_1 and θ_2 are the angles between the molecules and the intermolecular axis, and ϕ is the angle of pitch between them. Matrix elements for this potential are computed [155] and combined with a body-fixed to space fixed basis set transformation [156] to perform quantum scattering calculations.

The results, produced in collaboration with Andrew Shakespeare, [157] show that the dipole-dipole interaction has almost no effect at all on the reaction dynamics, or on T_Q: the ion-dipole potential energy term dominates the ultracold behaviour for all physically reasonable values of the dipole moments.

Symmetric Tops

Due to their symmetry properties, a large number of symmetric top molecules have a permanent dipole moment, and these are often relatively large. In addition, the helicity quantum number k, equal only to zero for a linear molecule, gives a large number of candidate states for manipulation by electric fields. As a result, molecules like methyl fluoride [25] and d_3-ammonia are regularly used within cold chemistry.

The ultracold dynamics that would be predicted for the thermalised capture process match those of the linear molecule case, as for the j=0 ground state, k=0 only. As

these molecules have comparatively small B and large μ_D values, calculated T_Q values tend to be rather small. For instance, in the previously studied case of Ca^+ + MeF [69], T_Q is calculated here to be 20 nK.

$^2\Pi$ Open Shell Molecules

Several radical species, mostly heteronuclear diatomics that can be formed in a molecular beam discharge, are excellent targets for Stark deceleration. Some, such as OH [158] have already been decelerated, whereas others such as CH are extremely promising candidates [159]. Many of these species have $^2\Pi$ ground electronic states, and so can be studied with a modified version of the quantum capture theory already used.

The extra electronic spin angular momentum gives rise to spin-orbit coupling. The combination of Σ and Λ quantum numbers gives rise to two possible Ω angular momentum quantum numbers, yielding two possible ground state molecular terms: $^2\Pi_{1/2}$ and $^2\Pi_{3/2}$. The ground state term depends upon whether the spin-orbit coupling constant A is positive or negative. This gives rise to two separate spin-orbit manifolds, illustrated in Fig. 2.11. Example cases for both are studied to see how the dynamics are affected by the different ground states. The ground electronic state also experiences significant perturbation from excited electronic states, and this gives rise to the Λ-doubling phenomenon, which can be straightforwardly described with parameters l_1 and l_2, and a Λ-doublet parity quantum number p. Several adiabatic capture channels are closed at all collision energies, but the Airy function capture boundary condition used can effectively deal with this.

Additional complications exist that are neglected in the present calculations. Capture dynamics and chemical reactions can occur on multiple electronic potential energy surfaces, which can give rise to features such as conical intersections and avoided crossings, which cannot be included within the current framework. Coupling of the electronic angular momentum to the nuclear angular momentum of the constituent

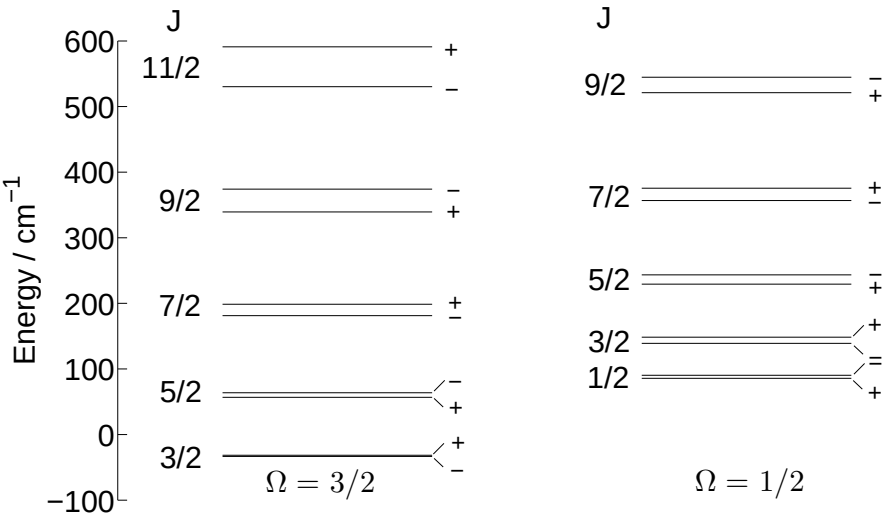


Figure 2.11: Illustrative spectrum of the rotational energy levels of the OH radical. The energy level structure shows two separate spin-orbit manifolds, and the Λ-doublet splitting of each energy level. Each Λ-doublet state is labelled by its corresponding value of the p quantum number,the $\pm$ labels corresponding to $p = \pm 1$. This splitting has been enhanced by a factor of 20 for visual clarity.

atoms, particularly hydrogen, can give rise to a rich hyperfine structure. This means there are too many quantum states to include in the basis with the available computing resources. Furthermore, nonadiabatic transitions are known to readily occur between Λ-doublet levels. It is possible to approximately include this effect within a time independent adiabatic capture theory by assigning additional probabilities corresponding to these transitions within various limits, such as the weak collision limit [160]. However, at the lowest temperatures, which are of interest here, these transitions are likely to be suppressed.

There exist several different coupling schemes for the angular momenta [161]. The formulation used here is based upon Hund's case A. Two different expressions are used for the molecular energy levels within the two spin-orbit manifolds [162]. For the $\Omega = 3/2$ states :

$$F_{j,p} = \frac{A}{2} + B\left[(j(j+1) - \frac{7}{4}\right] + \frac{pB}{2A}\left(2l_2 + \frac{l_1 B}{A}\right)\left(j - \frac{1}{2}\right)\left(j + \frac{1}{2}\right)\left(j + \frac{3}{2}\right) \quad (2.46)$$

and for the $\Omega = 1/2$ states:

$$F_{j,p} = -\frac{A}{2} + B\left[(j(j+1) + \frac{1}{4}\right] + \frac{l_1 p}{2}\left(j + \frac{1}{2}\right) \tag{2.47}$$

These energy levels form the elements of the diagonalised molecular Hamiltonian. The basis set used in these calculations is parity adapted in the following sense:

$$|jm\Omega\epsilon\rangle = \frac{1}{\sqrt{2}}(|jm\Omega\rangle + \epsilon|jm - \Omega\rangle) \tag{2.48}$$

where, the basis functions are similar to those used in eqn. 2.9:

$$|jm\Omega\rangle = \sqrt{\frac{2j+1}{4\pi}} D^{j*}_{m\Omega}(\phi, \theta, 0) \tag{2.49}$$

where all terms have the same meanings as before. The matrix elements of the complete potential energy function are, in this basis, most conveniently expressed in the space fixed frame of reference. They are given in terms of Wigner $3j$ and Wigner $6j$ symbols by [163]:

$$\begin{aligned}\langle j'L'\Omega'\epsilon|V(r,\theta)|jL\Omega\epsilon\rangle =& (-1)^{J+j+j'-\Omega}\sqrt{(2j+1)(2j'+1)(2L+1)(2L'+1)} \\ &\times \sum_l \begin{pmatrix} L' & l & L \\ 0 & 0 & 0 \end{pmatrix} \begin{Bmatrix} j' & L' & J \\ L & j & l \end{Bmatrix} \\ &\times \frac{1}{2}[1 - \epsilon\epsilon'(-1)^{j+j'+l}] \left[\begin{pmatrix} j' & l & j \\ -\Omega & 0 & \Omega' \end{pmatrix} \delta_{\Omega\Omega'} D_l(R) \right]\end{aligned} \tag{2.50}$$

This is diagonal in the total angular momentum J, and the $D_l(R)$ are the R-dependent coefficients of the total potential energy terms defined in equations 2.1, 2.3 and 2.4. The Langevin term corresponds to l=0, the ion-dipole term to l=1 and the ion-quadrupole term to l=2. This Hamiltonian is propagated using the techniques dis-

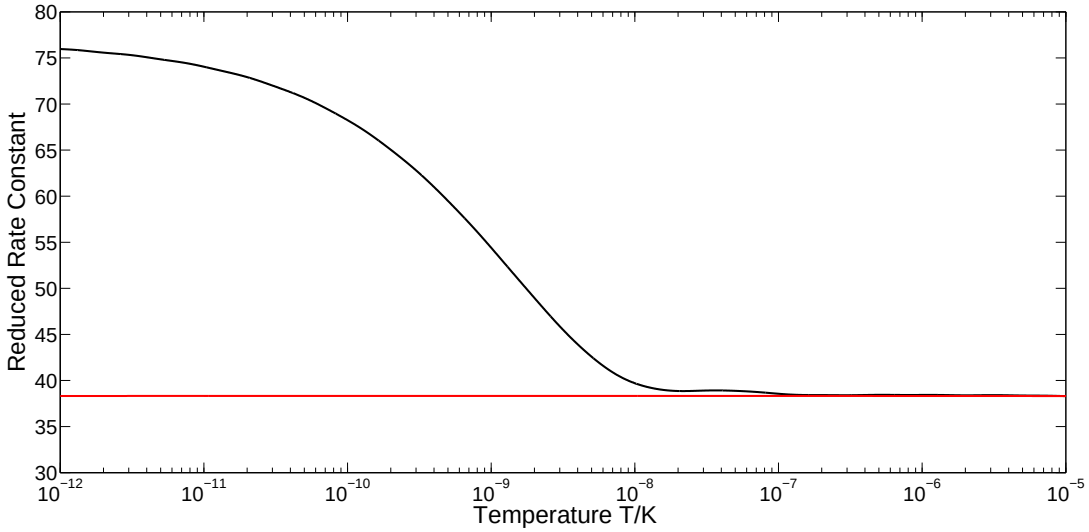


Figure 2.12: Reduced quantum capture rate constant for the NO ($^2\Pi_{1/2}$ ground state) capture process with C^+, over the range 1 pK to 10 μK, shown with the low temperature ACCl rate constant for comparison.

cussed in section 2.1.6. Classical calculations are also performed using the classical integral expression for the rate constant (eqn. 2.15), and the following perturbed rotor potentials [164]:

$$\begin{aligned} U_{jm\Omega} =& \frac{1}{R^4}\left(-\frac{\alpha q^2}{2} + \frac{q^2\mu_D^2}{2B}\left[\frac{(j^2-\Omega^2)(j^2-m^2)}{j^3(2j-1)(2j+1)} - \frac{(j+1)^2-\Omega^2)((j+1)^2-m^2)}{(j+1)^3(2j+1)(2j+3)}\right]\right) \\ &+ \frac{qQ(j(j+1)-3m^2)(j(j+1)-3\Omega^2)}{j(j+1)(2j+3)(2j-1)R^3} \\ &- \frac{s_m}{2}\sqrt{(\Delta F_j)^2 + \left(\frac{2q\mu_D|m|\Omega}{j(j+1)R^2}\right)^2} + \frac{s_m\Delta F_j}{2} \end{aligned} \tag{2.51}$$

where ΔF_j is the Λ-doublet splitting in a $|jm\Omega\rangle$ state and s_m is the sign of the m quantum number.

Fig. 2.12 shows the reduced rate constant for NO + C^+ capture, studied at higher temperatures by Troe [165]. The NO molecule has a $^2\Pi_{1/2}$ ground state, and is a weak dipole. T_Q is predicted to be approximately 200 nK, which from equation 2.44 is considerably lower than for a similar closed shell dipolar molecule such as CO.

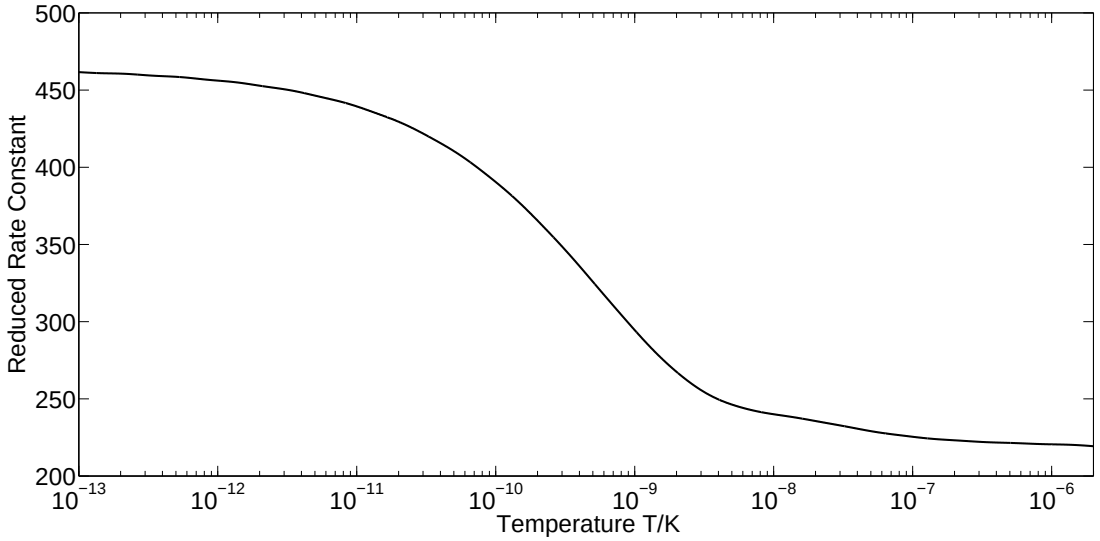


Figure 2.13: Reduced quantum capture rate constant for the OH ($^3\Pi_{3/2}$ ground state) capture process with H_3^+, over the range 1 pK to 2 μK.

Table 2.2: The parameters used for calculations on the NO + C^+ and OH + H_3^+ systems. The values are taken from [161] [163] and [164].

Parameter	NO + C^+	OH + H_3^+
B	1.7046 cm^{-1}	18.534 cm^{-1}
μ_D	0.063	0.657
α	11.337	7.693
μ	8.57 amu	2.55 amu
q	1	1
Q	-1.80	-1.27
A	124.2 cm^{-1}	-139.1 cm^{-1}
l_1	0.0117 cm^{-1}	0.235 cm^{-1}
l_2	0.0000941 cm^{-1}	-0.0387 cm^{-1}

Fig. 2.13 shows the reduced rate constant for OH + H_3^+ capture, studied classically by Clary [163]. This radical has a $^2\Pi_{3/2}$ ground state, and immediately it is clear that the shape of the low temperature rate constant is different, with the "bump" that allows for straightforward identification of T_Q almost completely smoothed out. In addition, a sensible estimate of T_Q seems to be of the order of 1 to 10 nK. Both effects can be ascribed to the j=3/2 ground state, where there are in fact two separate open channels at low temperatures those with projection quantum numbers of m=3/2 and m=1/2. Classical and quantum calculations both indicate that the m=3/2 channel is open at all temperatures, hence corresponds to the Bethe limit. The m=1/2 channel is closed below $T \approx$1nK, but is open above these temperatures. For all previous cases, only a single adiabatic channel was open close to T_Q. The m=-1/2 and m=-3/2 states are closed at all temperatures.

In conclusion, the $^2\Pi$ radicals seem to have even lower quantum-classical divergence temperatures than the closed shell dipolar molecules, and so would not make good candidate molecules for observing this transition.

2.3 Intermediate Temperature Behaviour For Selected Systems

2.3.1 The Ion-Dipole-Quadrupole Potential

The low temperature behaviour of the Langevin, ion-dipole and ion-quadrupole potentials have already been discussed. When the three terms are combined with the anisotropic polarisabilty, for reasonable values of the molecular parameters, the ion-dipole term always dominates the capture dynamics at the lowest temperatures. That said, the behaviour at intermediate sub-Kelvin temperatures is interesting, and provides a good example of the usefulness of the SACM and quantum capture methods

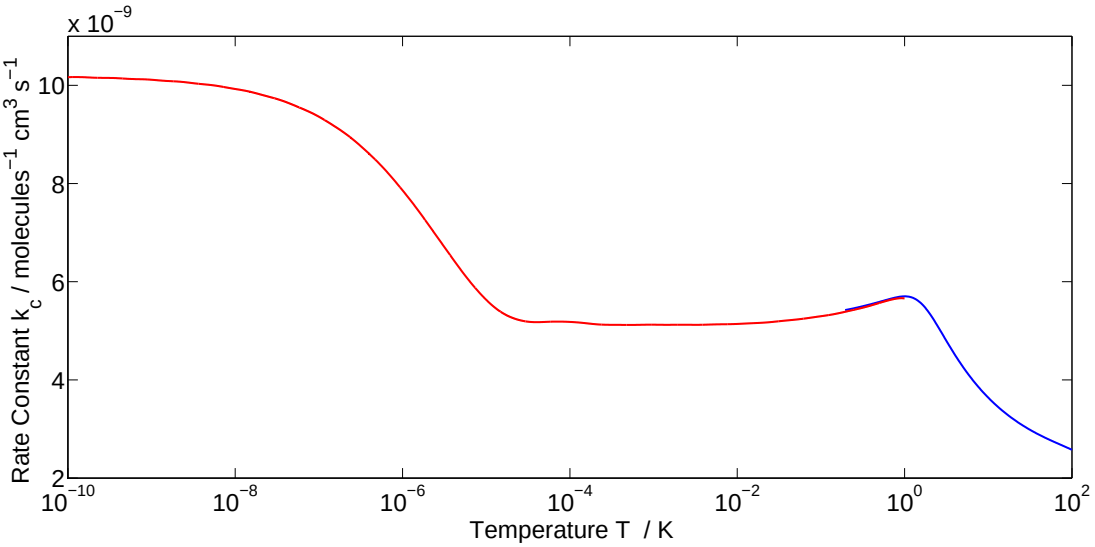


Figure 2.14: Capture Rate Constant for the CO + H_3^+ system over a large temperature range, using the quantum capture model (red) at low temperatures, and the SACM (blue) at higher temperatures. An intermediate region is shown as well to demonstrate the level of agreement between the two.

as a combined entity.

There are two possible situations: the sign of the quadrupole moment might be positive (repulsive) or negative (attractive). Consider a case with both an attracive quadrupole moment and a particularly weak dipole moment. Carbon Monoxide, CO, in the $^1\Sigma$ ground state is one such example. The reaction with H_3^+ is extremely important in interstellar chemistry, and has been extensively studied both theoretically [166, 167] and experimentally [168]. The computed capture rate constant over a wide temperature range is shown in Fig. 2.14. At the lowest temperatures, the rate constant is computed using quantum capture theory, and at higher temperatures the SACM is used, the transition being indicated by a change in colour.

The ion-dipole potential is of course seen to dominate the ultracold dynamics, but at temperatures just above 1 K there is a local maximum. This can be understood in terms of the weak dipole moment averaging essentially to zero, but the quadrupole moment as a planar rather than vector quantity, does not, and the potential is effec-

Table 2.3: The parameters used for calculations on the CO + H_3^+ system. All parameters are in Hartree atomic units unless otherwise stated.

Parameter	CO + H_3^+
B	1.9313 cm^{-1} [133]
μ_D	0.044 [169]
α	13.180 [170]
μ	2.71 amu
q	1
Q	-2.111 [171]
$\Delta\alpha$	11.5 [172]

tively the ion-quadrupole potential. As the temperature is lowered so is the available collision energy. This means that partial wave states with progressively lower L-values contribute to the rate constant, and the ion-dipole potential becomes more dominant as the averaging is reduced. Correspondingly, the capture radius increases. The neutral molecule samples the region of space near the ion to an increasingly lesser degree. A transition gradually occurs between an essentially pure ion-quadrupole potential at high temperature to a pure ion-dipole potential at low temperature. In this transition region, the statistically averaged rate constant is predicted to get smaller: an unusual result for an ion-multipole system.

It is also clear that the two methods are consistent with each other across the temperature range. The quantum capture theory would in principle compute the rate constant at all temperatures, but at an unfeasible computational cost. The SACM is orders of magnitude faster at higher temperatures, with equal precision. This gives confidence in the use of the SACM method for the purposes of experimental comparison at super-Kelvin temperatures.

2.3.2 Two-Temperature Rate Constant

Modern experimental methods are generally unable to produce the thermalised conditions that have so far been assumed. Different degrees of freedom are often cooled

to different characteristic temperatures, giving rise to highly non-thermal conditions.

The SACM can give insight into differential cooling of different degrees of freedom through the use of an approximate two-temperature rate constant [165]:

$$k_c(T_{trans}, T_{rot}) = \frac{kT_{trans}}{h}\left(\frac{h^2}{2\pi\mu kT_{trans}}\right)^{3/2}\frac{Z^*(T_{rot})}{Z(T_{rot})} \tag{2.52}$$

where the activated complex and rotational partition functions are calculated using the rotational temperature, and the translational partition function is computed using the translational temperature.

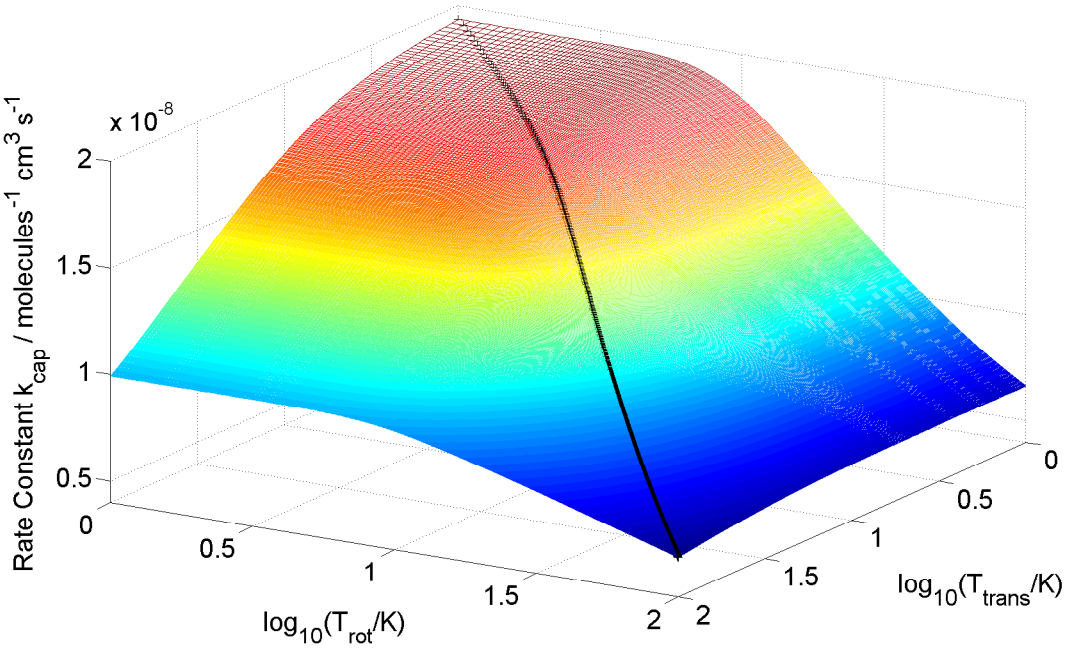


Figure 2.15: Two-temperature rate constant for the HCl + H_3^+ capture process over the range 1 to 100 K. The black line shows the thermalised rate constant discussed previously.

A full 2-dimensional SACM rate constant calculation for different translational and rotational temperatures is shown in Fig. 2.15 for the archetypal HCl + H_3^+ capture process. The temperatures considered are now in a more experimentally accessible regime than the rest of the work in this chapter, and may be used in future comparison

with experiment.

It is clear that being in the non-thermal regime has a significant effect on the rate constant. Consider for example the difference between the temperature dependent rate constants for a fixed value of T_{trans}=100 K or T_{rot}= 100 K. The rate constant increases more quickly, and tends to a higher value as T_{rot} decreases at the fixed T_{trans}, than as T_{trans} decreases at the fixed T_{rot}. This is perhaps expected, as a higher rotational temperature means additional averaging of the dipole moment, reducing the magnitude of the average potential, whereas a higher translational temperature affects only the collision energy.

2.4 Concluding Remarks

2.4.1 Suggested Experimental Directions

This work was motivated by the desire to experimentally observe quantum phenomena in a directly measurable statistical quantity. The results presented here suggest that there might be a few routes towards this goal.

The highest T_Q values, which in principle are the easiest to reach, unfortunately correspond to the weakest potentials, such as the Langevin potential, and the neutral molecules that might be well modelled by these potentials cannot be easily manipulated or cooled using current methods. The method of optical Stark deceleration, developed by Barker and coworkers, cools molecules by making use of their polarisability [173, 174]. This might be able to cool suitable molecules to a few mK in the future. However, with such a weak potential, the capture radius for the s-wave state is typically $10a_0$-$20a_0$, and in reality short-range effects are likely to play a significant role in the capture process in this regime.

One might also consider the possibility of using alkali metal dimers (in particular

homonuclear molecules) in these experiments. They have been made at low temperatures below quantum degeneracy by both photoassociation and Feshbach association [175], so might make excellent candidates for recently developed collision experiments that involve the superposition of an ion trap and a magneto-optical atom trap in a controlled manner [176, 177, 178].

The case of carbon monoxide is an interesting one. Due to its extremely weak dipole, T_Q is relatively high, around 100 μK. For the $^1\Sigma$ state of CO, this is far out of reach, but CO has a long lived $^3\Pi$ excited state. It has a radiative lifetime of around 3.2 ms [179] with a large dipole moment of 1.37 D. Stark deceleration of this state has been demonstrated by Bethlem *et al.* [55]. An experiment whereby metastable CO was created before Stark deceleration, and then repumped to the ground electronic state has been performed [180], and could potentially be combined with an ion trap.

More immediately, one might perform a velocity controlled experiment with Stark decelerated metastable CO to try and observe the maximum in the ion-molecule capture rate constant due to the transition between dominant ion-dipole and dominant ion-quadrupole regimes. The required temperature is lower than has been achieved thus far, but should be possible.

The m specific rate constants were demonstrated to exhibit quantum mechanical features at temperatures significantly higher than T_Q. If several of these parity states could be prepared, perhaps after cooling, it might make up for the current limitations in making cold molecules.

Advances in buffer gas cooling of molecular samples, combined with velocity selection should allow for sampling and testing of the two-temperature rate constant. A thermal distribution of neutral molecules can be formed at different temperatures with different buffer gases, eg 4 K for He and 17 K for Ne [181] yielding different rotational populations. The translational temperature could then be tuned for one of these rotational temperatures using a method such as velocity selection.

2.4.2 Limitations of the Model

The potential energy function used in these calculations is simple, only incorporating long-range effects. There are therefore certain kinds of behaviour that this model cannot predict, and any discussion of the calculations presented should reflect this.

The failure to include the hyperfine structure or short-range potential means that these calculations are not sensitive to non-statistical quantum effects, such as scattering resonances. These have been observed in a number of systems at collision energies corresponding to temperatures significantly above the quantum-classical divergence temperature defined here. Collision resonances might also occur in the lowest temperature regimes considered here, due to molecular hyperfine structure, although the Wigner threshold law is expected to dominate the behaviour. The lack of a short-range potential also introduces presumably large, although not quantifiable, uncertainties in the predictions made for non-dipolar molecules, depending on the effective capture radius. It also means that it is not possible to account for multiple reaction channels that might lead to different products. For instance, this is important in the understanding the full reaction between CO and H_3^+, where there are two experimentally observed isomeric products, HOC^+ and HCO^+ [168]. Reactions may also proceed on multiple, intersecting PES, especially in the open shell cases.

The simplicity of the model also renders it unable to enhance the understanding of subtle effects in chemical reactions. An example of this comes from a consideration of work by Gerlich and coworkers [182] that indicated that the reaction between H atoms and CH^+ did not proceed in the j=0 ground state of the ion, but did proceed in the j=1 excited state. The methods discussed above were used to try and understand this effect. The potential energy function appropriate to this case is:

$$V(R,\theta) = -\alpha\left(\frac{q^2}{2R^4} + \frac{4q\mu_D\cos\theta}{R^5} + \frac{\mu_D^2}{R^6}(3\cos^2\theta + 1)\right) \tag{2.53}$$

The leading order term is the Langevin potential, and when the rate constant is computed using statistical quantum scattering theory and the SACM, the ground rotational state of the CH^+ ion behaves precisely as one would expect any capture process proceeding under the Langevin interaction to occur, with a substantial ground state rate constant.

The calculations presented here are not promising, predicting quantum-classical divergence temperatures orders of magnitude below the reach of current experimental methods. Nevertheless, given the extremely rapid progression currently being made in the field of cold molecular science, it is not possible to predict the advancements in technology or experimental methods that may exist in the near future. The sub-mK temperature regime may well become accessible before long.

Chapter 3

The Stark Effect and Stark Decelerator Beamline for Ammonia

This chapter describes the first steps toward studying the ion-molecule reaction between cold, tunable-energy ammonia, and cold xenon ions. This involves a consideration of the manipulation of ammonia and its hydrogen/deuterium isotopologues by electric fields, in particular the removal of kinetic energy from ND_3 using the technique of Stark deceleration.

By way of introduction, the suitability of the isotopologues of ammonia for Stark deceleration is considered, by calculating the Stark effect in an asymmetric-top inversion doubled species. A Stark decelerator beamline, used as a tunable source of translationally cold ND_3 molecules, will be discussed, and its performance characterised. A set of new programs, used to simulate the experiment, are also introduced, and will be used both to illustrate the physics of the Stark decelerator beamline, and to gain further understanding of experimental time-of-flight spectra.

3.1 The Stark Effect for Ammonia Isotopologues

The Stark effect describes the lifting of the m-degeneracy of the rotational energy levels of a molecule in an applied electric field. This effect is exploited in a number of experimental techniques commonly used in the study of cold molecules, such as velocity selection, multipole guiding and focussing, and Stark deceleration.

There is an interest in producing cold samples of different isotopologues of a species such as ammonia (NH_nD_{3-n}) or water (OH_nD_{2-n}), and studying both the kinetic isotope effects that arise and branching ratios of the products. For instance, in cold dust clouds in the interstellar medium, large amounts of deuterated ammonia are present, and ion-molecule reactions can readily occur, due to their low or zero activation barriers, such as [183]:

$$NH_3 + H_2D^+ \longrightarrow NH_3D^+ + H_2$$

The NH_3D^+ ion can then recombine with an electron, losing one of the protons or the deuteron. The potentially resulting NH_2D molecule can then undergo the reaction again, to form $NH_2D_2^+$. The final equilibrium concentration of isotopologues is dependent on the relative rates of these reactions for the different isotopologues. In order to study such ion-molecule reactions in the laboratory, a sample of cold ammonia molecules must be prepared. The capacity to calculate the Stark effect for an asymmetric top with an off-axis dipole moment and inversion doubling quickly and efficiently is thus needed. The method presented here, based on work in [184], is used to diagonalise a single Hamiltonian matrix in a parity adapted basis set, which is necessary for the inclusion of molecular inversion.

The basis set used to calculate the Stark effect is the parity adapted symmetric top basis set defined in equations 2.9 and 2.10. The total Hamiltonian can be broken down into three terms:

$$\hat{H} = \hat{H}_{rot} + \hat{H}_{Stark} + \hat{H}_{inv} \tag{3.1}$$

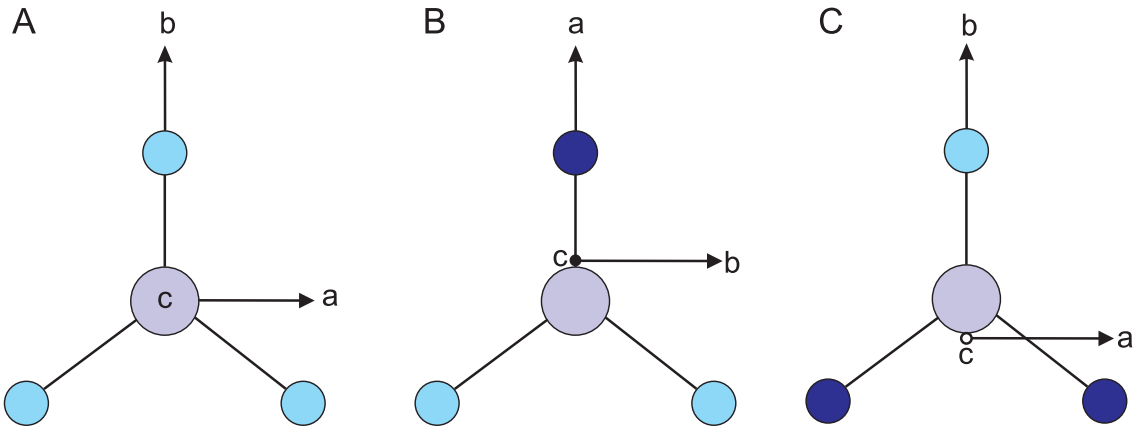


Figure 3.1: Schematic diagrams illustrating the locations of the a,b and c axes for NH_3 (A), NH_2D (B) and ND_2H (C). The c axis is directed out of the page for (A) and (C), and into the page for (B). The diagram for ND_3 is identical to that for NH_3.

where $\hat{H}_{rot}$ is the field-free rotational Hamiltonian, $\hat{H}_{Stark}$ is the field-dependent Stark Hamiltonian, and $\hat{H}_{inv}$ is a phenomenological Hamiltonian describing the inversion doubling of the energy levels. In the following discussion, all equations are in atomic units, unless otherwise specified.

3.1.1 Zero Field Hamiltonian

In field-free space, the rotational Hamiltonian operator is given by:

$$\hat{H}_{rot} = A\hat{\mathbf{J}}_a^2 + B\hat{\mathbf{J}}_b^2 + C\hat{\mathbf{J}}_c^2 \tag{3.2}$$

where $\hat{\mathbf{J}}_a$,$\hat{\mathbf{J}}_b$ and $\hat{\mathbf{J}}_c$ are the angular momentum operators about the a, b and c axes, and A, B and C are the corresponding rotational constants, designated such that $A \geq B \geq C$. These axes are shown in Fig. 3.1 for the four isotopologues of ammonia [185]. The asymmetric top Hamiltonian can be rewritten in terms of a reduced Hamiltonian:

$$\hat{H}_{rot} = \frac{1}{2}(A+C)\hat{\mathbf{J}}^2 + \frac{1}{2}(A-C)\hat{H}_{red}(\kappa) \tag{3.3}$$

where $\hat{\mathbf{J}}$ is the total angular momentum operator and $\hat{H}_{red}(\kappa)$ is the reduced Hamiltonian given by

$$\hat{H}_{red}(\kappa) = \hat{\mathbf{J}}_a^2 + \kappa\hat{\mathbf{J}}_b^2 + \hat{\mathbf{J}}_c^2 \tag{3.4}$$

where κ is Ray's asymmetry parameter:

$$\kappa = \frac{2B - A - C}{A - C} \tag{3.5}$$

The matrix elements of the total angular momentum operator are diagonal in all quantum numbers:

$$\langle jkm\epsilon|\hat{\mathbf{J}}^2|jkm\epsilon\rangle = j(j+1) \tag{3.6}$$

where j is the total angular momentum quantum number. The reduced Hamiltonian matrix has diagonal elements in the symmetric top basis set for all $k \neq 1$ given by [184]

$$\langle jkm\epsilon|\hat{H}_{red}(\kappa)|jkm\epsilon\rangle = \frac{1}{2}(\kappa+1)[(j(j+1) - k^2] - k^2 \tag{3.7}$$

and off-diagonal elements:

$$\langle jk \pm 2m\epsilon|\hat{H}_{red}(\kappa)|jkm\epsilon\rangle = \frac{1}{4}(\kappa-1)\sqrt{f(j,k\pm1)} \tag{3.8}$$

where

$$f(j,k\pm1) = [j(j+1) - k(k\pm1)][j(j+1) - (k\pm1)(k\pm2)] \tag{3.9}$$

Due to the parity adapted basis, a different expression is needed for the diagonal elements corresponding to k=1:

$$\langle j1m\epsilon|\hat{H}_{red}(\kappa)|j1m\epsilon\rangle = \frac{1}{2}(\kappa+1)[(j(j+1) - 1] + \frac{1}{4}\epsilon(\kappa-1)j(j+1) - 1 \tag{3.10}$$

Molecular inversion occurs because the isotopologues of ammonia can quantum

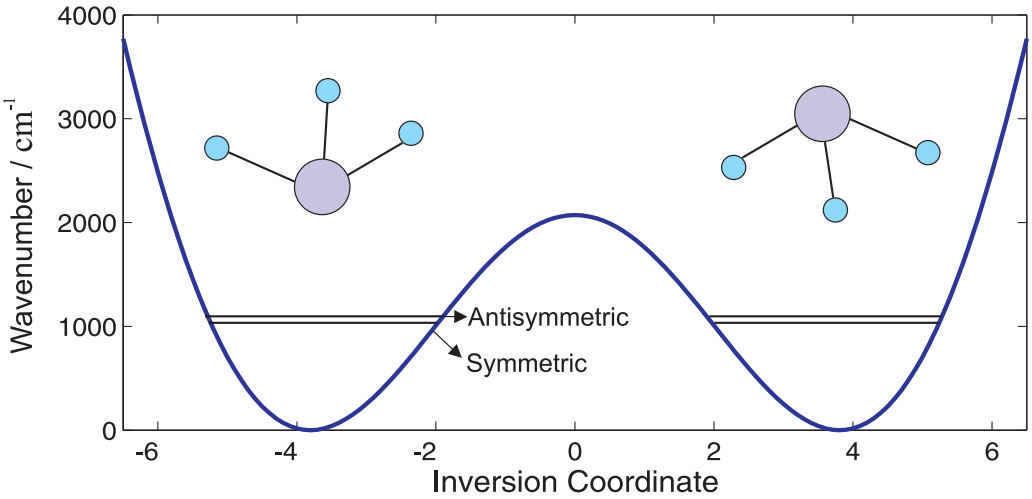


Figure 3.2: Double well potential for NH_3 inversion using the potential function of Manning [186], showing the splitting of the ground state wavefunction into symmetric and antisymmetric parity states. The inversion splitting of 0.712 cm^{-1} has been enhanced for clarity.

tunnel between two "inversion isomers" of C_{3v} or C_{2v} symmetry, proceeding via a planar D_{3h} or D_{2h} symmetry species. This leads to a double-well potential, and the eigenfunctions of such a motion are the parity-adapted basis functions of eq. 2.10. This is illustrated in Fig. 3.2. As the number of deuterium atoms in the isotopologue increases, the zero-point energy of the molecule decreases, and hence the relative barrier height in the potential increases.

This effect is introduced in a phenomenological manner, by noticing that the double-well potential breaks the degeneracy of the parity, an effect known as inversion doubling. Many empirical expressions exist for effective inversion Hamiltonians [187], although spectroscopic accuracy is not required for guiding and deceleration applications. In addition, only low-energy rotational states are used, removing the rotational state dependence. Hence, a simple Hamiltonian that gives a constant splitting between the parity states is used, the elements of which are diagonal in all quantum numbers

$$\langle jkm\epsilon|\hat{H}_{inv}|jkm\epsilon\rangle = \frac{1}{2}w\epsilon \tag{3.11}$$

where w is the spectroscopically measured inversion splitting, and ϵ takes values of ± 1.

3.1.2 The Stark Hamiltonian

The interaction between a dipole moment and an electric field gives rise to the Stark Hamiltonian, which describes the energy change of the dipole in the electric field. In the general case, this is given by the scalar product of the electric field $\mathbf{E}$ and the dipole moment $\boldsymbol{\mu}$:

$$\hat{H}_{Stark} = -\mathbf{E}.\boldsymbol{\mu} \tag{3.12}$$

This form is problematic for the present calculations, as the electric field is defined relative to some laboratory fixed frame of reference $F = \{X, Y, Z\}$, whereas the components of the dipole moment, μ_g are typically defined relative to the principal rotational axes $g = \{a, b, c\}$. If the direction of the electric field is defined to be the laboratory fixed Z axis, without loss of generality, then direction cosines Φ_{Fg} can be used to connect this to the rotating molecular frame:

$$\hat{H}_{Stark} = -\sum_{F}\sum_{g} E_F \mu_g \hat{\Phi}_{Fg} = -E_Z \sum_{g} \mu_g \hat{\Phi}_{Zg} \tag{3.13}$$

The matrix elements of the Stark Hamiltonian are then given by:

$$\langle jkm\epsilon|\hat{H}_{Stark}|j'k'm'\epsilon'\rangle = -E_Z \sum_{g} \mu_g \langle jkm\epsilon|\hat{\Phi}_{Zg}|j'k'm'\epsilon'\rangle \tag{3.14}$$

and the non-zero components of the direction cosine matrices are given by [187]:

$$\begin{aligned}
\langle jkm \pm |\hat{\Phi}_{Zc}| j+1 km \pm \rangle &= \sqrt{\frac{[(j+1)^2 - k^2][(j+1)^2 - m^2]}{(j+1)^2(2j+1)(2j+3)}} \\
\langle jkm \pm |\hat{\Phi}_{Zc}| jkm \mp \rangle &= \frac{mk}{j(j+1)} \\
\langle jkm \pm |\hat{\Phi}_{Zb}| j+1 k+1 m \pm \rangle &= -\sqrt{\frac{(j+k+1)(j+k+2)[(j+1)^2 - m^2]}{4(j+1)^2(2j+1)(2j+3)}} \\
\langle jkm \pm |\hat{\Phi}_{Zb}| jk+1 m \pm \rangle &= \frac{m\sqrt{(j-k)(j+k+1)}}{2j(j+1)} \\
\langle jkm \pm |\hat{\Phi}_{Za}| j'km \pm \rangle &= \pm i \langle jkm \pm |\hat{\Phi}_{Zb}| j'k \pm 1 m \pm \rangle
\end{aligned} \tag{3.15}$$

where $\pm$ and $\mp$ are used to represent the parity selection rules for each element, and i is the imaginary number. For the case $k = 0$, an extra factor of $\sqrt{2}$ must be included for the positive parity elements of the b- and c-axis direction cosine matrices, whilst the corresponding negative parity elements are zero.

3.1.3 Stark Splitting of Ammonia Isotopologues

The manipulation of molecules with electric fields in the Stark decelerator requires molecules to be low-field seeking (LFS) states. That is, the Stark energy is minimised when the molecules are in regions of zero electric field. The consequent repulsion from regions of high voltage allows for control of molecular trajectories: the force on the molecules is determined by the gradient of the Stark potential energy with respect to position.

Understanding the effect of the electric field on the molecular energy levels of the isotopologues is therefore necessary if the molecules are to be guided or decelerated. Stark maps showing this effect for the four hydrogen-deuterium isotopologues of ammonia were calculated in this work by the diagonalisation of the Hamiltonian using a self-written routine in Matlab. The results are shown in Fig. 3.3, for the j=1 rota-

Table 3.1: Literature values for the rotational constants, dipole moment components and the inversion splitting for the four hydrogen-deuterium isotopologues of ammonia

Parameter	NH_3 [187]	NH_2D [188]	ND_2H [189]	ND_3 [135]
A / cm^{-1}	9.4443	9.6775	7.445	5.1428
B / cm^{-1}	9.4443	6.4109	5.344	5.1428
C / cm^{-1}	6.1960	4.6964	3.753	3.1142
μ_a / D	0	-0.185	0	0
μ_b / D	0	0	0.21	0
μ_c / D	1.497	1.465	1.47	1.497
w / cm^{-1}	0.712	0.4059	0.171	0.053

tional manifolds, as the two parity states within the ground rotational state, $j = 0$, are both high-field seeking. Relevant molecular parameters are given in Table 3.1. The asymmetric top label τ [187] is not a quantum number, and is required because k is only a good quantum number for symmetric top molecules (where $A = B$ or $B = C$), such as ND_3 and NH_3, and not for asymmetric top molecules such as NH_2D and ND_2H.

Figure 3.3 shows that all four isotopologues have LFS states in this manifold. For the symmetric tops ND_3 and NH_3 this is the $|jkm\epsilon\rangle = |111+\rangle$ state within the current notation. For the asymmetric tops ND_2H and NH_2D, these are the $|j_\tau m\epsilon\rangle = |1_0 1\pm\rangle$ states. The Stark shifts are calculated to be about a factor of two larger in the symmetric top molecules than in the asymmetric tops, and this influences the prospects for Stark decelerating these species.

In this thesis, ND_3 is exclusively used for experimental Stark deceleration. This molecule has a a large Stark shift that is linear for almost all values of the electric field. In addition, nuclear spin statistics are important in determining quantum state populations due to the C_{3v} symmetry of ND_3 [50]. The rotational states transform according to the E or A_1 irreducible representations. The ground state transforms according to A_1, and states of this symmetry (*ortho*) account for approximately 40% of the sample. The $|111\pm\rangle$ states are the lowest energy states of E-symmetry (*para*), which account for the other 60% of the sample. In a molecular beam expansion of

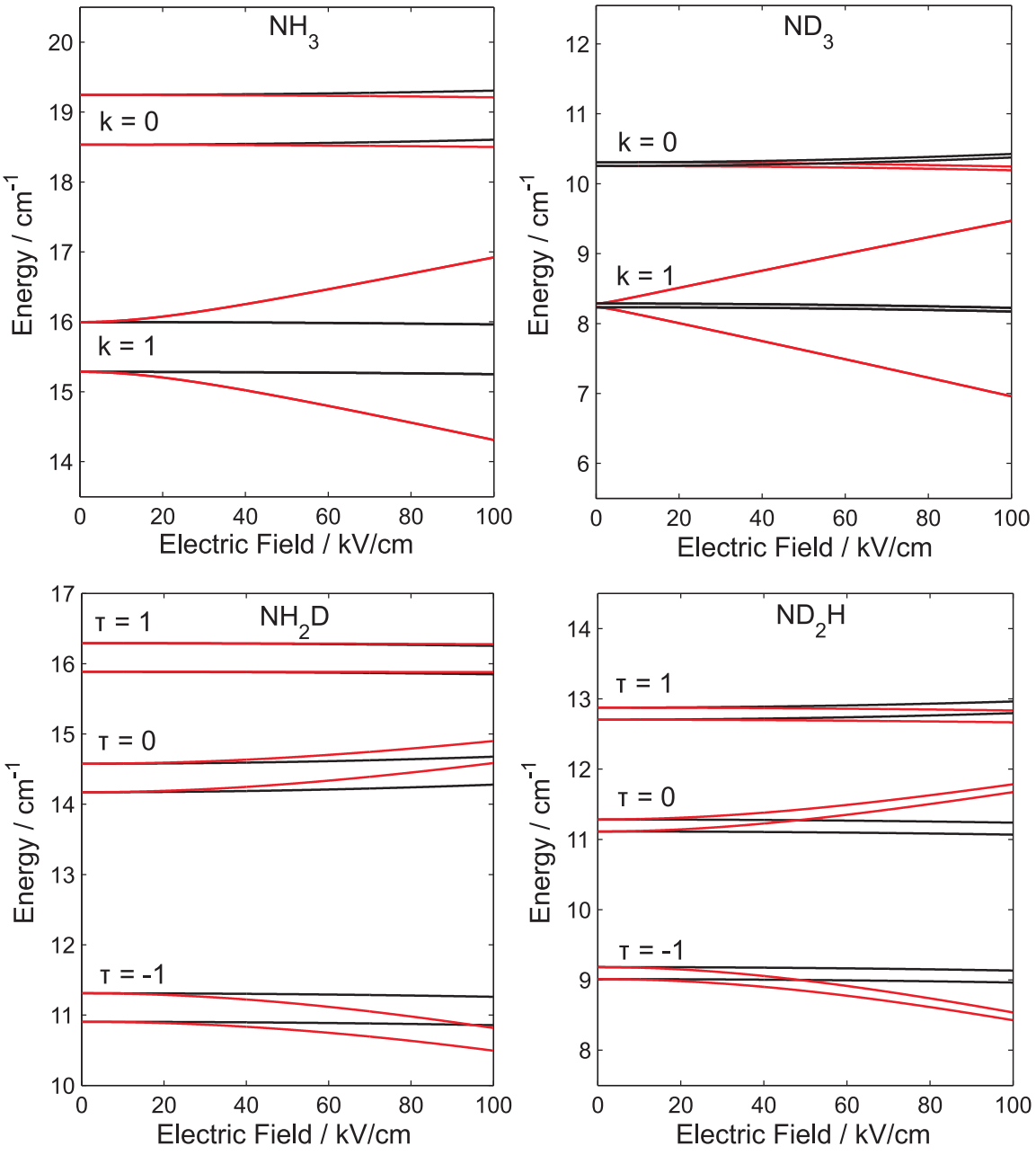


Figure 3.3: Energy level splittings of the j=1 rotational manifold of the four isotopologues of ammonia as a function of the applied electric field. The black lines correspond to states for which m=0, and the red lines to states for which m=1. The energies are calculated relative to the theoretical zero field energy in the absence of inversion doubling of the ground rotational state.

around 6 K, the majority of *para*-ND_3 molecules have been shown to be in the ground state, with approximately 6% in excited rotational states [190]. In total, 19% of molecules in the molecular beam are estimated be in the desired LFS quantum state.

Although it has recently become possible to Stark decelerate and detect NH_3 [191], the effective inversion barrier is much lower than in ND_3 (see Table 3.1), yielding a larger inversion splitting. As a result, a stronger electric field is required to quench the inversion: the Stark effect in NH_3 is quadratic up to fields of around 20 kV/cm, giving a linearly increasing force around the trap centre, rather than a constant one as for ND_3. This significantly reduces the force that molecules in the region experience.

The Stark deceleration of the mixed isotopologues has not been reported, although it has been attempted [192]. Detection is complicated by the reduced symmetry of these molecules. The nuclear spin statistics change, as there are now only two rather than three equivalent nuclei. This symmetry breaking means that the LFS state is no longer the ground state of an *ortho* or *para* set, hence there is no longer such a large population trapped in it. This reduces the number density of the decelerated species, making detection difficult. The Stark effect is also weak and quadratic for both ND_2H and NH_2D, the same limitation as for NH_3. Nevertheless, simulations can be performed (see section 3.2.1) to evaluate how efficient deceleration would be if sufficient population were achievable.

3.2 Stark Deceleration of Ammonia

The Oxford Stark decelerator is based on the original design by Meijer and Bethlem [193], and has been described previously by Bell [135]. In outline (see section 3.3 for more details), the decelerator consists of a linear array of pairs of parallel electropolished stainless steel cylindical rods. Adjacent pairs are arranged perpendicular to each other. The rods have a diameter of 3 mm, with a 2 mm gap separating each pair, and

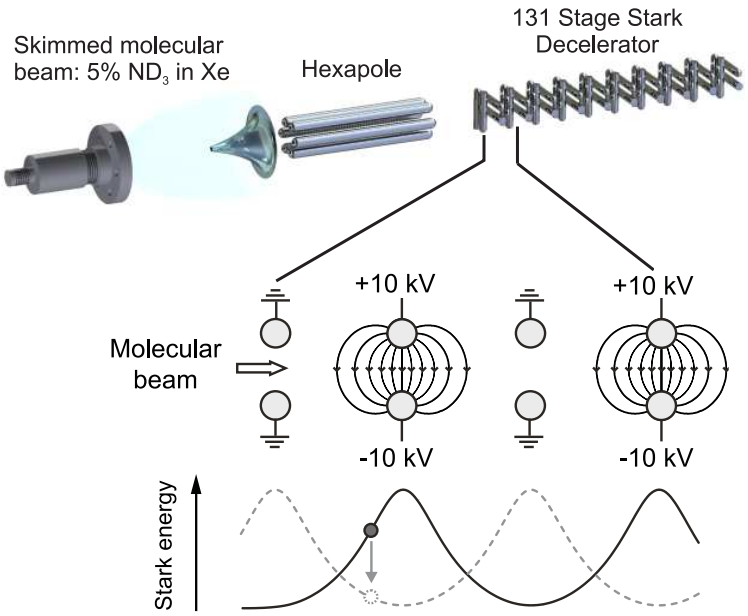


Figure 3.4: Schematic representation of the principle of Stark deceleration, illustrating the pattern of voltages that are applied to the electrodes and how the Stark energy changes during switching of the electrode voltages as a function of position. The render is not drawn to scale and the Stark decelerator only has the first 20 stages shown, for clarity. Figure adapted from [135].

a distance L=5.5 mm between electrode pairs. At a given moment, alternate electrode pairs are at ±10 kV, and the other electrodes are grounded (see Fig. 3.4). This creates a periodic electric field along the length of the decelerator. In order to achieve the time-varying electric fields necessary for Stark deceleration to occur [50], the high voltage is rapidly switched such that the grounded electrodes gain high voltage and *vice-versa*. This enables a pulsed supersonic molecular beam of 5% ND_3 seeded in xenon to be brought to a tunable final velocity.

The timing of the switching is such that the bunch of molecules is, for the majority of the time, on an upward slope of the field, as illustrated in Fig. 3.4. For each rise in potential energy, a small amount of kinetic energy is lost. The field is switched before the molecular bunch passes over the potential hill.

3.2.1 The Synchronous Trajectory

An essential concept in Stark deceleration is the consideration of the behaviour of a single idealised molecule along the z-axis of the Stark decelerator. The trajectory of such a molecule is used as a tool to calculate the switching times that are needed for optimal deceleration. The synchronous trajectory is chosen such that there is a constant kinetic energy loss per deceleration stage. As a result, switching occurs periodically in space, when the particle has travelled precisely a distance L (the electrode pair spacing).

A useful parameter that can be used to describe the motion of the molecules along the decelerator is the phase angle ϕ. If a single unit cell of the decelerator is assumed to begin at the centre of the grounded electrode pair, then at the position z,

$$\phi(z) = \left(\frac{z}{L} - \frac{1}{2}\right)\pi \tag{3.16}$$

With this definition, a phase angle of zero corresponds to a molecule being exactly between the grounded and high voltage electrodes, halfway up the potential hill. A phase angle of 90° corresponds to switching in the centre of the gap between the high voltage electrodes, at the top of each potential hill.

The phase angle can also be used to describe a switching sequence. The constant length intervals can be converted into constant phase angle intervals, and a switch occurs at a given phase angle ϕ_0 every time. When ϕ_0=0, there is no overall velocity change, as the molecule is symmetrically accelerated and decelerated by the field. This is referred to as "bunching" mode. When ϕ_0=90°, maximal deceleration occurs per stage.

The switching time sequence can be determined by integrating the equations of motion over sequential spatial intervals L. As the synchronous particle travels on-axis, only a one-dimensional simulation is required. Newton's Second Law is the relevant

equation of motion:

$$\frac{d^2z}{dt^2} = \frac{\mathbf{F}}{m} \tag{3.17}$$

where the force $\mathbf{F}$ is given by the spatial gradient of the Stark energy shift W:

$$\mathbf{F} = -\nabla W \tag{3.18}$$

The electric fields in the decelerator are computed using the SIMION package [194]. For the determination of the synchronous particle trjectory, only the z component is considered. The differential equation is integrated over precisely a distance L, and the corresponding time lapse used to compute the time sequence. The synchronous velocity change per stage is computed using the constant kinetic energy change per stage. Note that the pulses become more widely spaced in time as the molecules slow down.

Before attempting experimental deceleration of a species, the effectiveness of the process is simulated using the synchronous trajectory. Figure 3.5 shows the final velocity at the end of the Stark decelerator for the synchronous trajectory as a function of phase angle for the four ammonia isotopologues of section 3.1. Simulations were carried out at two different representative velocities. Experiments indicate that the typical molecular beam speed of a mixture of 5% ammonia in xenon from the pulsed valve is approximately 385 ms^{-1}. If the pulsed valve is cryogenically cooled, this drops to around 300 ms^{-1} [135].

It is apparent that, even with cryogenic cooling, neither of the mixed isotopologues ND_2D nor ND_2H can be effectively decelerated to low velocities using the 130 stages available in the Oxford Stark decelerator, although this would, in principle, be possible with a longer decelerator. Furthermore, there is the added complication of low populations present in the desired LFS states when using a pulsed nozzle source. By contrast, ND_3 and NH_3 can be effectively decelerated to extremely low velocities, both

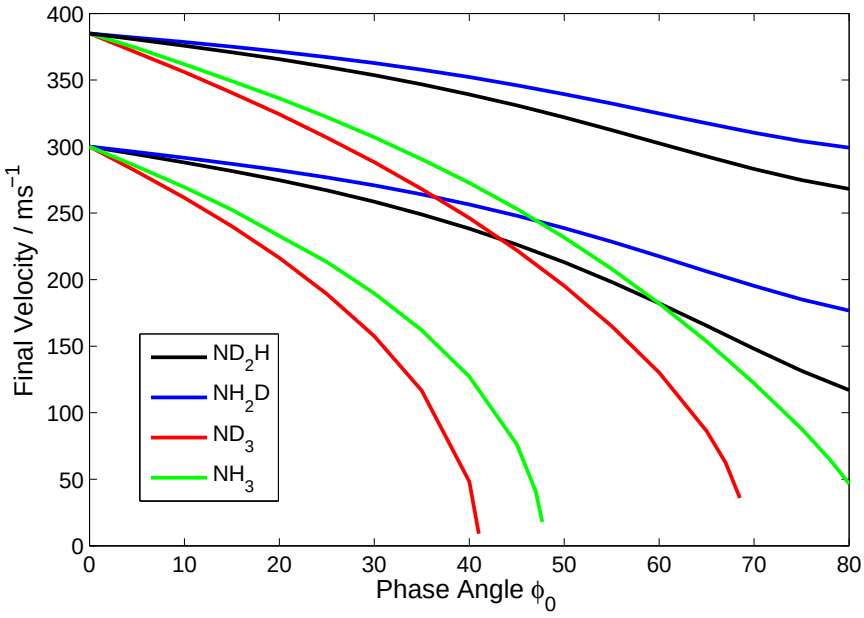


Figure 3.5: One dimensional simulations of the synchronous trajectory, showing the final velocities achieved for the four isotopologues of ammonia experiencing 130 stages of Stark deceleration in the $j = 1$ LFS states. Results are shown with initial velocities of 300 ms^{-1} and 385ms^{-1}.

at room temperature and under cryogenic conditions using the existing decelerator.

One-dimensional simulations indicate that the $|2_{-1}2\pm\rangle$ states of the mixed isotopologues might make good candidates for Stark deceleration, as they have larger Stark shifts. The fact that there exists a range of LFS states in low rotational energy manifolds makes these molecules good candidates for cooling techniques that make use of effusive molecular beams, such as velocity selection with or without buffer gas source cooling. The use of a neon buffer gas, for example, produces effusive beams with a characteristic rotational temperature of between 12 K and 20 K [195]. This populates several low-lying LFS rotational states, that could be guided using a bent electrostatic guide (see section 1.2.2)

The rest of this chapter will be concerned solely with simulations and experiments based on the Stark deceleration of ND_3.

3.2.2 Molecular Dynamics Simulations

Three-dimensional molecular dynamics (MD) simulations have been developed from code simulating the Stark decelerator (provided by Martin Bell), using a combination of the Fortran and Matlab languages to enable full characterisation of the Stark decelerator beamline experiment. A set of trajectories is run with a distribution of initial positions and velocities representing the initial molecular beam, selected using Monte Carlo methods. Transverse velocities are generated assuming a one-dimensional Maxwell Boltzmann distribution at 1 K, in line with observed temperatures of seeded xenon molecular beams [196, 197]. The active phase space is then modelled using a continuous uniform distribution over the interval -3 ms^{-1} $< (v_x, v_y) <$ 3 ms^{-1}. The transverse positions are generated assuming a uniformly opening disc, of diameter 1 mm, at the position of the pulsed valve. Rejection sampling is implemented at the position of the skimmer. Longitudinal velocities are generated according to the normal distribution, centred on the initial molecular beam velocity, with a standard deviation of 25 ms^{-1}, in line with the active phase space in [198].

The molecular beam is then propagated through the experiment using the velocity Verlet algorithm [199] for the velocity update and the Euler method [200] for the position update. If the current position and velocity of a particle i are $\mathbf{r}_i(t)$ and $\mathbf{v}_i(t)$, and the particle is being acted upon by a force $\mathbf{F}_i(t)$, then at a time δt later, they are updated to:

$$\begin{aligned} \mathbf{v}_i(t+\delta t) &= \mathbf{v}_i(t) + \frac{\delta t}{2m}[\mathbf{F}_i(t+\delta t) + \mathbf{F}_i(t)] \\ \mathbf{r}_i(t+\delta t) &= \mathbf{r}_i(t) + \delta t \mathbf{v}_i(t) \end{aligned} \tag{3.19}$$

where the force is computed as in equation 3.18 for the lowest LFS state of ND_3.

Each simulation requires an input file, detailing the electrode switching times relative to the pulse valve firing, as well as the synchronous velocity and position at the location of every switch. This is determined by the initial longitudinal velocity v_0 and

the switching phase angle ϕ_0. Additional input files, detailing the force vectors on a 3D grid of points in the Stark decelerator, hexapoles and buncher (see section 3.4) are pre-generated using SIMION [194]. Linear interpolation is used on this grid to find the actual force at an arbitrary position. The time steps are chosen such that there are an equal number per decelerator switching stage. Eight steps per deceleration stage give excellent convergence, as the gradient of the Stark potential does not change quickly over a deceleration stage.

These simulations neglect the presence of intermolecular forces between the particles, and hence the possibility of cluster formation. The breakdown of the clusters can be accompanied by an energy release, which is likely to accelerate some particles. However, clusters have a negligible dipole moment, and so are unlikely to be guided through the decelerator. Experimentally, cluster formation is minimised by using a low concentration of ammonia in the seeded xenon beam (although a small amount of clustering is still likely to occur). Molecular collisions are also neglected, although over the length of the decelerator this should be a valid approximation [201].

3.2.3 Non-Synchronous Longitudinal Trajectories

A real molecular beam pulse consists of molecules with a range of initial positions and velocities. The effect of the time-varying electric fields on the velocities of all of these molecules must be considered.

Consider the situation in Fig. 3.6. Simplistically, a particle that is moving faster and leads the synchronous particle will experience a greater decelerating force, losing an extra amount of kinetic energy ($\Delta W + \delta$) compared to that lost by the synchronous particle (ΔW). This particle is therefore decelerated more than the synchronous molecule. As such, the velocity and position of the leading particle approach the synchronous velocity and position, over many stages. This simple picture assumes that

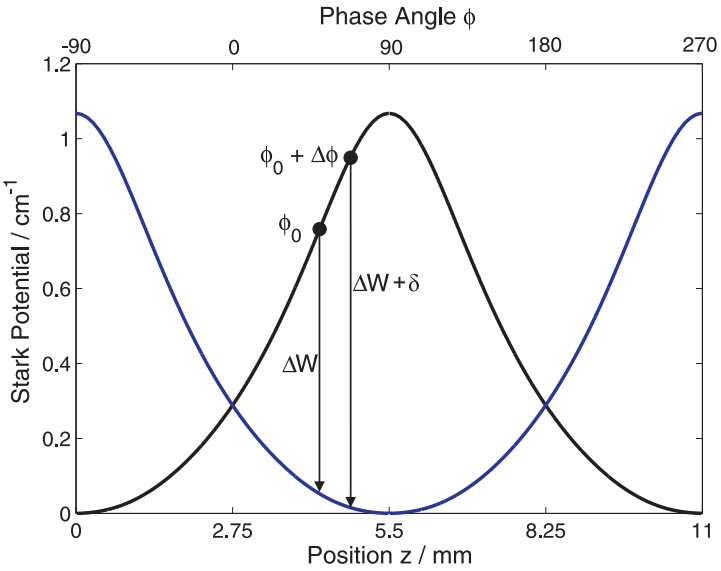


Figure 3.6: The Stark potential energy over the course of a single decelerator unit cell (black) and the instantaneously switched potential (blue). The synchronous particle and a particle leading it by a phase angle $\Delta\phi$ are shown. The potential shown is relative to its minimum value. The energy change for the synchronous particle upon switching the electric fields is ΔW; a molecule leading the synchronous molecule loses an additional amount of energy δ.

the effect of the Stark decelerator can be modelled as a set of molecules moving along the decelerator axis in a travelling potential well that is itself gradually decelerated. However, the time varying electric fields are generated by instantaneous switching, and this in fact generates a pseudo-travelling potential well, with more complex dynamics. This process has been studied for several molecules, including OH [53], CO [202] and ND_3 [50]. The longitudinal dynamics of a given particle are governed by:

$$\frac{mL}{\pi}\frac{d^2\Delta\phi}{dt^2} = -\left[\frac{\Delta W(\phi_0+\Delta\phi) - \Delta W(\phi_0)}{L}\right] \tag{3.20}$$

where $\Delta W(\phi)$ is the Stark energy lost per deceleration stage, $W(\phi) - W(\phi+\pi)$. Due to their periodicity, the energy differences induced by the instantaneous switching can

be expressed as a Fourier expansion [151]:

$$\Delta W(\phi_0) = \sum_n a_n \sin n\phi_0 \tag{3.21}$$

where fitting parameters of a_1 = 1.947×10^{-23} J, a_3 = -1.546×10^{-24} J and a_5 = 1.544×10^{-25} J are found to represent the potential for the experimental geometry and electric fields used in this thesis.

Fig. 3.7 illustrates the solution of equation 3.20 for switching phase angles of ϕ_0=30° and ϕ_0=60°. Phase space trajectory plots for molecules with different initial phase space conditions indicate that there exist two regions of phase space. A region close to the synchronous particle consists of stable, near-elliptical trajectories. This can be interpreted as a pseudo-travelling potential well, moving at the velocity of the synchronous particle, within which any particle will be decelerated. The extent of this region is defined by a separatrix (illustrated in all panels of Fig. 3.7), outside of which all particles follow unstable trajectories, and appear to accelerate away from the synchronous particle in its frame of reference. These particles, in unstable trajectories, appear as an undecelerated "main beam" in time-of-flight spectra. Both of these effects are observed in MD simulations of the deceleration process (shown in panels C and D of Fig. 3.7). After many stages of Stark deceleration, only a few non-phase stable molecules remain, and these follow trajectories along the separatrix. The vast majority are trapped inside the travelling potential well inside the separatrix (these potential wells are termed "buckets"). As ϕ_0 increases, the area enclosed by the separatrix, the "phase space acceptance", decreases [50]. This decreases the range of $\Delta\phi$ and Δv_z values that can be decelerated, hence tends to reduce the total number density of decelerated molecules.

The density of molecules inside the buckets is not uniform: the center of the bucket is dense. There is then a halo of low density, before a further increase in density near

the separatrix. The coupling of the transverse motion to the longitudinal motion, discussed in the next section, is the cause of this intensity variation.

A typical pulsed molecular beam will have sufficient duration to cover several unit cells of the decelerator. This means that, during a typical deceleration process, multiple adjacent buckets of the Stark decelerator will be filled. This can be seen in Fig. 3.7, where (particularly at $\phi_0 = 30°$) molecules from previous buckets that are following unstable trajectories are visible, outside of the plotted separatrix. This also indicates that, at the end of the decelerator, the decelerated beam and the falling edge of the main beam will be spatially overlapped.

The filling of multiple buckets is also illustrated by MD simulations in Fig. 3.8. The propagation of the molecular beam through the decelerator is shown at a variety of positions, and a total of eight buckets are occupied. At the end of the decelerator, buckets that lead the synchronous one are not decelerated to the correct final velocity, as they have left the decelerator before the synchronous particle has undergone the final stages of deceleration. This may therefore affect the velocity resolution of the output molecular beam. All of the buckets behind the synchronous one are, however, decelerated to the synchronous final velocity.

Any molecules within the phase space acceptance will be decelerated. In order to optimise the number of such molecules, the molecular beam pulse must overlap well with the initial synchronous trajectory. This is termed "phase space matching", and results in the synchronous bucket containing the highest phase space density of molecules.

3.2.4 Transverse Stability

As mentioned earlier, transverse effects have a large influence on the intensity variation of the phase space acceptance. These effects have been studied in detail [203] using

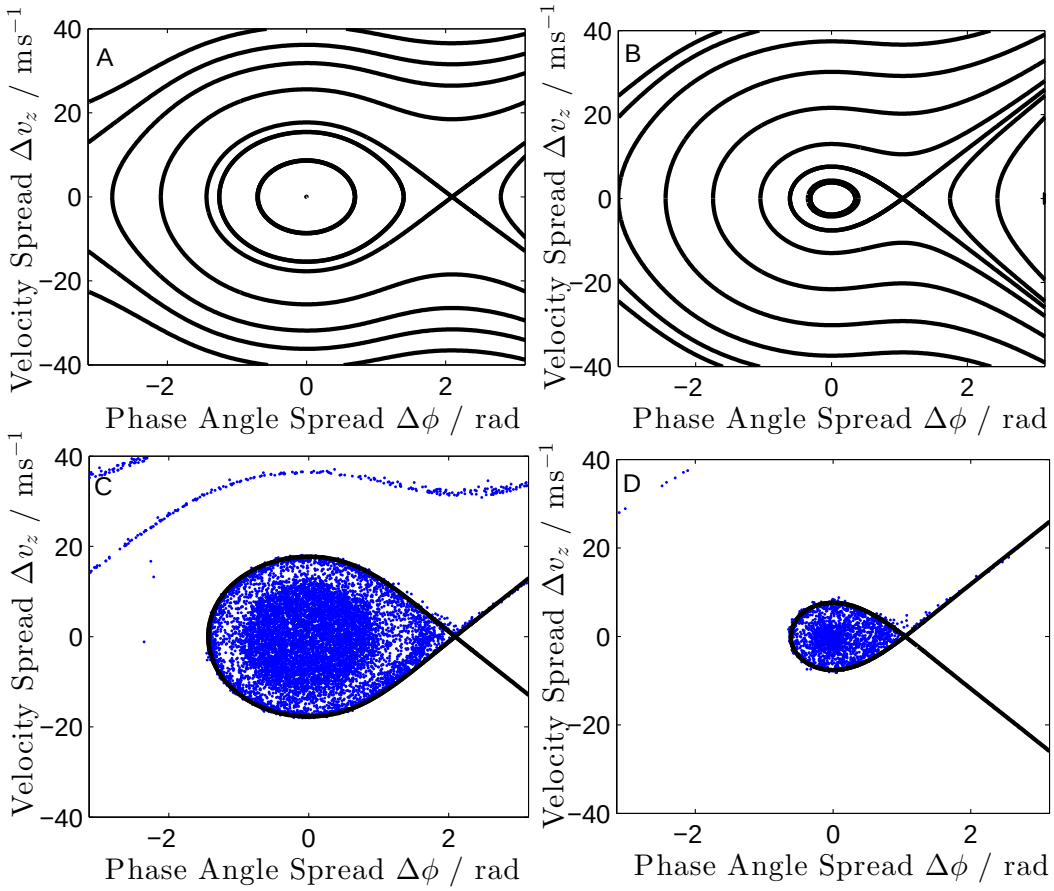


Figure 3.7: Longitudinal phase stability of the Stark decelerator over a single unit cell. Panels A and B show phase space trajectories of constant energy for ϕ_0=30° and ϕ_0=60° respectively. Stable closed trajectories are achieved inside the separatrix. This is compared with full MD simulation results in panels C and D (ϕ_0=30° and ϕ_0=60° respectively) for 130 stages of Stark deceleration, for which the final longitudinal phase space coordinates of trajectories with different initial conditions are plotted. A clear density variation of phase stable particles can be seen. The velocity and phase angle spread are calculated relative to the synchronous particle.

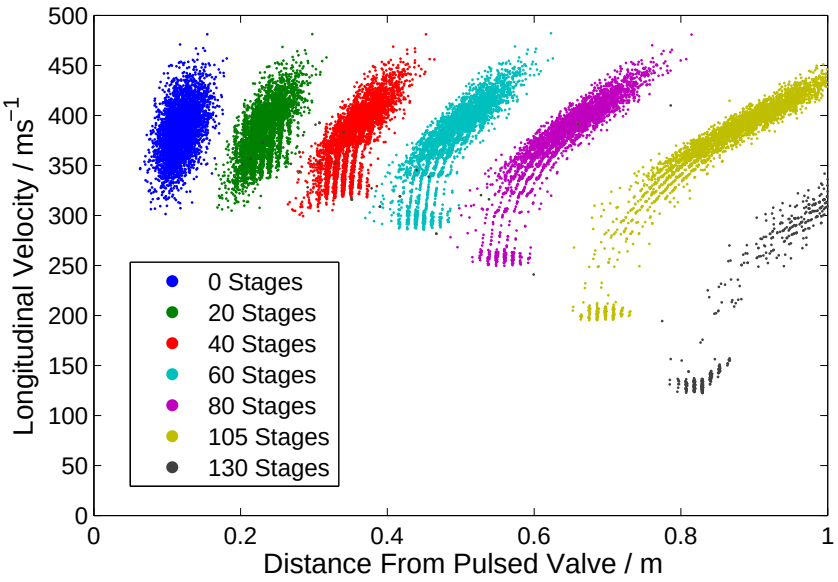


Figure 3.8: Simulated phase space propagation of a molecular beam pulse with an initial velocity of 385 ms^{-1} at seven different positions along the Stark decelerator at a phase angle of ϕ_0=60°. The molecular beam undergoes a complete 130 stages of Stark deceleration. Individual buckets of molecules from adjacent unit cells become visible at late times.

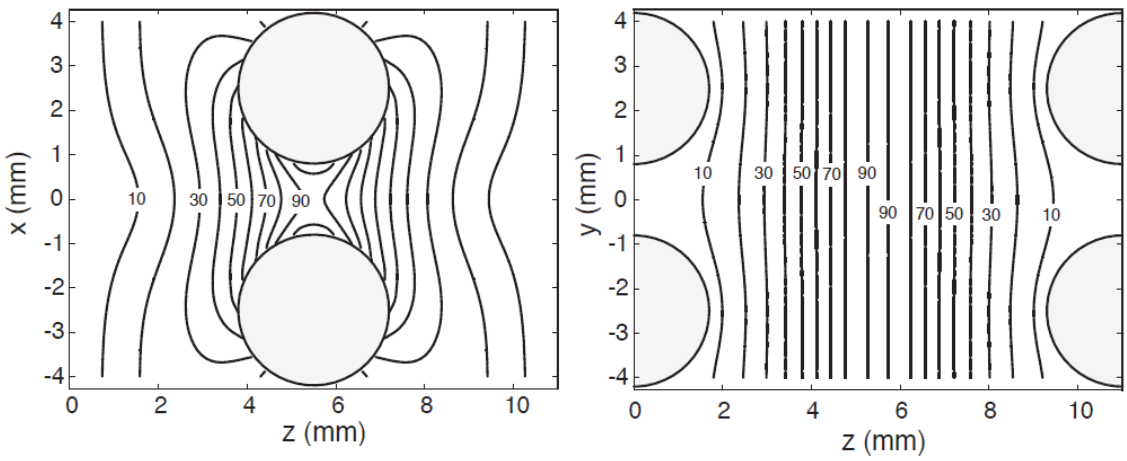


Figure 3.9: Calculated Electric field lines, in units of kV cm^{-1} for a single unit cell of the Stark decelerator in the $x-z$ and $y-z$ planes. The electrodes at z=0 are at high voltage, the electrodes at z=±5.5 mm are grounded. Figure reproduced from [135] with permission.

Mathieu theory, and can also be studied using MD simulations.

Consider the electric field lines shown in Fig. 3.9. Molecules travelling in the z-direction will be focussed in the x-direction due to the inhomogeneous electric field. However, in the y-direction, the field has more or less no gradient, hence very little focussing occurs. After a switch occurs, the opposite will be true. As a result, the transverse stability of molecules inside the decelerator is highly dependent on ϕ_0. If a low phase angle is chosen, the molecules spend relatively little time inside the regions of highest focussing, near the electrodes. If a high phase angle is chosen molecules will spend more time in the regions of highest focussing. So, the transverse phase space acceptance increases as a function of ϕ_0. This is illustrated using the results of MD simulations in Fig. 3.10. When performing experiments, 130 stages of the 131 stage Stark decelerator are in use. The Stark decelerator has fewer stages than are required for full separation of stable and unstable trajectories [135]. As a result, some particles that are following ultimately unstable trajectories are still transmitted, causing an excess of particles at the periphery of the phase space. The ideal 3D phase space acceptance for the instrument has been studied previously [135], by increasing the length of the decelerator by several hundred stages. This indicates that the optimal acceptance of the Stark decelerator occurs when $\phi_0 \approx 60°$.

Although not implemented in this experiment, several methods enabling an increase in the transverse phase space density of a Stark decelerator have been reported elsewhere. One method is to operate in so called $s = 3$, or third harmonic, mode [204]. Only every third stage is used for deceleration, with the two intermediate stages providing additional transverse focussing. This method provides a significant enhancement in phase space acceptance at low and intermediate phase angles, but overfocusses molecules at low velocity. It also requires a decelerator to be built that is three times the length of the current experiment, if the same number of deceleration stages are to be used. Another method that increases the phase space density at low velocities has

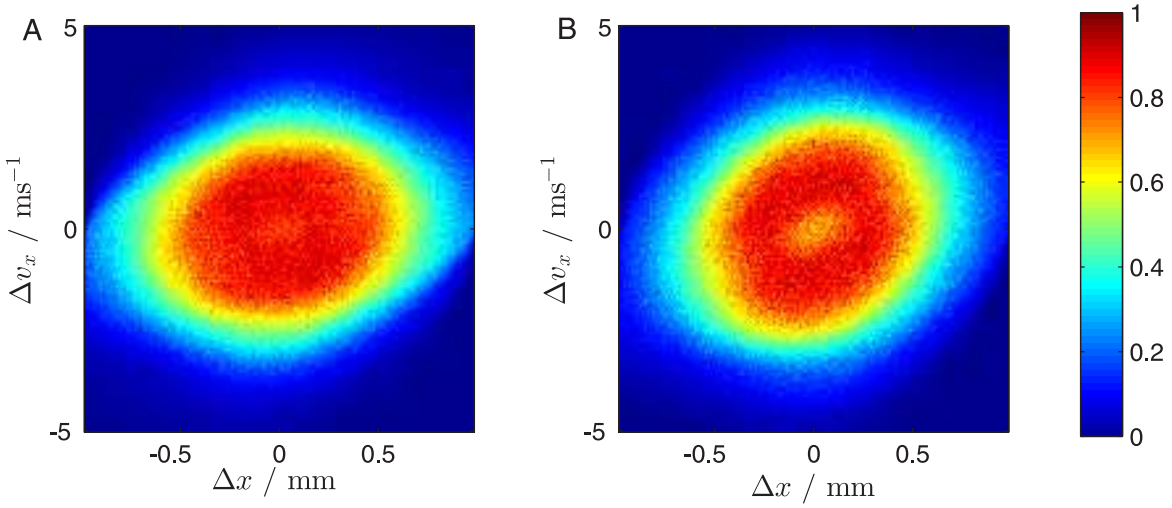


Figure 3.10: Transverse phase space after 130 stages of Stark deceleration for ϕ_0=30° (A) and ϕ_0=60° (B). A slightly larger phase space acceptance is observed for ϕ_0=60°, as well as a "hollowing out" of the centre of the phase space at the larger phase angle. The included colour map shows the relative acceptance density.

been suggested by Parazzoli *et al.* [205]. Molecules are aggressively decelerated at a high phase angle (typically 80°) to some final velocity when mid-way along the decelerator. The remaining decelerator electrodes are used to provide transverse guiding.

Meek *et al.* have recently developed a modified Stark decelerator, based upon the design of electrostatic traps, which operates by decelerating a molecular beam pulse using a true travelling wave potential well [206]. This results in a significantly improved phase space acceptance compared to the switched decelerator described in this thesis, enabling the phase stable deceleration of NH_3 as well as ND_3.

3.3 Experimental Setup

A schematic of the experimental setup employed in this thesis is shown in Fig. 3.11. The experimental design is based upon the Stark decelerator experiment of Bell [135] and the Stark decelerator beamline of Heiner [207]. A pulsed solenoid valve (modified General Valve 99 series, see [135]) is backed with approximately 5% ND_3 seeded in a

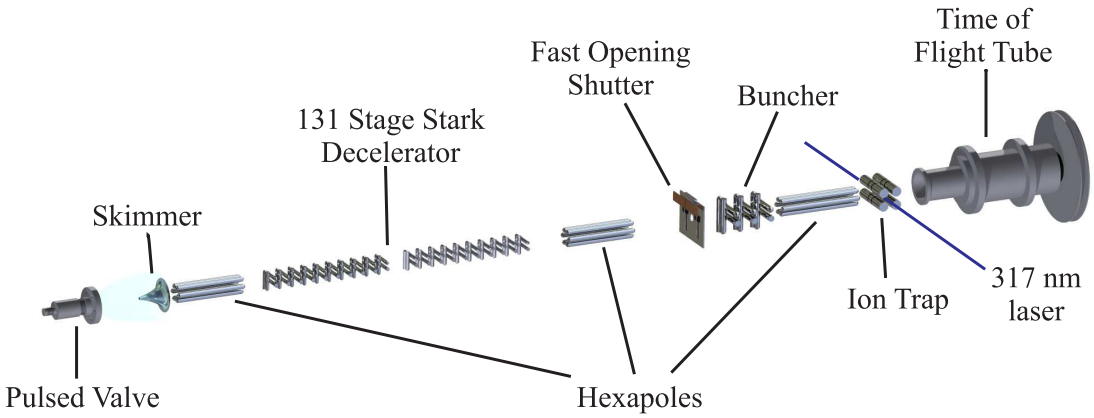


Figure 3.11: Schematic of the full experimental setup including the Stark decelerator, beamline and molecular detection apparatus. Experimentally, only the last 130 stages of the 131 stage Stark decelerator are actually used.

xenon carrier gas, at 3 bar backing pressure. The valve operates at an experimental repetition frequency of 10 Hz, with an opening pulse duration of 160 μs, allowing a supersonic expansion into a source chamber. The source chamber is held at 2.3×10^{-7} mbar, achieved using a rotary pump-backed turbomolecular pump (Leybold Turbomolecular 600C). This pressure rises to 6×10^{-7} - 1×10^{-5} mbar during pulsed valve operation. After 25 mm of free flight following the valve, the molecules pass through a 1 mm diameter skimmer and into the decelerator chamber. A second rotary-backed turbomolecular pump maintains the pressure in the decelerator chamber at around 5×10^{-9} mbar.

A further 20 mm after the skimmer, the molecules enter a 60 mm long hexapole. It consists of six stainless steel, electropolished rods, each 4 mm in diameter, sitting on a circle of radius 10 mm. They are mounted on MACOR insulator to minimise any conduction between them, and are alternately electrified to $\pm$10 kV. This voltage is produced via a contact to the odd numbered electrodes on the Stark decelerator. The first hexapole is pulsed for 150 μs and focusses LFS molecules into the decelerator, located 10 mm after the hexapole.

The decelerator geometry has been discussed in section 3.2. Physically, the de-

celerator is 715 mm in length, and consists of 132 pairs of electrodes, giving 131 stages, although the second stage is the first for which the electrodes are active. The electrodes are mounted on alumina supporting rods, with electrical contact coming from 4 ultrafast (less than 70 ns rise time) high voltage switches (Belke Elecctronic GmbH, HTS-150 PGSM) that enable near-instantaneous on-off switching of the electrodes. The peak electrode voltages are $\pm$10 kV. This is provided by power supplies backed by two large capacitors. The switching time sequence is calculated using a one-dimensional simulation, and uploaded to a custom built pulse generator, which controls the switches. A small bias voltage of 150 V is constantly applied to the decelerator to suppress any nonadiabatic transitions that might occur in zero field, a problem that is observed in electrostatic traps [208].

The second hexapole, identical in geometry to the first, is located 32 mm after the decelerator. This, with the third hexapole, is electrified by connection to the even Stark decelerator electrodes. After 28 mm, there is a vacuum compatible, fast-opening shutter (Uniblitz LS6TF-ECE including heat sink). This has an opening time of 800μs, which is sufficient to block any fast moving molecules that are not phase stable or are in free flight in weakly LFS or weakly HFS states, provided that ϕ_0 is large enough for the main beam and decelerated beam to be well separated.

The buncher, designed to provide longitudinal phase space focussing, is located 42 mm upstream from the shutter, and consists of a geometry identical to the Stark decelerator, but with all dimensions increased by a factor of two. The buncher consists of six pairs of electrodes of 6 mm diameter, with 11 mm between them. As such, the buncher is 55 mm in length, allowing for up to five stages of bunching. Typically only the last four stages are used. The need to pulse the electrodes in both switching states means that connections to both odd and even Stark decelerator electrodes are required. The third hexapole lies 11 mm later, and is geometrically the same as the other two, but 70 mm in length.

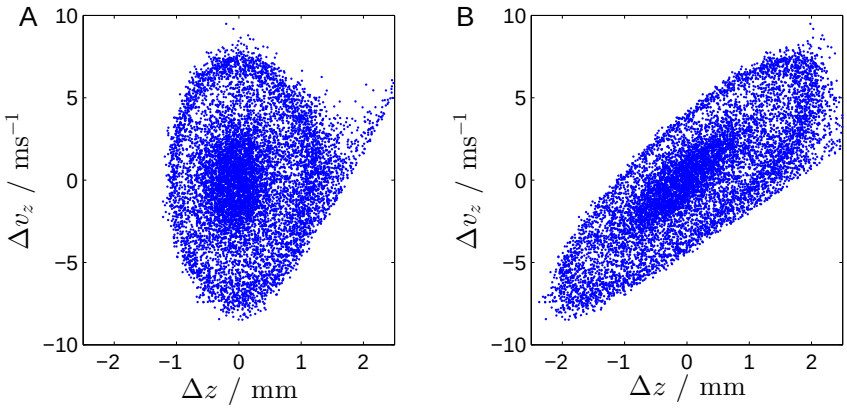


Figure 3.12: Simulated longitudinal phase space distributions for ND_3 (A): at the end of the Stark decelerator (B): after 3 cm of free flight. The faster molecules have moved ahead of the synchronous molecule, and the slower molecules behind, corresponding to a shearing transformation.

After a final 23 mm, the decelerated molecules arrive at the ion trap. During reaction studies, described in chapter 5, the ions in the trap act as the reaction target. For characterisation of the beamline, a focussed, pulsed dye laser (317 nm, 6-7 mJ/pulse) is sent through the centre of the ion trap. This selectively ionises the transmitted ammonia molecules in the LFS state by (2+1) resonance-enhanced multi-photon ionisation (REMPI), proceeding via the $B(v = 5)$ intermediate electronic state of ND_3 [209]. The front and back sets of the ion trap electrodes are electrified to +190 V and +300 V respectively, accelerating these ions toward a grounded time-of-flight tube, before colliding with a microchannel plate (MCP) for detection. The time-averaged, integrated MCP signal is proportional to the number of molecules in the laser focus volume, facilitating the recording of time-of-flight (TOF) spectra.

3.4 The Stark Decelerator Beamline

As Fig. 3.11 illustrates, the decelerated beam does not fly into the ion trap immediately upon exiting the Stark decelerator. Between the Stark decelerator and any other component, there is a period of free flight. This causes transverse expansion of the

decelerated packet, reducing the number density as a function of time. It also causes longitudinal separation of the packet, as illustrated in Fig. 3.12. This reduces the spatial resolution, as faster moving molecules move ahead of the synchronous particle, and slower molecules move behind it. In addition, the non-phase-stable main beam still passes through the decelerator, following approximately the same trajectory as the decelerated beam, but travelling ahead of it and containing orders of magnitude more molecules. If the main beam were to pass through the ion trap, it would react with the trapped ions before the decelerated beam had arrived, possibly dominating any observed reaction.

The Stark decelerator beamline employed in this thesis has been designed such that a dense, longitudinally resolved molecular beam is focussed into the ion trap. Transverse focussing into the buncher and into the ion trap is provided by the second and third hexapoles. A fast opening shutter is used to block the main beam from entering the buncher, with the opening time selected to admit only the decelerated beam. The buncher can be operated in two ways, designed to provide high spatial or energy resolution at the center of the ion trap, as discussed in section 3.4.2 below.

For all of the simulations discussed below, good convergence is obtained with 20 time steps along the length of the hexapole and 20 time steps per stage of bunching.

3.4.1 Transverse Hexapole Focussing

The ideal hexapole potential Φ for fixed applied voltages on infinitesimally small electrodes is [210]:

$$\Phi(x, y, z) = \frac{\Phi_0}{r_0^3}(x^3 - 3xy^2) \tag{3.22}$$

where Φ_0 is the applied potential relative to ground and r_0 is the distance from the centre of the trap to the centre of one of the electrodes. The electric field arising from this potential generates uniform circular electric field lines in the $x - y$ plane, so all

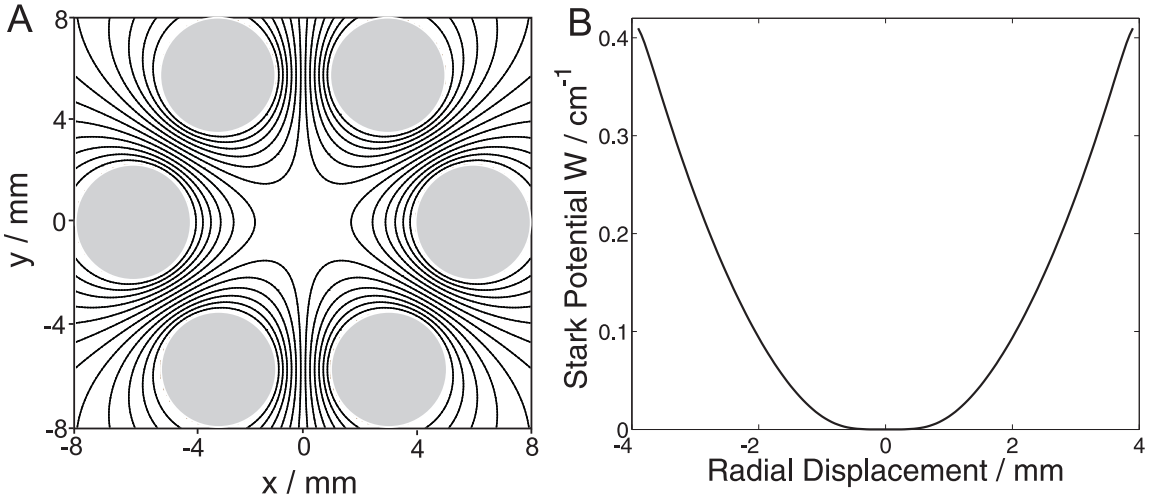


Figure 3.13: A: The potential generated by the hexapole arrangement used in the Stark decelerator beamline. The potential is 3-fold symmetric, and the illustrated equipotentials are at ±(0.8, 2.3, 3.8, 5.4, 6.9, 8.5) kV. The equipotentials increase away from zero field at the centre of the hexapole. B: The variation in the Stark potential energy of ND_3 as a function of radial displacement from the centre of the hexapole. The relationship is near quadratic, corresponding to harmonic focussing.

particles at a distance r from the centre of the trap will experience the same potential.

The potential in the hexapoles used in the Stark decelerator is, however, not ideal, due to the finite size of the electrodes. The SIMION [194] calculated equipotentials are shown in Fig. 3.13A, where the corresponding electric field lines can be inferred to form perturbed circles.

The corresponding variation in Stark potential energy for ND_3 with displacement from the trap centre is shown in Fig. 3.13B. As the Stark effect in ND_3 is linear, the function is nearly quadratic, implying a near-harmonic restoring force applied to molecules away from the trap centre. If this force were quadratic, the hexapole would act as a perfect lens for focussing a molecular beam of ND_3 molecules, with the focal length altered by the time for which the hexapole is pulsed [112]. This allows transfer matrix methods to be used to analyse the phase space behaviour [211]. The deviation from ideality can be interpreted as the introduction of small aberrations into the lens, although this effect is relatively small on the scale of the experiment.

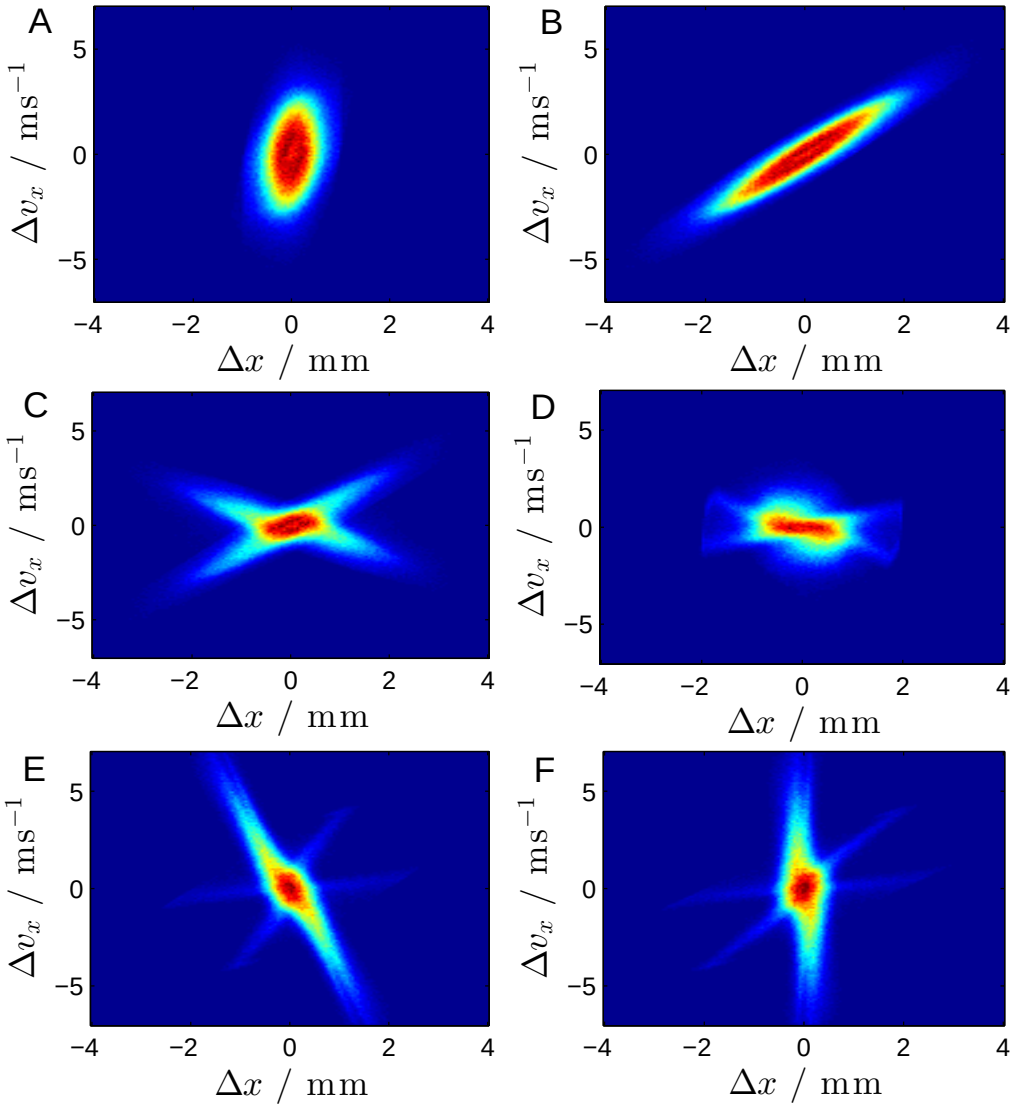


Figure 3.14: Simulated transverse phase for a ϕ_0=60° decelerated ND_3 beam at space at key points along the Stark decelerator beamline: at the end of the Stark decelerator (A), the point at which the second hexapole activates (B), the point at which it deactivates (C), the centre of the buncher (D), the point at which the third hexapole deactivates (E), and the centre of the ion trap (F). The colour map is the same as in Fig. 3.10. All components are operated at 10 kV. The second hexapole pulse time is 35 μs, the third hexapole pulse time is 65 μs, and the buncher operated for 240 μs over four stages of bunching.

The effect of the hexapole focussing on the transverse phase space is simulated in Fig. 3.14. Panel (A) shows the decelerated beam at the end of the Stark decelerator, with a final synchronous velocity of 130 ms^{-1}. This undergoes a free flight of 75 mm to panel (B). The second hexapole pulses for 32 μs at 10 kV to give the phase space distribution in panel (C). This can be seen to correspond to a rotation of the phase space for the molecules that are within the hexapole volume. A portion of the transverse phase space is outside of the hexapole, and is therefore unaffected. Panel (D) occurs after a further 114 mm of free flight and 2 stages of longitudinal bunching. Although the phase space spreads out, the physical dimensions of the buncher (see section 3.4.2) remove the most spatially peripheral molecules and it also provides some transverse focussing, in the same manner as the Stark decelerator. The third hexapole activates 67 mm after the final two bunching stages. Panel (E) shows the rotated phase space after 75 μs of focussing. The distribution at this point is such that the minimum transverse spatial width is obtained after the final free flight of 29 mm, shown in panel (F). As the hexapoles cannot change the phase space density, the reduced spatial extent of the decelerated beam corresponds to a larger velocity spread than in the original beam. If the hexapoles are pulsed for too long or too short a time, then the decelerated beam will be underfocussed or overfocussed, resulting in reduced density of molecules. It should be noted that the behaviour of the decelerated beam under the influence of the hexapoles is critically dependent on the exiting velocity from the decelerator.

3.4.2 Longitudinal Bunching

The buncher is used to focus the longitudinal phase space into the ion trap. The design of the buncher is based upon that of the Stark decelerator: it consists of pairs of parallel electrodes, with adjacent pairs perpendicular to each other (although it is

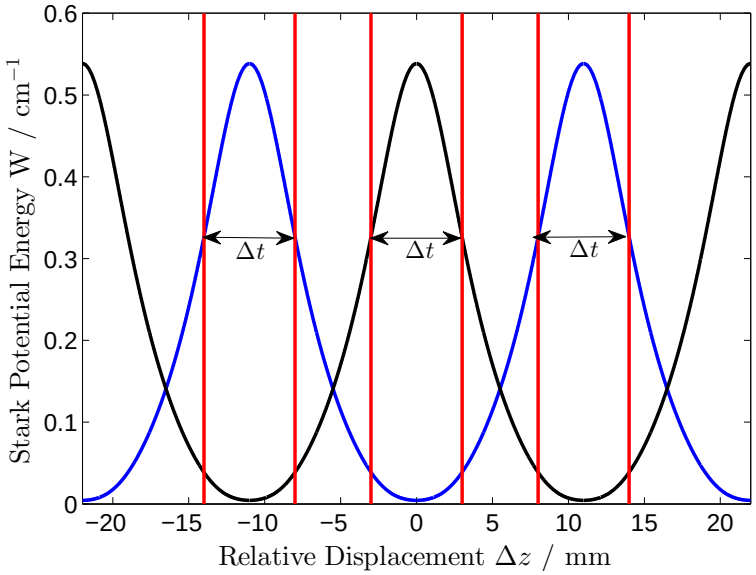


Figure 3.15: The principle of buncher operation. The Stark potentials in the buncher are shown for both switching states in blue and black, relative to the synchronous particle. The buncher electrodes are switched on symmetrically about the time that the synchronous particle reaches the potential minima, shown by the red vertical lines, where $\Delta t = \Delta t_b/n$.

twice as large in all dimensions, see Fig. 3.9). The operational principle of the buncher is illustrated in figure 3.15. The Oxford instrument has six pairs of electrodes, and hence a maximum of 5 stages of bunching are available.

The buncher acts much like a Stark decelerator operating at ϕ_0=0. Adjacent pairs of electrodes are at ±10 kV and ground, creating a periodic Stark potential, and the voltage is applied to the electrodes symmetrically in time about the potential minima. In this way, the synchronous molecule is equally accelerated and decelerated, with no overall change in velocity. Molecules leading the synchronous particle are therefore relatively decelerated, and those behind relatively accelerated. This corresponds to a rigid rotation of the longitudinal phase space distribution [207], although unlike the Stark decelerator the buncher is not continually at high voltage. There exist periods of time when it is completely grounded. This allows for careful control of the total time for which the buncher is at high voltage Δt_b for any given synchronous velocity

v_s, over n bunching stages. The larger dimensions compared to the Stark decelerator also enable multiple buckets to be combined and bunched together.

The buncher can be used to create a spatial focus (SF) for molecules at the location of the ion trap. This is used as a diagnostic tool for the buncher, as sharpened peaks become visible in REMPI time-of-flight spectra. If the distance from decelerator to the start of the buncher is L_1, the distance from the end of the buncher to the ion trap is L_2 and the phase space angular velocity during the bunching process is ω, then [207]:

$$\Delta t_{b,SF} = \frac{v_s(L_1 + L_2)}{\omega^2 L_1 L_2 - v_s^2} \tag{3.23}$$

is the total bunching time required to achieve this. The buncher can also be used to focus the molecules so that they have a narrow velocity distribution (VF), although at the cost of a high longitudinal spread. This would be particularly useful for the investigation of chemical reactions where fine control over the collision energy is required. The total bunching time required for this is:

$$\Delta t_{b,VF} = \frac{v_s}{\omega^2 L_1} \tag{3.24}$$

The simulated effect of the buncher on the longitudinal phase space distribution of the decelerated beam is shown in Fig. 3.16 for both spatial and velocity focussing modes of operation. The last four stages of the buncher are used, and the bunching times are 290 μs for spatial focussing and 100 μs for velocity focussing. The rotation of the phase space distribution is clear in both cases, as is the narrow spatial or velocity distribution achieved at the centre of the ion trap. Molecules from buckets that were behind the synchronous molecule in the decelerator are also visible. The results of these simulations show that, for the Oxford instrument, the angular velocity of the phase space distribution in the buncher is $\omega \approx 2.7 \times 10^3$ rad s^{-1}.

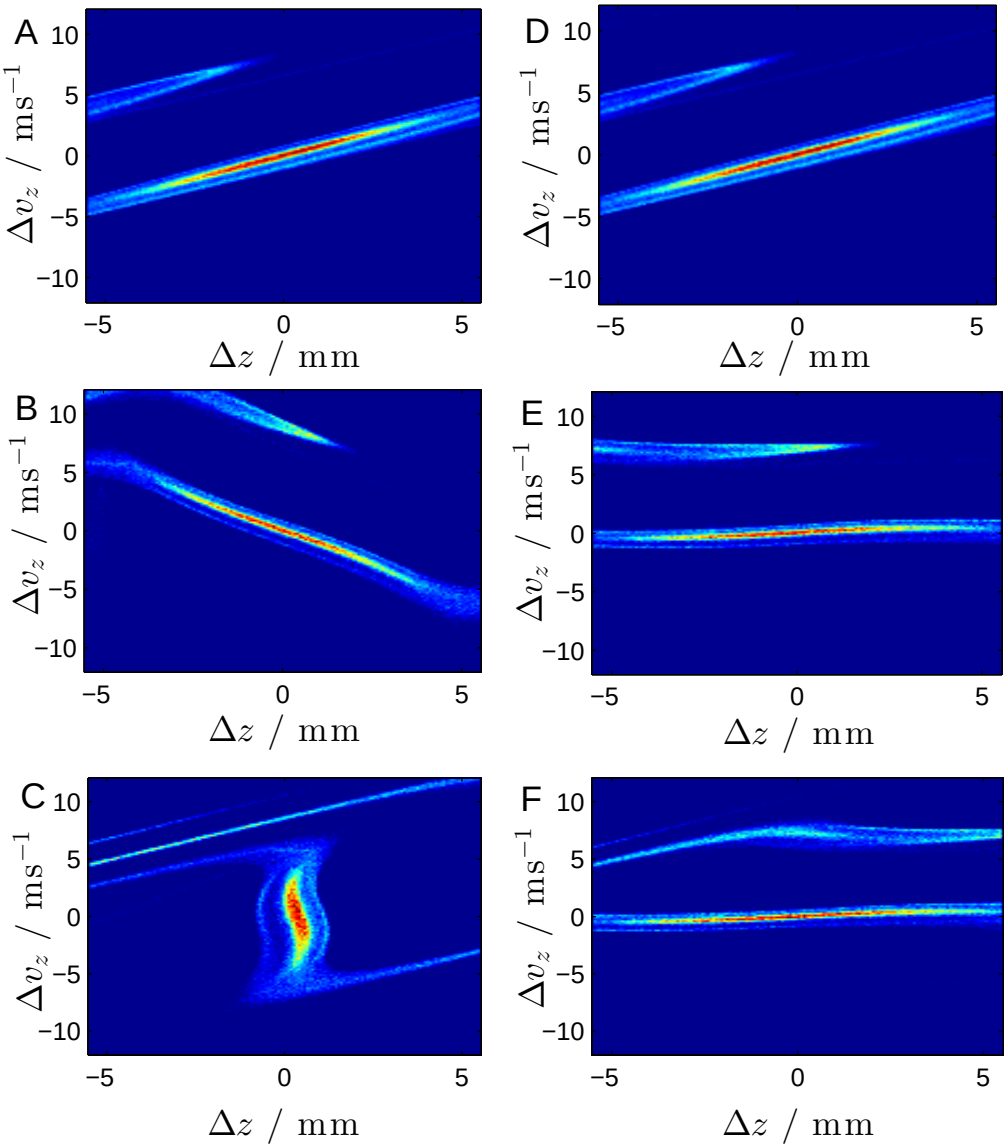


Figure 3.16: Simulated longitudinal phase for a ϕ_0=60° decelerated ND_3 beam before the buncher (A,D), after 4 stages of bunching (B,E) and at the center of the ion trap (C,F), for spatial focussing (A,B,C) and velocity focussing (D,E,F). The colourmap is the same as in Fig. 3.10, and the operational parameters as in Fig. 3.14.

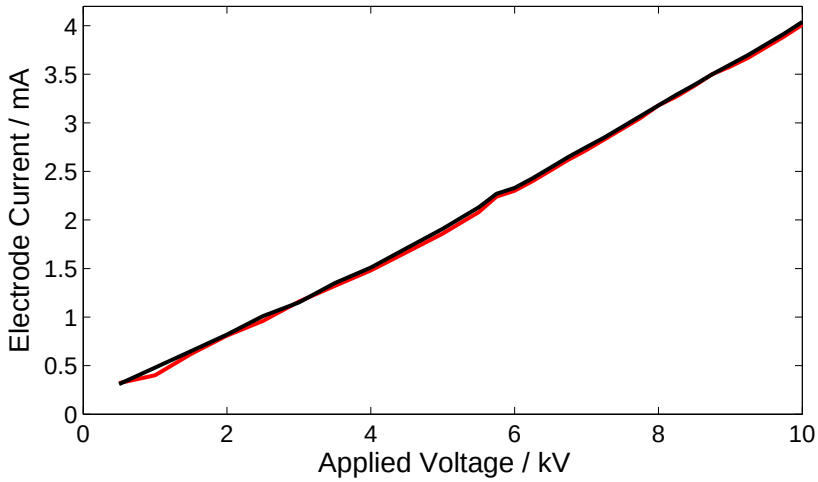


Figure 3.17: Typical conditioning of the Stark decelerator beamline switching in ϕ_0=0 mode, showing the current response to the applied voltage of the positive (red line) and negative (black line) electrodes.

3.5 Experimental Characterisation

3.5.1 High Voltage Conditioning

Due to the high voltages used in this experiment, great care must be taken to ensure that none of the electrodes are grounded, incorrectly connected, or otherwise transmitting current to other electrodes.

One approach to conditioning involves applying a constant DC voltage to the odd or even pairs of electrodes, while grounding the others. The capacitors and switches are disconnected, and the voltage slowly turned up to $\pm$ 12.5 kV, at an average rate of around 2.5 kV hour^{-1}. The current in the positive and negative electrodes is monitored, and if it rises above 0.1 μA, the process is halted until the current dissipates. If this succeeds, or the current builds to around 100 μA, the process is stopped, and the other set of electrodes undergoes the same process. If this fails, then the turbomolecular pumps are stopped, and the chamber vented with argon, to a rotary pump pressure of around 10^{-3} mbar, and the process repeated.

Another, more time-efficient, technique is to condition the experiment in the mode

in which it will operate [212]. This means loading a ϕ_0=0° pulse sequence, and slowly turning up the voltage to ±10 kV, whilst the current is continuously monitored. The rate of voltage increase is 500 V every 10 minutes up to 5 kV, and then 250 V every 10 minutes from 5 kV to 10 kV. The results of such an operation are presented in Fig. 3.17. A conditioning run is assumed to have been successful if a graph resembling this is obtained, even with small deviations from ideality. As of yet, this method has not failed in conditioning the experiment. The gradient of the lines in Fig. 3.17 is slightly different below and above 5 kV. This is reproducible, and indicates that there are two regimes of electrical behaviour at low and high voltage. This behaviour is observed in other Stark decelerators based on the same design [213].

Experience indicates that successful conditioning can be achieved by beginning with the first method, and applying it until the apparatus is conditioned to over 8 kV. If this method then does not succeed after a few more complete cycles, the second method is typically attempted.

3.5.2 Phase Space Matching

Experimentally, there is no direct way to measure the exact initial molecular beam velocity after the supersonic expansion, as there are uncertainties in both the composition of the molecular beam and the opening characteristics of the pulsed valve. However, it is possible to use the ϕ_0=0° mode of the decelerator to estimate this. The process of optimising this parameter is known as phase space matching: the centre of the molecular beam pulse should be at the synchronous point when the pulse sequence begins.

The expected time-of-flight spectrum for a correctly matched molecular beam is shown in Fig. 3.18. An intense central peak is observed at the expected arrival time of the synchronous molecule. There are also two broader, lower intensity side peaks

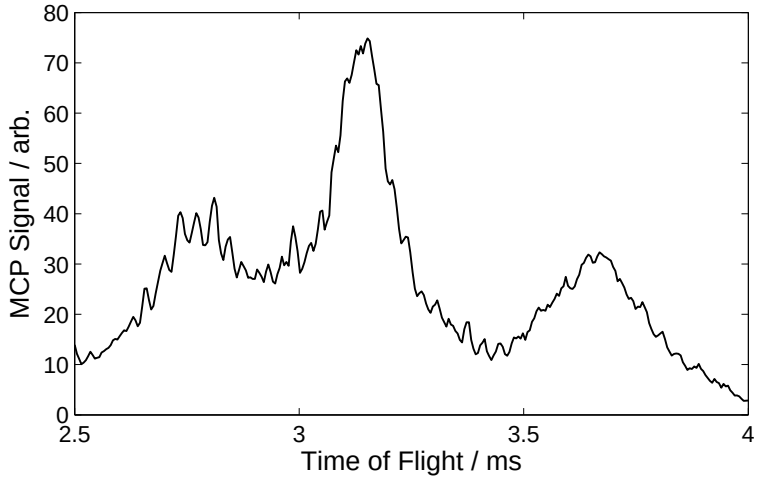


Figure 3.18: Experimental time-of-flight spectrum for a phase space matched molecular beam of 5% ND_3 seeded in xenon. The spectrum is taken with ϕ_0=0° and v_0 = 380 ms^{-1}. Note the presence of an intense central peak, and two approximately equal intensity side peaks.

corresponding to molecules that are not truly phase-stable in the Stark decelerator, but are still perturbed by the electric fields [214]. Phase space matching occurs when these peaks are distinct from the intense central peak, and of approximately equal intensity. This should be checked every time a new gas mix is made. For the particular gas mix used to produce Fig. 3.18, an initial beam speed of 380 ms^{-1} is found to be optimal. It should be noted that the results presented in the following sections were recorded with a range of ND_3/Xe gas mixtures.

3.5.3 Performance of the Stark Decelerator Beamline

After construction and installation, the performance of the buncher, hexapoles and shutter were assessed for a ϕ_0=60° decelerated molecular beam with initial velocity of 385 ms^{-1}, to a final synchronous velocity of 130 ms^{-1}. The results are presented in Fig. 3.19 and were produced in collaboration with James Oldham [215].

To evaluate the performance of the each hexapole, the REMPI detection laser delay time is set to a constant value, corresponding to the maximum value of the

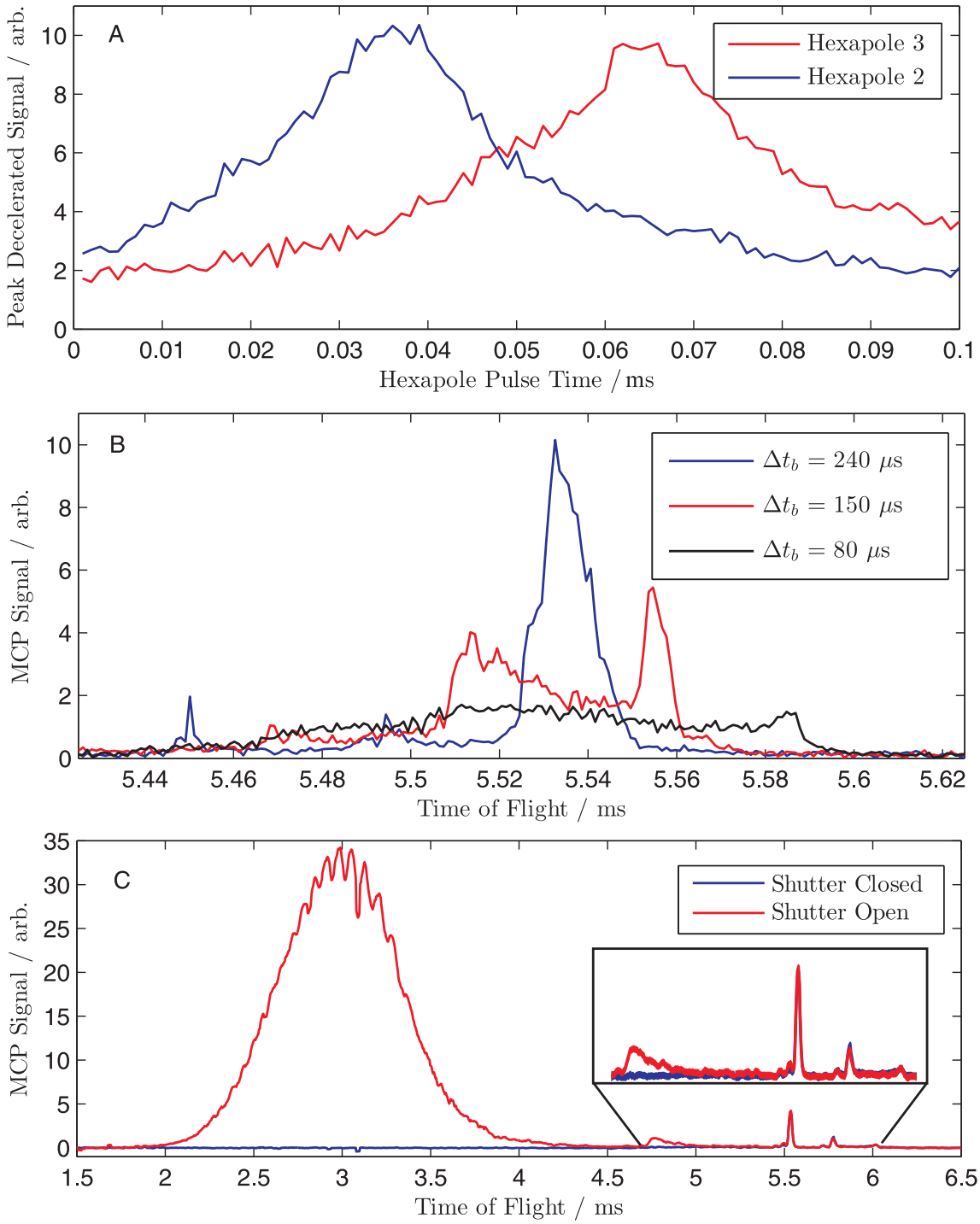


Figure 3.19: Scans illustrating the performance of the hexapoles (A), buncher (B) and shutter (C). The hexapole pulse time refers to the length of time for which the corresponding hexapole is at high voltage, and Δt_b is the total bunching time. Data was recorded for decelerated ND_3 ($\phi_0 = 60°$), and was taken in collaboration with James Oldham.

decelerated peak. The performance of the second hexapole is first established by setting the other beamline components to constant pulse times; the third hexapole is pulsed for $\Delta t_{h3} = 65$ μs, with the total bunching time set to $\Delta t_b = 240$ μs. A scan is performed whereby the amount of time for which the second hexapole is pulsed, Δt_{h2}, is varied. When this optimisation process is repeated for the third hexapole a value $\Delta t_{h2} = 35$ μs is used. The results of this experiment are shown in Fig. 3.19A. The two hexapole scans show the expected features. At low or high hexapole pulse times, underfocussing or overfocussing of the molecular packet into the laser ionisation volume is manifested in reduced signal. The optimised hexapole gives an enhancement factor of six or seven relative to a pulse time of zero. As the final synchronous velocity decreases, this enhancement factor would be expected to increase.

The ability of the buncher to spatially focus molecules is demonstrated in time-of-flight spectra showing the most intense bunched peak in Fig. 3.19B for three different bunching times. The hexapole pulse times were held at Δt_{h2}=35 μs and Δt_{h3}=65 μs. The emergence of a single longitudinally focussed peak as the bunching time increases to its experimentally optimal value of 240 μs is clear. At a low bunching time, a weak, broad peak is obtained, although this is likely to have a low velocity spread. An interestingly shaped peak occurs for intermediate bunching times, consisting of two distinct maxima. This is due to asymmetric distortions introduced into the longitudinal phase space by incomplete bunching followed by free flight. Optimal bunching clearly enhances the decelerated signal, whilst significantly reducing the spatial extent of the decelerated packet.

The effectiveness of the shutter is shown in Fig. 3.19C. Full time-of-flight spectra are presented, with both the buncher and hexapoles optimised. In the "shutter open" scan the shutter begins to open 0.5 ms before the pulsed valve fires. This allows both the decelerated beam and main beam into the detection region. In the "shutter closed" scan, the shutter opens 2.5 ms after the pulsed valve. This completely blocks the main

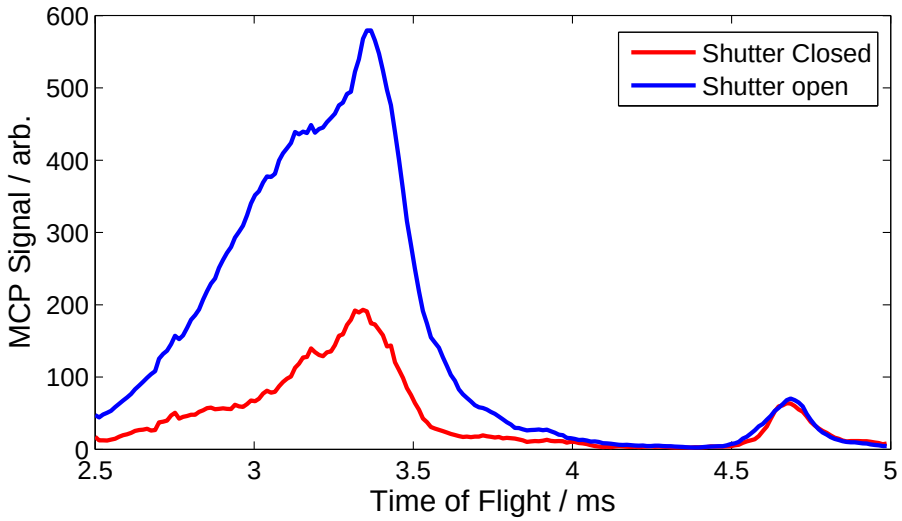


Figure 3.20: Time-of-flight spectra for the shutter in a broken state where only one of its springs is opening, and the other is forced open. Both shutter open and shutter closed states are shown for comparison. The intensity has been scaled such that both decelerated peaks have the same peak intensity. This dataset was taken for an initial speed of 375 ms^{-1} and ϕ_0=46.5°.

beam, ensuring that only the decelerated beam is admitted, as is clearly demonstrated in Fig. 3.19C.

By default, the shutter is closed. It opens through the application of a small voltage, whereby two mechanical springs simultaneously open the two leaves forming the shutter plate, with an opening time of 800 μs. A sudden loss of REMPI signal can result if one or both springs break such that the shutter becomes permanently half or fully closed. Alternatively, as shown in Fig. 3.20, one leaf may be opening and closing, and the other is forced into a permanently open position . In such a case, even though a large portion of the main beam is removed from the beamline, there are still many more undecelerated molecules than decelerated ones, and these would dominate any reactive processes.

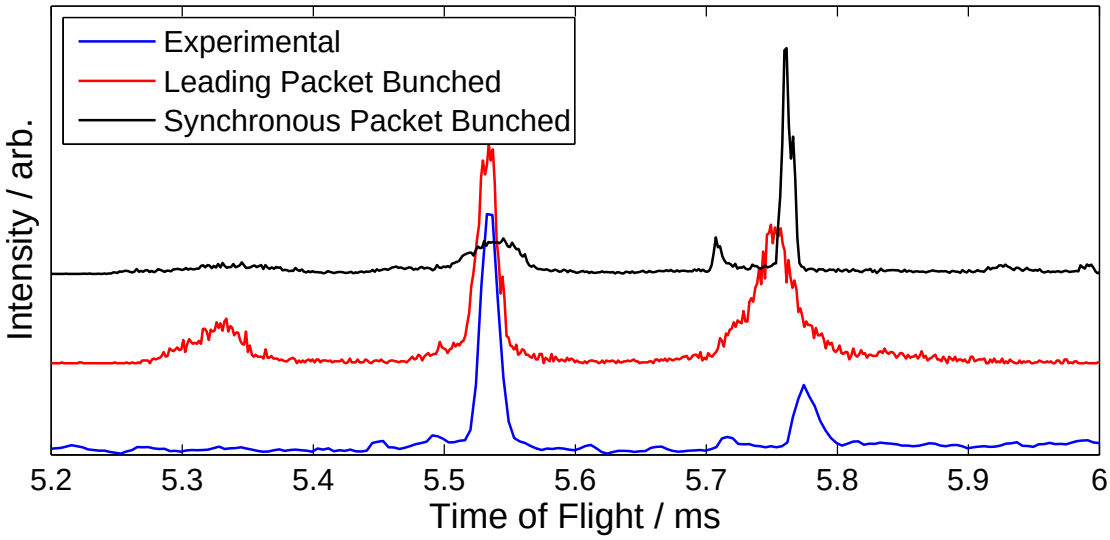


Figure 3.21: Simulation of time of experimental time-of-flight spectrum of Fig. 3.19C. The black curve is the simulated time-of-flight spectrum for optimised bunching of the synchronous packet at 380 ms^{-1}. The red curve is the simulated optimised bunching of the packet that leads the synchronous packet by one stage of bunching. The curves are offset for clarity.

Comparison With Beamline Simulations

The simulation programmes that have been developed in this thesis can be used to gain a deeper understanding of the experimental time-of-flight spectra, particularly with regard to the buncher.

Consider the full time-of-flight spectrum, with the shutter blocking the main beam, shown in the inset of Fig. 3.19C. The portion of this spectrum that shows the decelerated molecules is shown again in Fig. 3.21, alongside the results of two separate simulations. The simulation for the theoretically "optimised" bunching time of 290 μs (top trace in Fig. 3.21) yields two peaks with approximately correct arrival times. However, the peak intensities are reversed, and this "optimal" bunching time disagrees with the experimental value by 50 μs.

If one makes the assumption that, in this instance, the buncher is being switched on prematurely, so that the bucket that leads the synchronous molecule by a single

unit cell is being bunched instead, a "corrected" simulated time-of-flight spectrum (middle trace in Fig. 3.21) shows two peaks that compare more favourably with the experimental spectrum. The newly optimised bunching time of 250 μs is also much closer to the experimental bunching time. It is likely then that the buncher was not being operated for the synchronous trajectory: it was erroneously optimised based upon the wrong time-of-flight peak. This understanding will help to guide experimental conditions for future experiments.

Generally speaking, the disparities between theory and experiment can occur due to uncertainties in the initial molecular beam profile and the laser detection volume, and imperfections in the experiment, such as small misalignments of the beamline components.

3.6 Conclusions and Outlook

In this chapter, a new Stark decelerator beamline, and the accompanying simulation programmes, have been described. The experimental beamline components have been shown to perform within expectation. Agreement has been demonstrated between the experiment, and the simulations developed to describe it. With the current understanding of the apparatus now further developed through the comparison of simulations and experiments, future deceleration experiments will be able to fully utilise both the buncher and the hexapoles down to the lowest velocities.

As noted in section 3.5.3, the shutter is quite delicate and can require fairly regular replacement. The experiment could be used more efficiently if an alternative system were used to separate the main beam from the decelerated beam. For instance, the Stark decelerator could be offset at a slight angle to the ion trap. An electrostatic deflector could be used that was switched off as the main beam passed through it, but switched on to allow the decelerated beam access to the ion trap chamber. This would

require a redesign of the Stark decelerator beamline, but might pay dividends in the long term.

This apparatus produces a highly dense sample of neutral molecules at a set of well-defined velocities at the site of an ion trap, enabling ion-molecule reactions to be conducted where the collision energy of the neutral reactant can be finely controlled. The possibilities offered by this high degree of control are discussed in Chapter 5.

Chapter 4

Ion Trapping of Xenon Ions with Laser-Cooled Calcium Ions

This chapter describes the second component of the apparatus that is used to study the reaction between Stark decelerated ND_3 molecules and singly charged xenon cations. Laser-cooled, singly charged calcium cations are used to sympathetically-cool trapped, singly charged xenon cations. This bicomponent Coulomb crystal acts as a stationary ion target for the molecular beam of ammonia described in the previous chapter.

The ion trapping apparatus, and the theory behind it, are presented, as are the theoretical methods used to analyse and interpret the experimental results. The effect of background reactions and background loss from the ion trap are considered experimentally.

4.1 Spatial Confinement of Ions

4.1.1 The Principles of Ion Trapping

As ions have an electric charge, they can be easily manipulated using electromagnetic fields. Whilst one might think that an electromagnetic potential containing a deep

well would provide a region of space in which a set of ions might be stably confined, unfortunately, this is not possible. In free space, any static electromagnetic potential ϕ is described by Maxwell's equations, hence must obey Laplace's equation, a partial differential equation that can be expressed in Cartesian coordinates as:

$$\frac{\partial^2\phi}{\partial x^2} + \frac{\partial^2\phi}{\partial y^2} + \frac{\partial^2\phi}{\partial z^2} = 0 \tag{4.1}$$

Given a stationary point of a function, the criterion for this stationary point to be a potential minimum (along a given coordinate x_i) is that:

$$\frac{\partial^2\phi}{\partial x_i^2} > 0 \tag{4.2}$$

From equation 4.1, it is clear that one of the second differentials must have the opposite sign to the other two, hence it is impossible to have a true potential minimum that can trap ions with only static fields. This is the basis of Earnshaw's theorem [216]. The electric potential can at best form a saddle point with a maximum in a single direction, along which ions can escape along the corresponding path of steepest descent.

The simple solution to this is to apply an additional electric field that can be used to flip the saddle point between two orthogonal directions. This is achieved by switching the field between two orthogonal orientations. If this rotation occurs quickly enough relative to the translational motion of the ions, it is possible to dynamically confine the ions in three dimensions. Practically, radio frequency (RF) fields are sufficient to achieve stable ion trapping for prolonged periods of time: ions can be trapped for several days in some cases [217].

There exists a variety of different electrode geometries and electromagnetic field combinations with which it is possible to construct an ion trap. The linear Paul trap

design is used in this thesis, and will be described in some detail below. All Paul trap designs use quadrupolar electrostatic fields and time-varying RF electric fields to trap ions [136], and can also be used in conjunction with magneto-optical traps to study ion-atom reactions [99]. The trap described in this thesis generates the required quadrupolar electric fields using a cylindrical electrode geometry, but Paul traps have also been designed using bladed [218] and hyperbolic [219] electrode geometries.

Not all traps make use of time-varying electric fields. Penning traps are frequently employed by the fundamental physics community, and have been used to trap and weigh antiprotons at CERN [220]. The Penning trap uses spatially homogeneous magnetostatic fields and spatially inhomogeneous electrostatic fields to acheive confinement [221]. Another ion trap is termed the Orbitrap. A modern ion trap, the Orbitrap is based on the older Kingdon trap [222], and is now regularly used in protein mass analysers. It traps ions between two cylindrical electrodes with a finite angular momentum, with an additional axially confining electrostatic field [223].

Although the Penning trap and Orbitrap avoid time-varying fields, and the associated micromotion (described in section 4.3.1) heating, in both designs the trapped ions undergo orbital motion about the trap axis. This means that near-stationary confinement in a small volume is not possible, making them unsuitable for the applications discussed in this thesis.

4.1.2 The Linear Paul Ion Trap

The design of the ion trap used for the experiments in this thesis is shown in Fig. 4.1. The trap is based on a quadrupole design: it consists of four segmented cylindrical electrodes, each divided into three sections, and insulated from each other to allow each of the twelve electrodes to be, in principle, independently varied. Voltages are typically applied to the electrodes as shown in table 4.1.

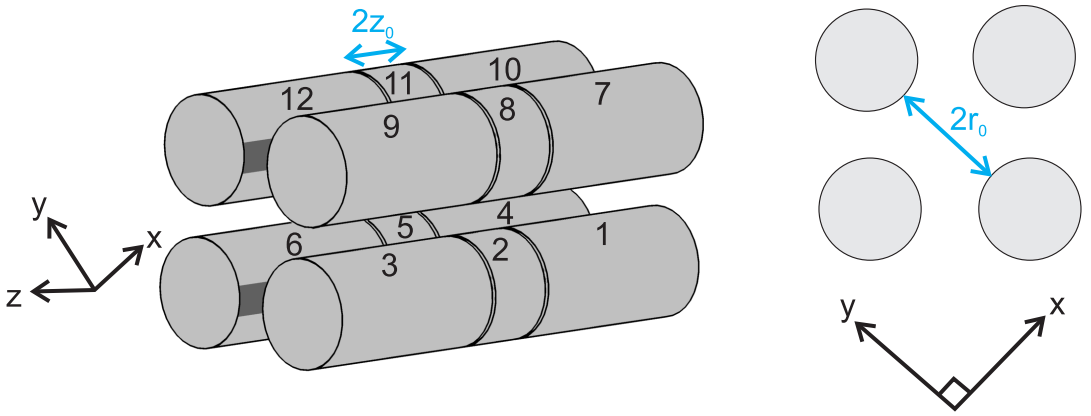


Figure 4.1: Illustration of the design of the linear Paul trap utilised in this thesis, with the twelve electrodes labelled, and the axis convention used within this chapter illustrated. The figure is not drawn to scale.

Axial confinement along the z-axis is achieved with a constant electrostatic voltage, V_{end}, of a few volts applied to the eight "end-cap" electrodes (1,3,4,6,7,9,10 and 12, see Fig. 4.1). A RF voltage, V_{RF}, is applied to all of the electrodes such that they form a quadrupolar configuration. This creates a saddle point potential in the $x-y$ (radial) plane. Dynamical trapping in these dimensions is achieved by varying V_{RF}. If the peak RF voltage is $V_{RF,0}$ and the angular radiofrequency is Ω_{RF}, then:

$$V_{RF} = V_{RF,0}\cos(\Omega_{RF}t) \tag{4.3}$$

and so the saddle point flips back and forth precisely once per complete RF cycle. Although cold ions ideally are located in the centre of the trap, imperfections in the trap may lead to small displacements from the trap centre. To compensate for this, static offset voltages of V_x and V_y can be applied to the electrode sets (4,5,6) and (1,2,3) respectively. Trapped ions are at the location of the physical trap centre when the static offset voltages are $(V_x,V_y) = (0,0)$.

The trap has been designed such that there is also the ability to apply static voltages to the electrode configurations (4,5,6,7,8,9), (1,4,7,10) and (3,6,9,12). Altering

the voltage on electrodes (4,5,6,7,8,9) results in a diagonal "squashing" of the ions in the trap. Changing the voltage on (1,4,7,10) and (3,6,9,12) translates trapped ions along the z-axis. Under typical operating conditions, the offset voltages required to perform these operations are set to zero.

For simplicity of analysis, a harmonic trapping potential is desirable [136]. A true harmonic potential can only be created using hyperbolic electrodes, but these are difficult to manufacture. However, it is possible to get a near-harmonic potential using a certain cylindrical electrode geometry [224]. This gives a harmonic potential scaled by a geometric factor κ. The analytical form of such a harmonic potential is:

$$\phi_{RF}(x, y, t) = V_0 \left(\frac{x^2 - y^2}{r_0^2} \right) \cos(\Omega_{RF} t) \tag{4.4}$$

$$\phi_{end}(r, z) = \frac{\kappa V_{end}}{z_0^2} \left(z^2 - \frac{r^2}{2} \right) \tag{4.5}$$

$$\phi = \phi_{RF} + \phi_{end} \tag{4.6}$$

The dynamical behaviour of the saddle point of the harmonic potential in the x-y plane is illustrated in Fig. 4.2 over half an RF cycle for operational values of the trap parameters. The saddle point can be seen to progressively transform into an almost flat maximum over a quarter of a cycle, corresponding to a pure endcap voltage. Over the next quarter cycle, the saddle point re-emerges, but in the perpendicular direction to before. What was previously the path of steepest descent is now the path of steepest ascent, and the ions are directed back towards the trap centre.

The equations of motion [225] for a single trapped ion in the x-y plane can be modelled by the Mathieu equations:

$$\frac{d^2 x}{dt^2} + [a_m + 2q_m \cos(\Omega_{RF} t)] x = 0 \tag{4.7}$$

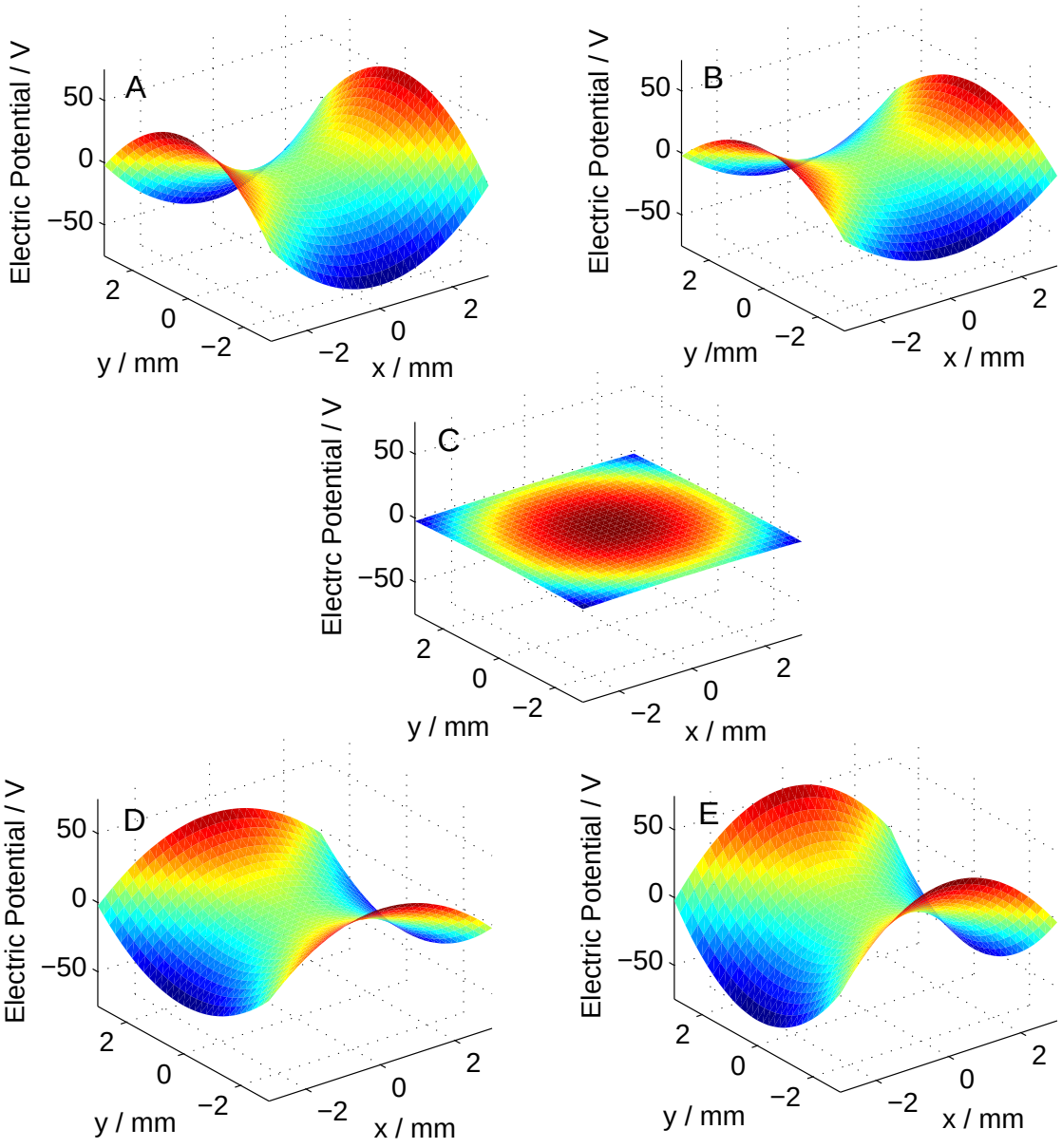


Figure 4.2: The dynamical flipping of the RF electrical potential in the radial x-y plane over half an RF cycle. The plots show $\Omega_{RF}t$ = (A) 0, (B) $\pi/4$, (C) $\pi/2$, (D) $3\pi/4$ and (E) π. The cut is through the trap centre, $z = 0$. The trap parameters are as set out in table 4.1, with $V_{end} = 4$ V and $V_{RF,0} = 150$ V.

Table 4.1: Voltages applied to each electrode in the linear Paul trap.

Electrodes	Applied Voltage
1 and 3	$V_{end} + V_y + V_{RF}$
2	$V_y + V_{RF}$
4 and 6	$V_{end} + V_x - V_{RF}$
5	$V_x - V_{RF}$
7 and 9	$V_{end} - V_{RF}$
8	$-V_{RF}$
10 and 12	$V_{end} + V_{RF}$
11	V_{RF}

$$\frac{d^2y}{dt^2} + [a_m - 2q_m \cos(\Omega_{RF}t)]y = 0 \tag{4.8}$$

$$\frac{d^2z}{dt^2} - 2a_m z = 0 \tag{4.9}$$

where a_m and q_m are the Mathieu parameters:

$$a_m = -\kappa\frac{4qV_{end}}{m\Omega_{RF}^2 z_0^2} \tag{4.10}$$

$$q_m = \frac{2qV_{RF}}{m\Omega_{RF}^2 r_0^2} \tag{4.11}$$

q/m being the charge-to-mass ratio of the ions.

These equations have been studied in detail [225, 226], including for the ion trap used in these experiments [136]. Along the z-coordinate, the particle undergoes simple harmonic motion, but the behaviour is more complex along along the x- and y-coordinates. The dynamic switching of the RF potential causes ions moving away from the trap axis to undergo rapid oscillations, known as micromotion (this is adiabatically separate from the slower radial secular motion of ions in the trap; see section 4.3.1). For poorly chosen values of a_m and q_m, the micromotion is unstable and increases exponentially until ions are lost from the trap. The experimental trap parameters used in the Oxford ion trap are given in table 4.2. For typical experimental parameters of $V_{RF,0} = 150$ V and $V_{end} = 4$ V, the characteristic frequencies of the secular harmonic

Table 4.2: Typical experimental parameters used for the trapping experiments described in this thesis.

Trap Parameter	Symbol	Value
RF frequency	Ω_{RF}	$2\pi \times 3.850$ MHz
RF voltage amplitude	$V_{RF,0}$	100-150 V
Endcap voltage	V_{end}	1-4 V
Endcap electrode separation	$2z_0$	5.5 mm
Diagonal electrode separation	$2r_0$	7 mm
Geometric factor	κ	0.244
Electrode radius	R	4 mm

motion of an ion on the trap are $2\pi \times 121$ kHz in the longitudinal direction and $2\pi \times 258$ kHz in the radial direction.

If there are ions of different mass (and/or charge) in a linear Paul trap, mass filtering occurs. Ions with a large charge-to-mass ratio experience a larger radial trapping potential than ions with a smaller charge-to-mass ratio. Therefore, the lighter the ion, the nearer to the trap axis it resides.

4.2 Production of Translationally Cold $^{40}Ca^{+}$ Ions

4.2.1 The Principle of Doppler Cooling

An ion trap will generate a spatially confined ensemble of translationally hot ions. This manifests itself as significant ion kinetic energy, present as both secular motion and micromotion. In order to remove this energy (particularly the large amplitude secular motion), a laser-cooling scheme using continuous wave (CW) diode lasers is implemented.

Laser cooling can be applied to a small range of neutral and ionic atomic species, enabling them to reach a range of different temperature regimes. For example, the use of three pairs of counter-propagating laser beams (a so-called "optical molasses") can cool selected atoms and atomic ions into the μK temperature regime [227]. Raman

transitions between hyperfine states, in conjunction with optical laser cooling, can cool species to below the photon recoil limit, into the nK regime [228]. The work described in this thesis employs the method of Doppler cooling, detailed below. For $^{40}Ca^{+}$ ions, the ideal Doppler limit has been computed to be approximately 500 μK, although for the experimental setup described in this chapter, temperatures an order of magnitude higher than that are expected [136].

A photon has a momentum given by the ratio of Planck's constant to the radiation wavelength h/λ. The cooling laser is aligned into the ion trap; if the photon is resonant with an electronic transition, it might be absorbed to give an electronically excited ion. Conservation of momentum implies a change in momentum of the ion will occur on photon absorption or emission. Using photons of a perfectly resonant wavelength, an equal number of ions will be accelerated or decelerated, depending on whether their z velocity component is aligned with or opposing the direction of laser propagation. In order to achieve overall cooling in the sample, the laser is detuned to a wavelength longer than the resonant wavelength, termed red-shifting. This takes advantage of the Doppler effect: in the frame of reference of a molecule travelling counter to the direction of laser propagation, the photon will have a shorter wavelength, bringing it into resonance. This guarantees that only photons propagating in the opposite direction to the ions are absorbed, always leading to a reduction of ion momentum on absorption.

Once in the excited state, the ion spontaneously relaxes back into the ground state. The accompanying photon emission is an isotropic process, and so in a given cycle of cooling, the momentum is reduced by sh/λ, where $s \sim U(0,2)\cos\theta$, with $U(0,2)$ being the uniform distribution on the interval [0,2] and θ being the angle of emission. Conservation of momentum consequently ensures that the mean momentum loss per cooling cycle is h/λ. Given a sufficiently large number of laser cooling cycles, mK temperatures are readily achieved. The Doppler cooling efficiency, hence the

theoretically achievable final temperature, is thus determined by the linewidth of the cooling transition. The ions can be detected by imaging the fluorescence resulting from the photon emission using a microscope objective lens and a charge couple device (CCD) camera.

4.2.2 Laser Cooling Scheme for $^{40}Ca^{+}$

In practise, laser cooling can be difficult to implement; very few species behave as an ideal two-level system. There do exist examples that are near-ideal though, almost exclusively alkali metal atoms and alkaline earth metal atoms and ions. These behave approximately like three-level systems, and can be manipulated to behave like effective two-level systems.

Laser cooling schemes exist for most of the alkaline earth metal ions, including Be^{+} [229], Mg^{+} and Ba^{+} [10], as well as the various isotopes of Ca^{+} [230]. The choice of ion depends upon the context of the experiment, with considerations including the charge-to-mass ratio of any ions that require sympathetic cooling (as sympathetic cooling is most efficient for species with charge-to-mass ratios similar to that of the directly cooled ion). Since Xe^{+} and ND_3^{+} are the species to be sympathetically cooled, the experiments described here are performed exclusively with laser cooled $^{40}Ca^{+}$ ions.

The laser cooling scheme utilised in this thesis for $^{40}Ca^{+}$ was first described by Ritter *et al.* [231], and is illustrated in Fig. 4.3. A near-UV diode laser drives the $^2S_{1/2} \longrightarrow {}^2P_{1/2}$ primary cooling transition at 397 nm. The $^2P_{1/2}$ state has a lifetime of around 7 ns [232], with rapid spontaneous emission to the $^2S_{1/2}$ state. However, the $^2P_{1/2}$ state can also spontaneously decay to the $^2D_{3/2}$ metastable state, with a branching ratio of around 1:12 favouring the ground $^2S_{1/2}$ state [136]. The $^2D_{3/2}$ state only decays to the ground state slowly, as the transition is electric-dipole forbidden (since $\Delta L = 2$ [233]), with a lifetime of just over a second [234]. Unaddressed, the

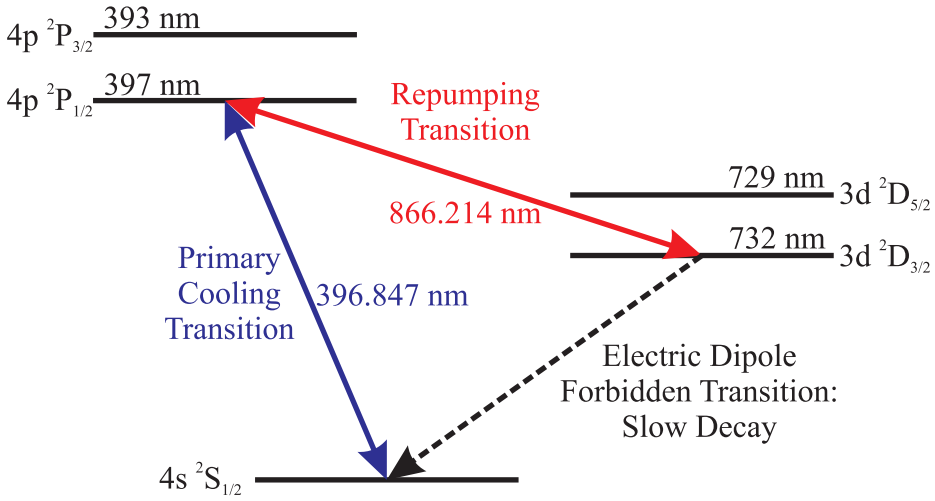


Figure 4.3: The relevant low-lying electronic states of the $^{40}Ca^+$ ion, neglecting spin-orbit coupling. The laser induced electronic transitions are shown. The wavelengths shown correspond to energies relative to the ground state.

population in the metastable state becomes large over many absorption-decay events, preventing effective laser cooling of the sample. One solution is to introduce a second diode laser in the near IR (at $\approx$ 866 nm) to continuously repump the metastable population back into the $^2P_{1/2}$ state. Other laser cooling schemes for $^{40}Ca^+$ exist, see for example [218], based on the same principle of repumping from the metastable state(s).

The calcium source used in these experiments does contain all of the naturally occurring calcium isotopes, with $^{40}Ca^+$ accounting for 96.94% [235]. The isotopic shifts in the electronic transitions are orders of magnitude larger than the transition linewidths, so it is not possible to laser cool all of these isotopes simultaneously with a single diode laser system. As such, we exclusively cool the $^{40}Ca^+$ ions.

As the calcium ions are non-resonantly ionised, other isotopes may be trapped alongside the $^{40}Ca^+$ ions. As these are not laser cooled, but may be sympathetically cooled (see section 4.3.2), they appear as "dark" ions in experimental fluorescence images. The diode lasers might also emit some light at 393 nm, exciting $^{40}Ca^+$ ions to the $^2P_{3/2}$ state. This state can decay to the $^2D_{5/2}$ metastable state, which is not

repumped. Ions that become trapped in this state may also appear as dark calcium ions in any fluorescence images.

4.3 Behaviour of Cold Trapped Ions

4.3.1 Coulomb Crystals

An ensemble of laser cooled ions can form a strongly interacting cold plasma within the ion trap. The behaviour of this plasma is governed primarily by 3 factors: the trapping potential, the Coulombic repulsion between the positive ions, and the secular kinetic energy available to the ions within the trap. At sufficiently high plasma temperatures (typically a few hundred mK), the secular kinetic energy is high relative to the Coulombic repulsion, and the ions freely undergo secular motion within the trap, but at much lower secular temperatures, the Coulombic repulsion between the ions dominates, and they can cannot freely move past each other. Under such conditions, the ensemble of ions resembles a fluid-like state. As the secular temperature is lowered further, a phase transition occurs, yielding an ordered three-dimensional lattice structure known as a Coulomb crystal.

The thermodynamic state of a one-component plasma can be described using the plasma coupling parameter. This is defined to be the ratio of the potential energy to the secular kinetic energy of the ions:

$$\Gamma = \frac{E_p}{E_k} = \frac{q^2}{4\pi\epsilon_0 a_{WS} k_B T} \tag{4.12}$$

where a_{WS} is the Wigner-Seitz radius, which gives the average inter-ion distance from the density of ions in the plasma, n_0:

$$\frac{1}{n_0} = \frac{4}{3}\pi a_{WS}^3 \tag{4.13}$$

The plasma coupling parameter has been theoretically studied through the use of molecular dynamics simulations [236, 237]. At low values of Γ, where the secular kinetic energy is greater than or similar to the potential energy of the ions, gas phase behaviour is observed. Spatial correlation, corresponding to the onset of liquid phase behaviour, begins to appear at $\Gamma \approx 2$ [238]. The phase transition to the Coulomb crystal state is observed for $\Gamma \geq 150$, as determined theoretically [236, 237, 239] and supported by experimental results [240].

The density of ions in the linear Paul trap is limited by the Coulombic repulsion to be of the order of 10^8 cm^{-3} [135]. Under these conditions, equation 4.12 predicts that the Coulomb crystal phase transition occurs at approximately 100 mK, a secular temperature that is easily attained with Doppler cooling. In addition, equation 4.13 indicates that the average inter-ion distance is on the order of 10 μm, approximately four orders of magnitude larger than the interatomic separation in a typical crystalline solid such as sodium chloride [241] (and, of course, all of the ions are positive in the present case).

The Temperature of a Coulomb Crystal

The motion, and hence the kinetic energy, of laser cooled ions in the ion trap can be adiabatically divided into two contributions: a low frequency ion drift, termed the secular motion, and a driven, higher frequency oscillation, termed the micromotion. The secular motion of the ions can be interpreted as the motion of the ions trapped with a time-averaged pseudopotential in the trap. It is this motion that can be laser-cooled. The micromotion is a driven oscillatory behaviour, induced by the RF switching. As mentioned previously, the degree of micromotion increases with radial distance from the trap centre, as the gradient of the radial potential increases.

The concept of temperature in an ion trap is therefore a complex one, as ions will have independent secular and micromotion kinetic energies. In addition, a laser

cooled Coulomb crystal cannot be considered to be a system at thermal equilibrium. Therefore, throughout this thesis, the concept of temperature is understood to mean the effective average kinetic energy of the crystal, expressed in units of Kelvin:

$$T = \frac{\langle E_K \rangle}{k_B} \tag{4.14}$$

For crystals of a few hundred ions, the average micromotion energy is generally used to define the crystal temperature, as it is typically several orders of magnitude larger than the secular temperature. A crystal of 900 ions in a linear Paul trap has been shown to have a characteristic temperature of 11.9 K, for instance [242]. An example experimental image of a calcium Coulomb crystal, consisting of 590 calcium ions with a temperature (as defined above) of the order of 500 mK, is shown in Fig. 4.4A. The image is effectively a slice through the centre, determined by the depth of focus of the microscope lens, parallel to the plane of the charge coupled device (CCD) detector.

4.3.2 Sympathetic Cooling of Dark Ions

While in principle it is possible to laser cool anything that has a bound state connected to a populated lower state by an optical transition, there are very few systems for which it is both practical (in terms of the number of lasers required to close the cooling cycle) and possible (with available narrow-band laser sources) to employ direct laser cooling. As such, sympathetic cooling has been increasingly employed to cool ions for which no simple direct cooling scheme exists.

In the process of sympathetic cooling, the continuously laser-cooled ions act as a heat sink for (hotter) non-laser-cooled trapped ions through Coulombic transfer of kinetic energy. This briefly increases the kinetic energy of the laser cooled ions, which is subsequently lost during the next laser-cooling cycle. As they cool down, the "dark"

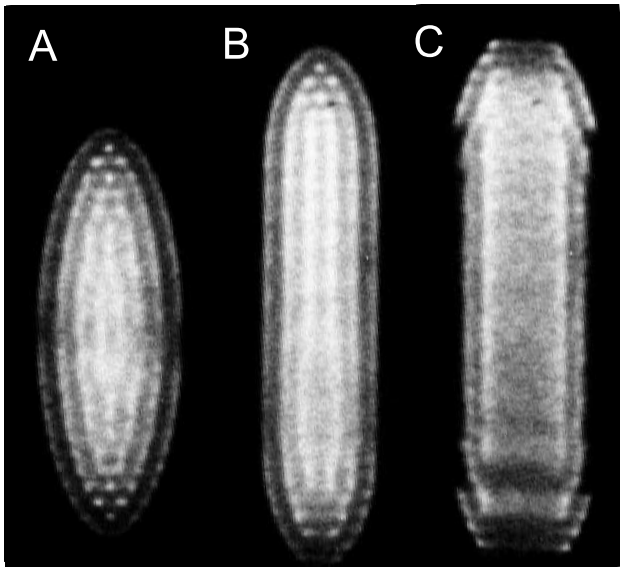


Figure 4.4: Experimental fluorescence images of Coulomb crystals. Image A contains only $^{40}Ca^{+}$, image B shows a two-component crystal containing calcium and "dark" (non-fluorescing) xenon ions, and image C shows a three-component crystal, containing calcium, xenon and ND_3^+ ions. The corresponding trap voltages are $V_{RF,0} = 130$ V and $V_{end} = 4$ V.

(non-fluorescing) ions are incorporated into the Coulomb crystal, leading to a visible change in shape of the laser-cooled ion framework. This process creates a multi-component Coulomb crystal, some examples of which are shown in Fig. 4.4. In image B, an atomic ion, Xe^+, is sympathetically cooled into a Ca^+ Coulomb crystal. In image C, both Xe^+ and a molecular ion, ND_3^+, are sympathetically cooled, illustrating the generality of the technique. Also, a couple of dark calcium ions (discussed in section 4.2.2) are clearly visible at the bottom of the z axis in image (B)

Only continuously fluorescing ions - those that are being laser-cooled - can be directly observed. The presence of dark ions can be inferred from the change in the crystal morphology and confirmed using MD simulations. Due to the mass-filtering properties of the linear Paul trap, ions with a smaller charge-to-mass ratio than the imaged ions experience a weaker trapping potential, and as such form an outer layer around the laser-cooled ions. This results in a compression of the upper and lower sides of the observed crystal image, and an expansion along the z-coordinate. Trapped ions

with a larger charge-to-mass ratio are trapped closer to the trap axis than the laser-cooled ions, forming an axially symmetric "dark core" in the crystal images.

Sympathetically-cooled dark ions can come from two different sources: ions can be generated inside the trap, for example by photoionisation of a neutral species introduced to the trap chamber, and subsequently sympathetically cooled into the crystal. Any ions produced via *in situ* chemical reactions can also be sympathetically cooled, assuming that their kinetic energy is lower than the effective trap depth.

Sympathetic cooling can be performed for an extensive range of molecular ion species. As alluded to earlier, for efficient sympathetic cooling and stable trapping to occur there must be a similar charge-to-mass ratio between the laser-cooled ions and the sympathetically-cooled ions. For instance, sympathetic cooling of hydrogen molecular ions such as H_2^+ and H_3^+ has been demonstrated using laser cooled Be^+ [243], whereas laser cooled Ba^+ has been utilised to cool charged organic dye ions [244] and multiply protonated proteins [245].

Multi-component Coulomb crystals provide a powerful method for following the progress of low temperature ion-molecule reactions. This will be discussed in detail in chapter 5.

4.4 The Ion Trapping Experiment

4.4.1 Experimental Apparatus

The ion-trapping apparatus utilised in this thesis is adapted from a set-up previously described by Alex Gingell [136]. The current apparatus differs in some minor aspects from the original design. One major difference is the incorporation of the Stark decelerator, which will be discussed in chapter 5. This has required the rearrangement of several of the ports attaching equipment to the chamber. Improvements have been

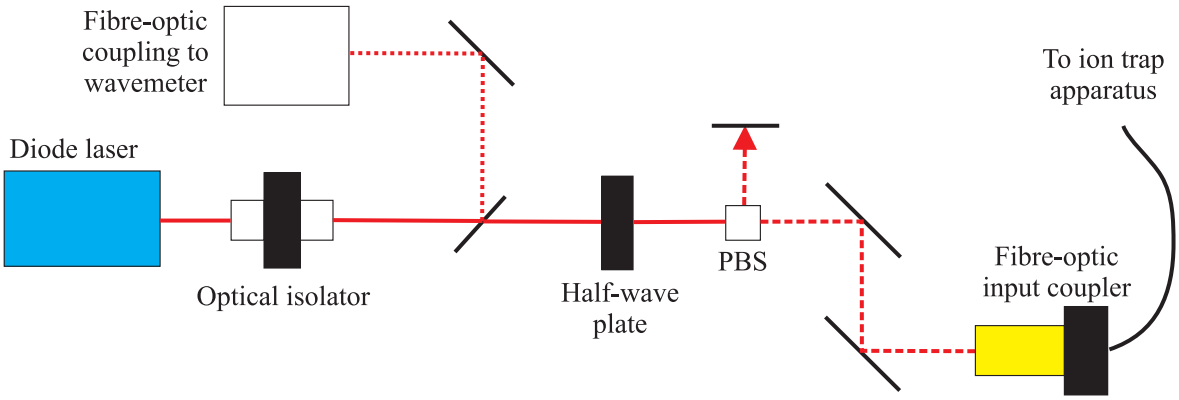


Figure 4.5: Schematic view of the fibre-optic coupling scheme. The layout is the same for both the 397 nm and 866 nm diode lasers. One of the laser beams that emerges from the polarising beam splitter (PBS) is blocked, to allow for future radial cooling or a future second ion trapping experiment.

made to the laser-cooling set-up to generate lower temperature Coulomb crystals, through the introduction of a fibre optic coupling arrangement.

Fibre-Optic Coupling Scheme

The diode lasers utilised in this (and previous) work have non-uniform beam shapes. The beams are approximately elliptical, with a non-uniform intensity variation, resulting in "hot spots" of high intensity separated by regions of low intensity. Some of these beam irregularities can be overcome by coupling the diode laser beams into fibre-optic cables. With a single-mode fibre, the output laser beam has an approximately Gaussian profile, resulting in uniform power distribution. The single-mode nature of the output beam (TEM_{00} [246]) stabilises the diode laser wavelength.

A schematic of the fibre-optic coupling setup is shown in Fig. 4.5. The 397 nm diode laser output (Toptica DL 100 Pro, 18 mW) passes through an optical isolator (Thorlabs IO-5-405-LP, 26 dB), to prevent any optical feedback to the diode laser. A beam pick-off diverts a small amount (around 100 μW) of light into a wavemeter (High Finesse WS-U). The beam passes through a half-wave plate, which can be used to alter the beam polarisation, and a polarising beam splitter (PBS), separating the beam into

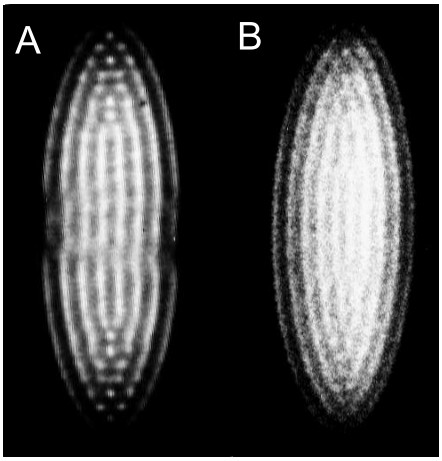


Figure 4.6: Experimental Coulomb crystal images after (A) and before (B) the fibre-optic coupling setup was installed. The trap parameters were $V_{end} = 4$ V and $V_{RF,0} = 150$ V, and the images were averaged over five frames. The lower temperature of crystal A can clearly be seen in the sharpness of the image. It should be noted that image B contains more ions than image A.

two components. The relative amount of power in each component can be controlled by the half-wave plate. In the experiments described here, only the output from one component is utilised (the other being blocked). The remaining beam is directed into a single mode optical fibre, with an angled connector (APC) end (used to minimise back reflections along the beam path). This setup yields output laser powers of between 150 μW and 1.1 mW of 397 nm light. The 866 nm diode laser (Toptica DL 100, 50 mW output) passes through an equivalent setup (Isolator: Thorlabs IOT-5-850-VLP, 57 dB) yielding a final output between 4.8 mW and 7.2 mW after fibre-coupling.

The benefit of this fibre coupling setup relative to the direct laser output setup in [136] is illustrated in Fig. 4.6. Both images were taken under the same conditions, with five-frame averaging, $V_{end} = 4$ V, and $V_{RF,0} = 150$ V. It is clear that image A, recorded after the fibre-optic coupling system was installed, contains a colder crystal than image (B). This is evidenced by a reduction in the blurring of image (A). In addition, the crystal brightness is more uniform with fibre-coupling, implying that a more uniform cooling process is taking place.

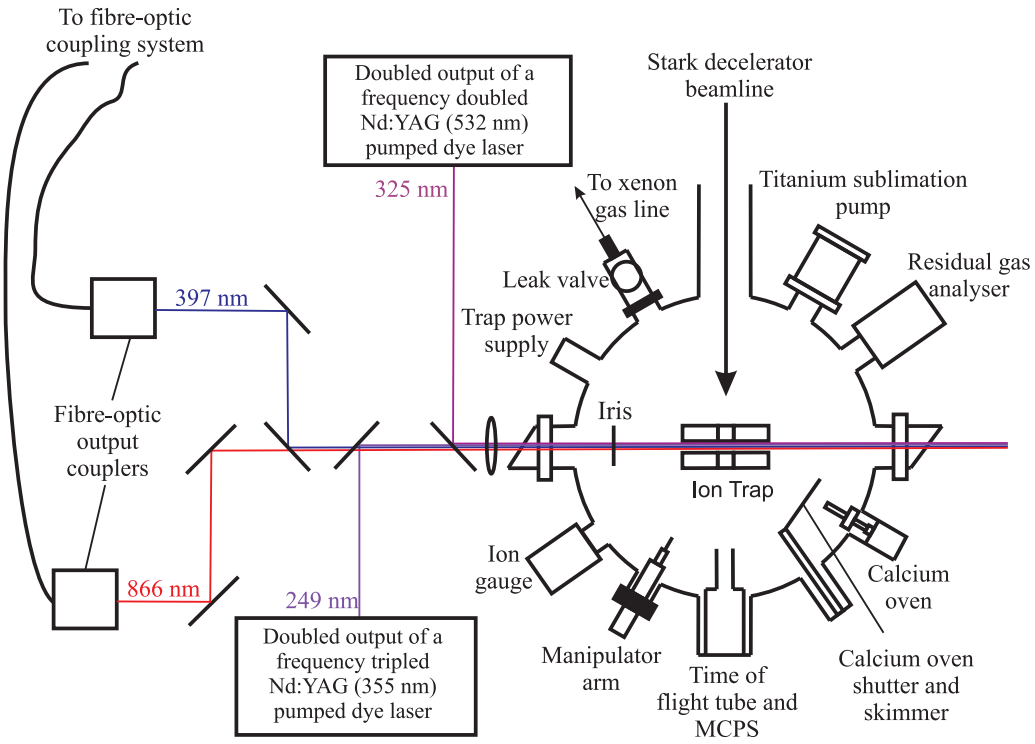


Figure 4.7: Representative top view of the ion trap chamber and the accompanying optics.

The Ion Trap Chamber

The ion trapping apparatus is constructed inside a custom-built ultra-high vaccum (UHV) chamber. Schematics of the trapping chamber in two complementary viewpoints are shown in Figs. 4.7 and 4.8. In these diagrams, the Stark decelerator has been omitted for clarity; details of the combined Stark decelerator ion-trap experiment can be found in chapter 5.

A shutter is used to block the effusive calcium atom beam when the ion trap is not being loaded, to prevent calcium deposition on the electrodes and thus the potential development of patch potentials. Up to four laser beams are involved in the experiments described in this thesis. The 866 nm and 397 nm cooling lasers are in continuous use. Calcium is ionised by a pulsed 325 nm laser (6-7 mJ/pulse), and xenon is ionised by a (2+1) REMPI process, (accessing the $5p^5 6p\ ^2P_{3/2}$ intermediate

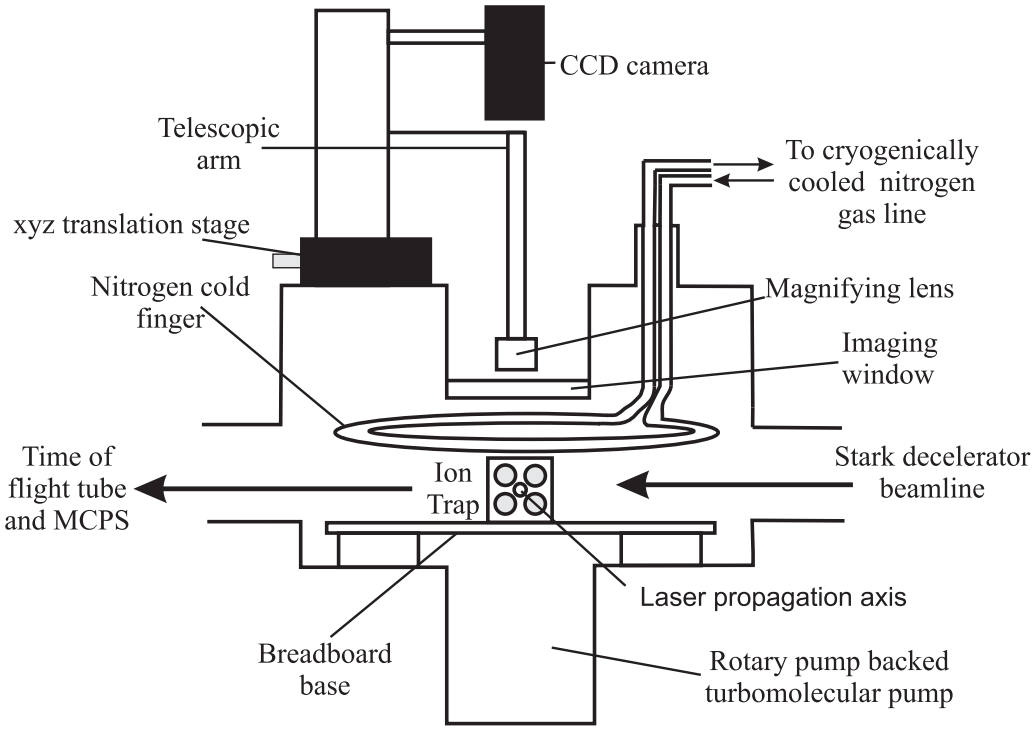


Figure 4.8: Representative side view of the ion trap chamber, viewed along the laser propagation axis.

state) with a pulsed 249 nm laser [247] (800 μJ/pulse). The 325 nm beam is made by frequency doubling the output of a dye laser (Sirah Cobra-Stretch, DCM dye) pumped by a frequency doubled ND:YAG laser (Surelite SSL). The 249 nm laser beam is made by frequency doubling the output of another dye laser (containing Coumarin 503 dye) pumped by a frequency tripled Nd:YAG laser. All four laser beams enter the chamber through a Brewster window, overlapping along the same propagation axis. This maximises the ionization volume within the ion trap, generating Ca^+ and Xe^+ ions close to the trap centre.

Low operational pressures are maintained using a rotary-backed turbomolecular pump (Leybold Turbovac 361) fitted to the underside of the chamber. A titanium sublimation pump (filament type, Varian) is used to further reduce the pressure by reactively removing low-mass background impurities, primarily hydrogen. The pressure is monitored by a hot-cathode ionisation gauge (Leybold Ionivac ITR90), and

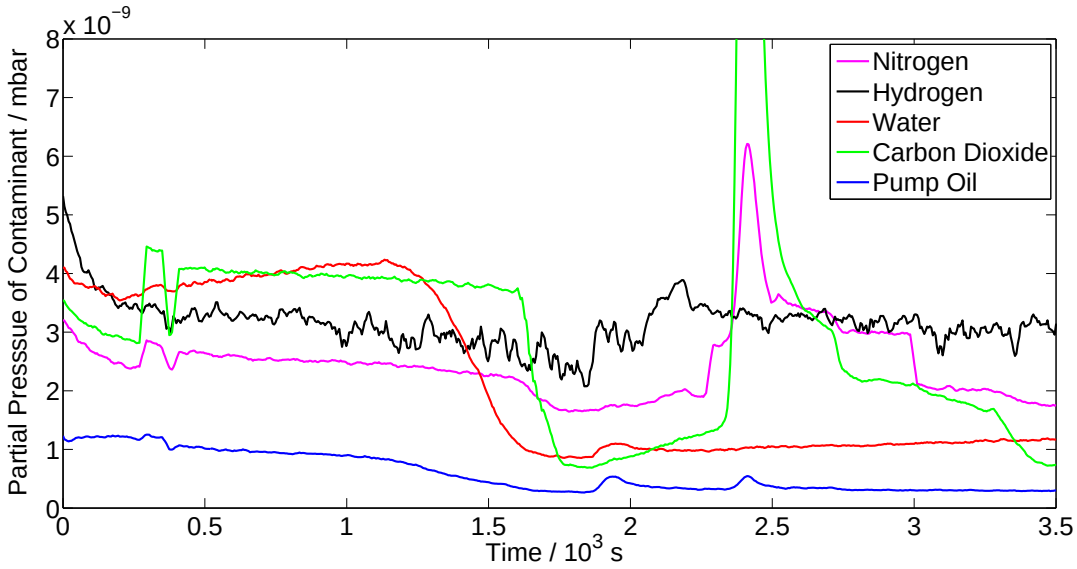


Figure 4.9: Residual gas analysis during a single cooldown event of the nitrogen cold finger for five common background contaminant gases within the ion trap chamber.

the relative concentrations of background gases can be further investigated using a residual gas analyser (RGA, SRS RGA100)

Nitrogen Cold Finger

With the addition of the Stark decelerator, it became difficult to maintain the chamber at the optimal pressure of $< 5 \times 10^{-10}$ mbar with the previous set-up. A low pressure is desirable to reduce the probability of reactive collisions of ions with background molecules. To this end, a nitrogen cold finger consisting of a double coil of copper tubing, has been installed in the chamber. A stream of nitrogen gas, which has been pre-cooled by passing through an external liquid nitrogen heat-exchange reservoir, is flowed through the chamber (see Fig. 4.8). The performance of the cold finger in removing several common contaminants has been analysed using the RGA, and the results are shown in Fig. 4.9.

The RGA filament generates a large amount of heat, and so the pressure readings in Fig. 4.9 should be interpreted in relative rather than absolute terms. There is a twenty

minute (1.2×10^3 s) delay time for the cold finger to become cold enough to freeze out any contaminants. Water and pump oil are gradually removed from the chamber, and carbon dioxide and nitrogen rapidly freeze once the nitrogen heat-exchanger is sufficiently cold (after approximately 1.6×10^3 s). If the nitrogen flow is disturbed (as at 2.3×10^3 s) there is a spike in both the carbon dioxide and nitrogen readings, corresponding to the initial thawing and subsequent pump removal of these species. Fig. 4.9 demonstrates that the cold finger only just reaches low enough temperatures to freeze N_2 and CO_2 molecules. Water and pump oil pressure readings are less affected by brief interruptions in the cooling nitrogen flow. Hydrogen is unaffected by the cold finger.

4.4.2 Experimental Details

The experiments described in this chapter are all conducted within the same ion trap chamber, but, as described later, two different optical set-ups are used. While the most recent optical arrangement was presented in section 4.4.1, some of the results presented in this chapter were obtained with the previous optical arrangement [215], using the direct output from the diode lasers without fibre coupling. The methods described here are generally applicable to either of these configurations.

Whenever the ion trap chamber is pumped down after venting, it is necessary to bake the ion trap chamber at high temperature (typically 180°C for 3-5 days). This process removes contaminants, in particular water and nitrogen, that become adsorbed onto the metallic inner surfaces of the chamber, allowing lower pressures to be obtained.

Initial Observation of Calcium Ion Fluorescence

When the ion trap is employed for the first time after a significant laser realignment, several steps are taken in order to reacquire ion fluorescence. This procedure achieves good laser alignment, and also compensates for potential imperfections in the effective trapping fields which might otherwise offset ions from accumulating in the trap centre.

A 400 μm diameter optical fibre is mounted on a manipulator arm (see Fig. 4.7), and this is visually placed in the approximate trap centre. The diode laser beams are aligned such that they are spatially overlapped, whilst also illuminating the fibre tip. The lens and telescopic arm (see Fig. 4.8) are positioned such that the magnified, illuminated optical fibre tip is located at the centre of the field of view. The CCD camera can then be mounted, with care taken to cover the camera to prevent light from outside the trap chamber affecting the images. The camera is positioned such that the illuminated optical fibre appears in the centre of the image, and the alignment of the diode lasers is optimised so that the maximum intensity image is obtained.

The diode laser wavelengths can be checked to ensure that they are resonant with the $^{40}Ca^{+}$ laser cooling transitions. This is achieved using a hollow cathode lamp exhibiting the optogalvanic effect [248]. Following optimisation, the primary cooling (397 nm) diode laser is detuned by approximately 40 fm from its resonant wavelength.

Coulomb Crystal Optimisation

The RF and endcap voltages are initially set at lower values than might typically be used for ion trapping, typically $V_{RF,0} = 100$V and $V_{end} = 2.5$ V. This makes the cloud of translationally hot confined ions large, increasing the probability of the cooling lasers interacting with the cloud, and therefore of observing Ca^{+} fluorescence. The static offsets are set to V_x = -2 V and V_y = -2 V, placing the effective trap centre at the approximate position of the optical fibre. The calcium oven is "turned on" (with the

shutter in place) at a current of 12 A, and left to heat up for five minutes. The 325 nm dye laser beam is carefully aligned through the trap chamber with the CCD camera switched off, and admitted for up to thirty seconds with the calcium oven shutter open. This generates calcium ions, after which the shutter is closed again.

At this stage there should be calcium ions loaded into the trap, although fluorescence may not be visible at this point, if for example the effective trap centre is misaligned relative to the cooling lasers. The static offset voltages V_x and V_y are systematically scanned, with the CCD amplifier at its maximum setting. This causes the effective trap centre, hence the ion cloud, to move. When the cooling lasers intersect the ion cloud, ion fluorescence is visible, initially (typically) as a dim, diffuse cloud. Once suspected, Ca^+ fluorescence can be confirmed by turning off the ion trap and watching the fluorescence disappear. It is also possible for reflections of the ion cloud fluorescence from the trap electrodes to be imaged. Such reflections can be identified by a non-linear displacement response to an adjustment of the static offset voltages. At this point the xyz-translation stage of the CCD camera is used to search for the true ion cloud.

To minimise the ionic kinetic energy, the ion cloud must be moved to the true trap centre, as opposed to the location of the optical fibre. This position corresponds to static offset voltages of $V_x = 0$ V and $V_y = 0$ V. As the static offset voltages are varied towards these values, the Coulomb crystal is correspondingly moved. The cooling laser beams must therefore also be moved. This can be done by adjusting the diode laser beams to maintain maximal ion fluorescence intensity, as the static offset voltages are adjusted.

Routine Experimental Procedure

A full re-optimisation is not necessary for the day-to-day operation of the ion trap. At the start of each day, all experimental parameters should be set to their final working

values from the previous day. After ionising calcium for 10-30 seconds, depending upon the required crystal size, fluorescence should be immediately visible. Small readjustments are typically all that is required for re-optimisation of the crystal. This is achieved by performing minute adjustments of the static offset voltages to optimise the crystal shape. For a detailed description of this step, see [136]. A well-centred crystal resembles the image in Fig. 4.4A. The crystal looks symmetrically elliptical, with symmetrical shells of ions containing no dislocations. Small drifts in laser alignment are also checked and, if necessary, corrected.

Once the cold crystals are well centred in the trap, xenon gas is admitted into the chamber through a leak valve, such that the total trap chamber pressure rises to 4×10^{-9} - 6×10^{-9} mbar. Single shots of the xenon ionisation laser (249 nm) are admitted to the trap chamber until a sufficient number of xenon ions have been visibly sympathetically cooled into the crystal. As a result of laser wavelength drift and fluctuations in laser power, this can vary between 10 to 50 shots. After loading the xenon ions into the Coulomb crystal, the leak valve is fully closed again, with the pressure in the trap chamber returning to below 10^{-9} mbar within around 20 seconds.

4.5 Characterisation of Coulomb Crystals

4.5.1 Simulation of Coulomb Crystals

Experimental Coulomb crystals can be simulated using MD simulations. Such simulations are vital in enabling us to ascertain characteristics such as crystal temperatures and ion numbers, both of fluorescing and dark components. The simulations are performed using a set of programs written by Martin Bell and optimised by Zhewei Zhou [249], based upon the Protomol MD simulation package [250]. The code has been written to make use of the processing power of a graphical processing unit (GPU).

The calculated force experienced by the ions consists of four terms:

$$\mathbf{F}_{total} = \mathbf{F}_{trap} + \mathbf{F}_{Coulomb} + \mathbf{F}_{laser} + \mathbf{F}_{heat} \tag{4.15}$$

The trapping force on the ion i is derived from the time-dependent trap potential:

$$\mathbf{F}_{trap,i} = q_i \left(\frac{V_0 \cos(\Omega_{RF} t)}{r_0^2}(x_i - y_i) + \frac{\kappa V_{end}}{z_0^2}(2z_i - (x_i + y_i) \right) \tag{4.16}$$

The Coulomb interaction is taken into account using pairwise addition of all of the inter-ionic forces, separated by a displacement vector $\mathbf{r}_{ij}$:

$$\mathbf{F}_{Coulomb,i} = \sum_{i \neq j} \frac{q_i q_j}{4\pi\epsilon_0 r_{ij}^2} \hat{\mathbf{r}}_{ij} \tag{4.17}$$

Since laser cooling occurs along the z-axis within the ion trap, the process is modelled using a simple viscous damping term:

$$\mathbf{F}_{laser,i} = -\beta \dot{\mathbf{z}}_i \tag{4.18}$$

Although there is a rigorous definition of β [136], for the purposes of this thesis it is sufficient to say that $\beta \approx 870$ kgs^{-1}. The final term $\mathbf{F}_{heat,i}$ is a stochastic heating term that is designed to model photon recoil and background collisions. It provides random velocity kicks to every ion at each time step, and adjusting it allows for control of the final temperature of the crystal.

In addition to this crystal simulation package, a program has been written to compute the volume of a calcium Coulomb crystal, assuming that it has an ellipsoidal shape [136]. This enables the number of ions to be estimated, using a number density

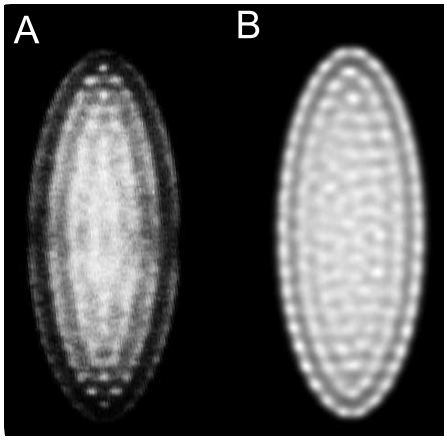


Figure 4.10: Experimental (A) and simulated (B) calcium Coulomb crystals, recorded using the linear Paul trap with $V_{RF,0} = 130$ V and $V_{end} = 4$ V. The simulation indicates that the crystal contains 590 ± 5 calcium ions.

derived from the fluid model of a trapped plasma at zero temperature:

$$n_0 = \frac{4\epsilon_0 V_{RF,0}^2}{m\Omega_{RF}^2 r_0^4} \tag{4.19}$$

where m is the mass of the singly charged ion. Although derived from a fluid model, it has been shown to be agree well with the number density of ions in large (> 100 ions) Coulomb crystals [251].

The MD simulations create a three-dimensional histogram containing the positions of all of the ions in the crystal. To simulate the experimental image, where the image is viewed along the camera axis, the individual layers are subjected to a Gaussian blur. The degree of blurring increases with increasing distance from the focal plane along this axis so that the visible spots in the images correspond to a slice through the three dimensional distribution. Simulated images are compared with experimental images to determine the ion numbers and temperature of the crystal. A simulation of the experimental calcium image in Fig. 4.4 is shown in Fig. 4.10. This simulation indicates that there are 590 ± 5 calcium ions in the experimentally observed Coulomb crystal.

While the simulations here have been demonstrated to work well [252, 249], unfortunately, they are also time consuming. Simulation of a bicomponent crystal, containing several hundred sympathetically-cooled ions, takes approximately an hour to complete. While this is not a long period of time, the large number of simulations required for a quantitative fit to experimental data makes this approach unsuitable for the analysis of every experimental image, hence an alternative approach is described below.

4.5.2 Dark Core Volume Analysis

For tricomponent Coulomb crystals, analysing the volume of the dark ion core of the Coulomb crystal, where the lightest sympathetically cooled ions reside, enables the number of light ions to be determined. A method has been developed to facilitate quick calculation of this volume from the experimental images, illustrated in Fig. 4.11.

For the Coulomb crystal image in Fig. 4.11, the camera gives an image resolution of 789×405 pixels. For every position along the z-axis (horizontal) of the crystal, the cross section intensity distribution is evaluated, illustrated in Fig. 4.11. This intensity cross section is smoothed using the Savitzky-Golay algorithm [253], which preserves local maxima. The maxima and minima are found by locating and interpolating for the zeros of the first derivative of the intensity distribution. The maxima that define the boundary of the dark core volume are usually the most intense points in the distribution above and below the dark core. In cases where this is not the case, the correct maxima can be assigned manually. The centre-line of the image at a given position along the z-axis is calculated using the mean of the intensity distribution.

In this manner, a bounding box enclosing the crystal is defined. The boundary lines are smoothed to give functions $y_u(p)$ and $y_l(p)$, describing the boundary lines above and below the centre line respectively. If the centre line is defined by the function

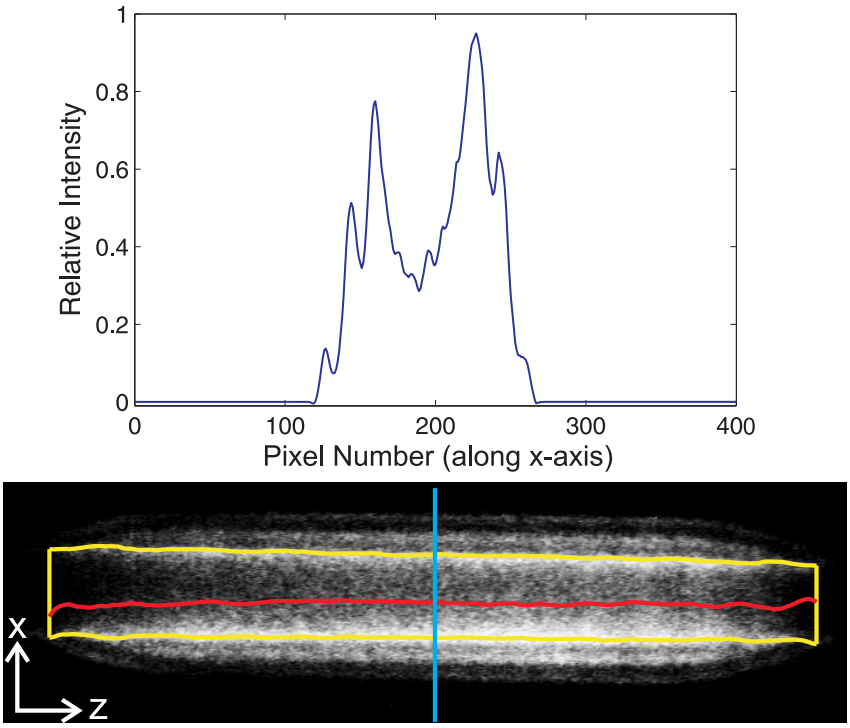


Figure 4.11: Illustration of the dark core volume analysis method. For every position along the z-axis of the image, the intensity cross section is calculated, shown in the graph above for the cross section along the blue line in the camera image. This intensity cross section is used to create a boundary box for the volume, shown in yellow. The centre line of the image, shown in red, is calculated as the mean of the intensity cross section distribution function.

$c(p)$, calculated from the mean of the intensity distribution function, then the volume of the dark core can be approximated to be the volume of a solid of revolution about $c(p)$ [151]. In order to compensate for errors in computing the boundary and centre lines, the volume is taken to be the average of the volumes obtained with the upper and lower boundaries:

$$V = \frac{\pi}{2} \int_{p_{min}}^{p_{max}} ([y_u(p) - c(p)]^2 + [y_l(p) - c(p)]^2) \mathrm{d}p \tag{4.20}$$

where p_{min} and p_{max} are the first and last positions along the crystal z-axis that make up the bounding box. With an appropriate calibration such that the scale of the CCD image is known, this volume can be used to calculate the number of light ions that are sympathetically cooled into the crystal.

4.5.3 Experimental Considerations

Contamination in the Trap Chamber

Xenon ions are extremely reactive with a wide variety of neutral partners. This presents a potential problem, as trace quantities of contaminants in the trap chamber with a lower ionisation potential than xenon (which has an ionisation potential of 12.1 eV [1]) can charge exchange with the sympathetically cooled Xe^+. In the presence of such contaminants, background reactions can occur very quickly. This is illustrated in Fig. 4.12, where a large dark core can be seen to form in a space of a few minutes. These images were recorded before the fibre-optic coupling was installed (with the optical setup in [136], and with trap voltages of $V_{RF,0} = 150$ V and $V_{end} = 4$ V.

The nature of the contaminant is unknown. It is present in such trace amounts that it is not detectable by the RGA. The nitrogen cold finger slightly reduced the rate of dark core formation, but not significantly. The unknown identity and concentration

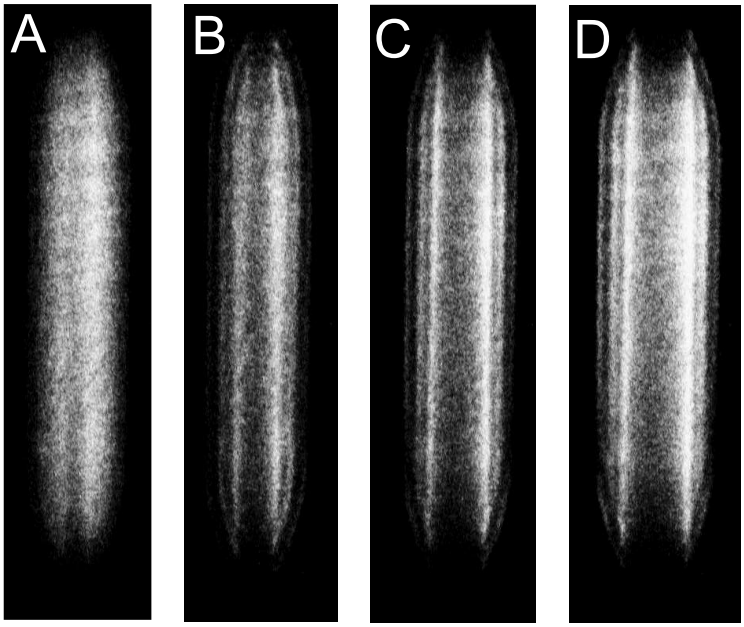


Figure 4.12: The growth of the dark core contaminant at four separate times after ionisation and loading of Xe^+. The experimental images were recorded at $t =$ (A): 10 s, (B): 21 s, (C): 74 s and (D): 189 s.

of the contaminant makes it impossible to interpret the background reaction kinetics.

Two strategies were adopted to eliminate contaminants from the ion trap chamber. The first, as always, is to bake the ion trap chamber at the higher temperature of 180°C for at least 3 days. When this was found to be insufficient, the leak valve was cleaned, and ultimately replaced. Changing to a new, clean valve was found to permanently remove the contaminant observed in Fig 4.12. This circumstantially implies that the primary contaminant responsible for the dark core was ammonia, since the original leak valve had been used in the past to admit ammonia into the trap chamber [242].

Background Loss of Ca^+ Ions

In order to ascertain the background loss rate of calcium ions from the ion trap with the new leak valve and the fibre-coupled diode laser beams, a single component Coulomb crystal was created in the ion trap and observed for an extended period of time.

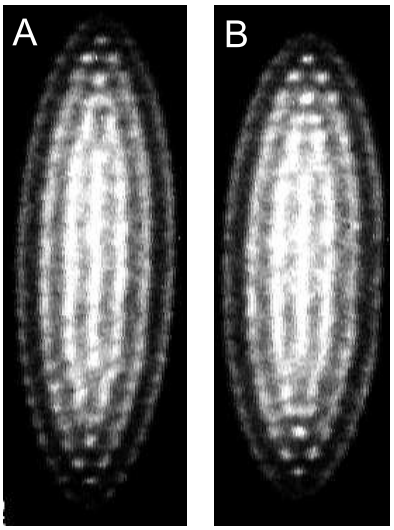


Figure 4.13: Experimental images of calcium Coulomb crystals (A): immediately after calcium crystal formation, (B): after 36 minutes of ion trapping. The number of ions is reduced from (540 ± 5) ions to (510 ± 5) ions.

Experimental images showing the Coulomb crystal immediately after formation and approximately 36 minutes later are shown in Fig. 4.13. These experimental images have been compared with MD simulations. Over the trapping period, the number of ions is reduced from (540 ± 5) ions to (510 ± 5) ions. This occurs more slowly than the timescale of the experiments described in Chapter 5, validating the approximation that the number of calcium ions can be assumed to be constant. However, xenon ions experience a weaker trapping potential due to their lower charge-to-mass ratio. Consequently, the loss rate of xenon ions from the trap may be significantly higher than the observed loss rate of calcium ions.

Analysis of the images in Fig. 4.13 also indicates that the trapping conditions are not constant throughout the course of the experiment. Simulations show that the initial crystal is trapped at the expected trapping voltages of $V_{end} = 4$ V and $V_{RF,0} = 150$ V, but the final crystal only agrees with simulations when the trapping voltages are set to $V_{end} = 4$ V and $V_{RF,0} = 140$ V. This drift in the RF voltage corresponds to a weaker RF trapping potential, and may therefore influence the results

of experiments that occur over timescales of several minutes.

4.6 Conclusions and Outlook

In this chapter, an updated design of an ion trapping experiment has been described, alongside the theoretical methods employed to analyse and characterise experimental calcium fluorescence images. In addition, methods have been discussed to eliminate rapid background reactions involving sympathetically-cooled xenon ions, and the background loss rate of calcium has been shown to be negligible.

This work forms the basis of the investigation into the ion-molecule reaction between sympathetically cooled Xe^+ and a tunable energy beam of Stark decelerated ND_3 molecules, described in the next chapter.

Chapter 5

Towards Tunable-Energy, State-Selected Ion-Molecule Reactions

5.1 Chemical Background

5.1.1 The Reaction of Xenon Ions with Ammonia

The chemistry of positively charged xenon ions and neutral ammonia molecules occurs mainly in extra-terrestrial situations. Ion-drive propulsion in modern spacecraft is achieved through the release of a directed stream of both singly and doubly charged xenon ions [254]. The reaction of these ions with common species, such as ammonia, in interstellar space [255] and the atmospheres of nearby planets [3] is therefore of interest (although at rather higher energies than the cold collisions of interest in this thesis). This chemistry may also be relevant to the demonstrated nano-etching of structured metal surfaces using a mixed $Xe/NH_3/CO$ plasma, a technique that may be important in the development of a silicon-based quantum computer [256].

Thermochemical calculations performed by Lavander and Chiu [257] indicate that there is only a single exothermic reaction channel in the reaction between singly charged ground state xenon ions and neutral NH_3 molecules, corresponding to a simple charge transfer reaction with ΔH = -2.1 eV :

$$Xe^+(^2P_{3/2}) + NH_3(^1A_1) \longrightarrow Xe(^1S_0) + NH_3^+(^2A_1) \tag{5.1}$$

All other channels (involving hydrogen abstraction or subsequent dissociation of the ammonia ion) are endothermic with $\Delta H \geq 1.0$ eV. Experimental evidence suggests that no other reaction products are formed in appreciable quantities during room temperature reactions [258, 259], however as there are three naturally occurring isotopes of xenon with abundances greater than 20% (^{129}Xe, ^{131}Xe and ^{132}Xe), this result is difficult to confirm through the mass spectrometric techniques that were used. The first spin-orbit excited state of the xenon ion lies 1.31 eV above the ground state [260]. Thus, under our experimental conditions, the reaction described in equation 5.1 is the only available reaction channel.

Scattering studies performed by Levandier and Chiu [257] at hyperthermal energies strongly suggest that reaction 5.1 proceeds via complex formation (due to ion-molecule capture). The capture theory methods introduced in Chapter 2 would therefore be expected to model this single channel reaction well. Rate constants for reaction 5.1 have been recorded using selected-ion flow tubes [260, 261] and drift-cell ion-cyclotron resonance [258, 259]. Collision-energy dependent cross-sections were obtained using octopole guiding through a collision cell [257]. These studies have yielded rate constants in the range of 6×10^{-10} molecules^{-1} cm^3 s^{-1} [258] to 8.3×10^{-10} molecules^{-1} cm^3 s^{-1} [260] for the ground electronic ground state of ammonia at a temperature of 300 K.

The relative simplicity of this single channel reaction at thermal temperatures, and

the existence of successful theoretical methods that describe the expected reaction mechanism, make this an excellent proof-of-concept reaction for the purposes of this thesis. It should be noted that there have not been any studies performed using deuterated ammonia. As there is no bond breaking or conformation change during this process, there is not expected to be any substantial kinetic isotope effect; the rate constant is assumed to be changed very little as a result of the isotopic substitution. Any changes will arise as a result of the slightly different ionisation energy of ND_3 compared with NH_3.

It is possible to compute the expected temperature dependence of the bimolecular rate constant as a function of translational temperature for ND_3 molecules in the $|j, mk\rangle = |1, -1\rangle$ state within the statistical adiabatic channel model introduced in section 2.1.5. This is the state that is selectively Stark decelerated in the experiments described in Chapter 3. The results of this calculation are shown in Fig. 5.1, and indicate that there is expected to be a significant decrease (approximately a factor of 2.5) of the state-specific rate constant as the translational temperature increases. Observation of the temperature dependence of the rate constant in this reaction should therefore be possible under the experimental conditions described in this thesis.

The predicted room temperature rate constant for the state selected reaction is approximately a factor of 5 larger than the experimentally observed thermal rate constant. This is to be expected. At higher temperatures, a large proportion of the molecule exist in highly excited rotational states. This means that the molecules possess a lower "effective" dipole moment, lowering the ion-molecule interaction potential for these molecules, and hence the overall rate constant.

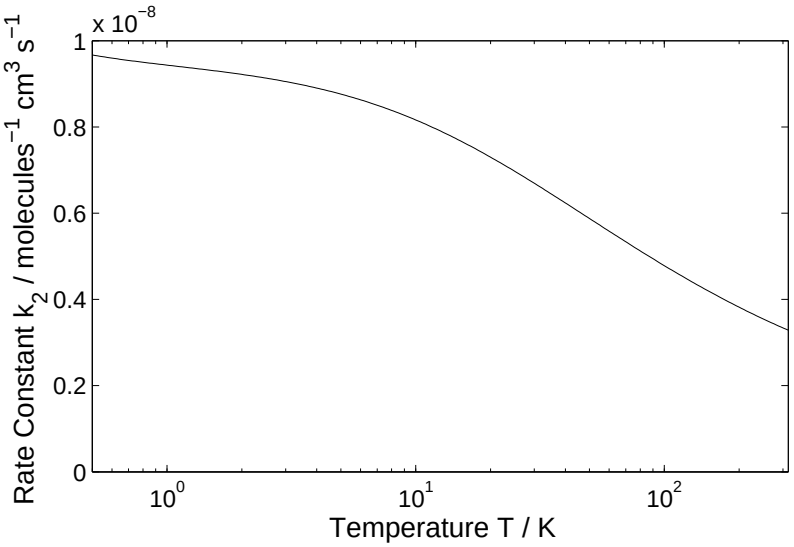


Figure 5.1: Predicted single state rate constant as a function of temperature for the $|j, mk\rangle = |1, -1\rangle$ state of ND_3, reacting with Xe^+. The calculation is performed within the framework of the statistical adiabatic channel model (see section 2.1.5). The range of translational temperatures shown corresponds to final velocities of 20 ms^{-1} to 500 ms^{-1}.

5.1.2 Chemistry Involving Sympathetically-Cooled Ions

The sympathetic cooling of atomic and molecular ions, by exploiting their interaction with laser-cooled atomic ions in an ion trap, has enabled the study of an increasingly broad range of low temperature ion-molecule reactions.

The use of sympathetically-cooled ions in chemical reactions was first demonstrated using reactions that involved the laser cooled ions as reactant species, such as [25, 262]:

$$Ca^+ + CH_3F \longrightarrow CaF^+ + CH_3 \tag{5.2}$$

$$Mg^+ + H_2 \longrightarrow MgH^+ + H \tag{5.3}$$

Both of these reactions yield singly charged product ions that are heavier than the laser cooled ions. As discussed previously, these ions will not fluoresce, and will be trapped further away from the trap axis than the laser cooled ions. The rate of

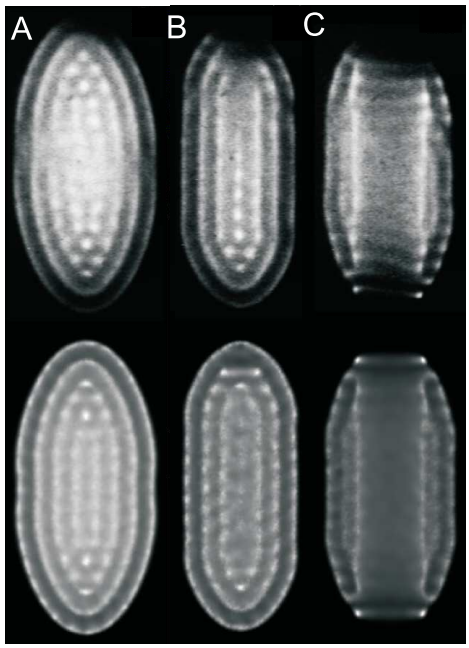


Figure 5.2: Experimental (top) and simulated (bottom) images from the reaction between velocity-selected ND_3 and sympathetically-cooled OCS^+ ions. The images were recorded (A) before sympathetic loading, (B) at time $t = 0$ s with OCS^+ sympathetically-cooled into the crystal, (C) at time $t = 65$ s, following the reaction between OCS^+ and ND_3. The rate of reaction can be calculated by evaluating the initial number density of OCS^+ through simulation, and by analysing the growth rate of the dark core of ND_3^+. Experimental images and simulations were supplied by Alex Gingell, see [242] for more details.

reaction can be inferred both from the reduction in the fluorescing volume of the Coulomb crystal (as the laser-cooled ions react), and by the flattening of the outside edges of the experimental images (as the number of dark sympathetically-cooled ions increases).

This principle has been expanded to include reactions between sympathetically-cooled ions and neutral molecules. An early example of this involved the charge-exchange reaction between sympathetically cooled OCS^+ and velocity selected ammonia, studied using a calcium Coulomb crystal [242]:

$$OCS^+ + ND_3 \longrightarrow ND_3^+ + OCS \tag{5.4}$$

Initially, the loading of sympathetically cooled OCS^+ caused a flattening of the experimental image. Since ND_3^+ is lighter than Ca^+, the product ammonia ions were trapped nearer the trap axis, resulting in the development of a dark core within the Coulomb crystals, as shown in Fig. 5.2. The resulting images were fit to MD simulations as a function of time, and rate constants subsequently calculated, both at room temperature and at a translational temperature of 8 K.

The velocity selection experiment has recently been taken a step further with the combination of an ion trap with a cryogenically cooled velocity selector apparatus [71]. This apparatus has been used to study the reactions between CH_3CN and sympathetically-cooled N_2H^+ ions within a calcium Coulomb crystal, down to temperatures of 3 K, close to the microwave background temperature of the Universe.

An ion trap has also been combined with a magneto-optical trap [99] to study the ion-atom reaction between sympathetically-cooled N_2^+ and laser-cooled rubidium atoms [176]. The magneto-optical trap cools the Rb atoms to around 200 μK, and so the effective chemical reaction temperature is dependent on the temperature of the N_2^+ (determined to be around 20 mK [176]).

It is also possible to perform quantum state selected reactions using Coulomb crystals, as demonstrated with state-selected Ca^+ ions [26] (reacting with CH_3F) and state selected Rb atoms [176] (reacting with N_2^+). A chemical reaction involving fully quantum state selected molecular ions in an ion trap has only recently been demonstrated for the charge exchange reaction between N_2^+ and N_2 [263]. Such studies are difficult, as although sympathetically-cooled trapped ions are translationally cold, the internal degrees of freedom can thermalise with black-body radiation (BBR) at the temperature of the ion trap chamber (around 300 K). Molecules with a permanent dipole or quadrupole moment can interact with this BBR field, resulting in energy redistribution into multiple quantum states. Calculations indicate that the cryogenic cooling of the ion trap to 77 K should suppress much of this population redistribution, maintaining

the state selectivity for longer timescales [264].

In this chapter, the reaction of Xe^+ with neutral ammonia is studied through observation of the rate of growth of a dark core (of ND_3 molecular ions) within the Coulomb crystal.

5.1.3 Determination of Rate Constants

For the charge-exchange reaction between Xe^+ and ND_3, the rate can be expressed as:

$$\frac{d[Xe^+]}{dt} = -k_2[Xe^+][ND_3] \tag{5.5}$$

where $[Xe^+]$ and $[ND_3]$ are the number densities of Xe^+ and ND_3 respectively, and k_2 is the bimolecular rate constant. Under the assumption that no Xe^+ is lost from the Coulomb crystal except by reaction with ND_3, then

$$[Xe^+] = [Xe^+]_0 - [ND_3^+] \tag{5.6}$$

where $[Xe^+]_0$ is the initial number density of Xe^+. Substituting equation 5.6 into equation 5.5 , the rate equation can be rewritten in terms of the formation of ND_3^+ ions:

$$\frac{d[ND_3^+]}{dt} = k_2[ND_3]\left([Xe^+]_0 - [ND_3^+]\right) \tag{5.7}$$

Expression 5.7 can be simplified further by assuming that the number density of $[ND_3]$ is constant. In the context of this experiment, where a repetitively pulsed source of ND_3 is employed, this assumption should be valid. As such:

$$\frac{d[ND_3^+]}{dt} = k_1\left([Xe^+]_0 - [ND_3^+]\right) \tag{5.8}$$

where k_1 is a pseudo first order rate constant. This equation can be integrated directly

to give:

$$[\mathrm{ND}_3^+](t) = [\mathrm{Xe}^+]_0 \left(1 - e^{-k_1 t}\right) \tag{5.9}$$

Thus, if the number density of ND_3 and the initial number density of Xe^+ are known, then the bimolecular rate constant can be evaluated.

5.1.4 Experimental Set-up

The interior of the reaction chamber for the combined Stark decelerator beamline and ion trap experiment has been shown in Fig. 4.7. Many of the features depicted have been discussed previously, in Chapters 3 and 4. Worth noting here is the presence of a grounded mesh attached to a stainless steel shield surrounding the final hexapole. These serve to electrically isolate the ion trap from the high voltages applied to the hexapole (in the absence of shielding, the electric field from the hexapole interferes with the electric field in the ion trap, causing the calcium ions to be lost).

During each experiment, calcium ions are laser cooled and trapped according to the method described in section 4.4.2, and xenon is sympathetically cooled into the crystal. During this process the pulsed valve is operated at a frequency of 10 Hz, but the transmission of ammonia into the trap chamber is prevented by the shutter. An experiment is deemed to begin when a voltage is first applied to the shutter, admitting ammonia molecules into the ion trap chamber.

5.2 Results

In the experiments discussed in this section, sympathetically cooled xenon ions are reacted with molecular pulses of ammonia that have been guided through the Stark decelerator in a configuration such that the decelerator behaves as an electrostatic guide. This represents the first steps towards a charge exchange reaction between cold,

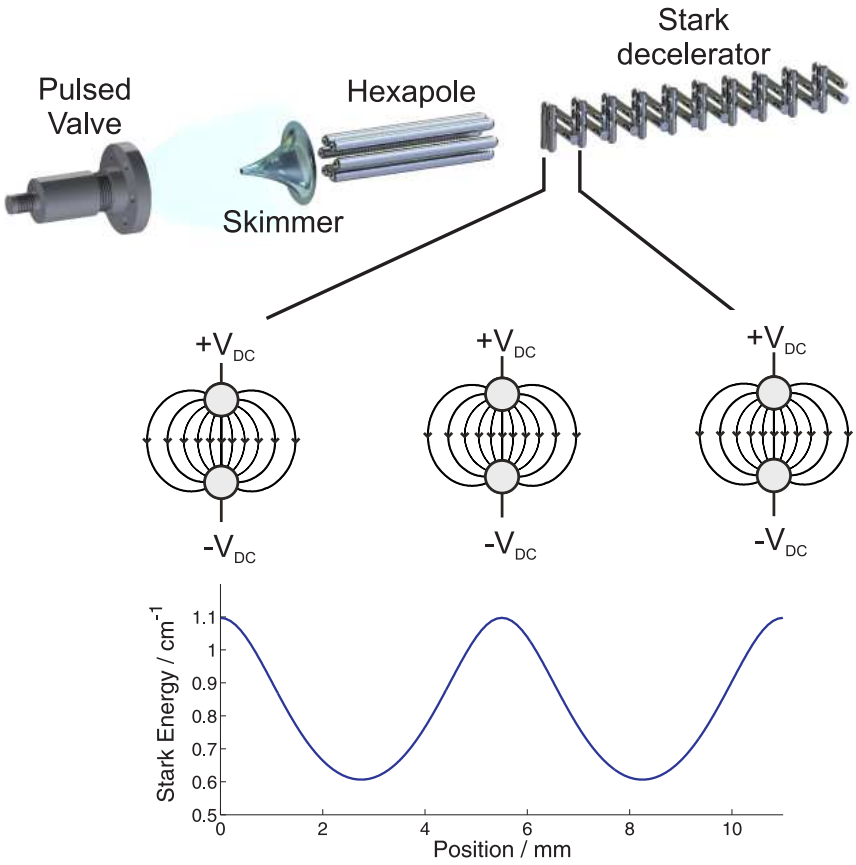


Figure 5.3: Illustration of the DC guiding mode of the Stark decelerator. All electrodes are held at constant voltage of $\pm V_{DC}$, where V_{DC} is typically in the range 0 - 8.5 kV. In this mode, molecules travel through a potential where there is no overall deceleration or acceleration, and there is a constant transverse force on the molecules. This increases the molecular transmittance through the decelerator.

trapped Xe^+ and state-selected, slow-moving ND_3 molecules, and the first demonstration of the possibility to combine an ion trap with a Stark decelerator.

5.2.1 The Stark Decelerator as an Electrostatic Guide

The operation of the Stark decelerator as an electrostatic guide is illustrated in Fig. 5.3. In this mode, the fast high-voltage switches are removed, and instead a constant DC voltage is applied to all of the electrodes. In every electrode pair, one of the electrodes is held at a voltage of $+V_{DC}$, and the other electrode is held at $-V_{DC}$. This configuration of voltages results in the longitudinal Stark potential shown in the lower

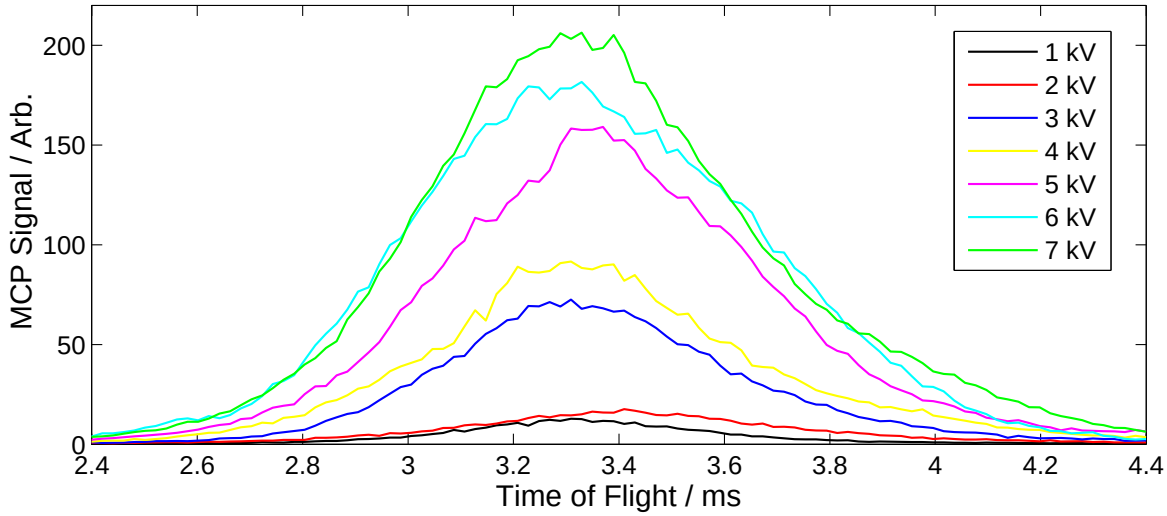


Figure 5.4: Time-of-flight spectra, recorded with the Stark decelerator in its DC guiding mode of operation, for DC guiding voltages between 1 kV and 7 kV. Guiding voltages are shown in the legend.

panel of Fig. 5.3 for the $|j, mk\rangle = |1, -1\rangle$ quantum state. This potential shows that there is no overall change in kinetic energy of the molecule as it passes over the length of the decelerator. As the electric fields are not switched, the longitudinal phase space acceptance is constant.

The advantage of this mode of operation is that a constant transverse focussing force is applied to the molecular beam. As discussed in section 3.2.4, successive electrode pairs are perpendicular to each other ensuring focussing in both transverse directions. As such, there is a high transverse phase space acceptance in the Stark decelerator. This means that the flux at the end of the Stark decelerator beamline is high, and can be controlled by varying the voltage. The flux of ND_3, measured as a function of voltage can be seen in Fig. 5.4, which shows experimental time-of-flight spectra recorded for guiding voltages between 1 kV and 7 kV. These spectra were recorded using the (2+1) REMPI scheme detailed in section 3.3, with the REMPI laser intersecting the molecular beam inside the ion trap and the ion trap electrodes used as repeller and extractor plates.

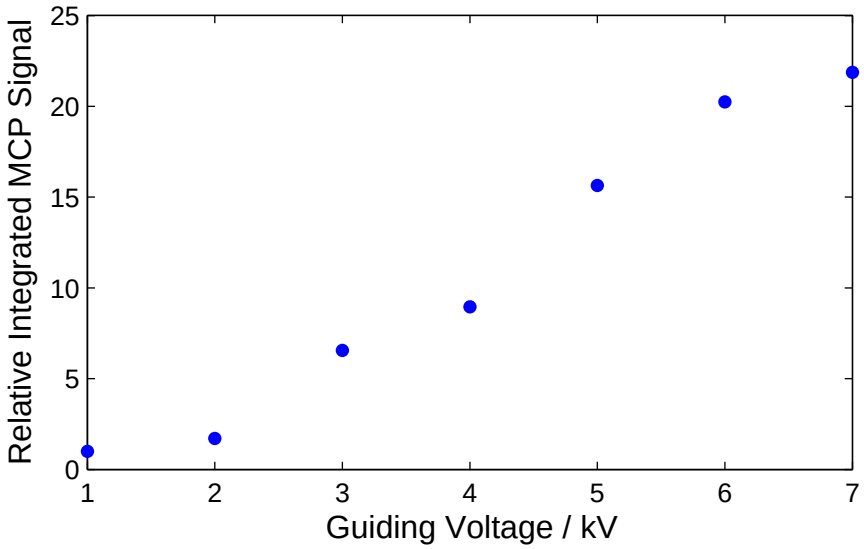


Figure 5.5: Integrated intensity of the ammonia molecular beam pulse, measured relative to the integrated intensity at a guiding voltage of 1 kV.

These time-of-flight spectra have approximately the same temporal width, and so the integrated area of the peaks can be used to estimate the relative number density of ammonia molecules in each molecular beam pulse, as a function of the guiding voltage (presented in Fig. 5.5). It was only possible to record a single data set, and so the uncertainties in the plotted data points are unknown. However, the data appear to show trends that have been observed in other research groups [213]. As the guiding voltage increases, so does the integrated ammonia signal, due to the increased transverse guiding force. There is little difference in intensity between guiding voltages of 1 kV and 2 kV, as neither voltage provides a sufficiently large transverse guiding force to prevent large transverse losses from the molecular beam between the electrodes. As observation of Fig. 5.5 illustrates, increasing the applied voltage from 6kV to 7 kV yields a smaller increase in integrated signal than is achieved by increasing the voltage from 5 kV to 6 kV. This is because the transverse phase space is large and, as such, the majority of the skimmed molecular beam pulse is transmitted through the decelerator. Further increases in guiding voltage (beyond 7 kV) are likely to produce diminishing

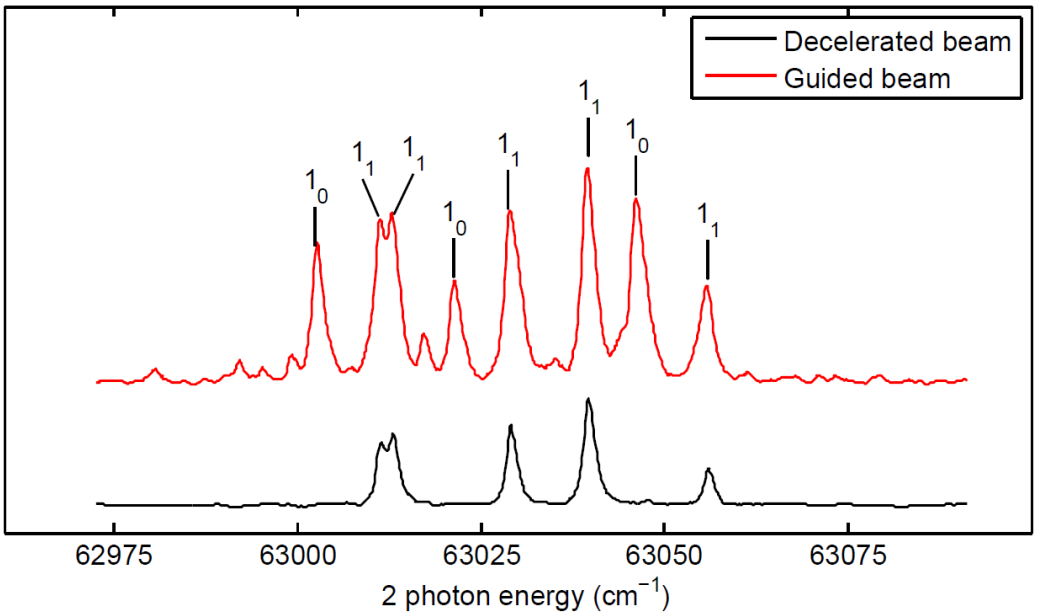


Figure 5.6: (2+1) REMPI spectra of the ND_3 molecular beam (using the $B(v = 5)$ intermediate state), recorded using the ion trap configuration described in section 3.3, with the Stark decelerator acting as an electrostatic guide at ±5 kV(upper trace), and as a decelerator at a phase angle of ($\phi_0 = 45°$). The peaks are labelled according to the lower states of the transitions. The spectra were recorded by Martin Bell.

returns in ND_3 number density at the ion trap.

It should be noted that this mode of operation places a large electrical load on the Stark decelerator electrodes. This has been observed to sometimes cause a significant current draw (see section 3.5.1), which can lead to electrical discharge. If this happens, there is a risk of damaging the electrodes. This is more likely to happen at voltages over 8 kV. A safer mode of operation, which will be implemented in future experiments, involves pulsing the electrodes for around 5 ms after the pulsed valve opens, at the experimental repetition rate of 10 Hz. In this manner, the molecular pulse would experience the same electric field that it would experience in the current configuration, with a reduced load placed on the electrodes.

5.2.2 State-Selectivity in the Stark Decelerator

The method of Stark deceleration is "state-selective". As previously discussed in section 3.2.1, the switching times of the Stark decelerator are calculated based upon the Stark shift of a single LFS state of ND_3, hence only one quantum state is expected to be phase stable. When in the guiding configuration, any molecule in a LFS state can, in principle, be transmitted to the ion trap.

The REMPI spectrum of the decelerated ND_3 beam, shown in Fig. 5.6 and recorded by Martin Bell [265], demonstrates the state selectivity of the method. Both the guided beam and the decelerated beam contain molecules in the $|j, mk\rangle = |1, -1\rangle$ state. However, the guided molecular beam clearly also shows a significant contribution from the $|1, 0\rangle$ state and additional small peaks that can be attributed to transitions from the $|2, -2\rangle$ state. By contrast, the decelerated spectrum shows only peaks from the $|1, -1\rangle$ state, demonstrating that the phase behaviour of the Stark decelerator only permits molecules from the $|1, -1\rangle$ state to be transmitted. Assignments are made using simulations of the REMPI spectra [266, 267].

5.2.3 Sensitivity to Sympathetically Cooled Xenon Ions

One of the key parameters in equation 5.9 is the initial number density of sympathetically-cooled xenon ions, $[Xe^+]_0$, in the ion trap. In order to calculate the rate constant, this quantity needs to be acccurately known. The Xe^+ ions cannot be observed directly in the experiment, only their effect on the morphology of the Coulomb crystal. We calculate the number of xenon ions initially in the crystal, $N_{Xe^+,0}$ (which is proportional to $[Xe^+]_0$) by comparing experimental images of the Ca^+ ions with simulated images. As xenon ions have a much smaller charge-to-mass ratio than calcium ions, they are trapped further from the trap axis, as shown by the simulation in Fig. 5.7.

This simulation illustrates that although the xenon ions are sympathetically cooled

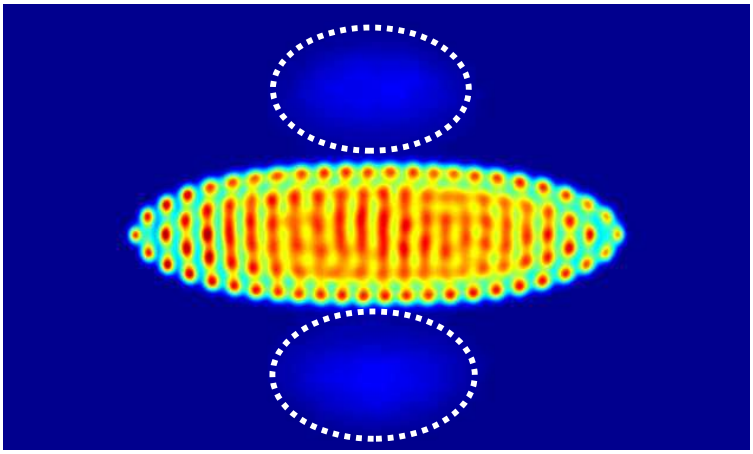


Figure 5.7: False colour image of a simulated Coulomb crystal containing 500 laser-cooled calcium ions and 100 sympathetically cooled xenon ions. All ions are shown, and the uncrystallised xenon ions can be seen as faint amorphous patches above and below the calcium crystal image, indicating that they are in a fluid plasma phase. The dotted lines serve as guides to the eye for the location of the diffuse xenon cloud

into the Coulomb crystal, they do not themselves crystallise. The individual calcium ions are visible, with the 100 xenon ions creating an amorphous cloud around the $^{40}Ca^{+}$. The spatial extent and low intensity of this cloud imply that this amorphous behaviour is not merely a consequence of the Xe^{+} ions not being in the focal plane of the image. Consideration of the plasma coupling parameter described in equation 4.12, indicates that the secular temperature of the non-crystalline xenon ions must be ≥ 60 mK. Also, the effect of co-trapped xenon ions on the calcium Coulomb crystal morphology is expected to be relatively small compared to previous studies (for instance [69, 242]), where the dark ions (of OCS^{+}) had a charge-to-mass ratio much closer to that of calcium. Although analytical models have been developed to explain the morphology of a one-component Coulomb crystal in a linear Paul trap [268], no robust model has been reported for a multi-component crystal.

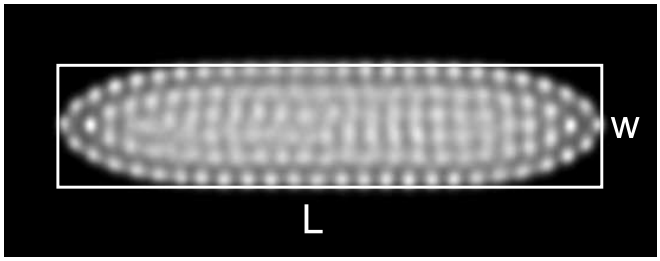


Figure 5.8: Evaluation of the length L and width w of a simulated Coulomb crystal. This crystal contains 500 calcium ions and 500 xenon ions, with trapping voltages of $V_{RF,0} = 150$ V and $V_{end} = 4$ V.

Bicomponent Crystal Analysis

Bicomponent crystals have been simulated using the program described in section 4.5.1 with different numbers of sympathetically-cooled xenon ions, and different numbers of laser-cooled calcium ions, over a range of RF and endcap voltages. The range of conditions under which crystals were simulated was selected to both indicate the experimental conditions which would yield more accurate estimates of $N_{\mathrm{Xe}^+,0}$, and to estimate the sensitivity of the typical operating conditions ($V_{RF,0} = 150$ V, $V_{end} = 4$ V) to the number of xenon ions sympathetically cooled into the crystal.

The parameter chosen to characterise the Coulomb crystal morphology is the aspect ratio, a, defined as the ratio of the length L of the fluorescing component of the Coulomb crystal to its width, w:

$$a = \frac{L}{w} \tag{5.10}$$

This parameter can be extracted from experimental crystal images without requiring knowledge of the image scale, allowing a straightforward comparison between theory and experiment. The length and width of the crystal are determined by fitting a box around simulated images, as illustrated in Fig. 5.8.

The results of this study are shown in Fig. 5.9. The plots on the left-hand side (A,C,E) show the variation of the aspect ratio as a function of the number of sympathetically-cooled xenon ions in the crystal. The plots show how the aspect ratio

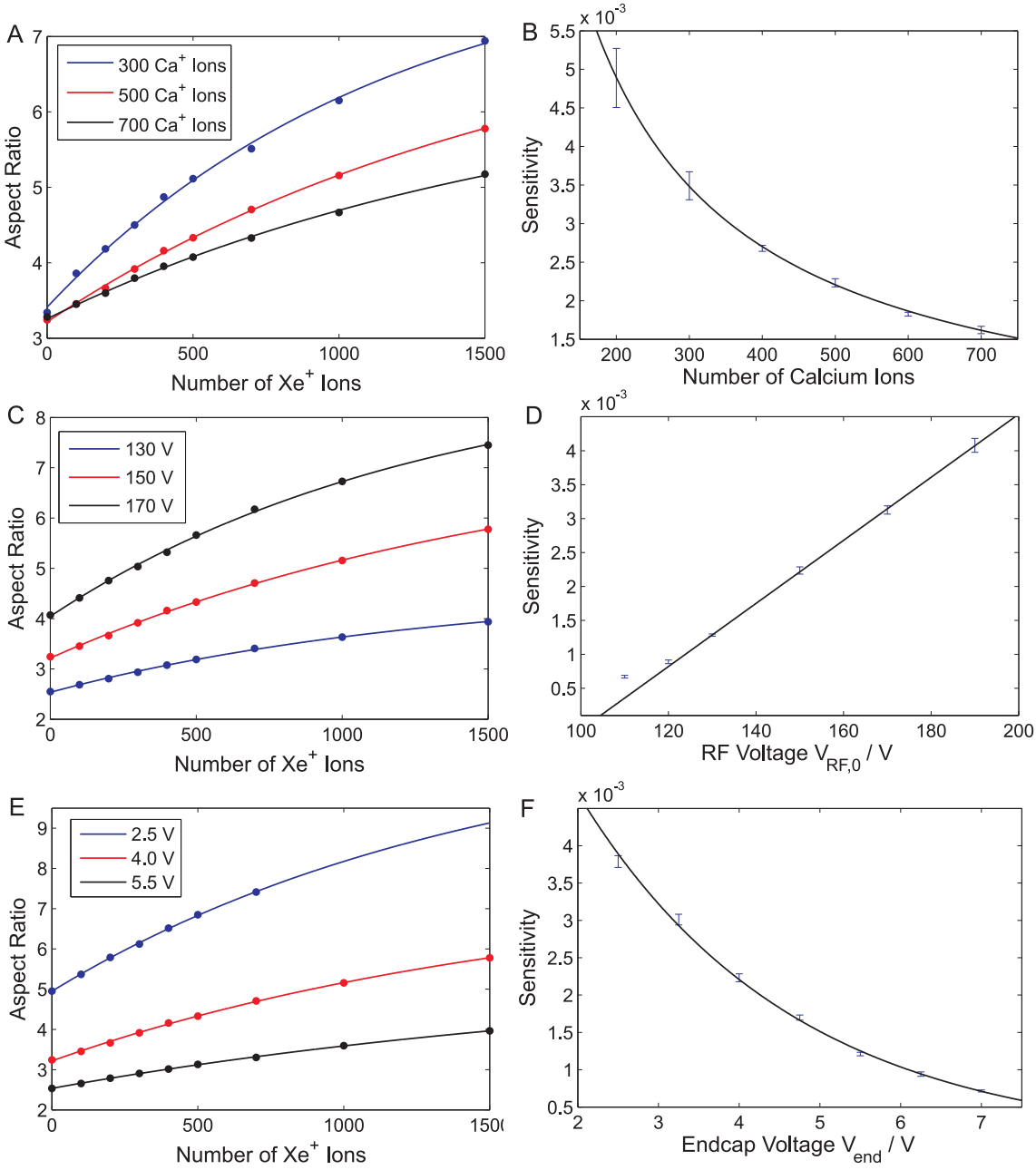


Figure 5.9: (A,C,E): Aspect ratio as a function of the number of Xe^+ ions for (A) varying numbers of $^{40}Ca^+$ ions, (C) varying RF voltage and (E) varying endcap voltage. (B,D,F): Sensitivity (defined as the gradient) of the aspect ratio in the linear region of 500 or fewer Xe^+ ions as a function of (A) the number of $^{40}Ca^+$ ions, (B) $V_{RF,0}$ and (C) V_{end}. When not the variable of interest, $N_{Ca^+} = 500$, $V_{RF,0} = 150$ V and $V_{end} = 4$ V. The fitting functions shown as black lines in (B,D,F) are those of equations 5.13, 5.14 and 5.15.

varies with the number of calcium ions, N_{Ca^+}, the RF voltage, and the endcap voltage. The sensitivity of the aspect ratio to the number of xenon ions added to the crystal, N_{Xe^+}, can be interpreted as the gradient of this function for a given set of experimental parameters. An exponential growth function containing three free parameters of the form:

$$a = c_1 + c_2(1 - e^{-c_3 N_{Xe^+}}) \tag{5.11}$$

is found to approximate the function well. This equation implies that there is a linear relationship between the aspect ratio and N_{Xe^+}, for small values of N_{Xe^+}. This regime corresponds approximately to $N_{Xe^+} < 500$. This is within the expected experimental range, and so the sensitivity S in panels (B,D,F) of Fig. 5.9 is computed by fitting the function in this range to a straight line:

$$a = a_0 + SN_{Xe^+} \tag{5.12}$$

where a_0 is the aspect ratio of the pure calcium Coulomb crystal. The error bars shown correspond to the standard error in the gradient of the least squares regression line [151], and arise due to human error in the fitting procedure.

As the number of calcium ions increases, the sensitivity of the aspect ratio to N_{Xe^+} decreases. This is in line with previous experimental work on bicomponent Coulomb crystals by Hornekaer *et al.* [269]. They observed that, in a crystal comprising two directly laser-cooled species $^{24}Mg^+$ and $^{40}Ca^+$, the ratio of the maximal radial distance from the z-axis of lighter ions to that of the heavier ions, r_{Mg^+}/r_{Ca^+} was constant, being independent of the trap endcap voltage. Assuming this is also approximately true as the number of ions is varied (and can be applied to bicomponent crystals containing Ca^+ and Xe^+), as the number of calcium ions increases, so will the radial distance of the outermost calcium ions. In order to keep the ratio r_{Ca^+}/r_{Xe^+} constant, r_{Xe^+} must increase. This means the xenon ions are further away from the laser cooled ions,

resulting in a weaker Coulombic interaction between the calcium and xenon ions. As shown in Fig. 5.9B, the sensitivity calculations for $V_{end} = 4$ V and $V_{RF,0} = 150$ V can be fit to:

$$S(N_{\mathrm{Ca}^+}) = \frac{1}{0.83N_{\mathrm{Ca}^+} + 38.4} \tag{5.13}$$

As the RF voltage of the ion trap increases, the RF trapping potential increases. This increases the number density of ions in the trap (see equation 4.19), bringing the calcium and xenon ions closer together. This increases the Coulombic force that each xenon ion exerts on the calcium ions. For $V_{RF,0} \geq 130$ V, $N_{\mathrm{Ca}^+} = 500$ and $V_{end} = 4$ V, the sensitivity is found to scale linearly with the trapping voltage, as shown in Fig. 5.9D:

$$S(V_{RF,0}) = 10^{-3}(0.0465V_{RF,0} - 4.76) \tag{5.14}$$

As the endcap voltage increases, the potential along the z-axis also increases. This causes an axial compression of the crystal, reducing the aspect ratio. The increase in the contribution of the axial potential to the total potential means that a higher Coulomb potential is required to see radial compression and axial elongation. Hence the sensitivity of the aspect ratio to the number of xenon ions is reduced. The sensitivity for $N_{\mathrm{Ca}^+} = 500$ and $V_{RF,0} = 150$ V has been fitted to an exponential decay function:

$$S(V_{end}) = e^{-(0.38V_{end}+4.6)} \tag{5.15}$$

The simulations suggest that the highest sensitivity to the number of xenon ions can be obtained with a large RF voltage, low numbers of laser cooled calcium ions and a low endcap voltage. However, a high RF voltage induces additional micromotion heating in the Coulomb crystal, and small Coulomb crystals cannot sympathetically cool as many Xe^+ ions as large crystals. A low endcap voltage might be an advantage, as it will show increased sensitivity to the formation of the dark core (comprised

of lightweight, dark ions). From these conclusions, the future experimental strategy for accurately determining the number of xenon ions will involve the trapping of a moderate-sized crystal ($N_{Ca^+} \approx 300$), followed by the loading of xenon ions at a high RF voltage (such as 190 V) and low endcap voltage of around 2.5 V. Before admitting ND_3 to initiate the reaction, the RF voltage would be lowered to 150 V, to reduce the micromotion heating, thus generating a colder, sharper crystal image.

There are several improvements that can be made to this study. The simulations could be extended to run on a true 3-dimensional grid of values of N_{Ca^+}, V_{end} and $V_{RF,0}$, to empirically create a multi-variable interpolation function that can convert an aspect ratio directly into a number of xenon ions for a given set of experimental parameters. Secondly, the errors in the sensitivity function increase as the sensitivity increases. This is due to the larger degree of radial compression that is induced when more xenon ions are added. This reduces the crystal width w, magnifying small errors in the manual fitting of simulated images. The errors could be significantly reduced by implementing an automated method of crystal fitting, which is currently being developed, based upon the intensity cross section in the radial and axial directions (see Fig. 4.11). The study could also be generalised for different ionic species by looking at the variation of sensitivity with the mass of the sympathetically cooled ion.

It should be noted that there may be discontinuity in the trends observed in this model when the heavy ion mass is reduced sufficiently such that it crystallises, which Xe^+ does not.

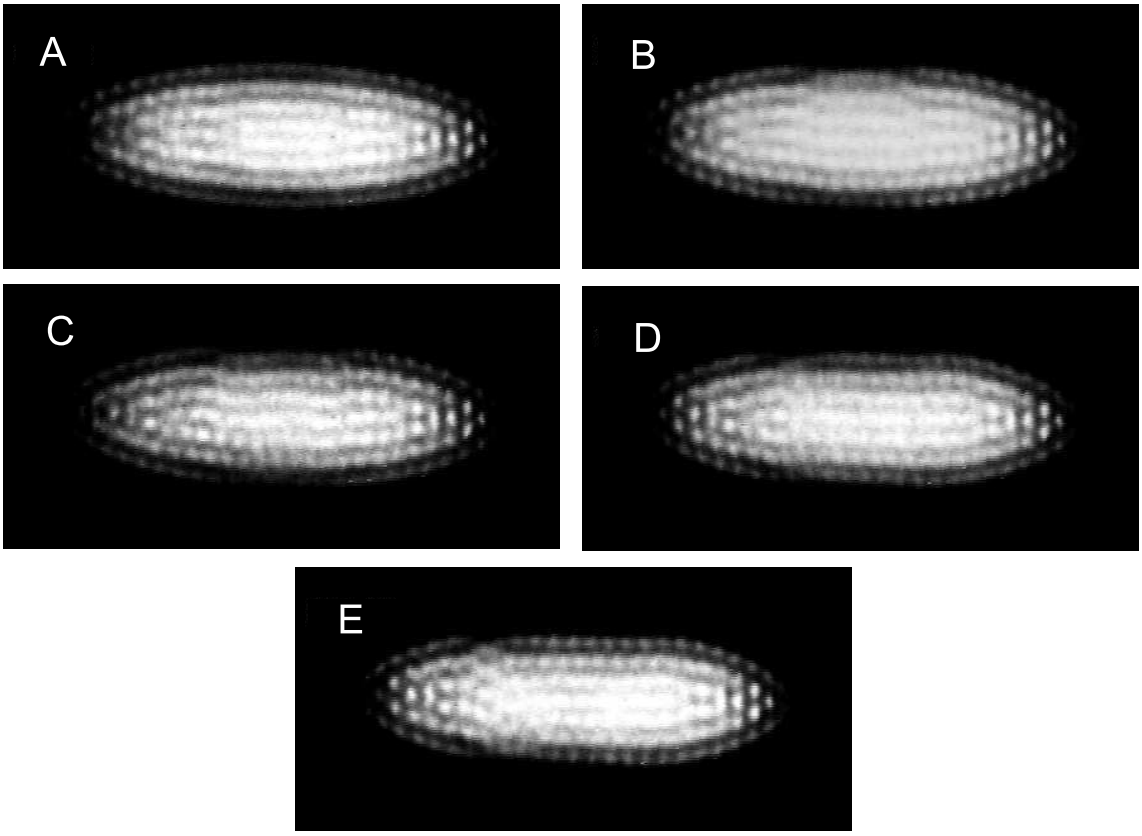


Figure 5.10: Coulomb crystals consisting of Ca^+ and Xe^+ ions. The crystal is loaded over a long period of time, and no dark core is formed. The images are taken with respect to the start of xenon loading at (A) $t = 0$, (B) $t = 60$ s, (C) $t = 230$ s, (D) $t = 500$ s and (E) $t = 1000$ s.

5.2.4 Reaction of Guided ND_3 with Sympathetically-Cooled Xe^+

Background Reaction Rate

Before any chemical reactions were performed, Coulomb crystals consisting of Ca^+ and Xe^+ ions were produced and stored in the ion trap for an extended period of time to observe the background reaction rate with residual gases in the ion trap chamber. Experimental images from this experiment are shown in Fig. 5.10. In this experiment, wavelength drifts led to a low rate of xenon loading, and xenon was slowly loaded over a period of approximately 8 minutes. These images show that, with the experimental techniques described in Chapter 4 to prepare the ion trap chamber for experimental work, there is a negligible dark core formation, hence a negligible background reaction rate, to produce ions with masses lower than 40 over the expected experimental timescales. As shown later, the reaction of Xe^+ to form ions with masses larger than 40 cannot be ruled out.

Guided ND_3 Reaction Results

The progress of the chemical reaction between ammonia molecules (guided through the Stark decelerator with the electrodes at ± 8 kV) and sympathetically cooled xenon ions has been examined. A selection of experimental images and the corresponding simulated images are shown in Fig. 5.11.

An initially pure calcium crystal is fitted to a simulation to determine the number of calcium ions present. The bicomponent crystal that results from Xe^+ loading is subsequently simulated (Fig. 5.11B), enabling an estimation of the initial number of xenon ions. Tricomponent crystals are then simulated for a range of numbers of Xe^+ and ND_3^+ ions (Fig. 5.11C and Fig. 5.11D). Individual frames in the experimental video (monitoring the reaction progress as a function of time) are matched up with

these simulations. An estimate of the error is made using the range of times that correspond to the experimental video frames that produce good matches with simulated images for given numbers of Xe^+ and ND_3^+ ions. Although expressed as an error in the time domain, the error bars arise due to the uncertainties in determining the exact number of ND_3^+ ions in each experimental image. As a result, the errorbars that appear in Fig. 5.12 are oriented along the x-axis.

The experimental images are not as sharp or well-defined as the simulated images. This arises from the sympathetic cooling of Xe^+, which temporarily raises the temperature of the Coulomb crystal. In principle, the aspect ratio of the experimental Coulomb crystal could be calculated, and equation 5.13 used to compute the number of xenon ions. Unfortunately, asymmetry in the trapping potential means that the Coulomb crystal is asymmetric, appearing to have a smaller width nearer the left hand side of the image, where the cooling lasers first make contact with the crystal. The presence of dark calcium ions (and potentially dark impurities) in the experimental image make an accurate determination of the length of the crystal difficult. For the purposes of this thesis, it is assumed that the dark ions are non-fluorescing calcium ions. Although it is possible that light impurity ions of indeterminate identity might be sympathetically-cooled into the Coulomb crystal during the xenon ionisation process, repeated loading cycles indicate that very few, if any, ions are loaded this way.

The uncertainty in estimating N_{Xe^+} can be illustrated by considering the aspect ratio of the crystal. Manual fitting of the experimental image suggests that $a = 3.87 \pm 0.15$, which corresponds to $N_{Xe^+} = 285 \pm 75$. When comparing the image in Fig. 5.11B with simulation, the best fit is in fact just outside of this range, $N_{Xe^+} \approx 375$, although the uncertainty in this manually fit parameter is large. Simulated tricomponent crystals were generated assuming an initial value of $N_{Xe^+} = 375$ (although the shape of the dark core, hence the number of ND_3^+ ions in each simulation, is quite insensitive to this). The error in estimating the number of ND_3^+ ions is much lower

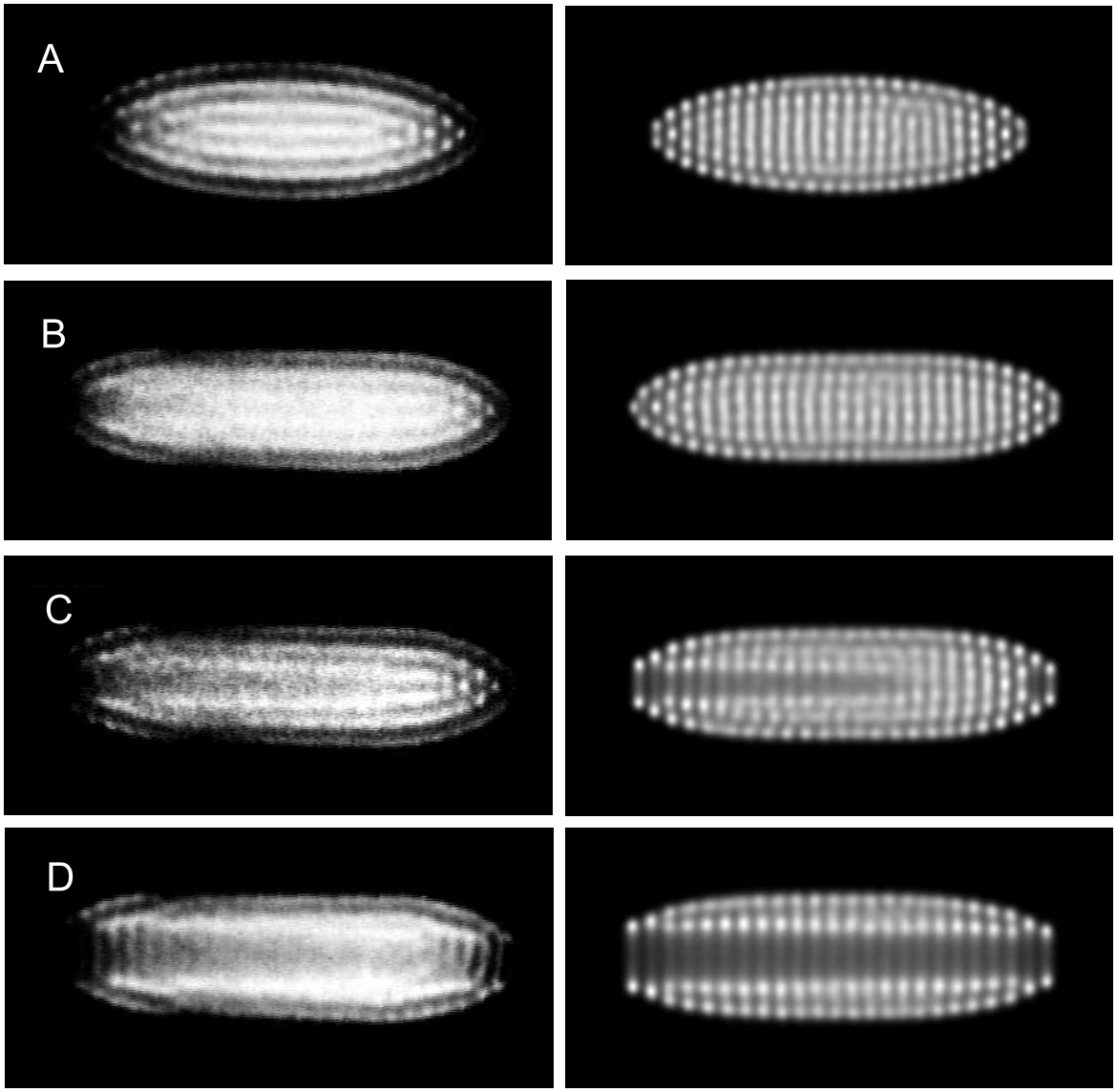


Figure 5.11: Experimental (left) and simulated (right) images of a series of Coulomb crystals, recorded over the course of a reaction between guided ND_3 and trapped Xe^+. The images correspond to: (A) immediately after calcium loading $N_{Ca^+} = 550$; (B) immediately after xenon loading, $N_{Ca^+} = 550$, $N_{Xe^+} = 375$; (C) $t = 12.9 \pm 1.0$ s after shutter opened, $N_{Ca^+} = 550$, $N_{Xe^+} = 355$, $N_{ND_3^+} = 20$; (D) $t = 108.8 \pm 6.5$ s after shutter opened, $N_{Ca^+} = 550$, $N_{Xe^+} = 275$, $N_{ND_3^+} = 100$. Operating voltages were $V_{RF,0} = 150$ V and $V_{end} = 4$ V. The cooling lasers are propagated from left to right. The fits are made to the shape of the Coulomb crystal only. The temperature of the Coulomb crystal will be significantly lower than the translational temperature of the guided molecular beam, so is not considered here.

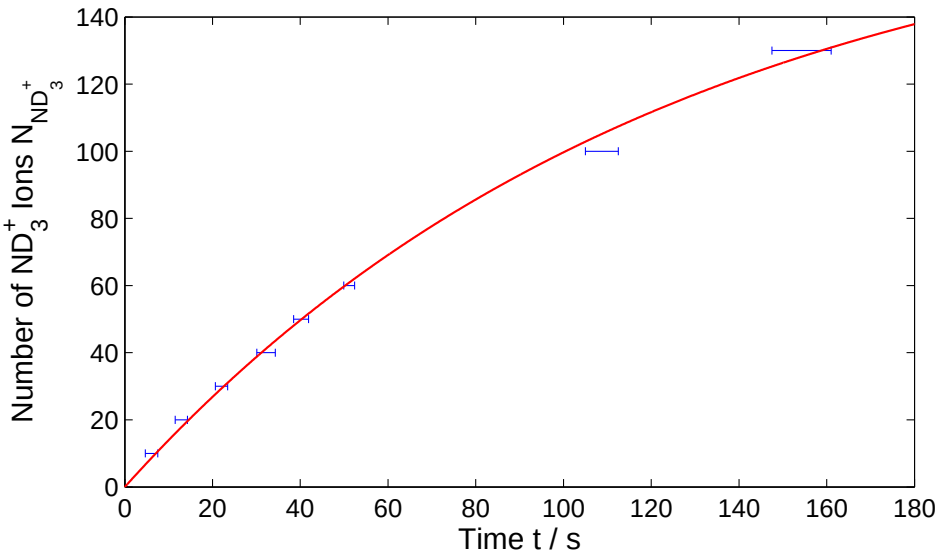


Figure 5.12: Experimentally observed increase in the number of ND_3^+ ions in the Coulomb crystal as a function of time. The data are fit to the exponential growth function of Equation 5.9, where both N_{Xe^+} and k_1 are treated as free parameters.

because of the much clearer appearance of the dark core.

The number of ND_3^+ ions present in the Coulomb crystal as a function of time is shown in Fig. 5.12. This data was fit to a function of the form of equation 5.9 using non-linear least squares fitting [151]. Both the initial number of xenon ions and the pseudo-first order rate constant were treated as free parameters. Fitting the data indicates that $N_{Xe^+,0} = (180 \pm 27)$ and $k_1 = (8.1 \pm 1.5) \times 10^{-3}$ s^{-1}. In order to determine the bimolecular rate constant k_2, it would be necessary to calibrate the density of the ND_3 molecular beam. In previous work with a bent electrostatic guide and an effusive molecular beam, this was done by placing an RGA at the position of the ion trap in a separate experiment [136]. This was attempted with the Stark decelerator, but the RGA did not have a sufficiently fast response time to be able to calibrate the density from the pulsed valve source that was used. Nevertheless, assuming a guided beam density of 10^9 molecules cm^{-3} [270], and reducing this by a factor of 10^2 due to the duty cycle of the pulsed valve (molecules are only present in the vicinity of the

Coulomb crystal for ≈ 1 ms every 100 ms), a value of $k_2 = 8 \times 10^{-10}$ molecules^{-1} cm^3 s^{-1} is obtained. This is reasonable consistent with the literature values. Although it may be difficult to obtain accurate absolute rate constants from the methods used in this thesis, interesting features will still be observable in relative rate constants, which can be found.

This initial number of xenon ions, 180 ± 27, is much lower than suggested by the simulated fits to experimental images. If there were such a small amount of xenon, the edge of the Coulomb crystal would become significantly less flat once 100 Xe^+ ions had reacted away. As inspection of Fig. 5.11 clearly illustrates, the flatness of the edge of the crystal is barely changing over the course of the reaction. This can be explained by the presence of a second reaction, between Xe^+ and a contaminant in the ion trap chamber. If this contaminant were heavier than calcium, and lighter than xenon, the outside edge of the Coulomb crystal would appear to be relatively unchanged with only a few dark impurity ions, despite a large loss of Xe^+ ions. If the reaction rate were comparable with that between Xe^+ ions and ND_3, this would leave an effective number of around 180 xenon ions available for reaction with ND_3. The most likely candidates for such a reaction are hydrocarbon molecules in the pump oil from the rotary pumps. Further experimental measurements are planned to test this hypothesis. These tend to have ionisation energies in the region of 10-12 eV [271], and hence can undergo charge exchange with Xe^+ ions.

It is clear that the largest uncertainty in the experiment lies in evaluating the initial number of xenon ions in the bicomponent Coulomb crystal. The experimental image is asymmetric and blurred. The asymmetry is a result both of imperfections in the ion trap electrodes, and unidirectional cooling of the Coulomb crystal. Asymmetry due to the electrodes can only be removed by constructing a new trap. This asymmetry could be reduced by installing a retroreflective mirror, to allow for laser cooling from two counterpropagating directions. The image becomes blurred during the process

of sympathetic cooling, where the calcium ions undergo heating. Allowing a longer cooling time than the ≈ 20 s in the experiments reported here should therefore reduce this blurring. Using a long exposure time for the image (≈ 10 s) will also make the resulting crystal images sharper.

It is also possible to record images of a Coulomb crystal at several different trap voltages before beginning an experiment. This will give multiple images that can be analysed to give a better estimate of the initial number of xenon ions.

5.2.5 Comparison With the Dark Core Volume Analysis

A comparison between the non-linear least squares fit (from Fig. 5.12) attained from simulations of the experimental data and the dark core volume analysis method outlined in section 4.5.2 is shown in Fig. 5.13. The computed volume shown is corrected for the small initial dark core volume, arising from background ions and dark calcium ions. No other parameters have been rescaled.

There is good agreement between the two methods at early times ($t < 50$ s) and at late times ($t > 100$ s), and the overall trend is reproduced in both plots. However, there is an apparent deviation from the exponential growth model between these two time regimes. This is most likely caused by instabilities in the primary cooling (397 nm) diode laser wavelength; the repumping (866 nm) transition is power broadened and resonant, so is less sensitive to wavelength drift over the time scale of the experiment. Variation in the 397 nm cooling laser wavelength with time causes both the crystal temperature and the fluorescence intensity to vary. Both of these can influence the fluorescence intensity cross-section, affecting the calculation of the dark core volume. For the images recorded in this thesis, the diode laser wavelengths were manually adjusted during the course of the reaction to counteract the wavelength drift. This has since been addressed: a program now automatically stabilises the wavelength

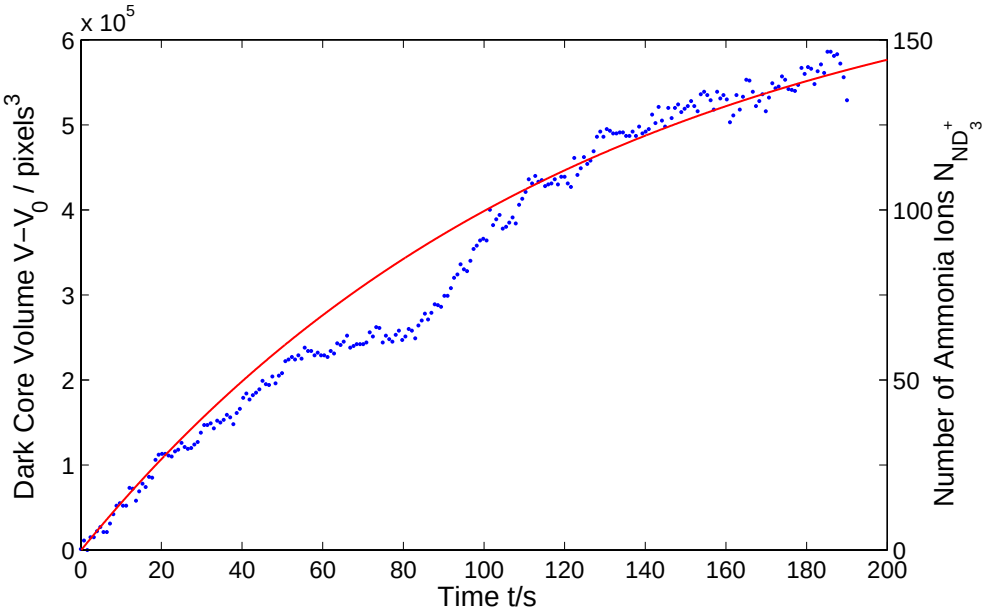


Figure 5.13: Comparison of the dark core volume, computed using the method of section 4.5.2 and the non-linear least squares fit described in section 5.2.4. The volume stated is calculated relative to the initial core volume from background dark ions, V_0.

utilising feedback directly from the wavemeter.

With the wavelength stabilisation program, the dark core volume is likely to be a good model for the number of ND_3^+ ions in the Coulomb crystal, with the same pseudo first order rate constant in both cases. Although more data is required for accurate calibrations, this method is very promising and should facilitate the analysis of large amounts of data quickly and self-consistently.

5.3 Conclusions and Outlook

In this chapter, significant progress has been reported towards the realisation of studying state-selected chemical reactions using a combined apparatus, consisting of a Stark decelerator and a linear Paul ion trap. The background-free reaction between a guided, pulsed molecular beam of ND_3 molecules and trapped, sympathetically-cooled xenon ions has been demonstrated. Progress has been made towards more accurately de-

termining the initial number of calcium and xenon ions present at the start of the reaction. The data have been analysed, and been shown to follow the exponential growth function expected of pseudo first order kinetics. It has also been demonstrated that, with some experimental improvements, the change in volume of the dark core as a function of time will likely model the change in the number of ND_3^+ ions in the crystal, allowing for the rapid, self-consistent analysis of experimental data sets. Several improvements in experimental methodology are also being implemented as a result of the work in this thesis.

The simulated fitting of the aspect ratio can also be improved, by using computational methods to calculate the aspect ratio rather than manually fitting the images. In particular, as the sensitivity of the aspect ratio to the number of xenon ions increases, the error in computing the sensitivity will not correspondingly increase. This might also allow for a generalisation of the method to ions with different masses. In the long term, after sufficient experimental benchmarking, this could become a powerful method to automate the evaluation of the number of calcium ions and heavy ions in an experimental bicomponent Coulomb crystal in real time. This would facilitate more consistent loading of a crystal, with reproducible ion numbers.

The observation that the fitted number of Xe^+ ions for the reaction is significantly lower than that derived from both simulations and the aspect ratio implies that there are heavy impurity ions in the Coulomb crystal. These might be ionised at the same time as the xenon atoms, or they might be formed in a secondary reaction process. These ions could potentially be identified by direct ejection from the ion trap into the time-of-flight tube and onto MCPs for detection. This should also enable a better estimate of the initial number of sympathetically-cooled Xe^+ ions to be made (using the relative total signal for all known xenon isotope masses compared to the Ca^+ signal, as the number of calcium ions can be accurately established from simulations). Whilst it is not currently possible to eject the trapped ions using the sinusoidal RF ion

trap, methodology is being developed in the Oxford group to develop a square-wave digital RF field, based on preliminary work by Drewsen and coworkers [272], which will facilitate ion ejection and subsequent detection.

While it is not currently possible to determine the absolute number density of ND_3 molecules at the location of the ion trap in the current experiment, only the relative number density is needed to observe the energy dependence of the rate constant. The immediate next step is to confirm that the integrated areas of the guided time-of-flight spectra introduced in section 5.2.1 are indeed directly proportional to the density of ND_3. This can be done by studying reactions at a range of guiding voltages, and confirming that the pseudo first order rate constant scales linearly with the integrated area. A preliminary set of data recorded for a set of different guiding voltages is presented in Appendix A. These show an increase in rate with guiding voltage, but were recorded under conditions of malfunctioning of the shutter, hence a detailed analysis was not carried out.

After the density calibration, the reaction between Stark decelerated ND_3 and sympathetically-cooled xenon can be studied. The relative number density of ammonia can be evaluated by considering either the integrated area of the decelerated peak or the intensities of the five peaks in the (2+1) REMPI spectrum (Fig. 5.6). The collision energy dependence of the rate constant can then be determined by changing the switching phase angle of the decelerator, ϕ_0, and hence the final velocity of the decelerated beam.

Chapter 6

Conclusions and Further Work

6.1 Summary

In this thesis, the first example of an experimental apparatus combining a linear Paul ion trap and a Stark decelerator beamline has been demonstrated. This represents a significant development beyond experiments that have been previously reported, such as the combination of a bent electrostatic velocity selector with an ion trap.

Unlike many other sources of cold molecular beams, the Stark decelerator has been demonstrated to produce cold ND_3 molecules primarily in a single quantum state ($|j, mk\rangle = |1, -1\rangle$ state), and with a tunable final velocity, determined by the switching sequence of the inhomogeneous electric fields. The free-flight of molecules between the end of the decelerator and the ion trap, and the large proportion of undecelerated molecules present along the molecular beam propagation axis, limits the practical use of the Stark decelerator on its own. A set of beamline components have been introduced to counter these issues. Their performance has been demonstrated experimentally and interpreted using a set of custom-written molecular dynamics simulation programs. Free-flight reduces the velocity resolution of the molecular beam, and a molecular buncher was introduced to counter this. The free-flight also reduces the

final number density of molecules, due to the transverse divergence of the molecular beam. Two hexapoles, one before and one after the buncher, were demonstrated to provide excellent molecular focussing, optimising the number of cold molecules that enter the ion trap. A fast opening shutter has also been demonstrated to block the molecules that are not decelerated from entering the ion trap chamber. These extra components have made the Stark decelerator into a useful source of cold, neutral molecules for studying collision-energy dependent dynamics at low temperatures.

The sympathetic cooling and stable storage of singly charged xenon cations by laser-cooled singly charged calcium-40 cations within a linear Paul ion trap has also been demonstrated. This was initially complicated by a rapid reaction with an unknown contaminant of low-mass. This contamination problem was mitigated by a combination of: installation of a nitrogen cold finger into the ion trap chamber; baking the ion trap chamber for a longer period of time at a higher temperature; and installation of a new leak valve. The experimental setup has been further improved by the implementation of fibre-optic coupling of the diode lasers employed in the laser cooling process. This produces a single-mode, Gaussian-profile beam, increasing the laser cooling efficiency.

This combination of the Stark decelerator and the ion trap will soon enable the study of collision-energy-tunable, state-selected ion-molecule reactions at low temperatures. In the experiments discussed in Chapter 5, the Stark decelerator was used as an electrostatic guide to produce a molecular beam that was shown to react with sympathetically-cooled Xe^+ ions. The kinetics of this reaction were evaluated both by comparison of experimental images with molecular dynamics simulations, and by using a new image analysis technique to evaluate the volume occupied by the ND_3^+ ions. The greatest source of error in these experiments was shown to be the estimation of the initial number of Xe^+ ions present in the Coulomb crystal. This uncertainty was explored by examining the effect of the number of xenon ions on the observed aspect

ratio of the fluorescing calcium component of the Coulomb crystal over a range of experimental conditions, using molecular dynamics simulations. This has since stimulated work towards a computer-based analysis method to both increase the accuracy with which the number of heavy ions in the Coulomb crystal is established, and to be able to compute this in real time during an experiment.

As well as the experimental developments, the theory of the capture mechanism for "fast" chemical reactions involving an ion and a neutral molecule has been developed further. In particular, the temperature at which the classically calculated statistical rate constant and its quantum mechanical counterpart diverge from each other has been elucidated for both the Langevin potential and the ion-dipole potential, applied to closed shell and open shell molecules. Although this temperature is currently beyond the range of current experimental techniques for studying ion-molecule reactions, it has been predicted that the highest quantum-classical divergence temperatures are obtained for the reaction of ions with non-dipolar and (ideally) non-quadrupolar neutral molecules. Current progress towards frequency chirped optical Stark deceleration schemes for non-dipolar molecules [62] may make this a reality soon.

6.2 Improvements and Future Work

There are several ways in which the laser cooling and ion trapping arrangement could be further improved. At the present time, laser-cooling is performed only in a single direction. The asymmetric radiation pressure along the z-axis causes significant asymmetry in the experimental images. This could be overcome by inserting a retroreflecting mirror at the end of the current diode laser beam path, to achieve laser cooling in both propagation directions along the z-axis. The temperature of the Coulomb crystals might be further reduced by the addition of an additional 397 nm beam (driving the main $^{40}Ca^{+}$ cooling transition) in the radial direction. The efficiency of the laser

cooling process is heavily dependent upon the wavelength of the diode lasers. This naturally drifts over time, causing heating of the Ca^+ ions. Work has recently been completed on devising a wavelength stabilisation program that uses direct feedback from a wavemeter to stabilise the wavelength and to more precisely control the output.

The shutter in the Stark decelerator beamline is a weak point in the experiment. A more robust method of separating the decelerated molecules from the undecelerated molecules might be to use an electric field analogue of the Zeeman deflector used by Narevicius and coworkers [12]. This could be utilised in such a way that only the decelerated molecules are deflected into the ion trap chamber, although this would give the limitation that the undecelerated molecular beam could not be detected in the ion trap.

At this time, the uncertainty in computing the initial number of Xe^+ ions that are sympathetically cooled into the Coulomb crystal is a large source of error. The simulation study of section 5.2.3 suggests that the aspect ratio can be used as a method of estimating the number of Xe^+ ions, and the sensitivity of this method can be optimised by using low endcap and high RF trapping voltages, as well as smaller Coulomb crystals. The computation of the aspect ratio from experimental images is in the process of being automated. This could be combined with an empirical interpolation formula obtained using the results of MD simulations to give an estimate of the number of heavy, dark ions (Xe^+ or otherwise) during the ionisation process. This would enable consistent loading, taking into account natural ionisation laser wavelength and power drifts.

The next step to realising the goal of studying a fully state-selected, tunable-energy ion-molecule reaction is to ensure that the integrated intensity of the time-of-flight spectrum is directly proportional to the ND_3 number density. This can be done by performing reactions between ND_3 and Xe^+ as a function of guiding voltage, and ensuring that the pseudo-first-order rate constant for the reaction scales linearly

with the integrated intensity of the time-of-flight spectrum. If not, then a calibration factor must be found. After this, the reaction between Xe^+ and decelerated ND_3 can be performed to evaluate the relative rate constant for the reaction as a function of collision energy.

Looking to the future, several interesting experiments could be conceived. The charge-transfer reaction of sympathetically cooled OCS^+ with velocity selected ND_3 has been previously studied [242]. It would be interesting to compare the results of this previous study - conducted using a bent electrostatic quadrupole guide - with reaction rates observed from Stark decelerated ND_3. This would help elucidate the effect of state-selection on a chemical reaction.

The ultimate goal of the Stark decelerator and ion trap apparatus must be the realisation of a fully state-selected reaction involving both a state-selected molecular ion and a state-selected molecule. The work that has been presented in this thesis shows significant progress towards this goal, by enabling the study of a state selected molecule with an atomic ion in a single electronic quantum state.

Appendix A

Supplementary Reaction Data

This appendix presents additional data on the reaction between sympathetically-cooled Xe^+ ions and electrostatically guided ND_3 molecules, as a function of the applied DC guiding voltage. Unfortunately, this attempt was hindered by damage to the fast-opening shutter, which resulted in it remaining predominantly closed throughout the reaction. Nevertheless, these results do illustrate some interesting points about the reaction process, and the Stark decelerator beamline. All of the data in this appendix was recorded using trapping voltages of $V_{end} = 3.5$ V and $V_{RF} = 150$ V; diode laser powers of $P_{397} = 150$ μW and $P_{866} = 4.8$ mW; and ionisation powers of $P_{Ca^+} = 6$ mJ / pulse and $P_{Xe^+} = 450$ μJ / pulse.

A series of experimental images of the multicomponent Coulomb crystals as a function of time after the loading of Xe^+ ions and admission of the ND_3 molecular beam is shown in Figs. A.1, A.2 and A.3 for applied guiding voltages of 5 kV, 7 kV and 8.5 kV respectively. Despite the constant near-closure of the shutter, a slow reaction still takes place. As expected, the rate of reaction - measured by the growth of the dark core - increases significantly when the guiding voltage is increased from 5 kV to 7 kV, and only slightly increases when it is further increased to 8.5 kV, in qualitative agreement with the trends observed in the guided flux measurements of

section 5.2.1. This increase in rate can occur as a larger flux of molecules reach the shutter, and hence can penetrate through the narrow opening. This implies that, in a fully Stark decelerated experiment, there might be a slow "background" reaction caused by the non-decelerated main beam leaking through the "closed" shutter. It is also worth noting that there is likely a minimum flux of decelerated molecules, below which it will not be possible to distinguish the rate constant attributed solely to the decelerated molecules from that of the undecelerated ones.

Another noteworthy feature presented in the following data sets is the relatively rapid loss of trapped ions, compared with the loss rate observed in section 4.5.3. This is particularly clear in the images corresponding to guiding at 5 kV, where the crystal was trapped for over 30 minutes. The crystal visibly reduces in size, and the dark core actually seems to contract at later times, having grown at earlier times, as both Ca^+ and ND_3^+ ions are lost from the crystal. This implies that there are possibly some small imperfections in the trapping potential, arising perhaps from fluctuations in the trap voltages (RF or endcap) or from physical flaws in the trap electrodes.

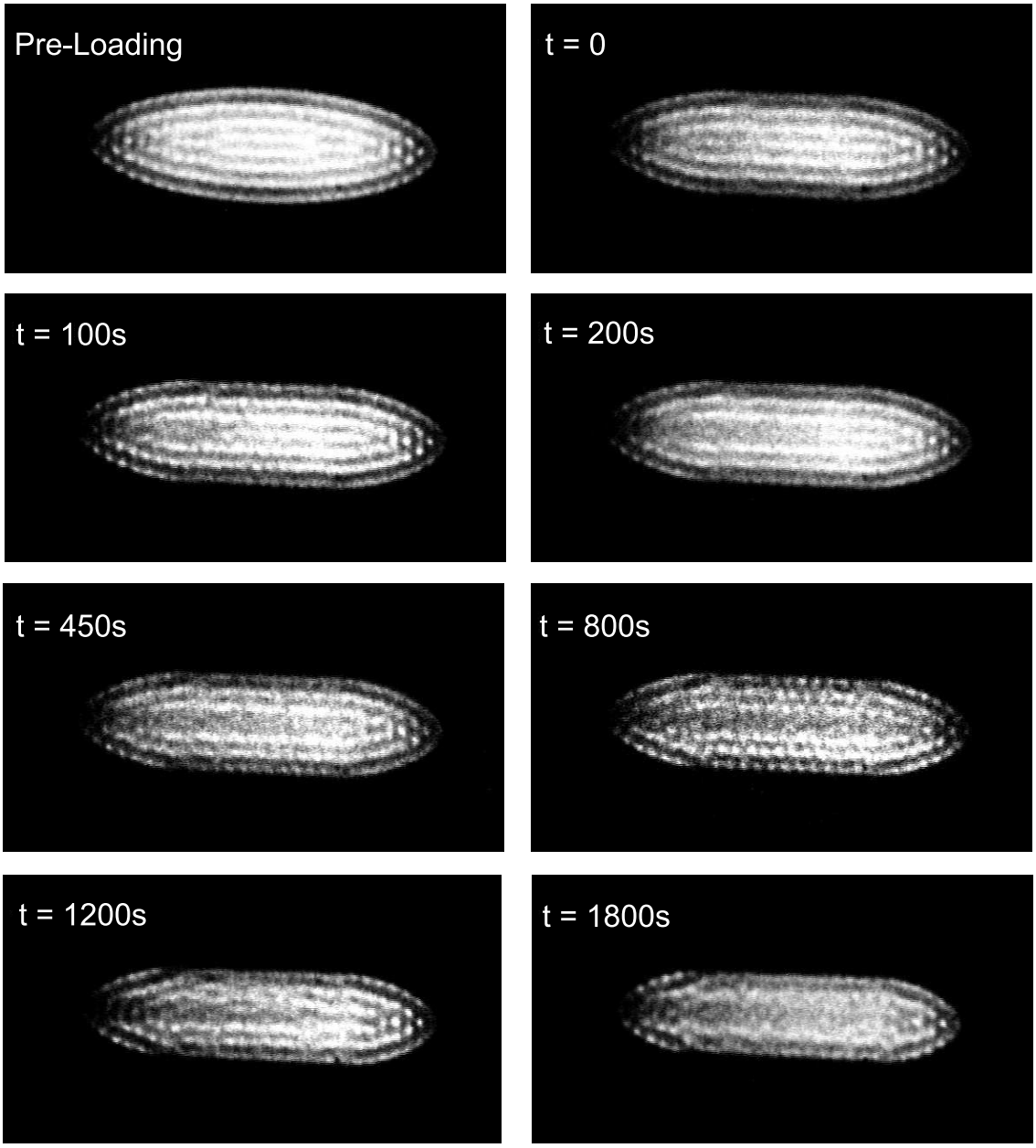


Figure A.1: Experimental images for the reaction between ND_3, guided at 5 kV, and sympathetically cooled Xe^+ ions. The time at which each image was taken with respect to the ionisation of Xe into the Coulomb crystal, t is indicated in each image.

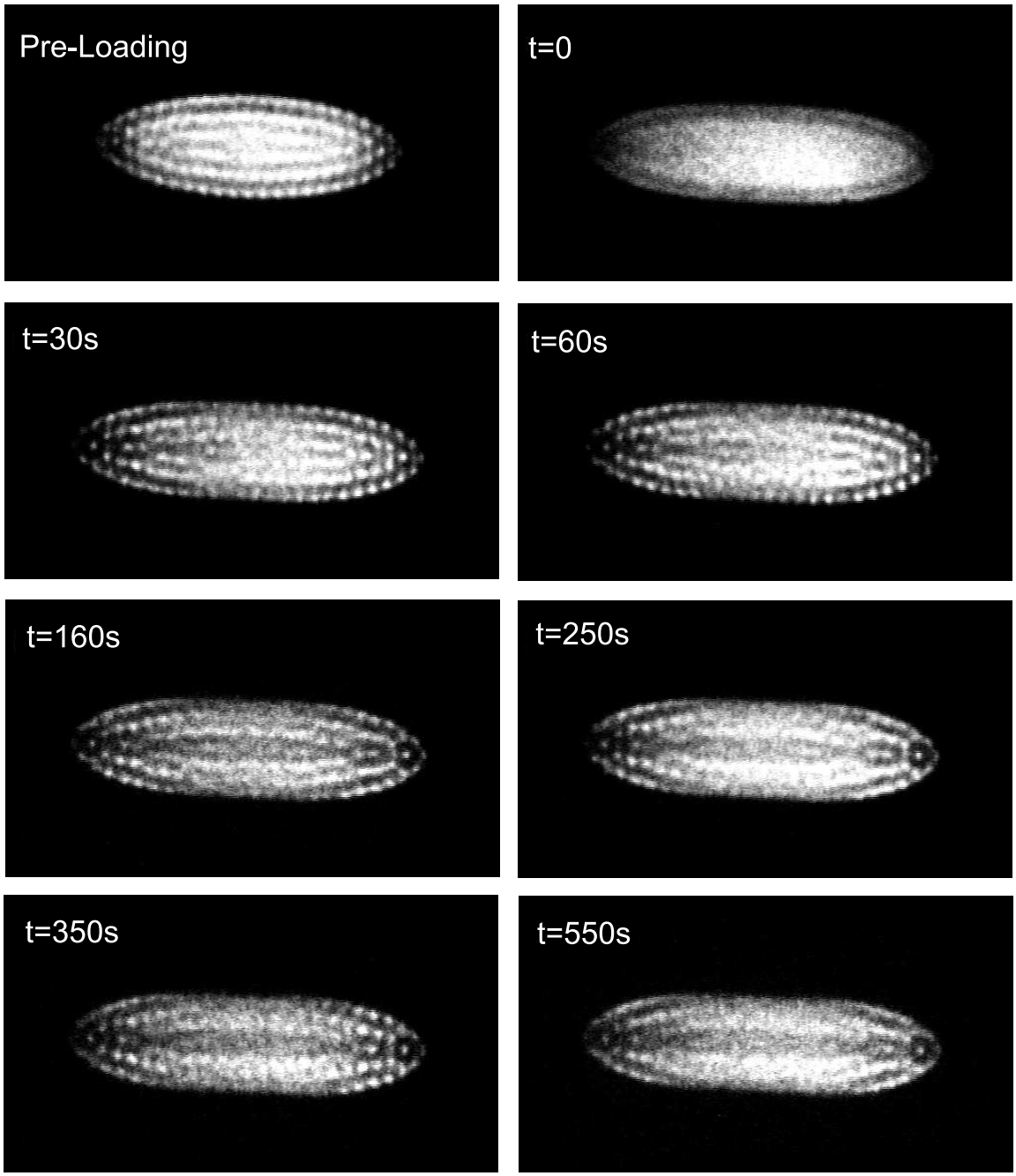


Figure A.2: Experimental images for the reaction between ND_3, guided at 7 kV, and sympathetically cooled Xe^+ ions. The time at which each image was taken with respect to the ionisation of Xe into the Coulomb crystal, t is indicated in each image.

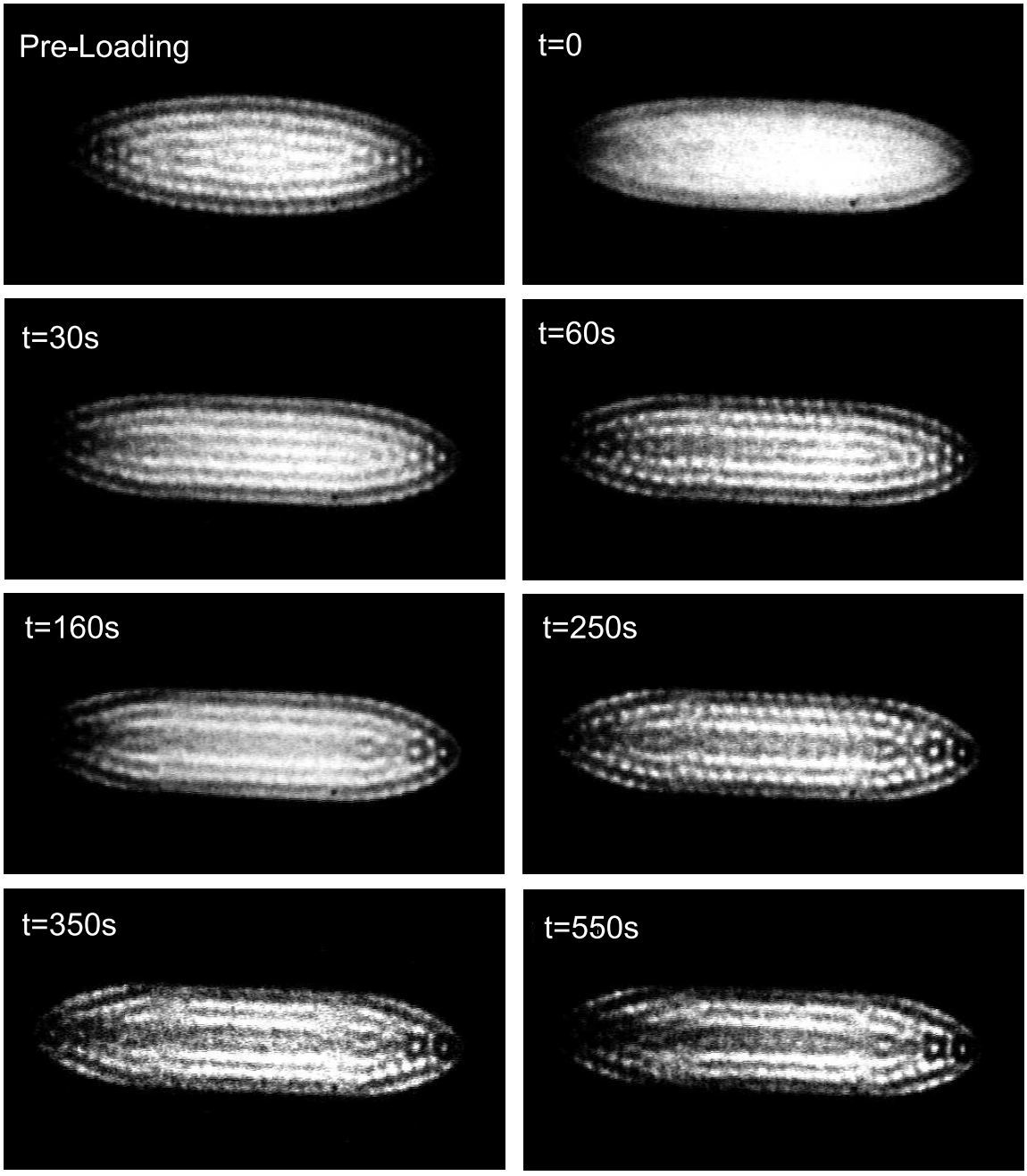


Figure A.3: Experimental images for the reaction between ND_3, guided at 8.5 kV, and sympathetically cooled Xe^+ ions. The time at which each image was taken with respect to the ionisation of Xe into the Coulomb crystal, t is indicated in each image.

References

[1] P. Atkins and J. de Paula. *Atkins' Physical Chemistry, Seventh Edition*. Oxford University Press, Oxford U.K., 2002.

[2] J. Keeler and P. Wothers. *Why Chemical Reactions Happen*. Oxford University Press, Oxford U.K., 2004.

[3] R. P. Wayne. *Chemistry of Atmospheres, Third edition*. Oxford University Press, Oxford U.K., 2000.

[4] S. Chapman. *Mem. Roy. Meteorol. Soc.*, **3**, 103–125, 1930.

[5] R. Sahai and L.-A. Nyman. *Astophys. J.*, **487**, L155–L159, 1997.

[6] T. P. Snow and V. M. Bierbaum. *Annu. Rev. Anal. Chem.*, **1**, 229–259, 2008.

[7] A. G. G. M. Tielens. *Ann. Rev. Astron. Astrophys.*, **46**, 289–337, 2008.

[8] T. Oka. *Proc. Natl. Acad. Sci.*, **103**, 12235–12242, 2006.

[9] D. Smith and N. G. Adams. *J. Chem. Soc. Faraday Trans.*, **2**, 1613–1630, 1989.

[10] D. Leibfried, R. Blatt, C. Monroe, and D. J. Wineland. *Rev. Mod. Phys.*, **75**, 284–324, 2003.

[11] A. Mody, M. Haggerty, J. M. Doyle, and E. Heller. *Phys. Rev. B*, **64**, 085418, 2001.

[12] A. B. Henson, S. Gerstien, Y. Shagam, J. Narevicius, and E. Narevicius. *Science*, **338**, 234–238, 2012.

[13] K.-A. Brickman Soderberg, N. Gemelke, and C. Chin. *New. J. Phys.*, **11**, 055022, 2009.

[14] I. Bloch, J. Dalibard, and S. Nascimbène. *Nature Phys.*, **8**, 267–276, 2012.

[15] D. C. Clary. *Annu. Rev. Phys. Chem.*, **41**, 61–90, 1990.

[16] R. D. Levine. *Molecular Reaction Dynamics*. Cambridge University Press, Cambridge U.K., 2005.

[17] D. Carty, A. Goddard, S. P. K. Kohler, I. R. Sims, and I. W. M. Smith. *J. Phys. Chem. A*, **110**, 3101–3109, 2006.

[18] J. A. Klos, F. Lique, M. H. Alexander, and P. J. Dagdigian. *J. Chem. Phys.*, **129**, 064306, 2008.

[19] R. G. Macdonald and K. Liu. *J. Chem. Phys.*, **93**, 2431–2442, 1990.

[20] M. B. Arfa, B. Lescop, M. Cherid, B. Brunetti, P. Candori, D. Malfatti, S. Falcinelli, and F. Vecchiocattivi. *Chem. Phys. Lett.*, **308**, 71–77, 1999.

[21] P. E. Siska. *Rev. Mod. Phys.*, **65**, 337–412, 1993.

[22] S. Jung, E. Tiemann, and C. Lisdat. *Phys. Rev. A*, **74**, 040701, 2006.

[23] O. Bucicov, M. Nowak, S. Jung, G. Meijer, E. Tiemann, and C. Lisdat. *Eur. Phys. J. D*, **46**, 463–469, 2008.

[24] A. C. Terentis, S. E. Waugh, G. F. Metha, and S. H. Kable. *J. Chem. Phys.*, **108**, 3187–3198, 1998.

[25] S. Willitsch, M. T. Bell, A. D. Gingell, and T. P. Softley. *Phys. Chem. Chem. Phys.*, **10**, 7200–7210, 2008.

[26] A. D. Gingell, M. T. Bell, J. M. Oldham, T. P. SOftley, and J. N. Harvey. *J. Chem. Phys.*, **133**, 194302, 2010.

[27] L. M. C. Janssen, A. van der Avoird, and G. C. Groenenboom. *Phys. Rev. Lett.*, **110**, 063201, 2013.

[28] E. P. Wigner. *Phys. Rev.*, **73**, 1002–1009, 1948.

[29] H. A. Bethe. *Rev. Mod. Phys.*, **9**, 69–244, 1937.

[30] M. T. Cvitas, P. Soldan, J. M. Hutson, P. Honvault, and J. M. Launay. *Phys. Rev. Lett.*, **94**, 200402, 2005.

[31] R. T. Skodje, D. Skouteris, D. E. Manolopoulos, S.-H. Lee, F. Dong, and K. Liu. *J. Chem. Phys.*, **112**, 4536–4552, 2000.

[32] L. D. Carr and J. Ye. *New J. Phys.*, 055009, 2009.

[33] J. D. Miller, R. A. Cline, and D. J. Heinzen. *Phys. Rev. A*, **47**, R4567–R4570, 1993.

[34] E. L. Raab, M. Prentiss, A. Cable, S. Chu, and D. Pritchard. *Phys. Rev. Lett.*, **59**, 2631–2634, 1987.

[35] M. H. Anderson, J. R. Ensher, M. R. Matthews, C. E. Wieman, and E. A. Cornell. *Science*, **269**, 198–201, 1995.

[36] K. M. Jones, E. Tiesinga, P. D. Lett, and P. S. Julienne. *Rev. Mod. Phys.*, **78**, 483–535, 2006.

[37] J. M. Hutson and P. Soldan. *Int. Rev. Phys. Chem.*, **25**, 498–526, 2006.

[38] K.-K. Ni, S. Ospelkaus, M. H. G. de Miranda, A. Pe'er, B. Neyenhuis, J. J. Zirbel, S. Kotochigova, P. S. Julienne, D. S. Jin, and J. Ye. *Science*, **322**, 231–235, 2008.

[39] M. Greiner, C. A. Regal, and D. S. Jin. *Nature*, **426**, 537–540, 2003.

[40] S. Jochim, M. Bartenstein, A. Altmeyer, G. Hendl, S. Riedl, C. Chin, J. Hecker-Denschlag, and R. Grimm. *Science*, **302**, 2101–2103, 2003.

[41] E. A. Donley, N. R. Claussen, S. T. Thompson, and C. E. Wieman. *Nature*, **417**, 529–533, 2002.

[42] D. Wang, J. Qi, M. F. Stone, O. Nikolayeva, H. Wang, B. Hattaway, S. D. Gensemer, P. L. Gould, E. E. Eyler, and W. C. Stwalley. *Phys. Rev. Lett.*, **93**, 243005, 2004.

[43] A.-C. Voight, M. Taglieber, L. Costa, T. Aoki, W. Wieser, T. W. Hänsch, and K. Dieckmann. *Phys. Rev. Lett.*, **102**, 020405, 2009.

[44] S. D. Kraft, P. Staanum, J. Lange, L. Vogel, R. Wester, and M. Weidemüller. *J. Phys. B: At. Mol. Opt. Phys.*, **39**, 993–1000, 2006.

[45] K.-K. Ni, S. Ospelkaus, D. Wang, G. Quéméner, B. Neyenhuis, M. H. G. de Miranda, J. L. Bohn, J. Ye, and D. S. Jin. *Nature*, **464**, 1324–1328, 2010.

[46] M. A. Baranov, M. Dalmonte, G. Pupillo, and P. Zoller. *Chem. Rev.*, **112**, 5012–5061, 2012.

[47] M. Gupta and D. Herschbach. *J. Phys. Chem. A*, **103**, 10670–10673, 1999.

[48] M. Strebel, F. Stienkemeier, and M. Mudrich. *Phys. Rev. A*, **81**, 033409, 2010.

[49] M. Gupta and D. Herschbach. *J. Phys. Chem. A*, **105**, 1626–1637, 2001.

[50] H. L. Bethlem, F. M. H. Cropmverts, R. T. Jongma, S. Y. T. van der Meerakker, and G. Meijer. *Phys. Rev. A.*, **65**, 053416, 2002.

[51] S. A. Meek, H. Conrad, and G. Meijer. *Science*, **324**, 1699–1702, 2009.

[52] H. L. Bethlem, M. R. Tarbutt, J. Küpper, D. Carty, K. Wolfhart, E. A. Hinds, and G. Meijer. *J. Phys. B: At. Mol. Opt. Phys.*, **39**, 263–291, 2006.

[53] S. Y. T. van der Meerakker, N. Vanhaecke, and G. Meijer. *Ann. Rev. Phys. Chem.*, **57**, 159–190, 2006.

[54] X. Wang, M. Kirste, G. Meijer, and S. Y. T. van der Meerakker. *arXiv*, 1301.2136, 2013.

[55] H. L. Bethlam, G. Berden, and G. Meijer. *Phys. Rev. Lett.*, **83**, 1558, 2004.

[56] N. Vanhaecke, U. Meier, M. Andrist, B. H. Meier, and F. Merkt. *Phys. Rev. A*, **75**, 031402, 2007.

[57] E. Narevicius, C. G. Parthey, A. Libson, J. Narevicius, I. Chavez, U. Even, and M. G. Raizen. *New J. Phys.*, **9**, 358, 2007.

[58] A. W. Wiederkehr, M. Motsch, S. D. Hogan, M. Andrist, H. Schmutz, B. Lambillotte, J. A. Agner, and F. Merkt. *J. Chem. Phys.*, **135**, 214202, 2011.

[59] E. Narevicius, A. Libson, C. G. Parthey, I. Chavez, J. Narevicius, U. Even, and M. G. Raizen. *Phys. Rev. A*, **77**, 051401, 2008.

[60] A. I. Bishop, L. Wang, and P. F. Barker. *New J. Phys.*, **12**, 073028, 2010.

[61] R. Fulton, A. I. Bishop, M. N. Shneider, and P. F. Barker. *J. Phys. B: At. Mol. Opt. Phys.*, **39**, 1097–1109, 2006.

[62] N. Coppendale, L. Wang, P. Douglas, and P. F. Barker. *Appl. Phys. B*, **104**, 569–576, 2011.

[63] P. B. Corkum, C. Ellert, M. Mehendale, P. Dietrich, S. Hankin, S. Aseyez, D. Rayner, and D. Villeneuve. *Faraday Discuss.*, **113**, 47–59, 1999.

[64] E. Vliegen, S. D. Hogan, H. Schmutz, and F. Merkt. *Phys. Rev. A*, **76**, 023405, 2007.

[65] S. D. Hogan, P. Allmendinger, H. Saßmannshausen, H. Schmutz, and F.Merkt. *Phys. Rev. A*, **76**, 023405, 2007.

[66] C. Seiler, S. D. Hogan, and F. Merkt. *Phys. Chem. Chem. Phys.*, **13**, 19000–19012, 2011.

[67] S. D. Hogan, C. Seiler, and F. Merkt. *J. Phys. B: At. Mol. Opt. Phys.*, **46**, 045303, 2013.

[68] S. A. Rangwala, T. Junglen, T. Riegler, and P. W. H. Pinkse. *Phys. Rev. A*, **67**, 043406, 2003.

[69] S. Willitsch, M. T. Bell, A. D. Gingell, S. R. Procter, and T. P. Softley. *Phys. Rev. Lett.*, **100**, 043203, 2008.

[70] M. Motsch, L. D. van Buuren, C. Sommer, M. Zeppenfeld, G. Rempe, and P. W. H. Pinkse. *Phys. Rev. A*, **79**, 013405, 2009.

[71] K. Okada, T. Suganuma, T. Furukawa, T. Takayanagi, M. Wada, and H. A. Schuessler. *Phys. Rev. A*, **87**, 043427, 2013.

[72] J. K. Messer and F. C. de Lucia. *Phys. Rev. Lett.*, **53**, 2555–2558, 1984.

[73] J. M. Doyle, B. Friedrich, J. Kim, and D. Patterson. *Phys. Rev. A*, **52**, R2515–R2518, 1995.

[74] J. Kim, B. Friedrich, D. P. Katz, D. Patterson, J. D. Weinstein, R. DeCarvalho, and J. M. Doyle. *Phys. Rev. Lett.*, **78**, 3665–3668, 1997.

[75] W. C. Campbell, E. Tsikata, H. I. Liu, L. D. van Buuren, and J. M. Doyle. *Phys. Rev. Lett.*, **98**, 213001, 2007.

[76] J. D. Weinstein, R. DeCarvalho, T. Guillet, B. Friedrich, and J. M. Doyle. *Nature*, **395**, 148–150, 1998.

[77] N. Brahms, T. V. Tscherbul, P. Zhang, J. Klos, H. R. Sadeghpour, A. Dalgarno, J. M. Doyle, and T. G. Walker. *Phys. Rev. Lett.*, **105**, 033001, 2010.

[78] S. C. Doret, C. B. Connolly, W. Ketterle, and J. M. Doyle. *Phys. Rev. Lett.*, **103**, 103005, 2009.

[79] C. Sommer, L. D. van Buuren, M. Motsch, S. Pohle, J. Bayerl, P. W. H. Pinkse, and G. Rempe. *Faraday Discuss.*, **142**, 203–220, 2009.

[80] L. D. van Buuren, C. Sommer, M. Motsch, S. Pohle, M. Schenk, J. Bayerl, P. W. H. Pinkse, and G. Rempe. *Phys. Rev. Lett.*, **102**, 033001, 2008.

[81] K. E. Strecker and D. W. Chandler. *Phys. Rev. A*, **78**, 063406, 2008.

[82] J. J. Kay, S. Y. T. van der Meerakker, K. E. Strecker, and D. W. Chandler. *Faraday Discuss.*, **142**, 143–154, 2009.

[83] J. J. Kay, J. Klos, M. H. Alexander, K. E. Strecker, and D. W. Chandler. *Phys. Rev. A*, **82**, 032709, 2010.

[84] A. Trottier, E. Wrede, and D. Carty. *Mol. Phys.*, **109**, 725–733, 2011.

[85] W. G. Doherty, M. T. Bell, T. P. Softley, A. Rowland, E. Wrede, and D. Carty. *Phys. Chem. Chem. Phys.*, **13**, 8441–8447, 2011.

[86] E. S. Shuman, J. F. Barry, and D. DeMille. *Nature*, **467**, 820–823, 2010.

[87] J. F. Barry, E. S. Shuman, E. B. Norrgard, and D. DeMille. *Phys. Rev. Lett.*, **108**, 103002, 2012.

[88] J. He, B. Yang, T. Zhang, and J. Wang. *Phys. Scr.*, **84**, 025302, 2011.

[89] J. van Veldhoven. Ph.D. thesis, Fritz-Haber-Institut der Max-Planck-Gesellschaft, Berlin, 2006.

[90] H. L. Bethlem, G. Berden, F. M. H. Cropmvoets, R. T. Jongma, A. J. A. van Roij, and G. Meijer. *Nature*, **406**, 491–494, 2000.

[91] S. Hoekstra, M. Metsälä, P. C. Zieger, L. Scharfenberg, J. J. Gilijamse, G. Meijer, and S. Y. T. van der Meerakker. *Phys. Rev. A*, **76**, 063408, 2007.

[92] M. Kirste, B. G. Sartokov, M. S. Schnell, and G. Meijer. *Phys. Rev. A*, **79**, 051401, 2009.

[93] B. C. Sawyer, B. K. Stuhl, D. Wang, M. Yeo, and J. Ye. *Phys. Rev. Lett.*, **101**, 203203, 2008.

[94] S. D. Hogan, A. W. Wiederkehr, H. Schmutz, and F. Merkt. *Phys. Rev. Lett.*, **101**, 143001, 2008.

[95] B. K. Stuhl, M. T. Hummon, M. Yeo, G. Quéméner, J. L. Bohn, and J. Ye. *Nature*, **492**, 396–400, 2012.

[96] M. T. Hummon, M. Yeo, B. K. Stuhl, A. L. Collopy, Y. Xia, and J. Ye. *Phys. Rev. Lett.*, **110**, 143001, 2013.

[97] M. Zeppenfeld, B. G. U. Englert, R. Glöckner, A. Prehn, M. Mielenz, C. Sommer, L. D. van Buuren, M. Motsch, and G. Rempe. *Nature*, **491**, 570–573, 2012.

[98] C. J. Myatt, E. A. Burt, R. W. Ghrist, E. A. Cornell, and C. E. Wieman. *Phys. Rev. Lett.*, **78**, 586–589, 1997.

[99] F. H. J. Hall, M. Aymar, N. Bouloufa-Maafa, O. Dulieu, and S. Willitsch. *Phys. Rev. Lett.*, **107**, 240202, 2011.

[100] W. G. Rellergert, S. T. Sullivan, S. J. Schowalter, S. Kotochigova, K. Chen, and E. R. Hudson. *Nature*, **495**, 490–494, 2013.

[101] M. Schwartz, O. O. Versolato, A. Windberger, F. R. Brunner, T. Ballance, S. N. Eberle, J. Ullrich, P. O. Schmidt, A. K. Hansen, A. D. Gingell, M. Drewsen, and J. R. Crespo-López-Urrutia. *Rev. Sci. Instrum.*, **83**, 083115, 2012.

[102] Y. Ovchinnikov and G. Marra. *Metrologia*, **48**, 87–100, 2011.

[103] N. Hinkley, J. A. Sherman, N. B. Phillips, M. Schioppo, N. D. Lemke, K. Beloy, M. Pizzocaro, C. W. Oates, and A. D. Ludlow. *arXiv*, 1305.5869, 2013.

[104] J. J. Hudson, D. M. Kara, I. J. Smallman, B. E. Sauer, M. R. Tarbutt, and E. A. Hinds. *Nature*, **473**, 493–496, 2011.

[105] M. R. Tarbutt, J. J. Hudson, B. E. Sauer, and E. A. Hinds. *Faraday Discuss.*, **142**, 37–58, 2009.

[106] H. L. Bethlem and W. Ubachs. *Faraday Discuss.*, **142**, 25–36, 2009.

[107] D. W. Trainor and D. O. Ham. *J. Chem. Phys.*, **58**, 4599–4609, 1973.

[108] H. Böhringer and F. Arnold. *J. Chem. Phys.*, **84**, 1459–1462, 1985.

[109] I. R. Sims and I. W. M. Smith. *Ann. Rev. Phys. Chem.*, **46**, 109–137, 1995.

[110] B. R. Rowe, G. Dupeyrat, J. B. Marquette, and P. Gaucheral. *J. Chem. Phys.*, **80**, 4915–4921, 1984.

[111] I. R. Sims, J.-L. Queffelec, A. Defrance, C. Rebrion-Rowe, D. Travers, P. Bocherel, B. R. Rowe, and I. W. M. Smith. *J. Chem. Phys.*, **100**, 4229–4241, 1993.

[112] I. W. M. Smith. *Low Temperatures and Cold Molecules*. Imperial College Press, London, 2008.

[113] J. J. Gilijamse, S. Hoekstra, S. Y. T. van der Meerakker, G. C. Groenenboom, and G. Meijer. *Science*, **313**, 1617–1620, 2006.

[114] M. Kirste, X. Wang, H. C. Schewe, G. Meijer, K. Liu, A. van der Avoird, L. M. C. Janssen, K. B. Gubbels, G. C. Groenenboom, and S. Y. T. van der Meerakker. *Science*, **338**, 1060–1063, 2006.

[115] S. Y. T. van der Meerakker and G. Meijer. *Faraday Discuss.*, **142**, 113–126, 2009.

[116] S. Knoop, F. Ferlaino, M. Berninger, M. Mark, H.-C. Nägerl, R. Grimm, J. P. D'Incao, and B. D. Esry. *Phys. Rev. Lett.*, **104**, 053201, 2010.

[117] S. Ospelkaus, K.-K. Ni, D. Wang, M. H. G. de Miranda, B. Neyenhuis, G. Quéméner, P. S. Julienne, J. L. Bohn, D. S. Jin, and J. Ye. *Science*, **327**, 853–857, 2010.

[118] M. H. G. de Miranda, A. Chotia, B. Neyenhuis, D. Wang, G. Quéméner, S. Ospelkaus, J. L. Bohn, J. Ye, and D. S. Jin. *Nature Phys.*, **7**, 502–507, 2011.

[119] M. Lara, J. L. Bohn, D. Potter, P. Soldan, and J. M. Hutson. *Phys. Rev. Lett.*, **97**, 183201, 2006.

[120] D. W. Chandler. *J. Chem. Phys.*, **132**, 110901, 2010.

[121] D. J. Wales. *Energy Landscapes*. Cambridge University Press, Cambridge U.K., 2003.

[122] D. Hyatt and L. Stanton. *Proc. Roy. Soc. Lond. A*, **318**, 107–118, 1970.

[123] A. Stone. *The Theory of Intermolecular Forces, Second Edition*. Oxford University Press, Oxford U.K., 2000.

[124] D. C. Clary. *J. Chem. Soc., Faraday Trans.*, **83**, 139–148, 1987.

[125] M. P. Langevin. *Ann. Chim. Phys.*, **5**, 245, 1905.

[126] D. Clary. *Mol. Phys.*, **53**, 3–21, 1984.

[127] S. C. Smith and J. Troe. *J. Chem. Phys.*, **97**, 5451–5464, 1992.

[128] A. I. Maergoiz, J. Troe, and C. Weiss. *J. Chem. Phys.*, **101**, 1885–1889, 1994.

[129] R. N. Zare. *Angular Momentum: Understanding Spatial Aspects in Chemistry and Physics*. Wiley, New York, 1988.

[130] E. E. Nikitin and J. Troe. *Phys. Chem. Chem. Phys.*, **7**, 1540–1551, 2005.

[131] J. Troe. *J. Chem. Phys.*, **87**, 2773–2780, 1987.

[132] J. Troe. *J. Chem. Phys.*, **105**, 6249–6262, 1996.

[133] K. P. Huber and G. Herzberg. *Molecular Spectra and Molecular Structure IV: Constants of Diatomic Molecules*. Van Nostrand Reinhold Co., New York, 1979.

[134] M. Merawa and A. Dargelosl. *J. Mol. Struc. (Theochem.)*, **528**, 37–48, 2000.

[135] M. T. Bell. DPhil Thesis, University of Oxford, 2008.

[136] A. D. Gingell. DPhil Thesis, University of Oxford, 2010.

[137] T. Su and M. T. Bowers. *J. Chem. Phys.*, **58**, 3027–3037, 1973.

[138] T. Su, E. C. F. Su, and M. T. Bowers. *J. Chem. Phys.*, **69**, 2243–2250, 1978.

[139] T. Su and M. T. Bowers. *Int. J. Mass Spectrom.*, **17**, 309–319, 1975.

[140] E. I. Dashevskaya, I. Litvin, E. E. Nikitin, and J.Troe. *J. Chem. Phys.*, **122**, 184311, 2005.

[141] E. I. Dashevskaya, A. I. Maergoiz, J. Troe, I. Litvin, and E. E. Nikitin. *J. Chem. Phys.*, **118**, 7313–7320, 2003.

[142] M. Quack and J. Troe. *Ber. Bunsenges. Phys. Chem.*, **78**, 240, 1974.

[143] E. J. Rackham, F. Huarte-Larranaga, and D. E. Manolopoulos. *Chem. Phys. Lett.*, **343**, 356–364, 2001.

[144] E. J. Rackham, T. Gonzalez-Lezana, and D. E. Manolopoulos. *J. Chem. Phys.*, **119**, 012895, 2003.

[145] E. Rackham. DPhil Thesis, University of Oxford, 2004.

[146] D. C. Clary and J. P. Henshaw. *Faraday Discuss. Chem. Soc.*, **84**, 333, 1987.

[147] M. Abramowitz and I. A. Stegum. *Handbook of Mathematical Functions, Tenth Edition.* Dover Publications, New York, 1972.

[148] D. E. Manolopoulos. Ph.D. thesis, University of Cambridge, 1985.

[149] P. Atkins and R. Friedman. *Molecular Quantum Mechanics, Fourth Edition.* Oxford University Press, Oxford U.K., 2005.

[150] C. Leforestier and W. H. Miller. *J. Chem. Phys.*, **002**, 733–735, 1993.

[151] K. F. Riley, M. P. Hobson, and S. J. Bence. *Mathematical Methods for Physics and Engineering, Second Edition*. Cambridge University Press, Cambridge U.K., 2004.

[152] E. E. Nikitin and S. Y. Umanskii. *Theory of Slow Atomic Collisions*. Springer, Berlin, 1984.

[153] S. Kotochigova, P. S. Julienne, and E. Tiesinga. *Phys. Rev. A*, **68**, 022501, 2003.

[154] G. Poulsen, Y. Miroshnychenko, and M. Drewsen. *Phys. Rev. A*, **86**, 051402, 2012.

[155] T. Stoecklin, C. E. Dateo, and D. C. Clary. *J. Chem. Soc. Faraday Trans.*, **87**, 1667–1679, 1991.

[156] T. G. Heil, S. Green, and D. J. Kouri. *J. Chem. Phys.*, **68**, 2562–2583, 1978.

[157] A. Shakespeare. MChem Thesis, University of Oxford, 2011.

[158] S. Y. T. van der Meerakker. Ph.D. thesis, Radboud Universiteit Nijmegen, 2006.

[159] G. B. Fu, L. Z. Deng, and J. P. Yin. *Chinese Phys. Lett.*, **25**, 923, 2008.

[160] D. Boulet and A. Omont. *Astron. Astrophys.*, **61**, 405–410, 1977.

[161] J. Brown and A. Carrington. *Rotational Spectroscopy of Diatomic Molecules*. Cambridge University Press, Cambridge U.K., 2003.

[162] M. H. Alexander. *J. Chem. Phys.*, **76**, 5974–5988, 1982.

[163] A. G. Wickham, T. S. Stoecklin, and D. C. Clary. *J. Chem. Phys.*, **96**, 1053–1061, 1992.

[164] M. Auzinsh, E. I. Dashevskaya, I. Litvin, E. E. Nikitin, and J. Troe. *J. Chem. Phys.*, **128**, 184304, 2008.

[165] E. I. Dashevskaya, I. Litvin, E. E. Nikitin, and J. Troe. *Phys. Chem. Chem. Phys.*, **9**, 1559–1567, 2007.

[166] H. Li, T. Hirano, T. Amano, and R. J. LeRoy. *J. Chem Phys.*, **129**, 244306, 2008.

[167] D. A. Dixon, A. Komornicki, and W. P. Kraemer. *J. Chem. Phys.*, **84**, 3603–3611, 1984.

[168] A. J. Illies, M. F. Jarrold, and M. T. Bowers. *J. Am. Chem. Soc.*, **83**, 2562–2565, 1983.

[169] R. D. Nelson Jr., D. R. Lide, and A. A. Maryott. *Selected Values of Electric Dipole Moments for Molecules in the Gas Phase.* National Bureau of Standards, Gaithersburg U.S.A., 1967.

[170] T. N. Olney, N. M. Cann, G. Cooper, and C. E. Brion. *Chem. Phys.*, **223**, 59–98, 1997.

[171] C. Graham, D. A. Imrie, and R. E. Raab. *Mol. Phys.*, **93**, 49–56, 1998.

[172] C. Asawaroengchai and G. M. Rosenblatt. *J. Chem. Phys.*, **72**, 2664–2669, 1980.

[173] P. F. Barker, S. M. Purcell, P. Douglas, P. Barletta, N. Coppendale, C. Maher-McWilliams, and J. Tennyson. *Faraday Discuss.*, **142**, 2562–2565, 2009.

[174] R. Fulton, A. I. Bishop, and P. F. Barker. *Phys. Rev. Lett.*, **93**, 243004, 2004.

[175] M. T. Bell and T. P. Softley. *Mol. Phys.*, **107**, 99–132, 2009.

[176] F. H. J. Hall and S. Willitsch. *Phys. Rev. Lett.*, **109**, 233202, 2012.

[177] L.Ratschbacher, C. Zipkes, C. Sias, and M. Kohl. *Nature Phys.*, **8**, 649652, 2012.

[178] S. Schmid, A. Harter, A. Frisch, S. Hoinka, , and J. Hecker-Denschlag. *Rev. Sci. Instrum.*, **83**, 053108, 2012.

[179] J. J. Gilijamse, S. Hoekstra, S. A. Meek, M. Metsala, S. Y. T. van der Meerakker, G. Meijer, and G. C. Groenenboom. *J. Chem. Phys.*, **127**, 221102, 2007.

[180] J. H. Blokland, J. Riedel, S. Putzke, B. G. Sartakov, G. C. Groenenboom, and G. Meijer. *J. Chem. Phys.*, **135**, 114201, 2011.

[181] D. Patterson, J. Rasmussen, and J. M. Doyle. *New J. Phys.*, **11**, 055018, 2009.

[182] R. Plastil, T. Mehner, P. Dohnal, T. Kotrik, J. Glosik, and D. Gerlich. *Astrophys. J.*, **737**, 60, 2011.

[183] H. Roberts and T. J. Millar. *Astron. Astrophys.*, **364**, 780–784, 2000.

[184] T. D. Hain, R. M. Moision, and T. J. Curtiss. *J. Chem. Phys.*, **111**, 6797–6806, 1999.

[185] U. Hollenstein, F. Merkt, L. Meyer, R. Seiler, T. P. Softley, and S. Willitsch. *Mol. Phys.*, **105**, 1711–1722, 2007.

[186] M. F. Manning. *J. Chem. Phys.*, **3**, 136–138, 1935.

[187] C. H. Townes and A. L. Schawlow. *Microwave Spectroscopy*. Dover Publications, New York, 1975.

[188] E. A. Cohen and H. M. Pickett. *J. Mol. Spectrosc.*, **93**, 83–100, 1982.

[189] C. P. Endres, H. S. P. Muller, S. Brunken, D. G. Paveliev, T. F. Giesen, S. Schlemmer, and F. Lewen. *J. Mol. Struc.*, **795**, 242–255, 2006.

[190] N. J. Fitch, D. A. Esteves, M. I. Fabrikant, T. C. Briles, Y. Shyur, L. P. Parazzoli, and H. J. Lewandowski. *J. Mol. Spec.*, **278**, 1–6, 2012.

[191] M. Quintero-Perez, P. Jansen, T. E. Wall, J. E. van den Berg, S. Hoekstra, and H. L. Bethlem. *Phys. Rev. Lett.*, **110**, 133003, 2013.

[192] H. L. Bethlem. Ph.D. thesis, Katholieke Universiteit Nijmegen, 2002.

[193] H. L. Bethlem and G. Meijer. *Int. Rev. Phys. Chem.*, **22**, 73–128, 2003.

[194] D. A. Dahl. *Int. J. Mass Spectrom.*, **200**, 3–25, 2000.

[195] D. Patterson, J. Rasmussen, and J. M. Doyle. *New J. Phys.*, **11**, 055018, 2009.

[196] H. J. Lewandowski, E. R. Hudson, J. R. Bochinski, and J. Ye. *Chem. Phys. Lett.*, **395**, 53–57, 2004.

[197] J. Fedor, J. Kocisek, V. Poterya, O. Votava, A. Pysanenko, M. L. Lipciuc, T. N. Kitsopoulus, and M. Farnik. *J. Chem. Phys.*, **134**, 154303, 2011.

[198] J. R. Bochinski, E. R. Hudson, H. J. Lewandowski, G. Meijer, and J. Ye. *Phys. Rev. Lett.*, **91**, 243001, 2003.

[199] W. C. Swope, H. C. Anderson, P. H. Berens, and K. R. Wilson. *J. Chem. Phys.*, **76**, 637–649, 1982.

[200] D. M. Hirst. *A Computational Approach to Chemistry.* Blackwell Scientific, Oxford U.K., 1990.

[201] D. M. Lubman, C. T. Rettner, and R. N. Zare. *J. Phys. Chem.*, **86**, 1129–1135, 1982.

[202] H. L. Bethlem, G. Berden, A. J. A. van Roij, F. M. H. Crompvoets, and G. Meijer. *Phys. Rev. Lett.*, **84**, 5744–5747, 2000.

[203] S. Y. T. van der Meerakker, N. Vanhaecke, H. L. Bethlem, and G. Meijer. *Phys. Rev. A*, **73**, 023401, 2006.

[204] L. Scharfenberg, H. Haak, G. Meijer, and S. Y. T. van der Meerakker. *Phys. Rev. A*, **79**, 023410, 2009.

[205] L. P. Parazzoli, N. Fitch, D. S. Lobser, and H. J. Lewandowski. *New J. Phys.*, **11**, 055031, 2009.

[206] S. A. Meek, M. F. Parsons, G. Heyne, V. Platschkowski, H. Haal, G. Meijer, and A. Osterwalder. *Rev. Sci. Instrum.*, **82**, 093108, 2011.

[207] C. E. Heiner. Ph.D. thesis, Fritz-Haber Institut der Max-Planck-Gesellschaft, Berlin, 2009.

[208] M. Kirste, B. G. Sartakov, M. Schnell, and G. Meijer. *Phys. Rev. A*, **79**, 051401(R), 2009.

[209] S. R. Langford, A. J. Orr-Ewing, R. A. Morgan, C. M. Western, M. N. R. Ashfold, A. Rijkenberg, C. R. Scheper, W. J. Buma, and C. A. de Lange. *J. Chem. Phys.*, **108**, 6667–6680, 1998.

[210] R. Rao and A. Bhutani. *Int. J. Mass. Specrom.*, **202**, 31–36, 2000.

[211] C. E. Heiner, H. L. Bethlem, and G. Meijer. *Phys. Chem. Chem. Phys.*, **8**, 2666–2676, 2006.

[212] R. Latham. *High Voltage Vacuum Insulation: Basic Concepts and Technological Practice*. Academic Press, London, 1995.

[213] H. J. Lewandowski. Private communication, 2013.

[214] S. Y. T. van der Meerakker, N. Vanhaecke, H. L. Bethlem, and G. Meijer. *Phys. Rev. A*, **71**, 053409, 2005.

[215] J. M. Oldham. DPhil Thesis, University of Oxford, 2013.

[216] S. Earnshaw. *Trans. Camb. Phil. Soc.*, **7**, 97–112, 1842.

[217] R. Blatt, P. Gill, and R. C. Thompson. *J. Mod. Optic.*, **39**, 193–220, 1992.

[218] K. Sheridan and M. Keller. *New J. Phys.*, **13**, 123002, 2011.

[219] E. Fisher. *Z. Phys.*, **156**, 1–26, 1959.

[220] G. Gabrielse. *Int. J. Mass. Spectrom.*, **251**, 273–280, 2006.

[221] K. Blauma, Y. N. Novikovb, and G. Werth. *Contemp. Phys.*, **59**, 149–175, 2009.

[222] R. Blumel. *Phys. Rev. A*, **51**, R30–R33, 1994.

[223] Q. Hu, R. J. Noll, H. Li, A. Makarov, M. Hardman, and R. G. Cooks. *Z. Phys.*, **156**, 1–26, 1959.

[224] J. R. Gibson and S. Taylor. *Rapid Comm. Mass Spectrom.*, **40**, 1960–1964, 2001.

[225] M. Drewsen and A. Broner. *Phys. Rev. A*, **62**, 045401, 2000.

[226] J. Prestage, G. Dick, and L. Maleki. *J. Appl. Phys.*, **66**, 1013–1017, 1989.

[227] W. D. Phillips. *Rev. Mod. Phys.*, **3**, 721–741, 1998.

[228] M. Kasevich and S. Chu. *Phys. Rev. Lett.*, **69**, 1741–1744, 1992.

[229] H. Schnitzler, U. Frohlich, T. K. W. Boley, A. E. M. Clemen, J. Mlynek, A. Peters, and S. Schiller. *Appl. Opt.*, **41**, 7000–7005, 2002.

[230] D. M. Lucas, A. Ramos, J. P. Home, M. J. McDonnell, S. Nakayama, J.-P. Stacey, S. C. Webster, D. N. Stacey, and A. M. Steane. *Phys. Rev. A*, **69**, 012711, 2004.

[231] G. Ritter, S.-M. Bae, and U. Eichmann. *Appl. Phys. B*, **66**, 609–612, 1998.

[232] J. Jin and D. A. Church. *Phys. Rev. Lett.*, **70**, 3213–3216, 1993.

[233] P. F. Bernath. *Spectra of Atoms and Molecules*. Oxford University Press, Oxford U.K., 1995.

[234] T. Gudjons, B. Hilbert, P. Seibert, and G. Werth. *Europhys. Lett.*, **33**, 595–598, 1996.

[235] J. Emsley. *The Elements*. Oxford University Press, Oxford U.K., 1995.

[236] E. L. Pollack and J.-P. Hansen. *Phys. Rev. A*, **8**, 3110–3122, 1973.

[237] R. Hasse and J. P. Schiffer. *Ann. Phys.*, **203**, 419–448, 1990.

[238] D. H. E. Dubin and T. M. O'Neil. *Rev. Mod. Phys.*, **71**, 87–172, 1999.

[239] W. L. Slattery, G. D. Doolen, and H. E. DeWitt. *Phys. Rev. A*, **21**, 2087–2095, 1980.

[240] D. J. Wineland, J. C. Berquist, W. M. Itano, J. J. Bollinger, and C. H. Manney. *Phys. Rev. Lett.*, **59**, 2935–2938, 1987.

[241] D. F. Shriver and P. W. Atkins. *Inorganic Chemistry, Third Edition*. Oxford University Press, Oxford U.K., 1999.

[242] M. T. Bell, A. D. Gingell, J. M. Oldham, T. P. Softley, and S. Willitsch. *Faraday Discuss.*, **142**, 73–91, 2009.

[243] P. Blythe, B. Roth, U. Frohlich, H. Wenz, and S. Schiller. *Phys. Rev. Lett.*, **95**, 183002, 2005.

[244] A. Ostendorf, C. B. Zhang, M. A. Wilson, D. Offenberg, B. Roth, and S. Schiller. *Phys. Rev. Lett.*, **97**, 243005, 2006.

[245] D. Offenberg, C. B. Zhang, C. Wellers, B. Roth, and S. Schiller. *Phys. Rev. A*, **78**, 061401, 2008.

[246] D. Meschede. *Optics, light and lasers, second edition.* Wiley-VCH, Weinheim, Germany, 2007.

[247] M. Stellpflug, M. Johnsson, I. D. Petrova, and T. Halfmannb. *Eur. Phys. J. D*, **23**, 35–42, 2003.

[248] H.-A. Bachor, P. J. Manson, and R. J. Sandeman. *Opt. Comm.*, **43**, 337–342, 1982.

[249] Z. Zhou. MChem Thesis, University of Oxford, 2013.

[250] T. Matthey. Protomol MD simulation package: protomol.sourceforge.net.

[251] L. Hornekaer, N. Kjaergaaard, A. M. Thommesen, and M. Drewsen. *Phys. Rev. Lett.*, **10**, 1994–1997, 2001.

[252] J. M. Oldham. MChem Thesis, University of Oxford, 2007.

[253] A. Savitzky and M. J. E. Golay. *Anal. Chem.*, **36**, 1627–1639, 1964.

[254] M. Martinez-Sanchez and J. E. Pollard. *J. Propul Power*, **14**, 688–699, 1998.

[255] A. C. Cheung, D. M. Rank, C. H. Townes, D. D. Thornton, and W. J. Welch. *Phys. Rev. Lett.*, **21**, 1701–1705, 1968.

[256] D. F. Wang, A. Takahashi, Y. Matsumoto, K. M. Itoh, Y. Tamamoto, T. Ono, and M. Esashi. *Nanotechnology*, **16**, 990–994, 2005.

[257] D. J. Levandier and Y. H. Chiu. *J. Chem. Phys.*, **133**, 154304, 2010.

[258] M. Chau and M. T. Bowers. *Chem. Phys. Lett.*, **44**, 490–494, 1976.

[259] R. Derai, G. Mauclaire, and R. Marx. *Chem. Phys. Lett.*, **86**, 275–280, 1982.

[260] N. G. Adams, D. Smith, and E. Alge. *J. Phys. B: At. Mol. Opt. Phys.*, **13**, 3235–3246, 1980.

[261] K. Giles, N. G. Adams, and D. Smith. *J. Phys. B: At. Mol. Opt. Phys.*, **22**, 873–883, 1989.

[262] K. Molhave and M. Drewsen. *Phys. Rev. A*, **62**, 011401, 2000.

[263] X. Tong, T. Nagy, J. Y. Reyes, M. Germann, M. Meuwly, and S. Willitsch. *Chem. Phys. Lett.*, **547**, 1–8, 2012.

[264] N. Deb. Private communication, 2013.

[265] M. T. Bell. Private communication, 2011.

[266] J. Bentley, B. J. Cotterell, A. Langham, and R. J. Stickland. *Chem. Phys. Lett.*, **332**, 85–92, 2000.

[267] M. N. R. Ashfold, R. N. Dixon, R. J. Stickland, and C. M. Western. *Chem. Phys. Lett.*, **138**, 201–208, 1987.

[268] D. H. E. Dubin. *Phys. Rev. Lett.*, **71**, 2753–2756, 1993.

[269] L. Hornekaer, K. Kjaergaar, A. M. Thommesen, and M. Drewsen. *Phys. Rev. Lett.*, **86**, 1994–1997, 2001.

[270] B. C. Sawyer, B. K. Stuhl, B. L. Lev, J. Ye, and E. R. Hudson. *Eur. Phys. J. D*, **48**, 197–209, 2008.

[271] G. Bieri, F. Burger, E. Heilbronner, and J. P. Maier. *Helv. Chim. Acta*, **60**, 2213–2233, 1977.

[272] N. Kjaergaard, K. Molhave, and M. Drewsen. *Phys. Rev. E*, **66**, 015501(R), 2002.